Université Fédérale
Toulouse Midi-Pyrénées

THÈSE

En vue de l'obtention du
DOCTORAT DE L'UNIVERSITÉ DE TOULOUSE

Délivré par l'Université Toulouse 3 - Paul Sabatier

Présentée et soutenue par

Bastien DAUPHIN

Le 14 décembre 2022

Dynamique de microdomaines pariétaux pendant le développement des cellules sécrétrices du mucilage

---

Ecole doctorale : **SEVAB - Sciences Ecologiques, Vétérinaires, Agronomiques et Bioingenieries**

Spécialité : **Developpement des plantes, interactions biotiques et abiotiques**

Unité de recherche :
LRSV - Laboratoire de Recherche en Sciences Végétales

Thèse dirigée par
Vincent BURLAT

Jury

Mme Gwyneth INGRAM, Rapporteure
M. Herman HöFTE, Rapporteur
M. Vincent BURLAT, Directeur de thèse
M. Christophe DUNAND, Président

Résumé

Les cellules sécrétrices du mucilage (CSM) de la graine d'*Arabidopsis thaliana* sont responsables de la synthèse et du relargage d'un mucilage pectique. Une fois réhydraté, le mucilage gonfle, rompant le sommet de la paroi radiale primaire, et s'étale vers l'extérieur. Le mucilage maintient son organisation et son adhérence grâce à son lien avec la columelle, un pilier cellulosique en forme de volcan au centre des CSM. Une extrusion correcte nécessite l'affaiblissement préalable du sommet de la paroi radiale primaire. Cela se fait par l'intermédiaire de *PEROXIDASE36* dans une zone de remodelage localisée constituant un microdomaine pariétal. PRX36 est ancrée grâce à un motif de méthylestérification sur des homogalacturonanes (HGs) créé par PECTIN METHYL ESTERASE INHIBITOR6 agissant sur une PME inconnue. Ce travail a pour but d'identifier d'autres membres de cet échafaudage moléculaire requis pour la libération du mucilage, ainsi que d'évaluer la dynamique et la fonction d'autres *PRXs* exprimées par les CSM pendant le développement de la graine.

Un premier criblage de 5 gènes ayant une co-expression spatiotemporelle avec *PRX36* a mis en évidence l'accumulation apoplastique similaire de PRX36, PMEI6 et deux autres PMEs dans ce microdomaine pariétal. Le degré de méthylestérification des HGs et ses conséquences sur l'ancrage de PRX36 ont été évalués, ce qui a mis en évidence une probable redondance fonctionnelle de PME16 et PME6/HMS dans la régulation de la méthylestérification de l'HG. Les criblages ont également mis en évidence *TBL38*, une autre enzyme de remodelage pariétal.

Une analyse intégrée de *TBL38* a révélé que TBL38 a une localisation pariétale contrairement à la plupart des *TBLs*; et qu'elle avait une activité acétylestérase atypique sur l'HG qui n'a jamais été observée chez d'autres TBLs. L'augmentation de l'acétylation des HGs chez *tbl38* a modifié l'affinité de l'HG pour effectuer des liaisons avec Ca^{2+}, ce qui pourrait faciliter l'ancrage de PRX36 comme le suggère une simulation informatique d'ancrage PRX36-HG.

Enfin, les tests de relargage du mucilage ont mis en évidence que *PRX56* pourrait être associé à la rigidification du sommet de la columelle. PRX56 s'accumule au sommet de la columelle près d'épitopes de protéines structurales de type extensines. Nos premiers résultats suggèrent que PRX56 pourrait polymériser localement des extensines pour renforcer la connexion entre columelle et la paroi primaire. Nous discutons de la possibilité d'un échafaudage moléculaire

similaire parallèle à celui de PRX36 qui pourrait expliquer l'accumulation différentielle de PRX56 dans un autre microdomaine pariétal du même type cellulaire.

Mots clés : *Arabidopsis thaliana*, microdomaines pariétaux, peroxydase, remodelage d'homogalacturonanes, TBL, acétylation

Abstract

Arabidopsis thaliana seed mucilage secretory cells (MSCs) are responsible for the synthesis and extrusion of a pectinaceous mucilage. Once rehydrated, the mucilage swells and expands manyfold; breaking the top of radial primary wall and expanding outwards. Mucilage maintains its organization and adherence through its linkage to the volcano-shaped columella, a cellulosic pillar at the center of MSCs. Proper extrusion requires the pre-weakening of the primary wall. This is done through PEROXIDASE36-mediated wall loosening in a local hotspot of remodeling situated in a wall microdomain. PRX36 is anchored there due to a pattern of methylesterification in homogalacturonan (HGs) created by PECTIN METHYL ESTERASE INHIBITOR6 working on (an) unknown PME(s). This work aims to identify other members of the PRX36-PMEI6 molecular scaffold required for mucilage release, as well as assessing the dynamics and function of other MSC-expressed *PRXs* during seed development.

Initial screening of 5 genes with spatiotemporal co-expression with *PRX36* highlighted similar apoplastic accumulation of PRX36, PMEI6 and two other PMEs in this wall microdomain. HG methylesterification status and subsequent consequence for PRX36 anchoring were evaluated which pointed to probable redundancy of PME16 and PME6/HMS in regulation of HG methylesterification. Screenings also highlighted *TBL38*, another putative wall remodeling enzyme.

Integrated analysis of *TBL38* revealed that TBL38 was a cell wall localized protein unlike most TBLs, and had an atypical acetylesterase activity on HG which was never observed. Increased *tbl38* acetylation modified HG affinity to Ca^{2+} binding which could facilitate PRX36 anchoring as suggested by *in silico* molecular docking.

Finally, tests of mucilage release defect highlighted *PRX56* which may be associated with wall stiffening. PRX56 accumulates at the top of the columella near epitopes of extensin structural proteins. We gave preliminary evidence suggesting that PRX56 could crosslink extensins to strengthened columella and primary wall connection and discuss the possibility of similar molecular scaffold to those of PRX36 which could explain PRX56 differential accumulation to another wall microdomain.

Key words: *Arabidopsis thaliana*, cell wall microdomain, peroxidase, homogalacturonan remodeling, TBL, acetylation

Remerciements

Devrais-je écrire pour tous ou pour chacun, et ainsi prendre le risque d'oublier quelqu'un ? Trois années plus tard, testons donc ma mémoire des noms.

Je souhaite d'abord remercier mes rapporteurs Gwyneth Ingram et Herman Höfte pour avoir accepté de prendre du temps afin d'évaluer mon manuscrit et Christophe Dunand pour l'éxamen de mes travaux. Merci aussi aux membres de mes comités de thèse : Marie-Christine Ralet, Jérôme Pelloux et Gregory Vert.

Merci à tous les membres du LRSV

Je remercie ensuite toute l'équipe Paroi ou « Dynamique et Evolution des Parois cellulaires végétales » comme on dit ces jours-ci, pour m'avoir accueilli depuis mon premier stage de Master. En particulier, je remercie Vincent pour m'avoir fait découvrir les merveilles de la paroi, mais aussi pour ton encadrement, ta pédagogie et SURTOUT pour toutes les expressions que j'ai pu apprendre. Peut-être qu'un jour, je pourrai apprendre à des nouvelles générations les joies des « retour chariots ». Du début jusqu'à la fin de thèse, c'était un plaisir de partager avec toi et même s'il me semble qu'on a tout les deux une tendance à parfois s'égarer dans plein de « projet annexes super intéressants », je garde affectueusement en mémoire les réunions de comptoirs et l'éveil des 17h.
Bien entendu, je remercie également Christophe, Josianne et David pour leur sympathie et les discussions, sans oublier Philippe et à tous les membres du projet ANR « MicroWall » pour la collaboration pendant certaines partie de ma thèse et Elisabeth pour tous ses conseils.

Merci à tous ceux qui ont partagé une place dans ce bureau ou celui d'à côté. Beaucoup ne sont plus là, mais les souvenirs demeurent.
Merci à Sebastien pour toutes les conversations philosophico-politico-ecolo-culturo-miammiamLeFromage qu'on a pu avoir et ta sympathie depuis ce stage de 2ème année. Je suis désormais addicte aux tomates séchées, aussi mon estomac te remercie aussi fort que mon budget te hait.
Merci à Ali, Hassan, Thomas pour leur amitié et l'incroyable quantité de nourriture qu'ils ont donné. Depuis votre départ, ma glycémie n'a plus jamais été la même.
Merci à Aurèlie pour ton amitié, les idées de rando et tous les échanges qu'on a pu avoir. Je n'ai jamais rencontré Monsieur T mais pourtant j'en rigole encore.

Merci à Fabien Nirina-Ramamonjy avec qui j'ai pu travailler pendant ton stage de Master 2. Ton enthousiasme et ta simplicité n'ont d'égale que tes compétences au Scrabble.
Merci à Karima pour toutes les conversations, le tour sur ton vélo d'compet, les 2.5kilos journalier de céréales qui te suivent perpétuellement et le soutient pendant cette fin de thèse (note que les deux derniers points sont assez liés). Tu ne fais pas partie de l'équipe mais tu finissais tellement souvent dans le bureau que tu as la place dans cette partie.

Je remercie bien sur la plateforme imagerie, toujours disponible et à l'écoute pour améliorer les observations -*SpinningDiskForever*-, la FRAIB pour l'aide apportée sur les chambres de cultures et le service culture qui ont tout fait pour améliorer nos conditions.

Enfin je souhaite remercier l'ensemble du LRSV, et particulièrement tous les « non-permanents» avec qui j'ai pu interagir, rigoler, jardiner, boire&manger. Je ne prendrai ici pas le risque de vous citer par peur de vous oublier. J'espère que vous savez, chacun, à quel point j'ai pris plaisir à partager ces années depuis le début de thèse ou de master avec vous. Je suis traditionnellement un hermite, aussi j'espère que vous m'excuserez de ne pas toujours avoir été présent à tous les évènements.

<u>Merci à ma famille et mes proches</u>

A l'écriture de ces mots, je pèse la chance qui m'a suivi pendant toute ma vie. Celle d'avoir été dans une famille qui m'a donné les meilleurs fondements possibles pour réussir. Éducation, resilience (ou comme on dit, SOLIDE), franchise, mais peut-être le plus important de tout, la curiosité. Vous m'avez toujours poussé à aller chercher ce que je souhaitais faire plutôt qu'un idéal de société ; bientôt 27 ans plus tard, je suis satisfait du résultat. Pour toutes ces raisons, et pour bien d'autre qui constituent une thèse en soi, merci à mes parents pour tout. Merci à mon frère, mon troisième pilier, pour tout cela et plus, pour l'ouverture culturelle, historique, et de m'avoir montré le chemin du Doctorat. *Solide*. (Officiellement tu fais toujours que 1m79, navré)

Merci à tous mes potes, l'idiot d'Arnaud, Tristan, Tom, Guillaume, l'autre idiot-bien-plus-idiot-encore d'Arnaud, Maxence et d'autres, pour les conneries, (les b1), les JDR, les sessions jeux et le soutien moral pendant la thèse sous forme de « bon t'as fini ? » « Elle est où ta thèse ? » « Ah tu peux pas partir en vacances faut que t'écrives ta thèse, c'est pas de chance ». C'est finalement la marque des vrais amis. J'ai une pensée particulière pour Arnaud et son permis, petit ange parti trop tôt au côté du Roi Soleil et son fidèle vélo, ainsi que petite Fleur défilant au 14 juillet.

Enfin, merci à mon petit soleil qui brille très fort à mes cotés depuis bientôt 6 ans. Encore maintenant c'est avec fierté que je te vois grandir (clairement, pas littéralement) et endurer bien des défis avec chaque semaine une force renouvelée. Merci pour tous les efforts que tu as dû faire quand le travail me rattrapait, et merci pour tout nos moments. Des mois plus tard, on l'a eu ce foutu puzzle. Peu de gens savent à quel point mon hyperactivité peut être épuisante ; j'ignore comment tu supportes mais ton sacrifice ne sera pas oublié.

Merci également à toute la famille Invernizzi, proche ou éloignée, pour m'avoir accueilli comme un des leurs, me laisser finir les plats et le limoncello.

Merci à Paint, Thesaurus et les pates sans qui rien n'aurait été possible.

Ah ouai y'a le chat aussi. Merci au gros tas d'poil pour les réveils 5h du mat et ses gouins. Vraiment, un plaisir. J'suis certain que ça partira facilement sur Leboncoin c'truc là…

À quiconque lirait jusqu'ici, j'offre la connaissance ultime : n'oubliez pas de vous hydrater correctement (environ 300 ml d'eau par 10kg de poids de corps) surtout en été (presque le double)
N'oubliez pas non plus que si vous avez un jour une assiette à finir, je ne serai jamais très loin.



Table des matières

Table des matières
Résumé ... 1

Abstract ... 3

Key words: *Arabidopsis thaliana*, cell wall microdomain, peroxidase, homogalacturonan remodeling, TBL, acetylation ... 3

Remerciements ... 4

Table des matières ... 7

1. Chapter one : Introduction ... 12

1.1. The primary cell wall ... 12

1.1.1. Cellulose ... 13

1.1.2. Hemicelluloses ... 14

1.1.3. Pectins ... 15

1.1.4. Golgi maturation of polysaccharides ... 16

1.1.4.1. Acetylation in the Golgi ... 17

1.1.4.1.1. REDUCED WALL *O*-ACETYLATION (RWA) ... 18

1.1.4.1.2. ALTERED XYLOGLUCAN ACETYLATION 9 (AXY9) and TRICHOME-BIREFRINGENCE-LIKE (TBLs) ... 18

1.1.4.2. De-acetylation by GDSL-esterases in the Golgi ... 19

1.1.4.3. Methylation in the Golgi ... 19

1.1.4.3.1. Hemicellulose methyl transferase in the Golgi ... 20

1.1.4.3.2. Pectin methyl transferase in the Golgi ... 20

1.1.5. Cell wall proteins ... 21

1.1.5.1. Diversity of CW proteins ... 21

1.1.5.2. Pectin acetyl esterases (PAEs) ... 22

1.1.5.3. Pectin methyl esterases (PMEs) ... 23

1.1.5.4. Pectin methyl esterase inhibitors (PMEIs) ... 25

1.1.5.5. Pectate lyases (PLs) and pectin lyases (PNLs) ... 26

1.1.5.6. Polygalacturonases (PGs) ... 26

1.1.5.7. Class III Peroxidases (CIII-PRXs) ... 28

1.1.5.8. Extensins (EXTs) ... 29

1.2. Introduction to the review article: ... 31

1.2.1. Cell wall microdomain remodeling controls critical developmental processes (Published review) ... **Erreur ! Signet non défini.**

1.3. *Arabidopsis thaliana* seed ... 51

1.3.1. Mucilage secretory cells (MSC) ... 51

1.3.1.1. The mucilage ... 51

1.3.1.2. The columella ... 53

1.3.1.3. The primary wall ... 53

1.4. Context and objectives ... 54

2. Chapter two: *PRX36-PMEI6* seed coat co-expression network is enriched in MSC-expressed genes and CW microdomain co-accumulating proteins ... 55

2.1. Generating a co-expression network focused on PEROXIDASE36 expression ... 56

2.2. The expression of four candidate genes is restricted to the MSCs ... 59

2.3. Mucilage release assays show contrasted phenotypes ... 61

2.4. Generating specific MSC wall surface-enriched fractions ... 62

2.5. Immunodotblots on MSC surface wall extracts show TBL38 involvement in HG remodeling - Immunofluorescence on paraffin sections shows HG methylation status on a spatial scale ... 65

2.6. PRX36 localization is unaffected in candidate gene mutants ... 71

2.7. Tag-RFP fusions of PMEI6, TBL38, PME6 and PME16 co-localized with PRX36 in this CW microdomain ... 73

2.8. Discussion ... 77

2.9.1. The *PRX36*/*PMEI6* co-expression network is enriched in MSC-specific candidate genes. ... 77

2.9.2. Different scale phenotyping provides complementary results though it did not identify clear actors of PRX36 molecular scaffold. ... 77

2.9.3. The *PRX36*/*PMEI6* co-expression network is enriched in proteins colocalizing with PRX36 to the MSC CW microdomain ... 81

2.9.4. Integrated analysis of results and literature for each candidate gene/mutant and perspectives ... 84

Technical interlude: growth condition and effect of temperature. ... 90

Chapter three: TBL38 is an atypical homogalacturonan acetylesterase with a peculiar cell wall microdomain localization ... 93

3. Introduction ... 94

3.1. Results ... 97

3.1.1. *TBL38* is co-expressed with *PRX36* and *PMEI6* in mucilage secretory cells at intermediate developmental stages of seed development. ... 97

3.2. TBL38-TagRFP is localized to the PRX36-PMEI6 outer periclinal/radial cell wall microdomain ... 99

3.3.* The mucilage release and anchoring of PRX36 are not significantly modified in *tbl38 ... 101

3.2.5. Analysis of dry seed surface-enriched abrasion cell wall fractions indicates that TBL38 displays an atypical acetylesterase activity towards CW polymers rather than the canonical acetyltransferase activity observed in other studied TBLs ... 107

3.2.6. TBL38 is a cell wall localized homogalacturonan acetylesterase ... 110

3.3. Discussion ... 115
3.3.1. TBL38 is atypically positioned in the PRX36/PMEI6 cell wall microdomain of MSCs ... 115
3.3.2. TBL38 as an CW acetylesterase of HG ... 116
3.3.3. HG fine tuning of esterification is affected in *tbl38* ... 118
3.3.4. Increased HG acetylation may benefit PRX36 anchoring ... 119
4. Chapter four: Role of MSC-expressed Class III-peroxidases in remodeling of other putative CW microdomains ... 139
4.1. Introduction ... 140
4.2. Results ... 141
4.2.1. Mucilage release is not impaired in mutated seeds ... 141
4.2.2. PRX56 is a CW protein localized around the top of the columella ... 145
4.2.3. PRX56 putative involvement in extensin polymerization ... 147
4.3. Discussion ... 149
4.3.1. PRX56 may stiffen walls at the top of the columella ... 149
4.3.2. PRX56 may be an extensin peroxidase ... 152
4.3.3. Prospect of a PRX56 docking valley ... 154
4.4. Supplementary data ... 158
5. Chapter five: Conclusions and perspectives ... 168
6. Chapter six: Material and Methods ... 173
6.1. Material ... 174
6.1.1. Plant material and growth conditions ... 174
6.1.1.1. *Arabidopsis thaliana* lines ... 174
6.1.1.2. *Arabidopsis thaliana in vitro* culture ... 176
6.1.1.3. *Arabidopsis thaliana* pot culture ... 176
6.1.1.4. *Nicotiana benthamiana* ... 177
6.1.2. Bacterial growth conditions ... 177
6.1.2.1. *Escherichia coli* ... 177
6.1.2.2. *Agrobacterium tumefaciens* ... 177
6.1.3. Plasmid and vector ... 177
6.1.3.1. Template DNA ... 177
6.1.3.2. Cloning vectors ... 178
6.1.3.3. Subcellular marker and fluorochrome properties ... 183
6.1.4. Primers ... 184
6.1.5. Silique sampling and dry seed storage ... 190
6.1.5.1. Developing seed sampling ... 190

6.1.5.2. Dry seed storage ... 191
6.1.6. Antibodies and histochemical dye ... 191
6.2. Methods ... 193
6.2.1. DNA extraction ... 193
6.2.2. RNA extraction and reverse transcription ... 194
6.2.3. PCR genotyping and DNA amplification ... 194
6.2.4. Agarose gel electrophoresis ... 194
6.2.5. Bacterial plasmid extraction ... 194
6.2.6. Sequencing ... 195
6.2.7. GoldenGate cloning ... 195
***6.2.7.1.* *In silico* assembly** ... 198
6.2.7.2. PCR reactions ... 198
6.2.7.3. Initial Level 0 blocs generation ... 199
6.2.7.4. Ligation in level 0 plasmid and transformation ... 199
6.2.7.5. Golden gate assembly of Level 1 vectors and *E. coli* transformation ... 200
6.2.7.6. Golden gate assembly of Level 2 vectors and *E. coli* transformation ... 200
6.2.7.7. Plasmid integration in *Agrobacterium tumefaciens* ... 203
6.2.8. Glycerol stock generation ... 204
6.2.9. *Agrobacterium tumefaciens*-mediated plant transformation ... 204
6.2.9.1.* *Arabidopsis thaliana ... 204
6.2.9.2.* *Nicotiana benthamiana ... 204
6.2.10. Stable *A. thaliana* transformation screening ... 205
6.2.11. Adherent mucilage release assays and semi-quantitative analysis ... 206
6.2.12. Dry seed MSC surface wall abrasive fraction ... 207
6.2.13. Immuno dotblot and semi-quantitative analysis from dry seed MSC abrasive fractions ... 208
6.2.14. SDS-PAGE and Western-blots from dry seed MSC abrasive fractions ... 210
6.2.15. Acetyl group deesterification and acetic acid semi-quantitative analysis from dry seed MSC abrasive fractions ... 211
6.2.16. Mass spectrometry analyses from dry seed MSC abrasive fractions ... 211
6.2.17. Arabidopsis silique fixation, paraffin tissue array embedding and microtomy ... 212
6.2.18. Developing seed and dry seed resin embedding, and (ultra)microtomy ... 213
6.2.18.1. *In situ* RNA hybridization on serial section of paraffin –embedded tissue arrays ... 213
6.2.19. Immunofluorescence on tissue-array sections ... 214
6.2.20. Confocal spinning disk microscopy of seed development kinetics of *A. thaliana* stable transformants (High throughput strategy) ... 215

6.2.21. Multiphoton confocal microscopy of leaves from *N. benthamiana* transient transformants (High resolution strategy) 216

6.2.22. Scanning electron microscopy 216

6.2.23. *In silico* model and docking simulations 216

General bibliography 218

1. Chapter one : Introduction

The year is 1665. England is oblivious to the upcoming Great Plague major outbreak. Robert Hooke just published *Micrographia*, a book in which he detailed his numerous observations of microscopic life using a primitive microscope. Amongst the superb engravings displaying imperceptible features in a way never seen before, one of the most defining plant characteristics is mentioned: the cell wall (though he was not fully aware of what it was). He went on to make similar observations between cork tissues and wood, which paved the way to forthcoming microbiology study.

More than three centuries after, we are just starting to comprehend the full cell wall dynamics at the ever-so-smaller scale, some of which is described in this manuscript.

1.1. The primary cell wall

The primary cell wall (CW) is an almost ubiquitous structure of the apoplast of each plant cell. Early reports described it as an incredibly complex network of polysaccharides and proteins serving a vast array of functions in each stage of plant development (Schindler, 1998; McNeil et al., 1984). Considering the current accumulated knowledge on primary wall, one might be wise to list the processes in which it is not involved rather than the opposite. Indeed, the primary wall is associated with cellular growth (Chebli and Geitmann, 2017), plant immunity (Malinovsky et al., 2014), response to abiotic stresses (Le Gall et al., 2015), reproduction (Mollet et al., 2013) and so on. Such functional diversity is equally matched with the impressive diversity found between cellular types. One glance at the microscopic level is enough to appreciate the variety of shapes which the primary wall can take. Squared, elongated, puzzle-shaped, pointy, curved… it is as if there is little limit to cell wall shape as long as there is a benefit in undertaking it (**Figure 1.1**). These forms are achieved through the combination of many parameters including the composition of each wall. Although main blocks of the wall architecture are commonly found everywhere, intra/inter-species differences in composition and remodeling can be responsible for major phenotypic traits (Fangel et al., 2012). CW components are synthesized either at the Golgi or the plasma membrane, and secreted, assembled and remodeled at the apoplast. Golgi-localized biosynthesis already encompasses a large panel of precise maturation processes, yet polysaccharides will also be methodically modified in the apoplast by secreted CW proteins. Such processes allow for tight control of CW mechanical properties throught polysaccharides-polysaccharides-proteins tripartite interactions in this complex matrix (Anderson and Kieber, 2020). Parts of this network will be discussed hereafter.

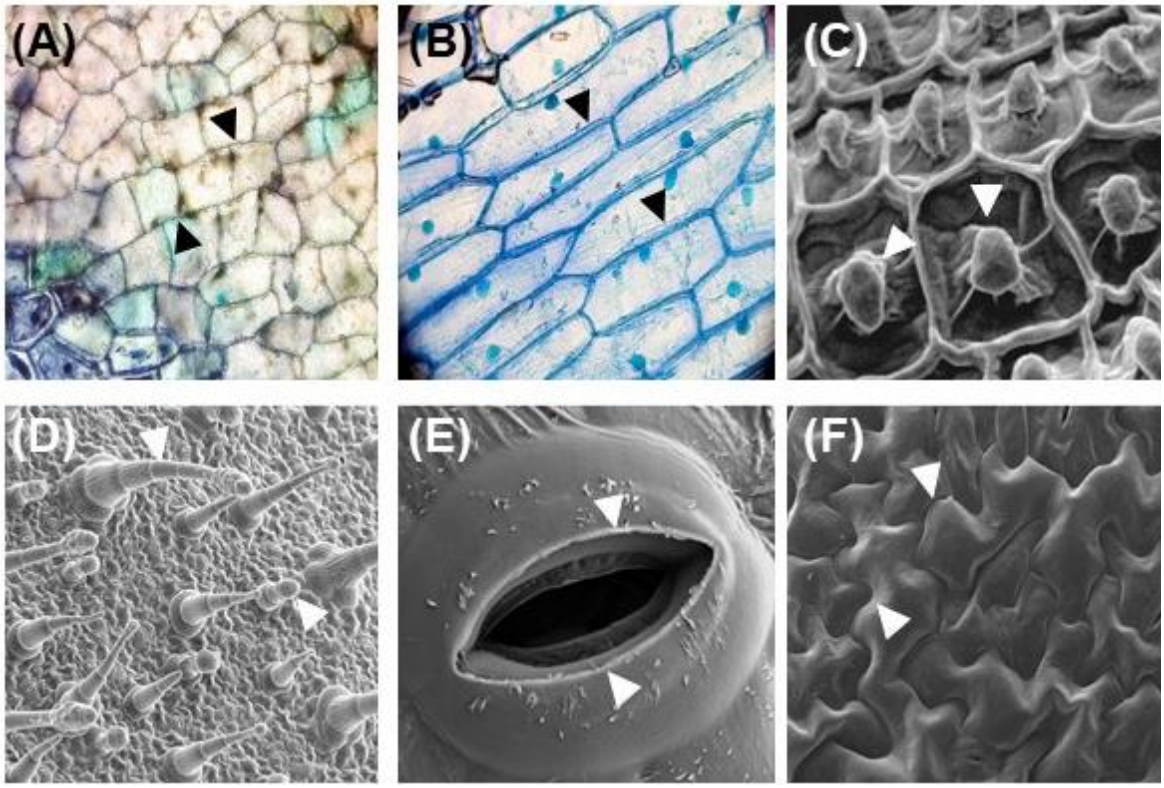

Figure 1.1: Some of the diverse shape of the primary wall across different cell types focusing on the epidermis. **(A)** oignon quared shaped epidermal cells **(B)** Magnolia petal rectangular shaped epidermal cells **(C)** *Arabidopsis thaliana* seed mucilage secretory cells with arrowhead poiting at the volcano-shaped columella **(D-F)** Sequential epidermal sections of different cell types showing diverse cellular shape specialization. **(D)** Trichome **(E)** Open stomata which guard cells (arrowhead) have curved cell wall **(F)** Puzzle-shaped leaf epidermis showing alternate neck of lobe formation (arrowhead). Figure sources are in order from: Umberto Salvagnin (A and B); https://www.flickr.com/photos/kaibara/4482548444/, MSC: this study; Louisa Howard - Dartmouth electron microscope facility; Herrera et al 2020 Journal of experimental botany; Geitmann et al 2019 https://www.biorxiv.org/content/10.1101/563403v1.full

1.1.1. Cellulose

Cellulose is arguably one of the main blocks (15-40%) participating in the load-bearing properties of the primary wall (Cosgrove and Jarvis, 2012). It is made of β-(1→4) bound glucose units (**Figure 1.2**) organized in microfibrils as a ribbon-shaped polymers whose size can vary (McFarlane et al., 2014; McNamara et al., 2015). It is one of the few CW polymers which is directly synthesized at the plasma membrane. Indeed, cellulose biosynthesis is done by a diverse set of glycosyltransferases (GTs) organized in a membrane bound Cellulose Synthase Complex (CESA) (Anderson and Kieber, 2020; McNamara et al., 2015). It was noted that microfibril orientation was dependent on microtubule which predominantly guide CESAs (Chan and Coen, 2020). In the wall, cellulose can interact with hemicelluloses (Somerville et al., 2004) and pectins (Griffiths and North, 2017) which creates this dense structure of remarkable mechanical properties.

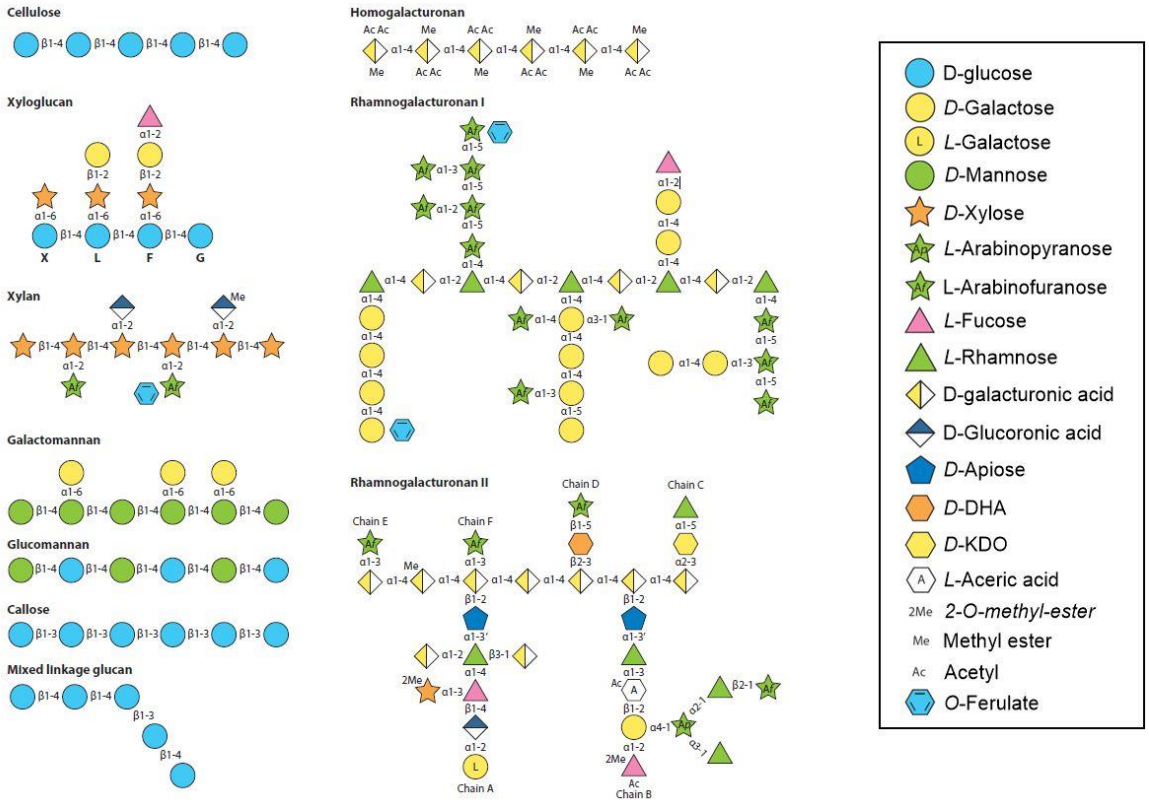

Figure 1.2: Schematic examples of the structures of cell wall polysaccharides. The composition of main CW polymers is described though this is not a comprehensive list. Adding to the complexity of CW is the possible polysaccharide interactions which creates the so-called CW matrix and is not represented here. Structures of polysaccharides, especially of side chains, are not comprehensive. (extracted from Anderson and Kieber 2020).

1.1.2. Hemicelluloses

As suggested by the deliberate use of the plural, the generic term hemicelluloses encompasses different β-(1→4)-linked polysaccharidic backbones such as xyloglucans, xylans and (gluco) mannans (Scheller and Ulvskov, 2010). Their backbones can be highly branched with different residues which participate to the diversity of this class of polysaccharides (**Figure 1.2**). It should be noted that the presence, diversity and amounts of quoted hemicelluloses greatly varies at the inter-species level (Scheller and Ulvskov, 2010). For instance, Xyloglucans can make up to 20 % of primary wall dry mass in many dicotyledons but as little as 5 % in Grasses (Park and Cosgrove, 2015). They are synthesized by an array of glycosyltransferases in the Golgi, some of which are well described. Although hemicelluloses have been associated with various biotic / abiotic phenotypes (Le Gall et al., 2015), one of their main role is to fortify the primary wall. Indeed, xyloglucans can non-covalently bind and crosslink cellulose microfibrils which may participate in overall wall stiffening, although not mandatory (Park and Cosgrove, 2015). In the

wall, hemicelluloses are dynamically remodeled through enzymatic activity to accommodate for current needs of CW properties and the control of cellulose-xyloglucan interactions is crucial during cell elongation (Scheller and Ulvskov, 2010).

1.1.3. Pectins

Pectins are the last main Golgi synthesized polymers which comprise 40-50 % of primary wall dry mass (Cosgrove and Jarvis, 2012), unequally distributed in homogalacturonan (HG), rhamnogalacturonan-I (RG-I) and II (RG-II) as that mass is mostly explained by HGs (Mohnen, 2008). HG is made of α-(1→4) linked galacturonic acids (GalA) which can be dynamically methylesterified and acetylated (**Figure 1.2**) as detaild in the next section. HG is not branched contrary to RG-I whose backbone is a repeat of Rhamnose α-(1→4)-GalA α-(1→2)-Rhamnose often linked to side chain features like galactans, arabinans or arabinogalactans (Ridley et al., 2001). Finally, RG-II are complex polymers with similar backbone to HG, although branched with a very high diversity of specific sugars (**Figure 1.2**) (Bar-Peled et al., 2012). As a whole, pectins are described as a gel-like matrix interacting with one another as well as other cellular components to regulate CW mechanical properties. For instance, HG, which was the most extensively described pectin component, can interact with cellulose to assume some of its load-bearing properties (Lin et al., 2016; Lopez-Sanchez et al., 2016). It is involved in wall elasticity which is critical to large amounts of developmental processes, including cellular growth, reproduction, cell adhesion (Mollet et al., 2013; Hocq et al., 2017b; Wolf et al., 2009; Driouich et al., 2007). Additionally, HG can be cleaved by various enzymes which creates small oligolacturonides that are crucial for control of CW integrity in plant-microorganism interactions (Ferrari et al., 2013; Shin et al., 2021). Finaly, HG can be crosslinked throught Ca^{2+} binding which creates a so-called “egg box” structure (**Figure 1.3A**) which is associated with CW stiffening (Brett and Waldron, 1990).

1.1.4. Golgi maturation of polysaccharides

The functional diversity which is observed in both hemicelluloses and pectins -particularly in HG- can sometimes be explained with chemical modifications like acetylation and methylation (**Figure 1.3B and C**). Such a maturation process first takes place in the Golgi right after biosynthesis by sets of proteins, although particular actors as well as some biomolecular pathway have yet to be fully elucidated.

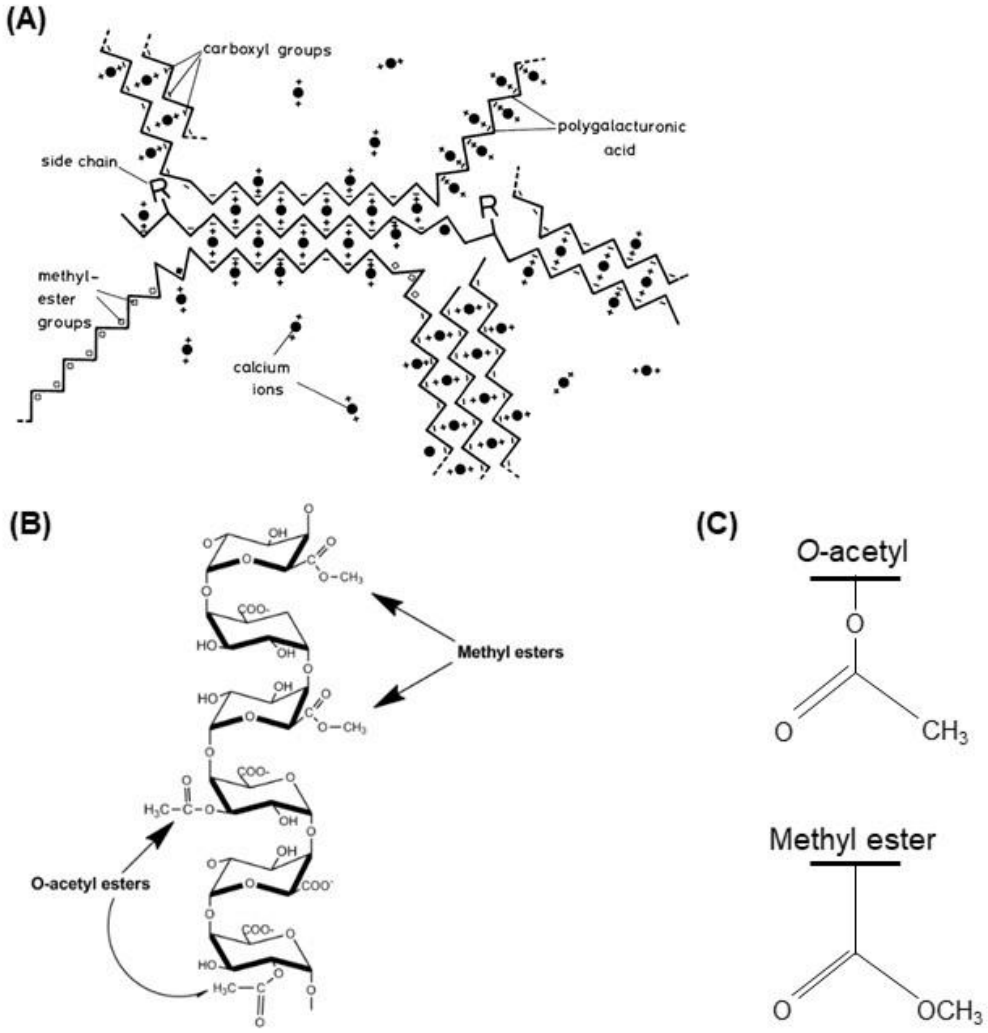

Figure 1.3 : Homogalacturonan egg box structure and maturation. (A) Simplified egg-box model extracted from (Brett and Waldron 1990) showing cross-linking between unsubstituted polygalacturonic acid and the factors that are likely to influence such cross-linking within the cell wall **(B)** Extrated from (Ochoa et al 2012). Homogalacturonan is a linear polymer of α-(1→4)-D galacturonic acid with methyl-esterified at C-6 and acetyls at positions *O*-2 and/or *O*-3. **(C)** Close-up representation of both *O*-acetyl group and Methyl ester group highlighting great structural similarity.

1.1.4.1. Acetylation in the Golgi

In the last decade, technical advancement allowed for great progress to study the occurrence and influence of polysaccharide *O*-acetylation during plant development. In the primary wall, this process is mainly restricted to xyloglucans, arabinoxylans, mannans as well as all pectic components (Gille and Pauly, 2012). The position of *O*-acetylation can vary with each polysaccharides, and inter-species variance of total acetylation was also observed (Gille and Pauly, 2012; Pauly and Ramírez, 2018). Disruption of the polysaccharide acetylation is associated with different developmental processes, such as CW integrity, biotic/abiotic stress

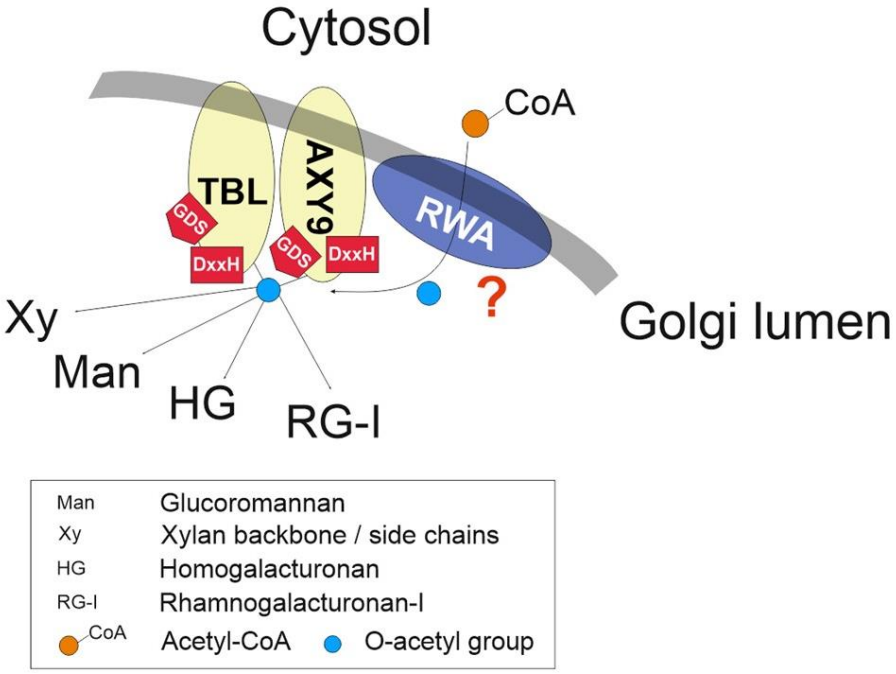

Figure 1.4: Golgi *O*-acetyation of CW polymers In the current paradigm, RWA proteins could transfer acetyl moieties from cytosolic acetyl-CoA in the Golgi which would then be transferred to TBLs via AXY9. TBLs catalyzes *O*-acetylation of various CW polymers supposedly in a gene-polymer specific manner. TBLs possess conserved GDS and DxxH motif similar to AXY9 though the latter activity was never demonstrated. Note that no experimental evidence has yet proven such interplay between RWA, AXY9 and TBLs. **Adapted from Pauly and Ramírez (2018).**

resistance and plant reproduction which further emphasizes the importance of *O*-acetylation and the actors responsible for it (Gou et al., 2012; Gao et al., 2017; Grantham et al., 2017; Chiniquy et al., 2019; Tian et al., 2021). Current data has identified three multigenic families of mostly Golgi-localized proteins that are described as acetyltransferases: ALTERED XYLOGLUCAN ACETYLATION9 (AXY9), REDUCED WALL O-ACETYLATION (RWA) and TRICHOME-BIREFRINGENCE-LIKE (TBLs) (**Figure 1.4**); all of which are also

further detailed in the introduction of Chapter 3 devoted to the characterization of a TBL candidate.

1.1.4.1.1. REDUCED WALL *O*-ACETYLATION (RWA)

Golgi *O*-acetylation implies the presence of an acetyl donor in this cellular compartment. Although capable of serving as such, acetyl-CoA cannot freely pass through Golgi membrane which suggests additional steps required for an adequate acetyl donor to be available (Oliver et al., 2009). The RWA family is only comprised of 4 members in *A. thaliana* (Manabe et al., 2011) that possess 10 predicted transmembrane domains (compare to only one in AXY9 / TBLs) and that are associated with non-specific *O*-acetylation of polymers. As such, it is hypothesized that RWAs transfers acetyl-CoA in the Golgi for AXY9 and TBLs activity (**Figure 1.4**).

1.1.4.1.2. ALTERED XYLOGLUCAN ACETYLATION 9 (AXY9) and TRICHOME-BIREFRINGENCE-LIKE (TBLs)

Actual acetylation of hemicelluloses is done by the non-specific activity of AXY9 whereas TBLs activity is more specific on a gene-to-gene basis. Both genes harbor similar conserved DxxH and GDS motif which were historically associated with opposite lipase/ esterase-type enzymes but rather linked to acetyltransferase activity in this context (**Figure 1.4**). AXY9 enzymatic activity was never formerly demonstrated and is rather thought to produce acetylated intermediates which can be used by TBLs (Schultink et al., 2015; Pauly and Ramírez, 2018). In the last decade, 21 out of the 46 *A. thaliana* TBLs members were described as acetyltransferases acting on xylan, glucomannan, xyloglucan, RG-I and homogalacturonan in a gene-dependent manner. The DxxH / GDS motif forms the catalytic site which is stabilized by a nearby Asparagine (Lunin et al., 2020; Zhong et al., 2017). It hydrolyses the acetyl moieties of the donor through the generation of an acyl enzyme intermediate. The following transfer reaction to the acceptor is likely stabilized by an Arginine close to the catalytic site (Lunin et al., 2020). It is however still unclear what determines the specificity of each TBLs. In the current dogma, acetyl group from cytosolic acetyl-CoA would be translocated to the Golgi lumen through RWAs and captured by AXY9 which would then be used by TBLs to perform polysaccharides specific *O*-acetylation (**Figure 1.4**) (Pauly and Ramírez, 2018). It should be noted that so far, evidence of such interplay between RWA, AXY9 and TBL has yet to be found.

1.1.4.2. De-acetylation by GDSL-esterases in the Golgi

As stated before, plant *O*-acetylation is a tightly regulated process encompassing a myriad of actors to achieve correct acetylation level. Additionally, regulation of *O*-acetylation may also be done at the molecular nanodomain scale, as the patterning of acetylation is equally important for polysaccharide function (Busse-Wicher et al., 2014; Grantham et al., 2017). This is achieved by the dynamic action between acetyltransferases and esterases, the latter removing acetyl groups from acetylated moieties. Surprisingly, only one gene has been described as Golgi acetylesterase, belonging to the GDSL-lipase/esterase family. GDSLs are part of the SGNH-hydrolases superfamily and are notably defined by their conserved GDSL motif which is made of their catalytic residue triad Ser-Asp-His (S-D-H) (Akoh et al., 2004). Therfore, the catalytic residues are similar to that of TBLs / AXY9 (**Figure 1.4**) which suggests common evolutionary origin despite opposite reactions (transferase vs esterase). Despite an extensive list of GDSL found in land plant (Volokita et al., 2011), only the rice BRITTLE LEAF SHEATH (BS1) was described as a Golgi-localized polysaccharide acetylesterase thus far (Zhang et al., 2017). Although GDSLs are thought to be non-specific lipase/esterases due to substrate-dependant conformational changes, BS1 only mediated xylan deacetylation thus suggesting that plant GDSL-esterases show specific activity to a particular substrate (Zhang et al., 2017; Akoh et al., 2004). Still, the molecular actors involved in polysaccharides deacetylation in the Golgi are largely unknown, particularly for non-xylan hemicelluloses and pectic polymers.

1.1.4.3. Methylation in the Golgi

Compared to *O*-acetylation, polysaccharides methylation is a lot more restricted as it was only found in xylans, arabinogalactans, HG and RG-II. It requires S-adenosyl methionine (SAM) as a methyl donor which is present in the cytosol and transported in the Golgi (**Figure 1.5**) by

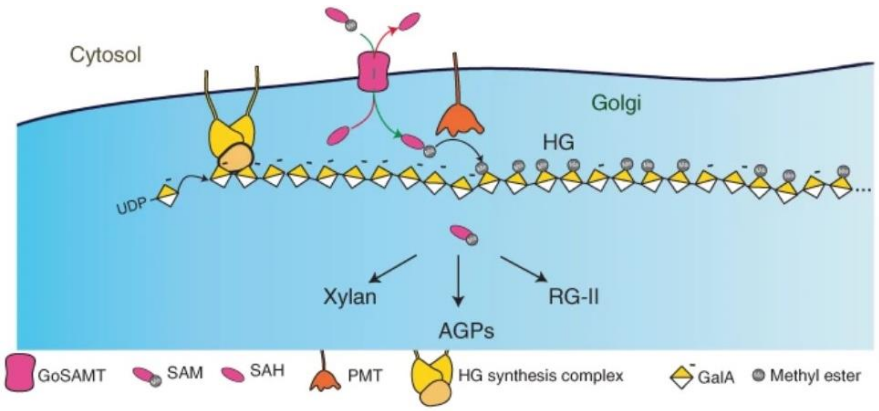

Figure 1.5: Polysaccharide methylation requires SAM transporters for translocation in the Golgi. PMT such as QUASIMODO2-3 then catalyzes *O*-methylation on various polysaccharides such as HG as represented. From Temple and Dupree (2020)

recently described transporter (Temple et al., 2022). While altered 4-*O* xylan methylation of substituted glucuronic acids was not linked to discernable phenotypes, pectin methylation has major developmental effects, particularly on HG which encompass the bulk of polysaccharides methylation. HG is synthesized and highly methylated at the *O*-6 position (COOH acidic function) to reduce its potential for interaction before secretion to the apoplast (Gu and Rasmussen, 2022). Pectin methylation is a highly regulated processes as it has major implication for CW loosening and stiffening through pectin degradation or crosslinking (Wormit and Usadel, 2018). Indeed, contrary to acetylation, methylation can affect the surface charge density of HG since it occurs at the COOH which is a decisive factor for HG involvement in the CW (Guo et al., 2022; Anderson and Kieber, 2020). Yet, only few Golgi methyltransferases were characterized thus far.

1.1.4.3.1. Hemicellulose methyl transferase in the Golgi

Xylan methylation is performed by GLUCURONOXYLAN METHYLTRANSFERASE1, 2 and 3 (GXM) which are capable of utilizing SAM to perform 4-*O* xylan methylation of glucuronic acid side chains (Lee et al., 2012). They present a conserved DUF579 domain which is associated with xylan synthesis or methylation. Following this idea, the two DUF579 containing ARABINOGALACTAN METHYLTRANSFERASE1 and 2 (AGM) were shown to methylate arabinogalactan in the Golgi (Temple et al., 2019). In both cases, methylation was done on a polysaccharides-specific basis with little to no impact on their biosynthesis, supporting the step-by-step biosynthesis and maturation of polysaccharides. Interestingly, neither GXM or AGM double mutant exhibited any developmental phenotype or change in CW structure, though AGM methylation is important in pollen tube guidance (Mizukami et al., 2016).

1.1.4.3.2. Pectin methyl transferase in the Golgi

So far, HG is the only pectic component for which methyltransferase have been identified. Indeed, *O*-6 methylation of HG is done by QUASIMO2 (QUA2) and 3 (QUA3), although it is likely that additional actors / *QUA* family member are also involved in this process (Mouille et al., 2007; Barnes et al., 2022; Miao et al., 2011; Driouich et al., 2012). It should be noted that *QUA*s do not display DUF579 motif described above and were only associated with HG methylation. So far, *qua2* mutation was associated with decreased cell-cell adhesion (Mouille et al., 2007), hypocotyl elongation (Du et al., 2020) and seed mucilage formation (Du et al., 2022b). However, because HG is involved in a variety of developmental processes and that

QUA2 is almost ubiquitously expressed (Miao et al., 2011), it is likely that future study will highlight additional effects of HG methylesterification disruption.

1.1.5. Cell wall proteins

1.1.5.1. Diversity of CW proteins

CW proteins make up for the last 10 % of the primary CW dry mass and are usually subdivided in functional classes. Although it is difficult to assess the full extent of CW protein diversity due to extractability issues, core CW proteome conserved across multiple species could be identified, with some outlier present at the inter-species level (Clemente et al., 2022). Although specific CW proteins may not be conserved across lineages, most functional classes in which they are organized are commonly distributed among species. So far, these are spread in nine functional classes (**Figure 1.6**) including proteins whose function has not been described yet (Albenne et al., 2013; Clemente et al., 2022). The large majority of identified CW proteins reside in the protein acting on carbohydrates and oxido-reductases classes, which perfectly highlights the critical role of CW proteins in dynamically regulating the mechanical properties of the wall. Key examples of such CW proteins in *A. thaliana* are described in the following sections.

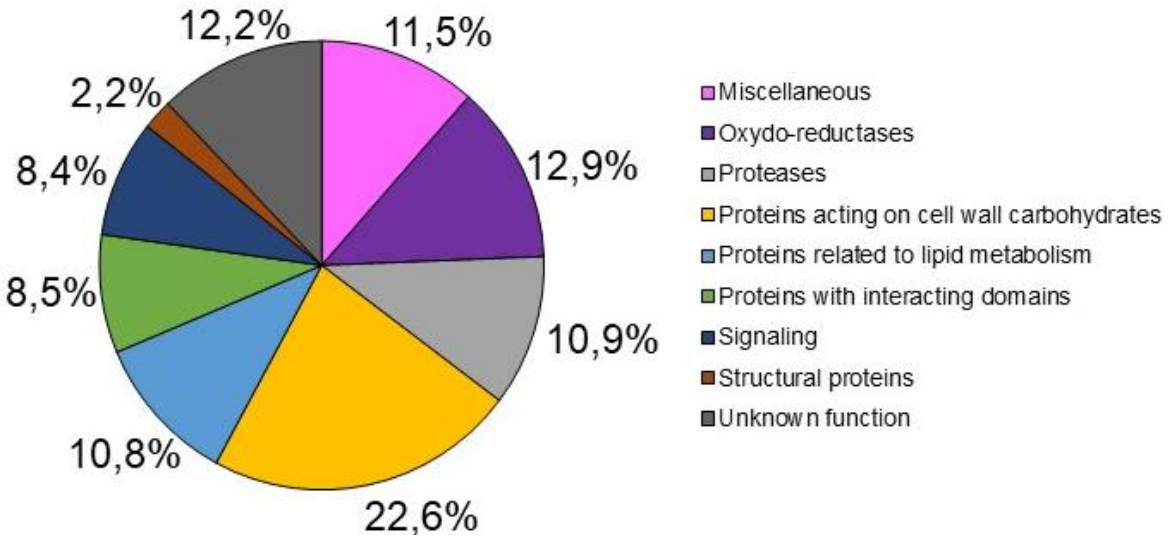

Figure 1.6: *A. thaliana* CW protein diversity as of the 24-09-2022. Similar repartition in nine functional classes can be observed in other studied species. Note that these are not representative of CW prediction but results from proteomic data corresponding to 1009 identified CW proteins in this species so far (San Clemente et al 2022).

1.1.5.2. Pectin acetyl esterases (PAEs)

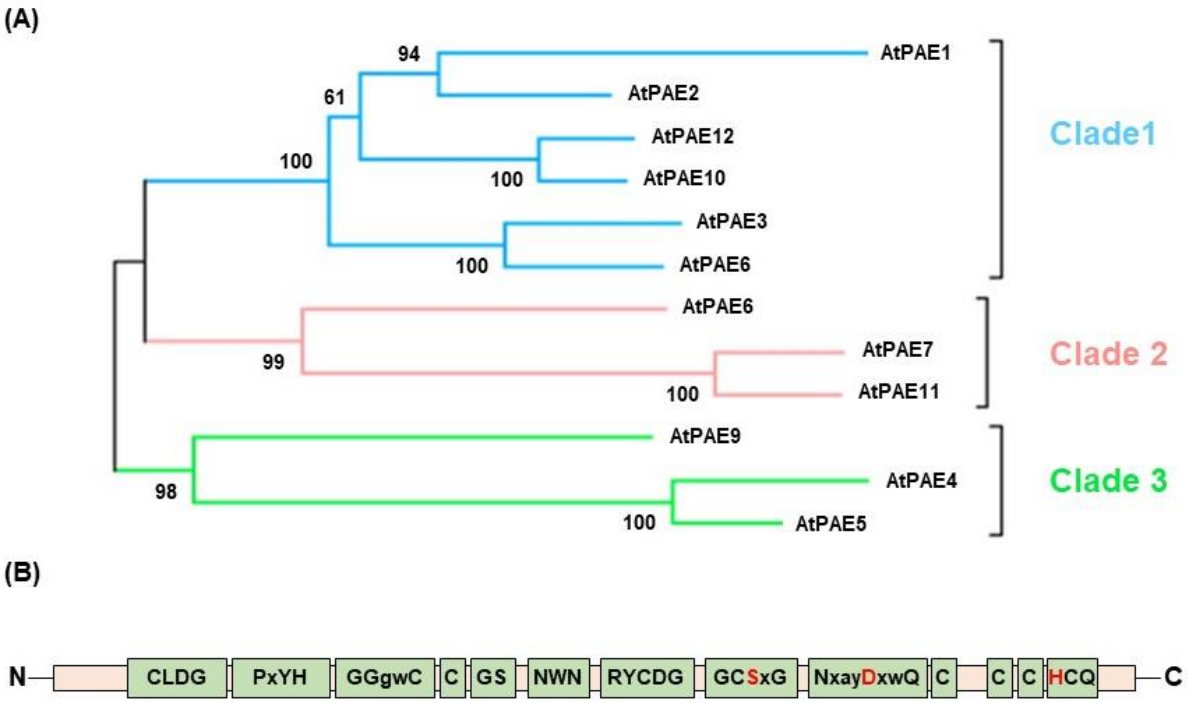

Figure 1.7: PAE multigenic family and conserved motif in *A. thaliana*. **(A)** The *A. thaliana* PAE phylogeny. The PAEs are separated into three clades which all have a caracteristic motif. **(B)** Consensus motif of *A. thaliana* PAE. The S-D-H catalytic site is in red. The GCSxG and NxayDxwQ motifs are likely similar to GDSl / DxxH motif found in GDSLs / TBLs / AXY9. Note that these results are based on bioinformatic prediction. Similar residues are in lowercase while conserved one are in uppercase. Adapted from (Philippe et al 2017).

Previously, we discussed pectin acetylation and deacetylation in the Golgi by the RWA/AXY9/TBL trio and GDSL-esterase, respectively. However, additional pectin maturation occurs dynamically in the apoplast. Pectins can be deacetylated by PAEs which form a 12-member multigenic family in *A. thaliana*. (**Figure 1.7**). Unsurprisingly, they possess similar S-D-H catalytic site as those found in AXY9, TBLs are GDSL-esterases (Philippe et al., 2017; Lunin et al., 2020). These key amino acid residues are spread in conserved PAE motifs which are similar to the DxxH and GDS motifs found in above mentioned protein families (**Figure 1.7**). In *A. thaliana*, *PAE* expression is highly gene-dependent as particular *PAE* are more broadly expressed than others (Philippe et al., 2017). As stated before, defects in acetylation level can lead to collapsed CW and subsequent growth phenotype which suggests that PAE should play an equally important role to modulate acetylation level in the apoplast. Unfortunately, in *A. thaliana*, only one study has described AtPAE8 and AtPAE9 as acetylating

RG-I in the inflorescence stem which is necessary for its proper growth. Impaired cell was also observed in *Populus trichocarpa*, as *PAE1* mutation show severe male sterility (Gou et al., 2012). The biochemical link between acetylation and cell growth is still unclear, but is it hypothesized that acetylation could change pectin hydrophobicity, binding potential to water / calcium ions (Dea and Madden, 1986; Ralet et al., 2003) and PME activity (see following section) which would modify its gel formation ability (Oosterveld et al., 2000). Although it is ambiguous if PAEs directly impact gel formation / properties on their own or through better PME activity *in vivo*, apoplastic pectin deacetylation is almost always linked to changes in pectin properties (Renard and Jarvis, 1999; Ralet et al., 2003).

1.1.5.3. Pectin methyl esterases (PMEs)

PMEs belong to a very large multigenic family of genes which is conserved in many species : 66 in *A. thaliana* (**Figure 1.8**), 88 in Poplar, 41 in rice, 127 in soybean, 43 if maize (Zhang et al., 2019a; Wang et al., 2021; Guo et al., 2022). Extensive list of studies has characterized and reviewed their functional role in plant development (Wolf et al., 2009; Micheli, 2001; Du et al., 2022b). They catalyze the specific demethylesterification of GalA residues of HG in at least two separate manners. First, HG demethylesterification can occur in a non-blockwise manner, leaving partially methylated GalA which can be cleaved by pectin cleaving enzymes (described below) to induce CW loosening (**Figure 1.9**). Non-blockwise demethylesterification is thought to be dependent on various parameters such as (i) the presence of particular amino acid residues and/or acetyl groups which may provide steric hindrance preventing uninterrupted PME activity (Oosterveld et al., 2000) and (ii) complementary inhibition by their inhibitors (Wormit and Usadel, 2018). Second, PME can perform blockwise demethylesterification which leaves consecutive non-methylated GalA (**Figure 1.9**). This process is usually associated with CW stiffening through Ca^{2+} mediated HG crosslinking (Liners et al., 1989). It should be noted that although particular HG degree of methylesterification (DM) is often associated with events of CW loosening or stiffening, experimental evidence does not support a clear-cut model. As such, PME activity, HG overall methylation and CW properties should always be studied as independent (although related) parameters. In *A. thaliana*, 14 out of the 66 PMEs were described in a myriad of processes, including plant development, reproduction, interaction and response to stresses (Guo et al., 2022) highlighting critical need to regulate HG DM in the apoplast.

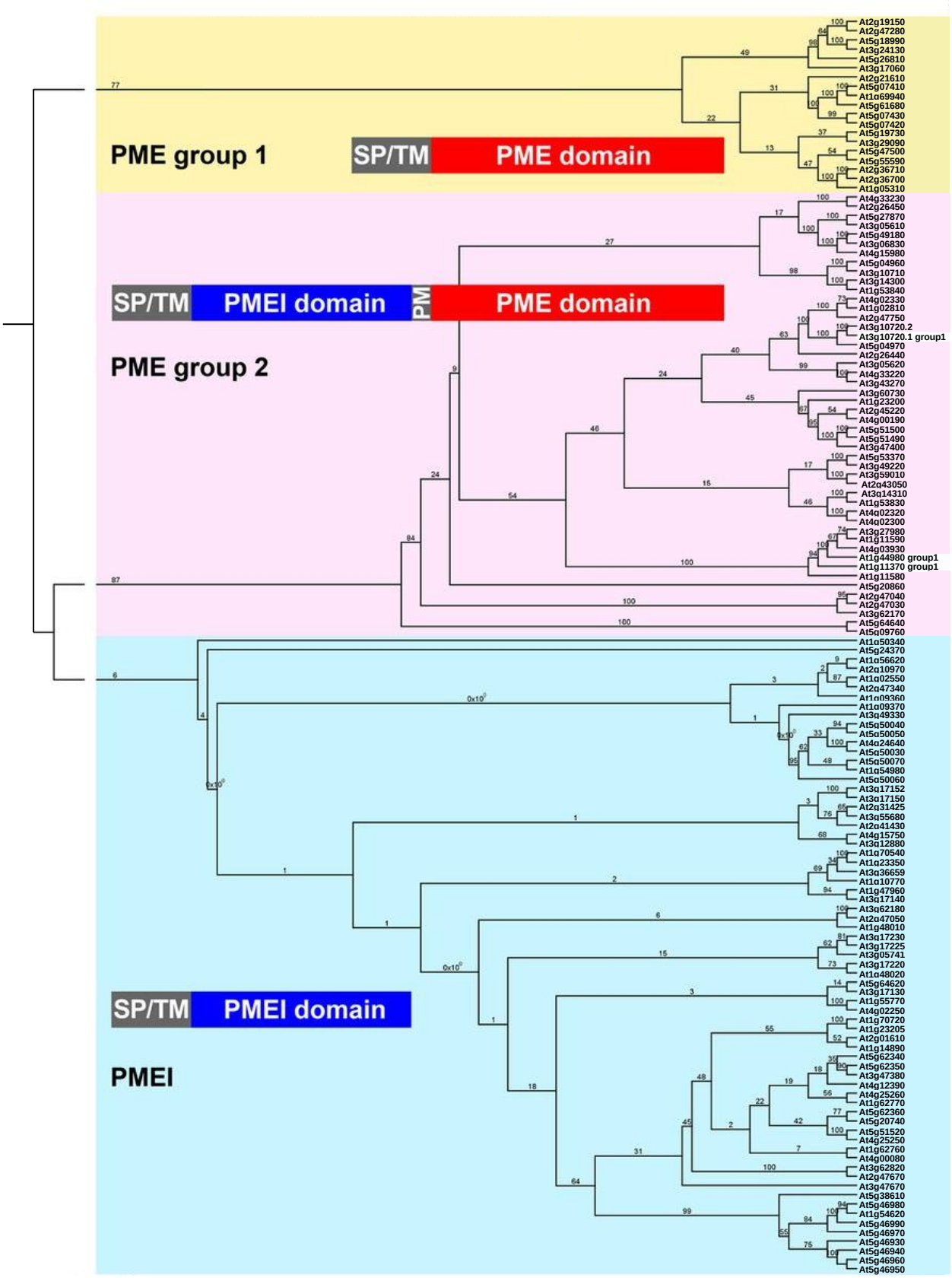

Figure 1.8: Phylogeny of *A. thaliana* PMEs and PMEIs). Phylogenetic analysis of the predicted full-length amino acid sequences of 136 PMEs and PMEIs reveals three distinct phylogenetic groups: PME group 1 (yellow) with a specific PME domain; PME group 2 (pink) with a PME domain and an inhibitory domain; and PMEI (blue) with just the inhibitory domain. Structural motifs are according to Pelloux et al. (2007): PM, processing motif; SP, signal peptide; TM, transmembrane domain. **Extracted from (Scheler et al 2015)**

1.1.5.4. Pectin methyl esterase inhibitors (PMEIs)

Although control of HG demethylesterification can be done through PME endocytosis (Mollet et al., 2013), steric hindrance (Oosterveld et al., 2000) and even possibly self-inhibition in group 2 PMEs (Scheler et al., 2015), their activity is mostly regulated in the apoplast by their inhibitors, PMEIs (**Figure 1.9**). They form an equally large multigenic family of 71 gene in *A. thaliana* (**Figure 1.8**), 54 in poplar and 35 in rice (Wormit and Usadel, 2018; Guo et al., 2022) which all possess the conserved N-terminal PMEI domain also found in group 2 PMEs (**Figure 1.8**) (Scheler et al., 2015). This domain is thought to bind in a pH-dependant manner to PME active site to restrict its activity (Hothorn et al., 2004). Despite the large number of described PMEI participating in a large array of processes (Coculo and Lionetti, 2022; Guo et al., 2022), only one clear case of PMEI-PME duo was demonstrated *in vivo* so far. (Röckel et al., 2008).

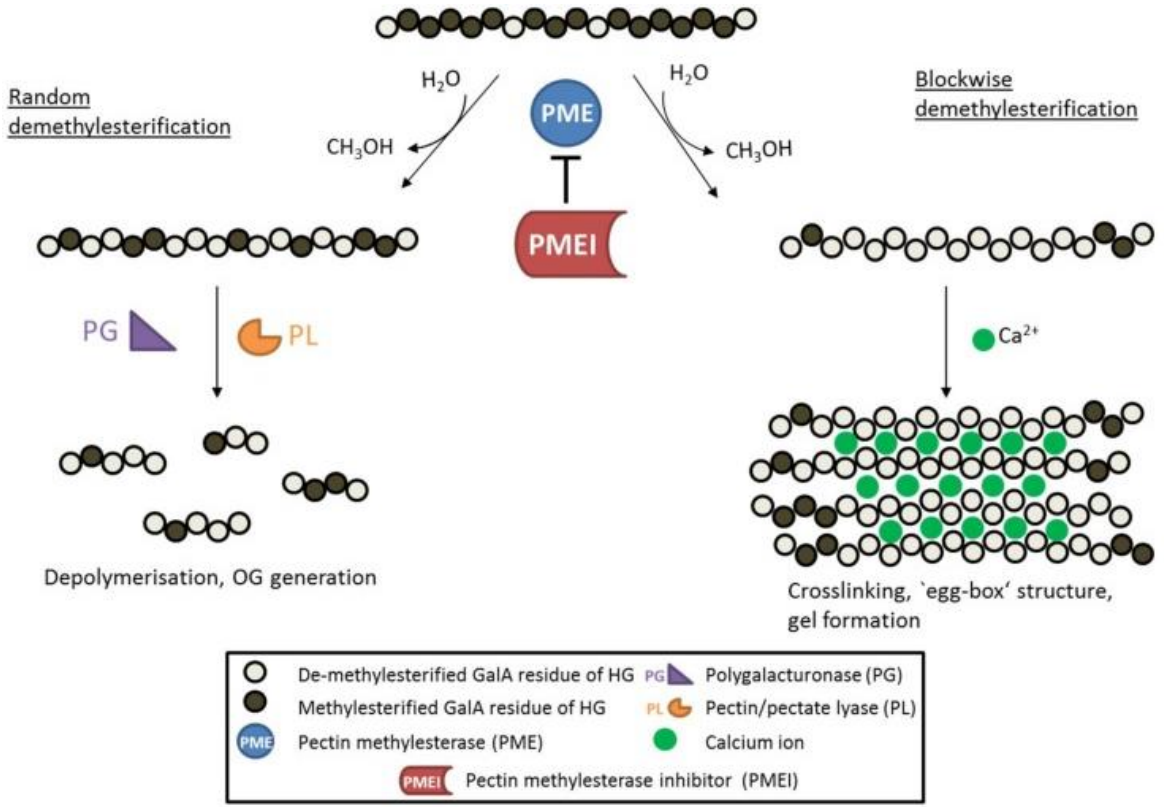

Figure 1.8: Schematic diagram showing the de-methylesterification of HG and the effects on its structure from Wormit and Usadel 2018. PMEs can de-methylesterify HG in a blockwise fashion, leading to several consecutive negatively charged backbones which can form crosslinks with cations like Ca^{2+}, leading to so called "egg-box" structures responsible for gel formation. Conversly, PMEs can de-methylesterify GalA residues in a non blockwise manner. Partially-methylesterified HG is depolymerized by pectin-degrading enzymes leading to oligogalacturonides formation (OG). PME activity can be inhibited by its proteinaceous inhibitor PMEIs.

However, *in vitro* domain analysis of PMEI7-PME3 duo highlights the importance of a Glutamic residue to stabilize the complex (Sénéchal et al., 2017) although it is unknown if other PMEI-PME duo would work similarly. It is also unclear if PMEIs have particular affinity for some PMEs, although likely (Xu et al., 2022). *In vitro* evidence also suggest that a PMEI can regulate multiple PMEs (Hocq et al., 2017a; Wormit and Usadel, 2018), possibly in a pH dependent manner (Bonavita et al., 2016; Hocq et al., 2017b). Rather, specificity in PMEI-dependant inhibition of PME could be explained by their spatial distribution. Particularly positioned PMEI in CW microdomain was necessary for proper pollen tube growth (Röckel et al., 2008) and seed mucilage release (Saez-Aguayo et al., 2013; Francoz et al., 2019b), highlighting the importance of co-expressed and co-localized PMEI-PME for proper control of PME activity. It should be noted that it is uncertain if *in vivo* PMEI-dependant inhibition would always lead to total removal of PME activity or partial inhibition which might result in HG with particular degrees of methylesterification; some of which might be targeted by HG cleaving enzymes.

1.1.5.5. Pectate lyases (PLs) and pectin lyases (PNLs)

As yet another tool to induce dynamical remodeling of the CW, HG can be degraded by various enzymes which have different affinity or activity. Both PL and PNL act by trans-elemination of α-(1→4) linkages of GalA and present a high degree of affinity for HG with a high DM (Yadav et al., 2009). PL activity was linked to processes such as fruit ripening, organ abscission or cell elongation (Uluisik and Seymour, 2020) through CW loosening. Although plant PNL have been reported, they are mostly produced by the fungal genera (Yadav et al., 2009) and used to similar end, particularly for industrial purposes (Zheng et al., 2021) or oligogalacturonan profiling (Voxeur et al., 2019).

1.1.5.6. Polygalacturonases (PGs)

Similar to PL and PNL, PG have been extensively described in fungal or bacterial species for their ability to hydrolyze the α(1→4) linkage between GalA (Sénéchal et al., 2014). PG from fungal origin are used in parallel with fungal PLs for OGA profiling (Voxeur et al 2019). They have particular affinity for HG with a lower DM as compared to PLs (Bonnin et al., 2002), suggesting tight interplay with PME activity. Indeed, PGs were found to accumulate in tissues which show high HG remodeling such as stomata (Rui et al., 2017, 2019). PG activity is usually associated with higher CW mobility and reduced cell-cell adhesion (Ogawa et al., 2009; Barnes et al., 2022) by promoting CW loosening. Interestingly, some PGs have particular positionning

also observed for other CW remodeling actors suggesting that tight regulation of their spatial accumulation is critical, though the underlying mecanisms are rarely described (Ogawa et al., 2009). Despite their activity, it is difficult to asses whether PG activity is linked to growth phenotype as the produced oligolacturonides (OGAs) can also serve as molecular signal for plant-microorganism interactions (Yang et al., 2018).

Altogether, these HG modifying enzymes allow fine tuning of the homeostasis of acetylation, methylation and polymerization of HG (**Figure 1.10**).

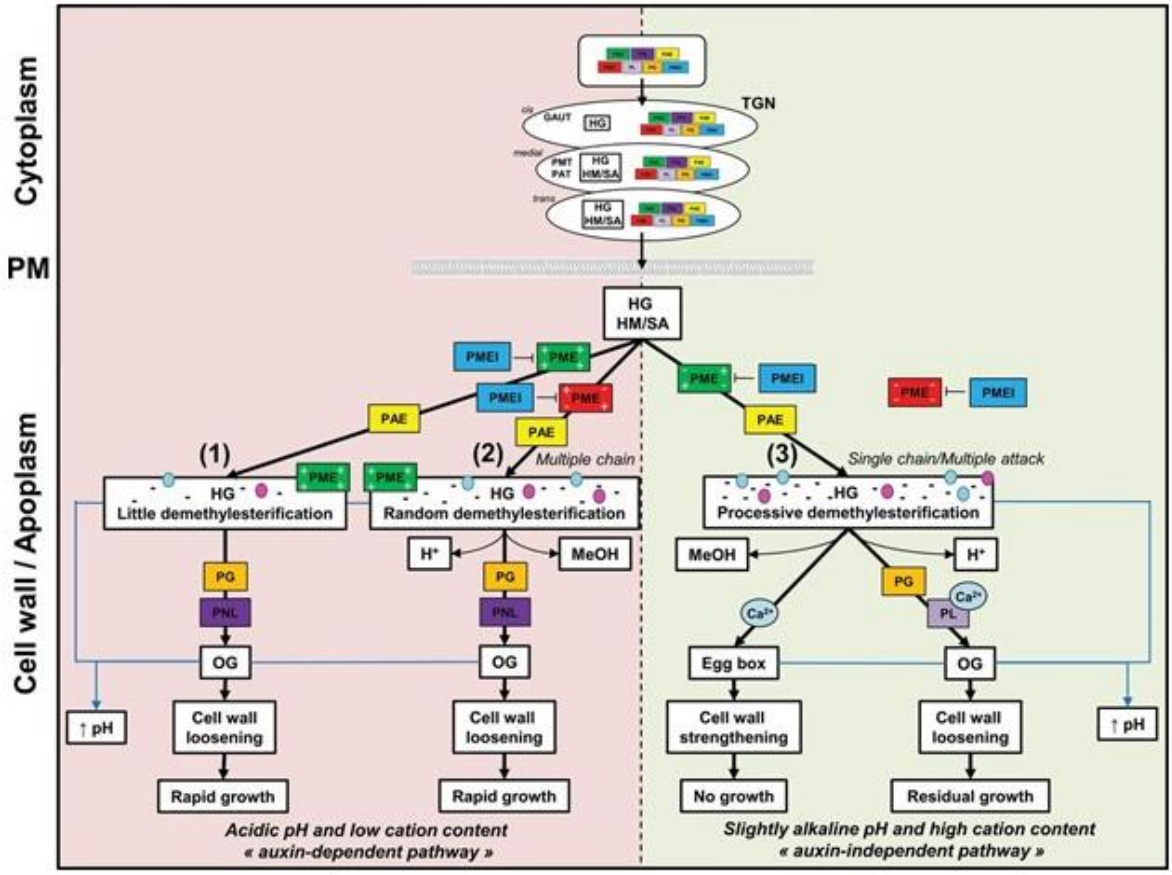

Figure 1.10: Simplified yet complex schematic diagram showing the regulation of HG methylation pools in distinct cell wall microenvironments and consequent effects on growth. Multiple apoplastic HG modifying enzymes such as PAE, PME, PMEI, PG, PL , PNL (all of which are described in this chapter) present high interplay in their activity / function which lead to tight regulation of HG and subsequent phenotype. In the Golgi, PMT: pectin methyltransferase, PAT: pectin acetyltransferase. Adapted from (Sénéchal et al 2014).

1.1.5.7. Class III Peroxidases (CIII-PRXs)

CIII-PRXs are ubiquitous among land plants and form extensive multigenic family of oxidoreductases (73 members in *A. thaliana*, 181 in *Eucalyptus grandis*, 138 in *Oryza sativa* and 143 in *Brachypodium distachyon*) (Fawal et al., 2013). Although vacuolar CIII-PRXs exist (Zipor and Oren-Shamir, 2013) related to a C-terminus putative vacuolar targeting sequence (Francoz et al., 2015b), we mainly describe CIII-PRXs here as secreted apoplastic proteins which encompass the majority of known isoforms (64 out of the 73 CIII-PRXs are predicted to reach the CW in *A. thaliana* (Francoz et al., 2015b). CW-localized CIII-PRXs play key roles in regulating / generating ROS isoforms which can be linked to signal transduction (Penel and Dunand, 2009), CW loosening or stiffening (Francoz et al., 2015b). Based on their conserved functional domain, there is little evidence supporting distinct CIII-PRX activity on a gene-gene basis. Rather, they activity is thought to depend on their molecular environment thus putting additional emphasis in their positioning in the CW (Francoz et al., 2015b). First, CW loosening is thought to happen through $OH^{\bullet}$ generation which breaks polysaccharides covalent linkages (**Figure 1.11**) (Francoz et al., 2015b). Experimental evidence of such activity *in vivo* is sparse (Muller et al., 2009) as it is difficult to correlate macromolecular CW phenotype with altered biomechanical properties. It is worth keeping in mind that CIII-PRXs are dependant on the activity of NADPH oxidases (RBOHs) and Super oxide dismutase (SODs) for the generation of their H_2O_2 substrate (Francoz et al., 2015b). Second, they catalyze H_2O_2 reduction using nearby aromatic compounds as electron donor which induces CW stiffening through their polymerization / crosslinking (**Figure 1.11**) (Passardi et al., 2005). In the apoplast, such substrates exist in the form of monolignols (Tobimatsu and Schuetz, 2019), suberin polyphenolic domain (Bernards et al., 2004), ferulic acids linked to arabinoxylans (Mnich et al., 2020) and tyrosine residues on extensin structural proteins (Mishler-Elmore et al., 2021; Pacheco et al., 2022).

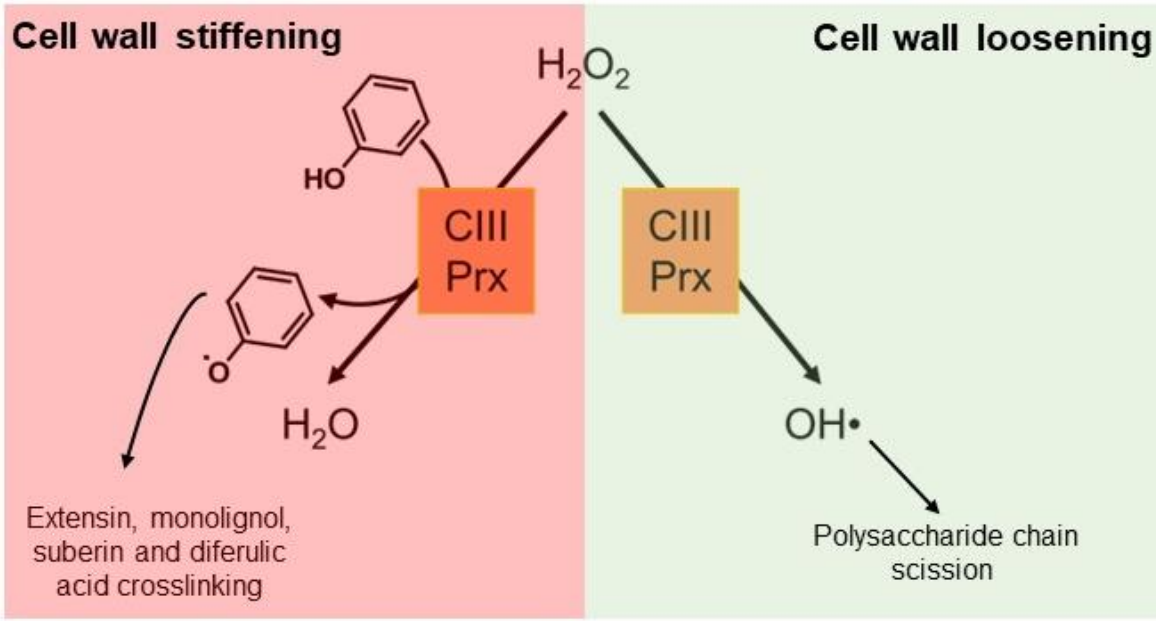

Figure 1.11: Class-III Peroxidases can induce both CW stiffening and loosening through their peroxidative and hydroxylic cycle, respectively. Aromatic cycle found in extensin, monolignol, suberin and diferulic acid can be oxidised by Class-III PRX through H_2O_2 reduction which allows for their crosslinking and CW stiffening. They can also generate ROS such as $OH^{\bullet}$ which break covalent bond within polyssacharides, resulting in CW loosening. Adapted from Francoz et al., (2015b)

1.1.5.8. Extensins (EXTs)

EXTs are part of the large Hydroxyproline Rich GlycoProteins family (168 members in *A. thaliana* including 20 EXTs) which is not conserved in all plant lineages. Notably, both gymnosperms and monocots lack traditional EXTs, though it is highly likely that other polymers such as glucuronoarabinoxylan substituted with ferulic acids perform similar cross-linking functions in grass (Mishler-Elmore et al., 2021). EXTs are defined by at least two conserved domains. First, the extensin domain which is a Ser/Hyp (3/5) repeat that is not specific to that group of protein (Borassi et al., 2016) and participate in non-covalent self-assembly of EXTs and *O*-glycosylation (Mishler-Elmore et al., 2021). Second, alternated repetition of Tyr residues which drives their CIII-PRX-dependant covalent crosslinking properties (Cannon et al., 2008) and result in a non-soluble EXT network which is the most abundant form *in vivo*. This explains the poor EXT extractability and subsequent poor representation in proteomic data (Clemente et al., 2022). Extensin peroxidases (EPs) are subsets of CIII-PRXs that are thought to be the main force of EXT crosslinking through H_2O_2 reduction (see 1.1.5.7) and reverse genetics in *A. thaliana* has succeeded in identifying some EPs (Jacobowitz et al., 2019) and EXTs (Hall and Cannon, 2002) although rarely in combination

(Mnich et al., 2020). However, it is also possible that CIII-PRXs do not act in a specific manner with EXT, but rather that spatio-temporal accumulation of both actors is key to proper CW mechanical properties and dynamics (Francoz et al., 2015b).

1.2. Introduction to the review article:

The additive properties of every (described and non-described above) polysaccharides and proteins create a large diversity of CWs with distinct features. Plant cells have differently composed and organized CWs which is the result of tight regulations of CW assembly and remodeling dynamics. As biocellular technologies advance further, we became increasingly aware of an additional layer of CW regulation. Not only could plant regulate their CW on a cellular level, but even at the subcellular level with precise positionning of proteins and polysaccharidic actors (Barros et al., 2015; Du et al., 2022a; Höfte and Voxeur, 2017). These subcellular modifications were once named “CW microdomains” as to characterize the local hotspots hosting particular CW remodeling enzymes which activity had major consequences in developmental processes. In the following review, we compiled the implication of recurrent actors of CW dynamics in various developmental processed. We discuss the biomolecular dynamics responsible for their precise accumulation in such CW microdomains, particularly focusing on the molecular actors studied during this PhD: HGs, HG modifying enzymes and CIII-PRXs.

Trends in Plant Science

CellPress

Review

Cell-wall microdomain remodeling controls crucial developmental processes

Bastien G. Dauphin,[1] Philippe Ranocha,[1] Christophe Dunand,[1] and Vincent Burlat[1,*]

Plant cell walls display cellular and subcellular specificities. At the subcellular level, wall regional territories with specific compositions are necessary for macroscopic developmental processes. These regional specificities were named differently throughout the years, and are unified here under the term 'cell-wall microdomains' that define the local composition and organization of wall polymers underlying territories of wall loosening and/or softening or stiffening. We review the occurrence and developmental role of wall microdomains in different cell types. We primarily focus on the contribution of two categories of wall-remodeling molecular actors: fine-tuning of homogalacturonan (HG; pectin) demethylesterification patterns and two classes of oxidoreductases [class III peroxidases (CIII PRXs) and laccases (LACs)], but we also highlight two different molecular scaffolds recently identified for positioning specific CIII PRXs.

Highlights

Plant cell function depends on plant cell shape.

Cell-wall microdomains are defined by local differences in cell-wall composition.

Cell-wall microdomains define local biomechanical properties and are subjected to non-polarized turgor pressure; cell-wall microdomains therefore define cell expansion and cell shape.

Cell wall-localized pectin-modifying enzymes and/or oxidoreductases can contribute to local cell-wall modifications.

Two models of molecular scaffolds enabling local positioning of plant cell-wall remodeling enzymes in discrete cell-wall microdomains are emerging.

Cell-wall microdomain history and definition

'Great things […] are a succession of small things linked together' (V. van Gogh, 1882; http://webexhibits.org/vangogh/letter/11/237.htm). Originally intended to paint life as a whole, advances in cell biology have consistently proved that this quotation holds true at the smallest scale of life. As sessile organisms, plants must encompass various mechanisms to overcome the many developmental and environmental challenges they face from germination to reproduction. A crucial specificity of plant cells is their cell wall. This polysaccharide matrix surrounding each cell is crucial during growth for cell shape achievement, and is involved in diverse processes such as mechanosensing, signaling, maintaining structural integrity, and defense [1–3]. The primary wall is mainly made of cellulose, hemicelluloses, and pectins, whereas lignin or sporopollenin may be additionally found in cells that develop a secondary wall as well as in some specialized primary walls. Both walls also contain a high diversity of cell-wall proteins that have a plethora of roles [4]. Interestingly, the wall composition shows multiscale specificities at the evolutionary, tissular, cellular, and even subcellular levels [5–7]. Depending on the cellular context, these subcellular cell-wall features have been described using various terms such as cell wall (sub)layers, lamellae, patches, decorations or ornamentations, patterns, cell-wall domains, and **cell-wall microdomains** (see Glossary). The term 'wall (micro)domain' was introduced in the early 1990s and has since then been more rarely used (Table S1 in the supplemental information online). This relative underutilization might be because (i) each scientific field tends to use its own specific vocabulary, and (ii) possible fear of confusion with protein domains, polysaccharide (e.g., pectin) domains, or lipid membrane microdomains. However, the pioneering conceptual definition by Keith Roberts was very clear and cleverly covered all the regional possibilities of wall subcellular territories (Table S1 in the supplemental information online) [8,9]. Hereafter, in association with the specific vocabulary classically used in each cellular context, we employ the binomial generic term 'cell-wall microdomains' to unify the regional occurrence of subcellular wall territories as conceptually exemplified (Figure 1). We choose to keep the prefix 'micro' in this unifying term, regardless of the size and pattern of the wall territory considered. This has the advantage that it

[1]Laboratoire de Recherche en Sciences Végétales, Université de Toulouse, Centre National de la Recherche Scientifique (CNRS), Université Paul Sabatier Toulouse 3, Institut National Polytechnique de Toulouse, 24 chemin de Borde Rouge, 31320 Auzeville-Tolosane, France

*Correspondence:
burlat@lrsv.ups-tlse.fr (V. Burlat).

© 2022 Elsevier Ltd. All rights reserved.

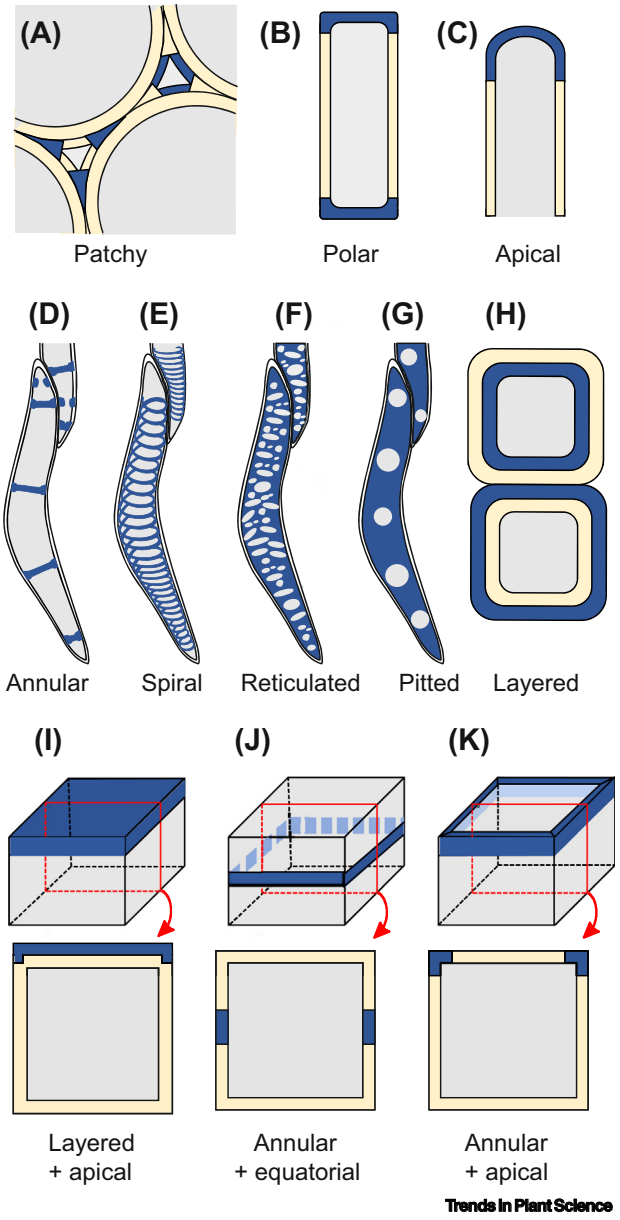

Figure 1. Diverse regional patterns of specific molecular compositions and properties are examples of so-called plant cell-wall microdomains. To highlight the regional diversity of wall microdomains regardless of the type of molecular features considered, a unique color code was used: neutral blue, wall microdomains; pale yellow, other walls; light gray, cytoplasm/lumen/air spaces. (A) Among the first experimental descriptions of wall microdomains are the patchy patterns around the air spaces formed during the isotropic cell growth of cortical parenchyma cells [19]. Other non-exhaustive examples are: longitudinal sections illustrating the molecular specificities of (B) polar, or (C) apical wall occurring during anisotropic or tip cell growth, respectively. Longitudinal surface view of (D) annular, (E) spiral, (F) reticulated, and (G) pitted lignin decoration series of primary xylem tracheary elements. Sections illustrating (H) radial layers (e.g., middle lamella/cell corner vs primary wall vs secondary wall; primary wall and/or secondary wall sublayers). (I–K) Comparison of 3D views and sections of wall microdomains combining two regional dimensions: (I) layered and apical (epidermis cuticle), (J) annular and equatorial (root endodermis Casparian strip), (K) annular and apical (*Arabidopsis thaliana* seed mucilage secretory cells, discussed in this review).

Glossary

Cell-wall microdomains: 'every cell has an extracellular matrix that should be regarded […] as a mosaic of wall (micro)domains with different and specific compositions and functions' [8]. For sake of clarity, we have unified under the common term 'cell-wall microdomain' the various cell-wall regional peculiarities discussed in the text.
Columella: in *Arabidopsis thaliana* (arabidopsis), a volcano-shaped polarized non-lignified secondary wall in seed coat mucilage secretory cells.
Lobe: in an epidermis pavement cell, a curved protrusion constituting a primary wall microdomain that extends into the neck of a neighboring pavement cell.
Loosening: 'cell wall modifications that result in wall stress relaxation and chemorheological creep (irreversible, time-dependent extension as a result of a protein-mediated process)' [100]. Loosening and softening are two close phenomena that are either associated or independent [100]. There are many molecular mechanisms leading to loosening or softening, some of which are discussed in this review.
Neck: in an epidermis pavement cell, a curved indentation constituting a primary wall microdomain into which the lobe of a neighboring pavement cell protrudes.
Residuum cells: cells located on the border of the main plant body during abscission.
Secession cells: cells located on the border of the falling organ during abscission.
Seed mucilage: in many angiosperms, a cell wall-like gelatinous structure composed of polysaccharides. In arabidopsis it contains large amounts of rhamnogalacturonan type I pectins and smaller amounts of HG pectins, cellulose, and hemicelluloses.
Shank: in tip elongating cells such as pollen tubes, a cell-wall microdomain located on the side walls below the tip.
Softening: 'wall modifications that result in reduction in cell-wall stiffness, measured by various rapid force/deformation assays' [100]. Mechanical softening is sometimes used as an indicator of wall loosening, but these two close phenomena may be independent [96].
Stiffening: 'cell wall modifications changing bulk elasticity (Young's modulus) and resistance, regardless of its irreversibility' [100]. The two main examples of molecular mechanisms

clearly encompasses wall regional patterns at the microscopic scale and not only at the molecular scale. This prevents confusion with the possible parallel use of 'domain' (without 'micro') at the molecular scale. In other words, a cell-wall microdomain corresponds to a wall territory with a specific molecular composition, some of which may correspond to specific molecular domains (e.g., pectin domains).

Turgor pressure is homogeneous across the cell, as demonstrated by the spherical shape of wall-deprived plant cell protoplasts [10]. Therefore, plant cells rely on a patchwork of wall microdomains with contrasting composition and mechanical properties to achieve particular shapes

leading to stiffening that are discussed in this review are calcium pectate formation and lignin polymerization.

and properties necessary for their functions. For instance, such wall microdomains can contribute both to isotropic growth of parenchyma cells separated by air spaces (Figure 1A) and to cell elongation during anisotropic growth or tip growth (Figure 1B,C). Lignification patterns of tracheary elements at different developmental stages can be defined as wall microdomains (Figure 1D–G). Similarly, the radial dimension of wall heterogeneity leading to various (sub)layers of various composition constitutes wall microdomains (Figure 1H). The accurate deposition of the epidermis cuticle, of the endodermal Casparian strip, and of the polarized opening zone of the *Arabidopsis thaliana* (arabidopsis) **seed mucilage** secretory cells constitute final examples of bipartite wall microdomains (Figure 1I–K). Each of these wall microdomains provides different elasticity and resistance properties to the cell. The assembly and remodeling of wall microdomains is governed by numerous intracellular factors such as the synthesis of specific secretory pathway proteins in the endoplasmic reticulum, specific polysaccharide biosynthetic pathways in the Golgi [11], and spatial and temporal control over the biosynthesis of monolignols in the cytosol [12]. The dynamics of the cytoskeleton is also crucial for polarized secretion of wall components during tip growth [13]. In the following we focus on molecular remodeling events occurring within the wall itself. An ever-increasing amount of cell-wall proteins have been related to wall remodeling. These are classically categorized as contributing to either wall **stiffening** or **loosening**. A distinction was recently elegantly made at the molecular level between loosening and **softening**. However, the papers reviewed here do not always address this subtlety, and we therefore refer to loosening/softening in most instances. We particularly focus on the separate contributions of two categories of wall molecular actors to the remodeling of wall microdomains in different cell types: (i) finely tuned patterns of HG (pectin) demethylesterification and modifying enzymes, and (ii) two classes of oxidoreductases (CIII PRXs and LACs). We finally present two recent models of molecular scaffolds including a molecular link between specific patterns of HG demethylesterification and the positioning of specific CIII PRXs. Although the review is primarily focused on arabidopsis, the conservation of these remodeling events will be discussed and expanded upon because this model species is clearly insufficient to understand the full diversity of wall microdomain remodeling events and their purposes.

Focus on two categories of molecular actors contributing to wall microdomain remodeling

HG patterns and HG-modifying enzymes

Pectins are mainly subdivided into HG and rhamnogalacturonans I and II. They form a polymer matrix that contributes to the local control of the mechanical stiffening versus loosening/softening balance of the cell wall, and also to signaling [14]. HGs are galacturonic acid polymers synthesized in the Golgi and exported to the cell wall in a methylesterified form. In the wall, the methyl decorations can be selectively de-esterified in a non-blockwise (Figure 2A) or blockwise (Figure 2B) manner [15]. This fine-tuning occurs through pectin methylesterase (PME) activity which, in turn, can be inhibited by PME inhibitors (PMEIs). On the one hand, non-blockwise HG demethylesterification leads to specific partial methyl decoration patterns on HGs that can be targeted by different HG-cleaving enzymes such as pectate and pectin lyases (PNLs and PLs) and polygalacturonases (PGs), in turn contributing to wall loosening/softening or signaling (Figure 2A). These pectin-modifying enzymes are involved in many developmental processes and their specificity is determined by relatively increasing HG demethylesterification patterns (Figure 2A) [15–18]. By contrast, blockwise HG demethylesterification either contributes (i) to wall loosening/softening through PG activity, or (ii) to wall stiffening through calcium pectate gel formation (Figure 2B) [19]. In addition, specific HG demethylesterification patterns can act as anchoring platforms for CIII PRXs (Figure 2A,B), as discussed in detail at the end of the review. Specific HG demethylesterification patterns can be visualized at the wall microdomain level by using panoply of antibodies or probes (Figure 2A,B and Table S1 in the supplemental information online).

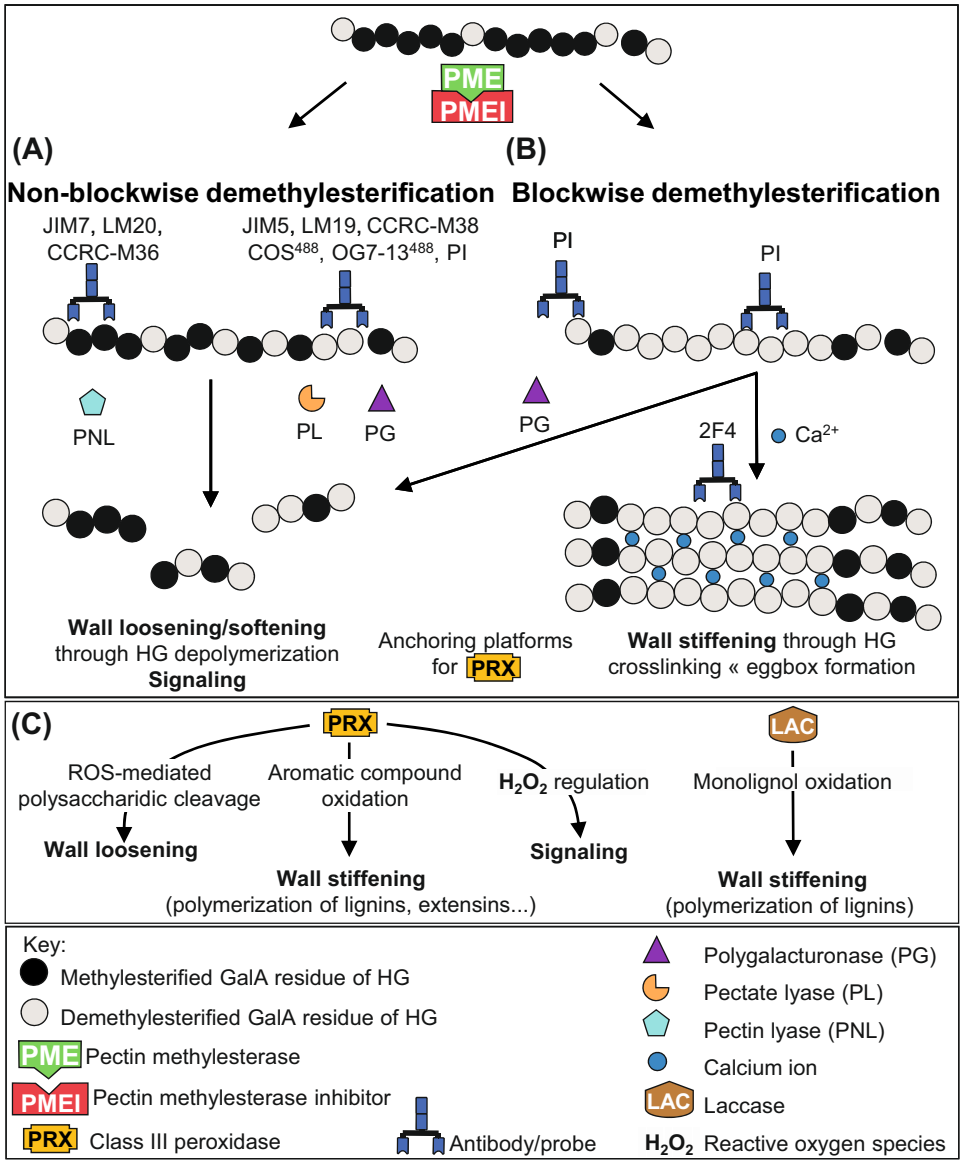

Figure 2. Fine-tuning of homogalacturonan (HG) demethylesterification and oxidoreductases contribute to cell-wall (microdomain) remodeling. Regulation of HG demethylesterification by pectin methylesterase (PME)–PME inhibitor (PMEI) complexes has different outcomes: (A) non-blockwise demethylesterified HGs can be further depolymerized by enzymes whose hydrolyzing capacities rely on HG patterns with different degree of methylesterification. (B) Blockwise demethylesterification can either lead to HG depolymerization or to the formation of calcium pectate 'egg box' gel. The direct wall remodeling consequences (loosening/softening or stiffening) are annotated as well as the indirect roles in signaling and as anchoring platforms. HGs with different degree of methylesterification can be labeled with various antibodies/probes, although their exact epitopes are rarely known [15]. (C) Class III peroxidases (CIII PRXs) and laccases (LACs) are oxidoreductases with different substrates. CIII PRXs can either induce wall loosening, wall stiffening, or signaling, whereas LACs support wall stiffening. (A,B) adapted from [15]; (C) adapted from [20,21]. Abbreviation: ROS, reactive oxygen species.

LACs and CIII PRXs

The second class of molecular actors selected here for their contribution to remodeling of wall microdomains comprises members of two oxidoreductase multigene families: LACs and CIII PRXs

(Figure 2C). LACs are specifically related to stiffening through polymerization of oxidized monolignols. CIII PRXs are either able to (i) oxidize aromatic compounds such as monolignols and tyrosine residues in extensin monomers, thus inducing stiffening by radical polymerization, or (ii) loosening via the production of reactive oxygen species (ROS), leading to non-enzymatic polysaccharide cleavage (Figure 2C). This makes these oxidoreductases prime candidates for contrasting remodeling of wall microdomains [20,21].

The contribution of these two types of molecular actors to cell development through wall remodeling will be first considered separately within wall microdomains from different cell types in different cellular contexts.

Fine-tuning of HG demethylesterification

Tip growth in pollen tubes and root hairs, as well as shaping of epidermal pavement cells and guard cells, are good examples to illustrate the involvement of pectin-modifying enzymes to fine-tune the loosening/softening versus stiffening properties of HGs within wall microdomains.

Control of cell shape is achieved by shifting the mechanical properties of targeted wall microdomains in a symmetry-breaking manner [16,22]. This concept is pushed to the extreme in tip growing parts of the plant, where single-cell growth must be achieved while maintaining appropriate wall integrity. Such processes are documented in pollen tube and root hair growth, especially in the former. Despite having vastly different growth environment and constrains, pollen tubes and root hairs are often compared [23–25]. In arabidopsis pollen tube, tip growth is achieved through a complex regulatory system leaving 'soft' pectins at the tip and 'hard' pectins in the **shank**, thus constituting two contrasting wall microdomains (Figure 3A,B). These were revealed by differential labeling of relatively high and low methylesterified HG using JIM7/LM20 and JIM5/OG7-13^{488} monoclonal antibodies or probes, respectively (Table 1A,B and Figure 3A,B) [26–30]. Such local wall microdomain modifications were not explained by the accumulation of PME1 in either tip and shank wall microdomains, but instead through local PMEI2-mediated inhibition of PME1 activity at the tip (Table 1A,B and Figure 3A,B) [28,31,32]. Similar enzymes such as VANGUARD1/PME5 have been highlighted as being necessary for proper pollen tube growth, but it is unclear how PME5 acts alongside other PME/PMEI actors [33]. The apical positioning of the cell machinery necessary for pollen tube tip growth is additionally favored by cytoskeleton-driven deposition of wall microdomain plugs composed of intracellular callose (Table 1C and Figure 3C) [34]. Complementary JIM7 and JIM5 labeling to the tip and the shank wall microdomains, respectively, was also observed in rice pollen tubes [35] as well as across various species, as recently reviewed [36]. This suggests that similar events of HG remodeling are implicated in these wall microdomains in angiosperms. However, the patterns of HG deposition are more diverse in pollen tubes from various Gymnosperm species, as recently reviewed [37].

Cell-wall regulation in root hair tip growth is not as well understood and does not show a complementary HG distribution between tip and shank wall microdomains. It instead shows a counter-intuitive homogeneous colocalization of low and relatively high methylesterified HGs in both tip and shank [25]. Although pectin degradation via pectinase/pectate lyase was found to fully inhibit root hair growth, the full wall mechanics underlying root hair growth are not as clear [23,38].

The arabidopsis leaf epidermis is a tissue that houses several complex cell shapes including pavement cells shaped like jigsaw puzzle pieces and kidney-shaped guard cells. These cells form a tight waterproof protection/gas-exchange structure with many developmental purposes [39,40]. The molecular basis of pavement cell morphogenesis, including the formation of anticlinal **neck** (Figure 3D) and **lobe** (Figure 3E), was recently reviewed [41]. We emphasize here the

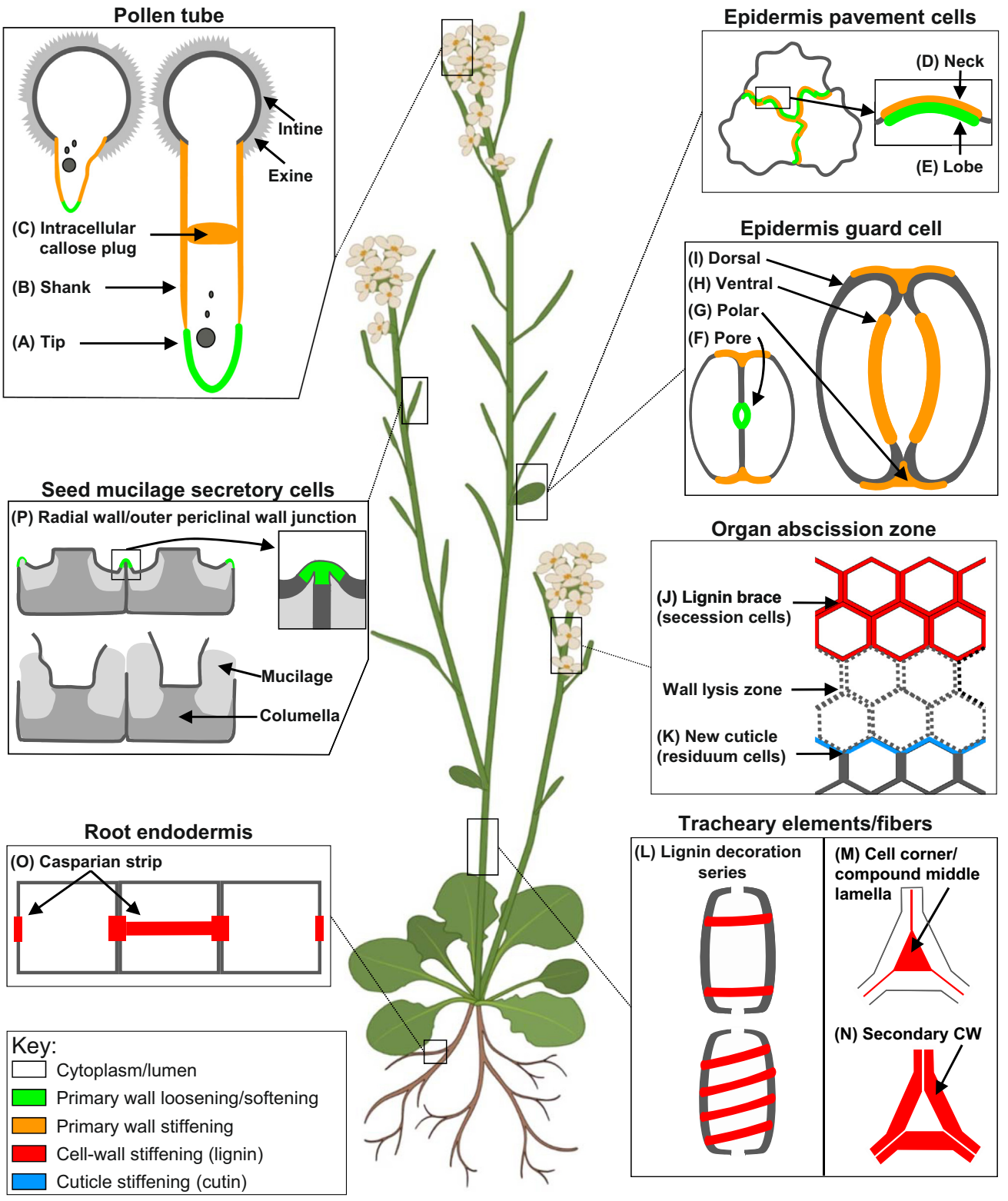

Trends in Plant Science

(See figure legend at the bottom of the next page.)

particular positioning in arabidopsis pavement cells of weakly and partially methylesterified HGs in the neck and lobe wall microdomains, respectively [42–46]. This contrasting pattern is in relative theoretical agreement with the possible stiffening and loosening/softening properties (Figure 2A,B) of neck and lobe wall microdomains, respectively (Figure 3D,E). However, atomic force microscopy experiments showed a lower or higher apparent elastic modulus in the neck and lobe wall microdomains, respectively [42]. In turn, this favors the opposite hypothesis that the anticlinal lobe is stiffer than the anticlinal neck [42]. These complex remodeling patterns illustrate that the specific local composition of wall microdomains is necessary to either initiate or enhance such curvature. A recent study even proposed a model in which HGs are solely responsible for wall curvature, regardless of local cellulose accumulation or turgor pressure [44]. Indeed, overexpression of PMEI3 or PME5 was sufficient to alter curvature width. However, elements that are still lacking include (i) the subcellular localization of an uninhibited PME in the neck, and (ii) the absence of PMEs or the additional presence of a PMEI in the lobe, to explain the formation of the subtle demethylesterification patterns of HGs. Interestingly, the epidermis of a variety of species revealed particular labeling patterns of HG demethylesterification in the neck and lobe, often similar to what has been observed in arabidopsis [41,47]. Although this suggests conservation of the mechanism, the exact level of involvement of the aforementioned polysaccharides and remodeling enzymes remains unclear.

Similar HG demethylesterification patterns are also observed in wall microdomains of the neighboring stomata guard cells. Weakly and partially methylesterified HGs labeled with propidium iodide or COS^{488} and JIM7, respectively, were abundant in the stomatal pore initiation wall microdomain (Table 1F and Figure 3F) [48]. These complex patterns were associated with local loosening, and PGX1–PGX3 are probably responsible for HG cleavage in this location (Figure 2A) [48,49]. Nevertheless, the precise HG features of the pore wall microdomain and conditions for PG recognition are not fully understood. Several studies have also located weakly methylesterified HGs on polar (Table 1G and Figure 3G) and ventral (Table 1H and Figure 3H) wall microdomains [49–51]. These labeling patterns are in agreement with atomic force microscopy observation showing that polar and ventral wall microdomains (Figure 3G,H) are significantly stiffer than the dorsal wall microdomain (Figure 3I) [51]. PME-dependent HG demethylesterification is needed for a full range of stomata opening/closing responses because both *pme6* and *pme34* mutants display impaired stomatal movements [50,52,53]. Although this could be associated with stiffer walls as discussed [50], the precise destiny of modified HGs (e.g., egg-box formation or enzyme-mediated depolymerization of HGs; Figure 2A,B) is unclear. In addition, it is still unknown whether these enzymes act specifically on ventral and/or polar wall microdomains because their precise subcellular localization has not been determined. JIM7/JIM5 labeling in *Zea mays* guard cells revealed patterns of HG methylesterification in polar and ventral wall microdomains similar to those observed in arabidopsis [54]. The necessity of similar regulation of PMEs–PMEIs was also demonstrated in *Vicia faba* and *Commelina communis* for local wall stiffening and the correct properties of guard cell walls [55].

The precise positioning of HG remodeling enzymes is best-documented in pollen tubes, and such information is necessary to better understand the dynamics of wall microdomain remodeling during the development and regulation of pavement cells and guard cells.

Figure 3. Examples of wall microdomain remodeling events that contribute to major processes of cellular development. (A–P) Eight examples of cell types whose function necessitates a particular cell shape that is achieved during growth through the remodeling of wall microdomains. Three main types of remodeling events are color-coded: loosening (green) or stiffening (orange) of primary wall microdomains, and stiffening (red) of primary or secondary wall through lignification. The letters (A–P) are the same as those used in Table 1 that provides further details including the identified molecular actors. The central image was created with biorender.com. Abbreviation: CW, cell wall.

Table 1. Remodeling events of cell-wall microdomains and associated key molecular actors highlight the recurrent use of both similar wall polymers and similar wall-remodeling enzymes in arabidopsis[a]

Cell types (cellular role/developmental process)	Cell-wall microdomain (CWM) identification and function[a]			Wall polymers and probes[b]		Enzymatic remodeling actors[c]		Refs
	ID	CWM Name	Remodeling function	Wall polymer	Molecular feature and probes	Remodeling enzymes	Molecular function	
Pollen tube (tip growth/reproduction)	(A)	Tip	Loosening	HG	HG partial ME (JIM7/LM20)	PME1;PMEI2	PMEI2 locally inhibits PME1 activity	[31]
	(B)	Shank	Stiffening		HG low ME (JIM5/ OG7-13)	PME1; PME5	HG demethylesterification	[31,33]
	(C)	Intracellular plugs	Stiffening favoring tip growth)	Callose	Aniline blue (callose)	CALS3	Local deposition of callose plugs	[34]
Epidermal pavement cells (puzzle shape/protection)	(D)	Neck	Stiffening	HG	HG low ME (COS^{488}/JIM5) HG no ME (PI/2F4)	Unknown PME/PMEI	Control of HG ME	[42,44]
	(E)	Lobe	Loosening	HG	HG partial ME (LM20)	Unknown PMEI	Control of HG ME	[44]
Epidermal guard cells (donut shape/gas exchange)	(F)	Pore	Loosening	HG	HG weak ME (PI) HG partial ME (JIM7)	PGX3 PGX1	HG cleavage	[48,49]
	(G)	Polar	Stiffening		HG weak ME (COS^{488}) HG low ME (LM19)	?	Stomatal movements	[50]
	(H)	Ventral				PME6	HG demethylesterification	[50,51]
	(I)	Dorsal	?	Whole wall	TEM[d] thickness	?	?	[52]
Abscission zone (cell separation/organ abscission)	(J)	Secession cell lignin brace	Stiffening	Lignins	Lignin autofluorescence	RBOHD/F	Local accumulation of H_2O_2	[56]
						LAC7, LAC15	Lignin polymerization	[56]
	(K)	(New cuticle) Residuum cell	Stiffening	Cutin/cuticle	TEM	?	Cuticle formation	[56]

Tracheary elements (reinforcement/conduction)	(L)	Lignin decoration series	Stiffening, impermeabilization	Lignins	Lignin autofluorescence	LAC4, LAC17, PRX72	Lignin polymerization	[66,88]
Fibers (reinforcement/support)	(M)	Cell corner/compound middle lamella				LAC4, PRX64, PRX71		[69,88]
	(N)	Secondary wall				LAC4, LAC17, PRX72		[69,88]
Root endodermis (apoplastic barrier/water loading control through symplasm)	(O)	Casparian strip	Stiffening, impermeabilization	Lignins	Lignin autofluorescence	CASP1	Serves as an anchoring platform	[79]
						RBOHF	H_2O_2 local accumulation	[78]
						PRX64	Lignin polymerization	[78]
Seed mucilage secretory cell (mucilage hydrogel release upon imbibition/seed germination)	(P)	Radial outer wall/periclinal wall junction	Loosening during development to later enable rupture during imbibition	HG	HG partial ME (JIM7/LM20)	PME6	Creates HG anchoring platform for PRX36	[97,98]
						PRX36	Local loosening of the CWM	[95,97]

[a]The CW microdomain (CWM) ID and remodeling functions correspond to those used in Figure 3.
[b]Similar polysaccharides and phenolic compounds are associated with remodeling events involved in a variety of processes throughout plant development. These have been characterized using a large number of probes (Table S1 in the supplemental information online for detailed legend) and stains specific for polysaccharides decorations such as the degree of methylesterification (ME) of HG.
[c]In addition, CWM coverage was expanded with fluorescent-tagged remodeling enzymes positioned in local CWM hotspots. Most actors belong to multigenic families of CW remodeling proteins and may be recruited to several CWMs. Anchoring platforms for these enzymes are necessary for local activity but their formation is poorly known, making molecular scaffolds mediated by CASPs and PMEI6 prime examples to explain the spatial restriction of CWM remodeling.
[d]Abbreviation: TEM, transmission electron microscopy.

Stiffening events of wall microdomains

The abscission zone, tracheary elements, and fibers illustrate the involvement and positioning of oxidoreductases for the stiffening of wall microdomains though polarized lignification.

Although only a few studies have sought to investigate abscission, the underlying processes have started to be uncovered. The spatial control of sepal and petal abscission requires (i) the formation of a lignin molecular brace in **secession cells** (Figure 3J), allowing (ii) the compartmentation of several wall-hydrolyzing enzymes to the adjacent secession cells, and (iii) the transdifferentiation of the facing **residuum cells** into epidermal cells with the *de novo* formation of a cuticle (Figure 3K) [56]. The targeted wall hydrolysis of secession cells is supported by the identification of two polygalacturonases QRT2 and ADPG2 that are responsible for organ abscission in arabidopsis [57]. Interestingly, these PGs were also involved in anther and/or silique dehiscence, suggesting that similar processes may be found in other abscission zones. In addition, the pectate lyase PLL18 was restricted to the abscission zone, and ectopic accumulation of PLL18 was observed when lignin biosynthesis was chemically impaired [56]. This further demonstrates how this molecular brace allows local loosening/degradation of the adjacent wall. Lignification of the wall microdomain requires CIII PRX, LAC activities, and H_2O_2 production [56]. *LAC7* and *LAC15* expression is restricted to the secession cells where the lignin-brace microdomain is formed (Table 1J and Figure 3J) [56]. Local production of H_2O_2 may be associated with the redundant activity of two NADPH oxidases, RBOHD and RBOHF, because a double mutant lacks lignin formation, and complementation with either isoform was sufficient to restore lignin production (Table 1J and Figure 3J) [56]. Whether or not LAC and CIII PRX play a redundant role remains unclear and accurate localization of individual candidates to the abscission zone wall microdomains is needed. Recent studies on corolla detachment in *Nicotiana benthamiana* provided evidence of both lignin deposition at the base of the corolla and conservation of similar abscission-regulating enzymes [58,59]. Interestingly, similar enzymes were found to control floral organ abscission, inner root-tissue hydrolysis allowing lateral root emergence, and root cap detachment, suggesting that conserved mechanisms control physiological wall-degradation processes [60].

Arabidopsis has two main types of lignified tissues: (i) tracheary elements (tracheids and vessels) that conduct water and nutrients, and (ii) interfascicular fibers that provide mechanical support. Tracheary element differentiation is an interesting non-cell-autonomous process which ends in remodeling events of wall microdomains after cell death, as reviewed in detail [61,62]. Indeed, neighboring living parenchyma cells deliver the H_2O_2 and O_2 necessary for CIII PRX and LAC-mediated lignin polymerization of the dying tracheary elements, respectively. During the sequential differentiation of tracheary elements from protoxylem to metaxylem, lignification of the secondary wall occurs in specifically patterned wall microdomains (Figure 1D–G and Figure 3L) most likely due to sequential positioning and colocalization of wall-remodeling actors at the lignification sites [63,64]. Because H_2O_2 and O_2, can diffuse through the wall, it is likely that the specific pattern of lignification is not due to particular localization of these co-substrates for CIII PRXs and LACs, respectively, but instead to positioning of these two types of monolignol-oxidizing enzymes [65]. LAC4 and LAC17 were found to drive lignification in protoxylem tracheary elements [66,67]. Interestingly, both enzymes were precisely localized to the lignification sites, illustrating their contribution to the patterning of lignification [64]. In addition, PRX72 has a similar activity and localization, indicating that CIII PRXs can also act in concert with LACs for monolignol polymerization [68,69]. Likewise, in interfascicular fibers from arabidopsis floral stem, multiple CIII PRXs and LACs are involved in lignin polymerization. LAC4, PRX64, and PRX71 were localized to the cell corner/compound middle lamella microdomain (Table 1M and Figure 3M) [69]. Interestingly, during fiber development, while PRX64 remained at the cell corner, LAC4 localization switched from the cell corner to the secondary wall microdomain, resulting in complementary non-overlapping

localization patterns (Table 1M,N and Figure 3M,N) [69]. This suggests that these oxidoreductases may have different protein mobility and/or anchoring properties and complementary roles. Local lignification of wall microdomains can provide further roles in addition to mechanical support, impermeabilization, or compartmentation. In *Cardamine hirsuta*, seed dispersion is 'explosive'. Interestingly, precise lignification of inner wall microdomains of the endocarp b was required for energy accumulation and release. Such lignification was found in multiple *Cardamine* species, suggesting that the actors positioning lignin polymerization are conserved, although their identities remain unknown [70]. Altogether, genetic evidence for the involvement of LAC and CIII PRX isoforms at the wall microdomain level is accumulating. Although most of these studies used lignin autofluorescence or lignin histochemical staining to assess lignification patterns, future work might reach another level of resolution by linking reverse genetics and microscopy approaches such as immunogold labeling [71–73] or more recently developed *in vivo* biorthogonal click chemistry [74–76], thereby allowing to visualize the heterogeneity of lignin monomers and inter-unit linkages within wall microdomains.

Two emerging models of molecular scaffolds

The Casparian strip in the root endodermis and the opening zone in seed mucilage secretory cells are two different cell-wall microdomains that have been extensively studied over the past decade. Both wall microdomains implicate a specific CIII PRXs but with opposite roles (stiffening and loosening, respectively). Moreover, these wall microdomains led to two emerging models of molecular scaffolds to explain the positioning of these specific CIII PRXs in wall microdomains.

Role of CASP transmembrane proteins in PRX64-dependent lignification of the Casparian strip

The Casparian strip of the root endodermis was described early on [77]. It is a dense layer of lignified primary wall that restricts apoplastic diffusion of nutrients and pathogens into the stele (Figure 1J and Figure 3O). In-depth characterization of its development provided an exhaustive list of the molecular actors involved and of their relationships. Lignification of the Casparian strip is achieved through PRX64 activity supported by RBOHF-dependent ROS production [78]. Accurate positioning of PRX64 to the Casparian strip and of RBOHF to the neighboring plasma membrane region requires CASP1, a transmembrane protein that colocalizes with RBOHF (Table 1O and Figure 4A,B) [78,79]. The nature of the molecular interaction is not known, but CASP1 is additionally able, when ectopically expressed, to determine PRX64 positioning [78,79]. This discovery highlighted how plants can position particular actors to remodel a specific wall microdomain. Since then, multiple actors involved in either CASP1 positioning or Casparian strip integrity were identified [80–84]. The regulatory and molecular processes influencing Casparian strip formation have been beautifully reviewed [85,86], and the importance of LAC versus CIII PRX for lignifying the Casparian strip was recently highlighted [87]. Leaving little space for functional redundancy, the authors obtained a nonuple *lac* mutant and a quintuple *cIII prx* mutant for endodermis-specific candidate genes. Although Casparian strip formation was little or unaffected in the nonuple *lac* mutant, lignification of the strip was abolished in the quintuple *cIII prx* mutant and fully restored by complementation with *PRX64* [87]. This strongly suggests that, although the activity of both families of proteins could theoretically lead to similar lignin polymerization, the availability of (co)substrates (monolignols, H_2O_2, O_2) and the localization of specific members of these oxidoreductase multigenic families to wall microdomains could functionally separate them *in muro*, in agreement with the complementary localization of PRX64 and LAC4 in fiber wall microdomains discussed in the previous section [69,88]. The occurrence of the Casparian strip can be traced as far back as 400 million years ago [89]; it is therefore not surprising to observe this lignifying strip in the roots of most plants. The promoters of arabidopsis *CASP1*, of the tomato ortholog of *PRX64*, and of regulatory genes involved in Casparian strip formation in arabidopsis were all active in tomato root endodermis, suggesting a conserved

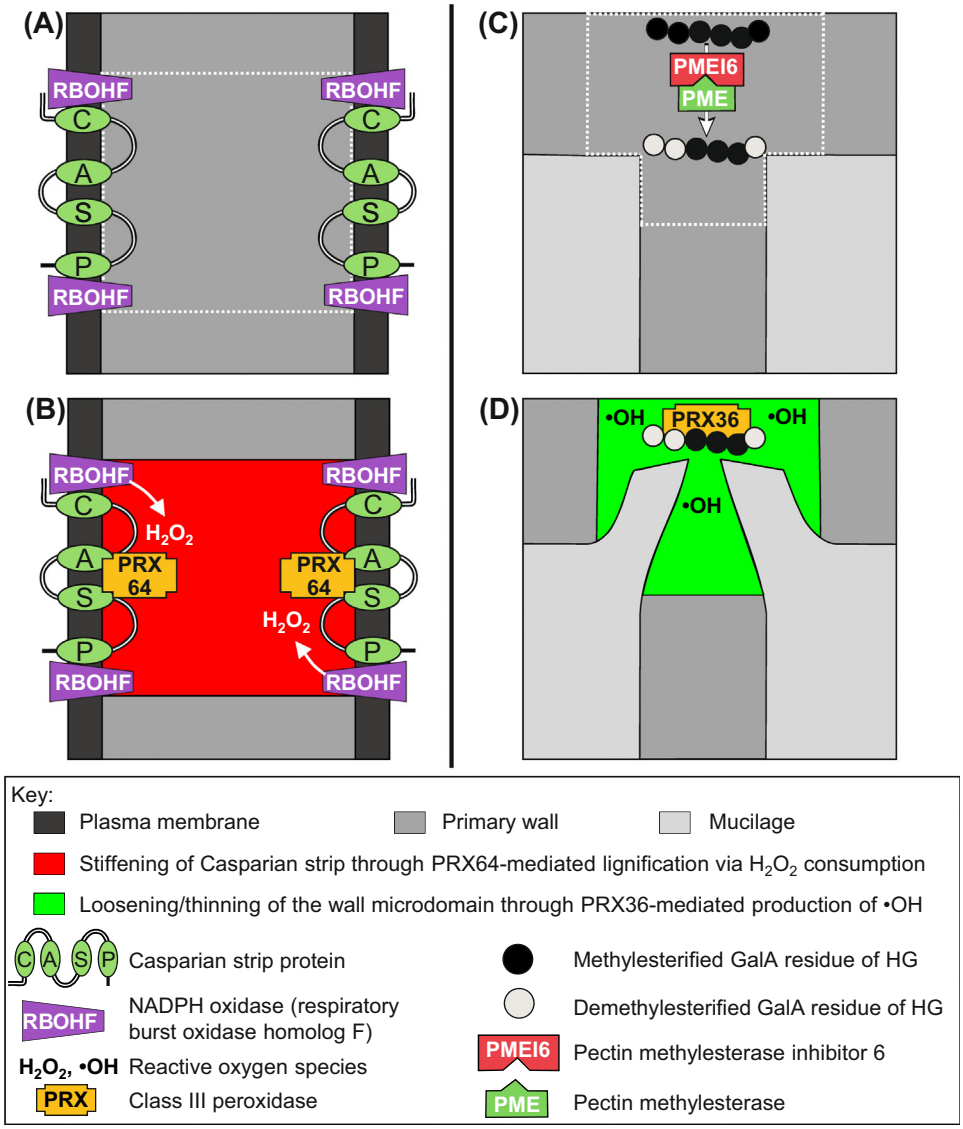

Figure 4. Two molecular scaffolds explain the positioning of remodeling enzymes in key wall microdomains of *Arabidopsis thaliana*. (A,B) In the root endodermis (Figure 3O), CASP1 is localized to the plasma membrane facing the future Casparian strip (wall microdomain delimited by white dots) [79]. CASP1 colocalizes and is responsible for (i) the complementary positioning of RBOHF in the same plasma membrane microdomain (A), and (ii) the recruitment of PRX64 in the facing wall microdomain (B) [78]. RBOHF-dependent H_2O_2 accumulation through an undescribed superoxide dismutase allows PRX64-driven local lignin polymerization of the Casparian strip that serves as an apoplastic barrier in the root (B). Note that CASP1–RBOHF–PRX64 physical interaction was not strictly demonstrated. (C,D) In the seed mucilage secretory cells (Figure 3P), PMEI6 controls a so far unidentified pectin methylesterase (PME) to create a partially demethylesterifed homogalacturonan (HG) bar-code pattern that is localized to the radial/outer periclinal primary wall interface (wall microdomain delimited by white dots) (C). This pattern acts as the anchoring platform to localize PRX36 to this wall microdomain (D). In turn, PRX36 is able to perform its purported localized loosening function through •OH-dependent non-enzymatic cleavage of nearby polysaccharides [95] akin to the wall microdomain thinning observed by transmission electron microscopy (TEM) [97]. Upon seed imbibition, this wall microdomain simultaneously ruptures in all seed mucilage secretory cells, allowing proper mucilage release around the seed.

mechanism [90]. However, it is also known that the Casparian strip is slightly different in monocotyledonous plants such as rice: the endodermis lignification process additionally encompasses the inner periclinal wall, leaving only the outer periclinal wall unlignified [91]. This 'U-shaped' strip is characteristic of monocots, and raises additional questions about how this is achieved.

Role of a specific HG anchoring platform for PRX36-dependent loosening of a wall microdomain in seed mucilage secretory cells

So far, examples of CIII PRX activity have focused around wall stiffening induced by monolignol polymerization or extensin polymerization, as discussed elsewhere [92–94]. However, CIII PRXs can also be responsible for wall loosening through polysaccharide cleavage due to ROS production [21], as suggested in a peculiar wall microdomain of mucilage secretory cells (MSCs) in arabidopsis seed [95]. MSCs are the outermost seed coat cell layer and an interesting model for studying wall remodeling [96]. MSCs synthesize a mucilage made of a pectinaceous hydrogel that is compressed between the primary wall and the **columella** – a volcano-shaped non-lignified secondary wall that supposedly acts as a structural pillar (Figure 3P). Upon seed imbibition, a mucilage crown is released around the seed through simultaneous rupture in each MSC of a wall microdomain localized at the interface of the radial and outer periclinal primary walls (Figure 1K; green wall in Figure 3P) [96]. This programmed polarized rupture is made possible by the suggested local loosening and observed thinning of this peculiar wall microdomain earlier during seed development. The loosening is supposedly achieved by non-enzymatic cleavage due to PER36/PRX36 activity restricted to this area, although evidence of local ROS production was not provided [95]. The thinning was documented though ultrastructural observations [97]. Interestingly, the *pmei6* mutant had a similar mucilage release defect as observed in *prx36* [98], and a previous study showed that an apoplastic CIII PRX could be bound on calcium-pectate sites [99]. These results recently inspired the discovery of a molecular scaffold that can explain the relationship between PMEI6 and PRX36 [97]. First, PMEI6 locally inhibits the activity of a so far unidentified PME to generate a HG demethylesterification pattern restricted to the MSC rupture zone. This pattern is labeled by JIM7/LM20 in wild-type seeds and lost in the *pmei6* mutant (Table 1P and Figure 4C) [97]. In turn, this HG demethylesterification pattern acts as a specific amphiphilic platform that allows PRX36 anchoring in this peculiar wall microdomain (Table 1P and Figure 4D) [97]. It is interesting to note that this pioneering example establishes a conceptual relationship between the two categories of molecular actors that were first discussed separately in this review. This might pave the way for additional combinations of PME/PMEI isoforms and new molecular patterns of HG demethylesterification that could act as specific anchoring platforms for other CIII PRXs in distinct wall microdomains in arabidopsis as well as in other species.

In the future, the functional characterization of CASP-like proteins and of other HG demethylesterification patterns might explain the positioning of other CIII PRXs. The fact that PRX64 and PRX36 display opposite remodeling roles does not preclude that CASP-like-driven and PME/PMEI-driven positioning of other CIII PRXs might be exclusively related to stiffening and loosening, respectively. The presence/absence of stiffening substrates such as monolignols or extensin monomers is probably the main explanation for how a given CIII PRX can have stiffening versus loosening *in muro* roles in a given wall microdomain.

Concluding remarks and future perspectives

Overall, although it is evident that the generation and remodeling of wall microdomains does not exclusively involve HG demethylesterification patterns and oxidoreductases, it is striking to see the recurrent contributions of these molecular actors in many wall microdomains discussed here. Similarly, we do not expect that CASP or CASP-like isoforms and specific patterns of HG

Outstanding questions

Will the future identification and subcellular localization of individual PMEs and PMEIs explain the recurrent specific patterns of pectin demethylesterification observed by immunolabeling in numerous plant cell-wall microdomains?

Will the state-of-the-art lignin-imaging tools explain the function of the lignin-polymerizing oxidoreductases that are specifically deposited in wall microdomains?

Could the two current concepts of molecular scaffolds that allow positioning PRX64 and PRX36 to their specific wall microdomains in root endodermis and seed mucilage secretory cells, respectively, be translated to other wall microdomains by using other combinations of the multigene family-encoded proteins?

Which technological advancements will allow us to better elucidate the complexity of the molecular composition of wall microdomains, particularly considering the dynamic changes occurring during development?

Which additional plant model species other than arabidopsis could contribute to deciphering the molecular basis of wall microdomain remodeling?

Beyond plant development, how will the fields of plant–microorganism interaction (either beneficial or pathogenic) contribute to the molecular understanding of wall microdomain remodeling?

demethylesterification are the sole anchoring platforms for remodeling enzymes in wall microdomains, but these constitute promising conceptual templates for other member of the multigene families considered. Finally, we emphasize that these peculiar remodeling events for regional wall microdomains are important for wider-scale cellular and developmental outcomes (see Outstanding questions).

Acknowledgments

This work was supported by grants from Paul Sabatier Toulouse 3 University and the CNRS. This work was also supported by the French Laboratory of Excellence project 'TULIP' (ANR-10-LABX-41; ANR-11-IDEX-0002-02). This work and the PhD stipend of B.G.D. were specifically funded by the French National Research Agency project 'MicroWall' (ANR-18-CE20-0007).

Declaration of interests

No interests are declared.

Supplemental information

Supplemental information associated with this article can be found at https://doi.org/10.1016/j.tplants.2022.05.010.

References

1. Malinovsky, F.G. *et al.* (2014) The role of the cell wall in plant immunity. *Front. Plant Sci.* 5, 178
2. Bacete, L. and Hamann, T. (2020) The role of mechanoperception in plant cell wall integrity maintenance. *Plants* 9, 574
3. Zhang, B. *et al.* (2021) The plant cell wall: biosynthesis, construction, and functions. *J. Integr. Plant Biol.* 63, 251–272
4. Duruflé, H. *et al.* (2017) Cell wall proteome analysis of *Arabidopsis thaliana* mature stems. *Proteomics* 17, 1600449
5. Seifert, G.J. and Blaukopf, C. (2010) Irritable walls: the plant extracellular matrix and signaling. *Plant Physiol.* 153, 467–478
6. Lee, K.J.D. *et al.* (2011) Cell wall biology: perspectives from cell wall imaging. *Mol. Plant* 4, 212–219
7. Popper, Z.A. *et al.* (2011) Evolution and diversity of plant cell walls: from algae to flowering plants. *Annu. Rev. Plant Biol.* 62, 567–590
8. Roberts, K. (1990) Structures at the plant cell surface. *Curr. Opin. Cell Biol.* 2, 920–928
9. Roberts, K. (1994) The plant extracellular matrix: in a new expansive mood. *Curr. Opin. Cell Biol.* 6, 688–694
10. Cocking, E.C. (1972) Plant cell protoplasts – isolation and development. *Annu. Rev. Plant Physiol.* 23, 29–50
11. Gu, Y. *et al.* (2022) Cell biology of primary cell wall synthesis in plants. *Plant Cell* 34, 103–128
12. Anterola, A.M. and Lewis, N.G. (2002) Trends in lignin modification: a comprehensive analysis of the effects of genetic manipulations/mutations on lignification and vascular integrity. *Phytochemistry* 61, 221–294
13. Guo, J. *et al.* (2020) Exocytosis and endocytosis: coordinating and fine-tuning the polar tip growth domain in pollen tubes. *J. Exp. Bot.* 71, 2428–2438
14. Ridley, B.L. *et al.* (2001) Pectins: structure, biosynthesis, and oligogalacturonide-related signaling. *Phytochemistry* 57, 929–967
15. Wormit, A. and Usadel, B. (2018) The multifaceted role of pectin methylesterase inhibitors (PMEIs). *Int. J. Mol. Sci.* 19, 2878
16. Hocq, L. *et al.* (2017) Connecting homogalacturonan-type pectin remodeling to acid growth. *Trends Plant Sci.* 22, 20–29
17. Uluisik, S. and Seymour, G.B. (2020) Pectate lyases: their role in plants and importance in fruit ripening. *Food Chem.* 309, 125559
18. Yang, Y. *et al.* (2018) A profusion of molecular scissors for pectins: classification, expression, and functions of plant polygalacturonases. *Front. Plant Sci.* 9, 1208
19. Willats, W.G.T. *et al.* (2001) *In-situ* analysis of pectic polysaccharides in seed mucilage and at the root surface of *Arabidopsis thaliana*. *Planta* 213, 37–44
20. Berthet, S. *et al.* (2012) Role of plant laccases in lignin polymerization. In *Lignins: Biosynthesis, Biodegradation and Bioengineering* (Jouanin, L. and Lapierre, C., eds), pp. 145–172, Academic Press
21. Francoz, E. *et al.* (2015) Roles of cell wall peroxidases in plant development. *Phytochemistry* 112, 15–21
22. Trinh, D.C. *et al.* (2021) How mechanical forces shape plant organs. *Curr. Biol.* 31, R143–R159
23. Rounds, C.M. *et al.* (2011) Propidium iodide competes with Ca^{2+} to label pectin in pollen tubes and *Arabidopsis* root hairs. *Plant Physiol.* 157, 175–187
24. Mendrinna, A. and Persson, S. (2015) Root hair growth: it's a one way street. *F1000Prime Rep.* 7, 23
25. Schoenaers, S. *et al.* (2017) Molecular mechanisms regulating root hair tip growth: a comparison with pollen tubes. In *Pollen Tip Growth: From Biophysical Aspects to Systems Biology* (Obermeyer, G. and Feijó, J., eds), pp. 167–243, Springer
26. Bosch, M. *et al.* (2005) Pectin methylesterase, a regulator of pollen tube growth. *Plant Physiol.* 138, 1334–1346
27. Dardelle, F. *et al.* (2010) Biochemical and immunocytological characterizations of *Arabidopsis* pollen tube cell wall. *Plant Physiol.* 153, 1563–1576
28. Mollet, J.C. *et al.* (2013) Cell wall composition, biosynthesis and remodeling during pollen tube growth. *Plants* 2, 107–147
29. Luo, N. *et al.* (2017) Exocytosis-coordinated mechanisms for tip growth underlie pollen tube growth guidance. *Nat. Commun.* 8, 1687
30. Mravec, J. *et al.* (2017) An oligogalacturonide-derived molecular probe demonstrates the dynamics of calcium-mediated pectin complexation in cell walls of tip-growing structures. *Plant J.* 91, 534–546
31. Röckel, N. *et al.* (2008) Elaborate spatial patterning of cell-wall PME and PMEI at the pollen tube tip involves PMEI endocytosis, and reflects the distribution of esterified and de-esterified pectins. *Plant J.* 53, 133–143
32. Cascallares, M. *et al.* (2020) A complex journey: cell wall remodeling, interactions, and integrity during pollen tube growth. *Front. Plant Sci.* 11, 599247
33. Jiang, L. *et al.* (2005) VANGUARD1 encodes a pectin methylesterase that enhances pollen tube growth in the *Arabidopsis* style and transmitting tract. *Plant Cell* 17, 584–596
34. Qin, P. *et al.* (2012) Callose plug deposition patterns vary in pollen tubes of *Arabidopsis thaliana* ecotypes and tomato species. *BMC Plant Biol.* 12, 178
35. Li, G. *et al.* (2018) Rice morphology determinant-mediated actin filament organization contributes to pollen tube growth. *Plant Physiol.* 177, 255–270
36. Dehors, J. *et al.* (2019) Evolution of cell wall polymers in tip-growing land plant gametophytes: composition, distribution, functional aspects and their remodeling. *Front. Plant Sci.* 10, 441
37. Breygina, M. *et al.* (2021) Pollen germination and pollen tube growth in gymnosperms. *Plants* 10, 1301

38. Park, S. *et al.* (2011) A role for CSLD3 during cell-wall synthesis in apical plasma membranes of tip-growing root-hair cells. *Nat. Cell Biol.* 13, 973–980
39. Javelle, M. *et al.* (2011) Epidermis: the formation and functions of a fundamental plant tissue. *New Phytol.* 189, 17–39
40. Ziv, C. *et al.* (2018) Multifunctional roles of plant cuticle during plant-pathogen interactions. *Front. Plant Sci.* 9, 1088
41. Liu, S. *et al.* (2021) Solving the puzzle of shape regulation in plant epidermal pavement cells. *Annu. Rev. Plant Biol.* 72, 525–550
42. Majda, M. *et al.* (2017) Mechanochemical polarization of contiguous cell walls shapes plant pavement cells. *Dev. Cell* 43, 290–304
43. Higaki, T. *et al.* (2017) Exogenous cellulase switches cell interdigitation to cell elongation in an RIC1-dependent manner in *Arabidopsis thaliana* cotyledon pavement cells. *Plant Cell Physiol.* 58, 106–119
44. Haas, K.T. *et al.* (2020) Pectin homogalacturonan nanofilament expansion drives morphogenesis in plant epidermal cells. *Science* 367, 1003–1007
45. Sampathkumar, A. *et al.* (2014) Subcellular and supracellular mechanical stress prescribes cytoskeleton behavior in Arabidopsis cotyledon pavement cells. *eLife* 3, e01967
46. von Wangenheim, D. *et al.* (2017) Adding a piece to the leaf epidermal cell shape puzzle. *Dev. Cell* 43, 255–256
47. Sotiriou, P. *et al.* (2018) Local differentiation of cell wall matrix polysaccharides in sinuous pavement cells: its possible involvement in the flexibility of cell shape. *Plant Biol.* 20, 223–237
48. Rui, Y. *et al.* (2017) POLYGALACTURONASE INVOLVED IN EXPANSION3 functions in seedling development, rosette growth, and stomatal dynamics in *Arabidopsis thaliana*. *Plant Cell* 29, 2413–2432
49. Rui, Y. *et al.* (2019) Synergistic pectin degradation and guard cell pressurization underlie stomatal pore formation. *Plant Physiol.* 180, 66–77
50. Amsbury, S. *et al.* (2016) Stomatal function requires pectin demethyl-esterification of the guard cell wall. *Curr. Biol.* 26, 2899–2906
51. Carter, R. *et al.* (2017) Stomatal opening involves polar, not radial, stiffening of guard cells. *Curr. Biol.* 27, 2974–2983
52. Yi, H. *et al.* (2018) Mechanical effects of cellulose, xyloglucan, and pectins on stomatal guard cells of *Arabidopsis thaliana*. *Front. Plant Sci.* 9, 1566
53. Wu, H.C. *et al.* (2017) Pectin methylesterase is required for guard cell function in response to heat. *Plant Signal. Behav.* 12, e1338227
54. Giannoutsou, E. *et al.* (2016) Spatio-temporal diversification of the cell wall matrix materials in the developing stomatal complexes of *Zea mays*. *Planta* 244, 1125–1143
55. Jones, L. *et al.* (2005) A conserved functional role of pectic polymers in stomatal guard cells from a range of plant species. *Planta* 221, 255–264
56. Lee, Y. *et al.* (2018) A lignin molecular brace controls precision processing of cell walls critical for surface integrity in *Arabidopsis*. *Cell* 173, 1468–1480
57. Ogawa, M. *et al.* (2009) *Arabidopsis* dehiscence zone polygalacturonase1 (ADPG1), ADPG2, and quartet2 are polygalacturonases required for cell separation during reproductive development in *Arabidopsis*. *Plant Cell* 21, 216–233
58. Wu, X.M. *et al.* (2012) The tobacco BLADE-ON-PETIOLE2 gene mediates differentiation of the corolla abscission zone by controlling longitudinal cell expansion. *Plant Physiol.* 159, 835–850
59. Ventimilla, D. *et al.* (2021) IDA (INFLORESCENCE DEFICIENT IN ABSCISSION)-like peptides and HAE (HAESA)-like receptors regulate corolla abscission in *Nicotiana benthamiana* flowers. *BMC Plant Biol.* 21, 226
60. Shi, C.L. *et al.* (2019) Control of organ abscission and other cell separation processes by evolutionary conserved peptide signaling. *Plants* 8, 225
61. Turner, S. *et al.* (2007) Tracheary element differentiation. *Annu. Rev. Plant Biol.* 58, 407–433
62. Escamez, S. and Tuominen, H. (2014) Programmes of cell death and autolysis in tracheary elements: when a suicidal cell arranges its own corpse removal. *J. Exp. Bot.* 65, 1313–1321
63. Gardiner, J.C. *et al.* (2003) Control of cellulose synthase complex localization in developing xylem. *Plant Cell* 15, 1740–1748
64. Schuetz, M. *et al.* (2014) Laccases direct lignification in the discrete secondary cell wall domains of protoxylem. *Plant Physiol.* 166, 798–807
65. Ros Barceló, A. (2005) Xylem parenchyma cells deliver the H_2O_2 necessary for lignification in differentiating xylem vessels. *Planta* 220, 747–756
66. Berthet, S. *et al.* (2011) Disruption of LACCASE4 and 17 results in tissue-specific alterations to lignification of *Arabidopsis thaliana* stems. *Plant Cell* 23, 1124–1137
67. Zhao, Q. *et al.* (2013) LACCASE is necessary and nonredundant with PEROXIDASE for lignin polymerization during vascular development in *Arabidopsis*. *Plant Cell* 25, 3976–3987
68. Herrero, J. *et al.* (2013) Bioinformatic and functional characterization of the basic peroxidase 72 from *Arabidopsis thaliana* involved in lignin biosynthesis. *Planta* 237, 1599–1612
69. Hoffmann, N. *et al.* (2020) Laccases and peroxidases co-localize in lignified secondary cell walls throughout stem development. *Plant Physiol.* 184, 806–822
70. Hofhuis, H. *et al.* (2016) Morphomechanical innovation drives explosive seed dispersal. *Cell* 166, 222–233
71. Joseleau, J.P. and Ruel, K. (1997) Study of lignification by noninvasive techniques in growing maize internodes (an investigation by Fourier transform infrared cross-polarization-magic angle spinning ^{13}C-nuclear magnetic resonance spectroscopy and immunocytochemical transmission electron microscopy). *Plant Physiol.* 114, 1123–1133
72. Goujon, T. *et al.* (2003) Down-regulation of the AtCCR1 gene in *Arabidopsis thaliana*: effects on phenotype, lignins and cell wall degradability. *Planta 2003 217:2* 217, 218–228
73. Kiyoto, S. *et al.* (2014) Relative deposition of xylan and 8-5′-linked lignin structure in *Chamaecyparis obtusa*, as revealed by double immunolabeling by using monoclonal antibodies. *Planta* 241, 243–256
74. Lion, C. *et al.* (2017) BLISS: a bioorthogonal dual-labeling strategy to unravel lignification dynamics in plants. *Cell Chem. Biol.* 24, 326–338
75. Simon, C. *et al.* (2018) Visualizing lignification dynamics in plants with click chemistry: dual labeling is BLISS! *J. Vis. Exp.* 2018, e56947
76. Morel, O. *et al.* (2021) REPRISAL: mapping lignification dynamics using chemistry, data segmentation, and ratiometric analysis. *Plant Physiol.* 188, 816–830
77. Bonnett, H.T. (1968) The root endodermis: fine structure and function. *J. Cell Biol.* 37, 199–205
78. Lee, Y. *et al.* (2013) A mechanism for localized lignin deposition in the endodermis. *Cell* 153, 402–412
79. Roppolo, D. *et al.* (2011) A novel protein family mediates Casparian strip formation in the endodermis. *Nature* 473, 381–384
80. Pfister, A. *et al.* (2014) A receptor-like kinase mutant with absent endodermal diffusion barrier displays selective nutrient homeostasis defects. *eLife* 3, e03115
81. Kalmbach, L. *et al.* (2017) Transient cell-specific EXO70A1 activity in the CASP domain and Casparian strip localization. *Nat. Plants* 3, 17058
82. Li, B. *et al.* (2017) Role of LOTR1 in nutrient transport through organization of spatial distribution of root endodermal barriers. *Curr. Biol.* 27, 758–765
83. Nakayama, T. *et al.* (2017) A peptide hormone required for Casparian strip diffusion barrier formation in *Arabidopsis* roots. *Science* 355, 284–286
84. Reyt, G. *et al.* (2020) Uclacyanin proteins are required for lignified nanodomain formation within Casparian strips. *Curr. Biol.* 30, 4103
85. Nakamura, M. and Grebe, M. (2018) Outer, inner and planar polarity in the *Arabidopsis* root. *Curr. Opin. Plant Biol.* 41, 46–53
86. Barbosa, I.C.R. *et al.* (2019) The Casparian strip – one ring to bring cell biology to lignification? *Curr. Opin. Biotechnol.* 56, 121–129
87. Rojas-Murcia, N. *et al.* (2020) High-order mutants reveal an essential requirement for peroxidases but not laccases in Casparian strip lignification. *Proc. Natl. Acad. Sci. U. S. A.* 117, 29166–29177

88. Yi Chou, E. *et al.* (2018) Distribution, mobility, and anchoring of lignin-related oxidative enzymes in *Arabidopsis* secondary cell walls. *J. Exp. Bot.* 69, 1849–1859
89. Geldner, N. (2013) The endodermis. *Annu. Rev. Plant Biol.* 64, 531–558
90. Li, P. *et al.* (2018) Spatial expression and functional analysis of Casparian strip regulatory genes in endodermis reveals the conserved mechanism in tomato. *Front. Plant Sci.* 9, 832
91. Cai, X. *et al.* (2011) Development of Casparian strip in rice cultivars. *Plant Signal. Behav.* 6, 59–65
92. Mishler-Elmore, J.W. *et al.* (2021) Extensins: self-assembly, crosslinking, and the role of peroxidases. *Front. Plant Sci.* 12, 664738
93. Pacheco, J.M. *et al.* (2022) Apoplastic class III peroxidases PRX62 and PRX69 promote *Arabidopsis* root hair growth at low temperature. *Nat. Commun.* 13, 1310
94. Jacobowitz, J.R. *et al.* (2019) PRX9 and PRX40 are extensin peroxidases essential for maintaining tapetum and microspore cell wall Integrity during *Arabidopsis* anther development. *Plant Cell* 31, 848–861
95. Kunieda, T. *et al.* (2013) Spatiotemporal secretion of PEROXIDASE36 is required for seed coat mucilage extrusion in *Arabidopsis*. *Plant Cell* 25, 1355–1367
96. Francoz, E. *et al.* (2015) *Arabidopsis* seed mucilage secretory cells: regulation and dynamics. *Trends Plant Sci.* 20, 515–524
97. Francoz, E. *et al.* (2019) Pectin demethylesterification generates platforms that anchor peroxidases to remodel plant cell wall domains. *Dev. Cell* 48, 261–276
98. Saez-Aguayo, S. *et al.* (2013) Pectin methylesterase inhibitor6 promotes *Arabidopsis* mucilage release by limiting methylesterification of homogalacturonan in seed coat epidermal cells. *Plant Cell* 25, 308–323
99. Carpin, S. *et al.* (2001) Identification of a Ca^{2+}pectate binding site on an apoplastic peroxidase. *Plant Cell* 13, 511–520
100. Zhang, T. *et al.* (2019) Disentangling loosening from softening: insights into primary cell wall structure. *Plant J.* 100, 1101–1117

Supplemental Information

Cell wall microdomain remodeling controls critical developmental processes

Bastien G. Dauphin[1], Philippe Ranocha[1], Christophe Dunand[1] and Vincent Burlat[1,*]

[1]Laboratoire de Recherche en Sciences Végétales, Université de Toulouse, CNRS, UPS, Toulouse INP, 24 chemin de Borde Rouge, 31320 Auzeville-Tolosane, France.

** Corresponding author:* V. Burlat (burlat@lrsv.ups-tlse.fr)

Table S1. Selected occurrence of the terms cell wall (CW) domain or CW microdomain in the literature[a]

CW (micro)domain theoretical definition or experimental description	Review (definition or description) Probe (description)	Refs.
"every cell has an extracellular matrix that should be regarded […] as a mosaic of **wall domains** with different and specific compositions and functions"	Review (Definition)	[S1]
"distinct zones of pectin distribution are detectable in each primary CW lamellae, thus reinforcing our notion of the importance of **domains in wall architecture**"	JIM5, JIM7 mAbs	[S2]
Differential distribution of XG and HG/RG-I epitopes to particular **CW domains** in Clover root tip cortical cells * The term "domain" is also used to describe RGI and HG pectinaceous molecular domains bringing some confusion of scale (CW vs molecule)	αXG, αHG/RGI pAbs	[S3]
Spatiotemporal +/- methylesterified HG **CW microdomains** of Tomato developing fruit pericarp	JIM5, JIM7 mAbs	[S4]
Definition of the **CW** continuum as being divided up like a patchwork quilt into **domains** or patches, each of which may have distinct compositions, architectures and properties	Review (definition)	[S5]
Calcium pectate in middle lamella, corner of intercellular air spaces, corner of the cell separation spaces of Tomato developing fruits corresponded to **CW microdomains**	JIM5 mAb, SIMS (Ca^{2+})	[S6]
+/- methylesterified HG **CW microdomains** in middle lamella and three-way junctions of Potato stem	JIM5, JIM7 mAbs	[S7]
Calcium pectate in middle lamella, corner of intercellular spaces, wall area surrounding air-spaces of Flax hypocotyl cortical parenchyma corresponded to **CW microdomains**	endoPGase-gold/SIMS (Ca^{2+})	[S8]
Calcium patterns in **CW microdomain** of middle lamella vs intercellular spaces of Apple pericarp	^{44}Ca (exogenous) and ^{40}Ca SIMS	[S9]
Localization of CW polysaccharide epitopes in well-defined **domains within the CW** of *A. thaliana* root epidermis	CCRC-M1, M2, M7 mAbs	[S10]
Erwinia chrysanthemi PL and PME polymorphism reflecting **CW microdomains** of host plants	RFLP in pathogenic bacteria	[S11]
CW microdomain containing low esterified HG without calcium surrounding plasmodesmata of apple fruit	cationic gold and JIM5 mAb +/- EDTA	[S12]
Colocalization of low esterified HG and PME epitopes in **CW microdomains** of flax hypocotyls cortical tissues	JIM5 mAb, αPME pAb	[S13]
Cellulose-microfibril-xyloglucan network, network of pectins and network of structural cell wall proteins presented as distinguished local primary **CW microdomains**	Review (definition)	[S14]
Discrete **CW microdomains** with various HG demethylesterification patterns around air spaces of pea stem cortical parenchyma resulting in complex combinations of physical properties	LM7, JIM5, PAM1 mAbs	[S15]
Endoxylanase characterization during Papaya fruit ripening linked to **CW microdomain**-specific hydrolysis		[S16]
Local variations of the CW composition of a given cell named **CW microdomains**	Review (description)	[S17]
Overview of fluorescent tags used to explore CW structure and dynamics including **CW microdomains** within a single CW	Review (description)	[S18]
Laccases direct lignification in the discrete secondary **CW domains** of protoxylem	Laccase-mcherry	[S19]

New reciprocal COS probes to spatially track HG processing within discrete **CW microdomains** of *A. thaliana* stem parenchyma cells and other tissues	JIM7 mAb, COS^{488}	[S20]
Overview of targeting of given CIII-PRX isoforms to discrete **CW microdomains** to perform local CW remodeling	Review (description)	[S21]
Different spatial organization of incorporation and processing of HG in **CW microdomains** of *A. thaliana* stem pith parenchyma, pollen tubes and root hairs	2F4, JIM5, JIM7 mAbs; $OG7\text{-}13^{488}$	[S22]
A partially methylesterified HG epitope controlled by PMEI6 is necessary for anchoring PRX36 in a *A. thaliana* seed mucilage secretory cell **CW domain** allowing proper mucilage release	JIM7, LM20 mAbs, αPRX36 pAb	[S23]
Wall regional specificities of micropillar endosperm from dry seeds labeled by polysaccharide specific antibodies suggest the occurrence of **CW microdomains**	LM25, LM15, LM19, LM6, LM13, LM16 mAbs	[S24]

[a]COS^{488}, chitosan oligosaccharide probe tagged with Alexa fluor 488, CIII-PRX, class III peroxidase; DP, degree of polymerization; HG, homogalacturonan; mAb, monoclonal antibody; $OG7\text{-}13^{488}$, mixture of oligogalacturonans of DP7 to DP13 tagged with Alexa fluor 488; pAb, polyclonal antibody; RFLP, restriction fragment length polymorphism; RGI, rhamnogalacturonan I; SIMS, secondary ion mass spectrometry; XG, xyloglucan

Supplemental references

S1 Roberts, K. (1990) Structures at the plant cell surface. *Curr. Opin. Cell Biol.* 2, 920–928

S2 McCann, M.C. *et al.* (1992) Complexity in the spatial localization and length distribution of plant cell-wall matrix polysaccharides. *J. Microsc.* 166, 123–136

S3 Lynch, M.A. and Staehelin, L.A. (1992) Domain-specific and cell type-specific localization of two types of cell wall matrix polysaccharides in the clover root tip. *J. Cell Biol.* 118, 467–479

S4 Roy, S. *et al.* (1992) Immunocytochemical study of the deesterification patterns during cell wall autolysis in the ripening of cherry tomato. *Plant Physiol. Biochem.* 30, 139–146

S5 Roberts, K. (1994) The plant extracellular matrix: in a new expansive mood. *Curr. Opin. Cell Biol.*6, 688–694

S6 Roy, S. *et al.* (1994) Analytical detection of calcium ions and immunocytochemical visualization of homogalacturonic sequences in the ripe cherry tomato. *Plant Physiol. Biochem.* 32, 633–640

S7 Marty, P. *et al.* (1995) Composition and localization of pectic polymers in the stems of two *Solanum tuberosum genotypes*. *Plant Physiol. Biochem.* 33, 409–417

S8 Rihouey, C. *et al.* (1995) Calcium and acidic pectin distribution in flax cell walls: evidence for different kinds of linkages in the cell junction and middle lamella of the cortical parenchyma of *flax hypocotyl*. *Plant Physiol. Biochem.* 33, 497–508

S9 Roy, S. *et al.* (1995) Use of secondary ion mass spectrometry to image ^{44}calcium uptake in the cell walls of apple fruit. *Protoplasma* 189, 163–172

S10 Freshour, G. *et al.* (1996) Developmental and tissue-specific structural alterations of the cell-wall polysaccharides of *Arabidopsis thaliana roots*. *Plant Physiol.* 110, 1413–1429

S11 Nassar, A. *et al.* (1996) Characterization of *Erwinia chrysanthemi* by pectinolytic isozyme polymorphism and restriction fragment length polymorphism analysis of PCR- amplified fragments of pel genes. *Appl. Environ. Microbiol.* 62, 2228–2235

S12 Roy, S. *et al.* (1997) Characterization of the cell wall microdomain surrounding plasmodesmata in apple fruit. *Plant Physiol.* 114, 539–547

S13 Morvan, O. *et al.* (1998) Immunogold localization of pectin methylesterases in the cortical tissues of flax hypocotyl. *Protoplasma* 202, 175–184

S14 Schindler, T.M. (1998) The new view of the primary cell wall. *Z. Pflanz. Bodenkunde* 161, 499–508

S15 Willats, W.G.T. *et al.* (2001) In-situ analysis of pectic polysaccharides in seed mucilage and at the root surface of *Arabidopsis thaliana*. *Planta* 213, 37–44

S16 Roy, S. *et al.* (2003) Endoxylanase expressed during papaya fruit ripening: purification, cloning and characterization. *Funct. Plant Biol.* 30, 433–441

S17 Zhong, R. and Ye, Z.H. (2007) Regulation of cell wall biosynthesis. *Curr. Opin. Plant Biol.* 10, 564–572

S18 Gonneau, M. *et al.* (2012) Fluorescent tags to explore cell wall structure and dynamics. *Front. Plant Sci.* 3, 145

S19 Schuetz, M. *et al.* (2014) Laccases direct lignification in the discrete secondary cell wall domains of protoxylem. *Plant Physiol.* 166, 798–807

S20 Mravec, J. *et al.* (2014) Tracking developmentally regulated post-synthetic processing of homogalacturonan and chitin using reciprocal oligosaccharide probes. *Development* 141, 4841–4850

S21 Francoz, E. *et al.* (2015) Roles of cell wall peroxidases in plant development. *Phytochemistry* 112, 15–21

S22 Mravec, J. *et al.* (2017) An oligogalacturonide-derived molecular probe demonstrates the dynamics of calcium-mediated pectin complexation in cell walls of tip-growing structures. *Plant J.* 91, 534–546

S23 Francoz, E. *et al.* (2019) Pectin demethylesterification generates platforms that anchor peroxidases to remodel plant cell wall domains. *Dev. Cell* 48, 261-276

S24 Jemmat, A.M. *et al.* (2020) Coordination of five class III peroxidase-encoding genes for early germination events of *Arabidopsis thaliana*. *Plant Sci.* 298, 110565

1.3. *Arabidopsis thaliana* seed

1.3.1. Mucilage secretory cells (MSC)

A. thaliana MSCs are the outermost layer of the seed coat (**Figure 1.12A**) and serve as a great model to study CW dynamics (Arsovski et al., 2010; Francoz et al. 2015a; Griffiths and North, 2017; Šola et al., 2019a). Indeed, their development encompasses unique CW architectural changes at the subcellular scale. Throughout development, the cytoplasmic space is gradually replaced by two distinct CW structures: the columella and the mucilage (**Figure 1.12**). As the seed matures, the cytoplasmic hardly takes any place which makes localizing cytoplasmic/membrane bound proteins difficult and eventually impossible in dry seed MSCs made only of CW material. However, this makes MSC an ideal model to study apoplastic proteins. Both mucilage and columella, along with the surrounding primary wall present distinct pectocellulosic and protein composition. This highlights a likely high degree of spatio-temporal control of CW polyssacharides and their remodeling enzymes in compartmented space. As implied, MSC were given their name for their ability to produce the mucilage, a highly complex trait that is not present in all plant species and which various ecological functions are still not fully understood (Viudes et al., 2020).

1.3.1.1. The mucilage

The *A. thaliana* mucilage is a pectin polymer mostly made of poorly branched RG-I, though small amounts of HGs, arabinans, xylans and cellulose are also present (Phan and Burton, 2018). During seed maturation, its synthesis starts at around 7 DAP and it is compartmentalized between the columella and the primary wall (**Figure 1.12B**). The mucilage is likely remodeled by various CW proteins such as PMEs (Francoz et al., 2015a; Turbant et al., 2016). Interestingly, its hydrophilic properties provided by large quantities of pectins allow it to swell during inbibition and to break the primary wall in remote zones (top of radial primary walls) to be homogenously released around the seed. At this point, it can be visually separated in two distinct layers (i) the adherent mucilage which stays cohesive with seed MSCs at the basis of the columella and (ii) the non-adherent mucilage (**Figure 1.12B**). It is still unclear how both types of mucilage are organized in developing MSCs though it is possible that both layers are blended during MSC development. The non-adherent mucilage high solubility was associated with a lack of cellulose, xylan and pectin content / interaction. (Griffiths et al., 2016). Interestingly, the adherent mucilage cellulose fibrils are likely associated with the nearby volcano-shaped columella which serve as anchor point to the

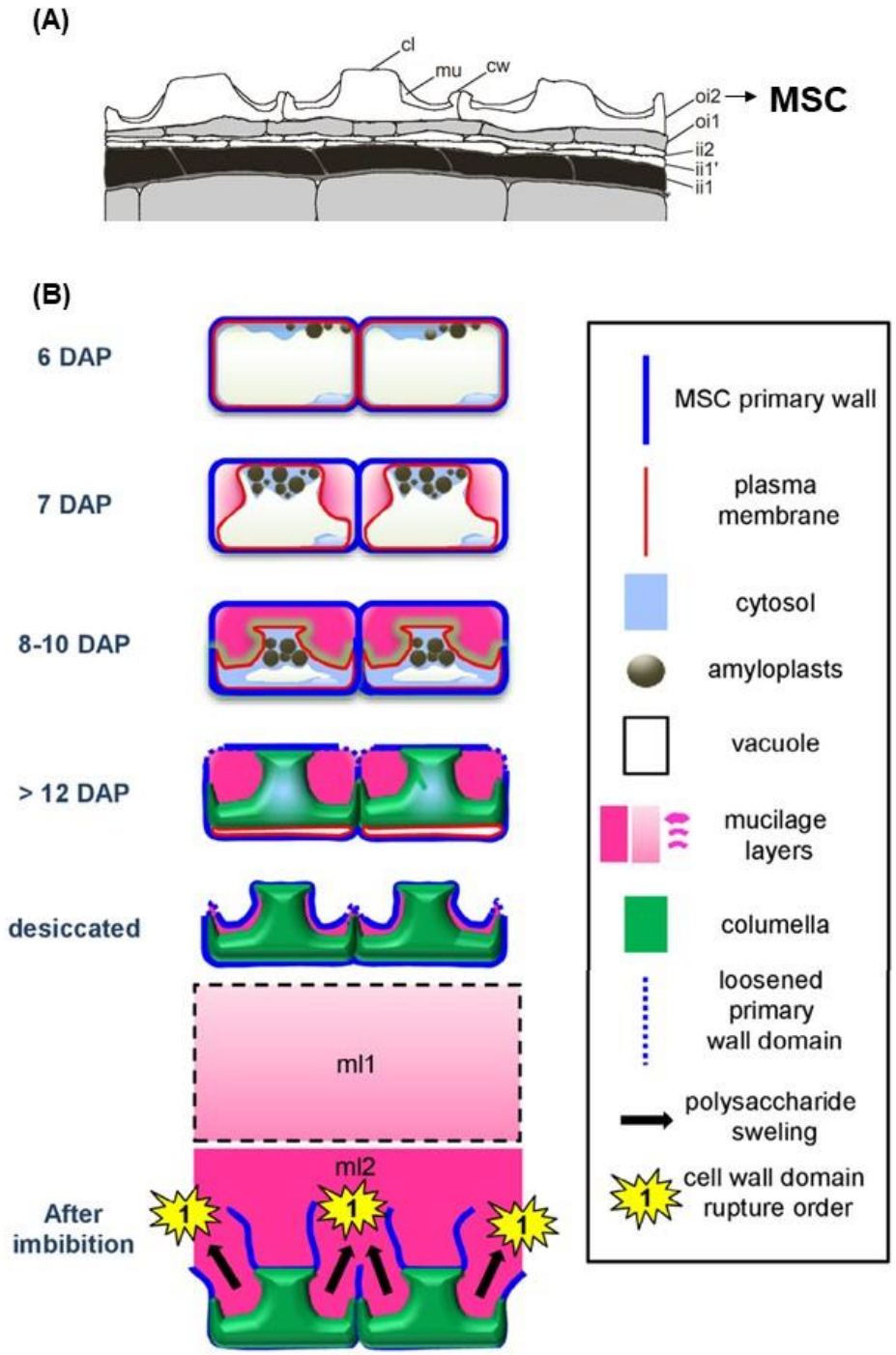

Figure 1.12: *A. thaliana* seed mucilage secretory cell (MSC) development illustrating the diversity of cell wall dynamics confined in one single cell layer. (A) Section of mature seed coat from (Debeaujon et al 2007). MSCs are the outermost epidermal layer also named outer integument 2 (oi2). Note the volcano-shape columella surrounded by the pectinaceous mucilage. **(B)** Kinetics of MSC development in the historical model *A. thaliana* from (Viudes et al 2020), It highlights the complex cell wall dynamics with the presence of a volcano-shaped columella, the simultaneous rupture of primary cell wall domain in each MSC and the distinction between adherent mucilage (am) and non-adherent mucilage layers (nam). oi: outer integument, ii: inner integument, DAP: day after pollination,

organized released adherent mucilage (Griffiths et al., 2016; Griffiths and North, 2017)

1.3.1.2. The columella

MSC surface observations immediately highlight the columella which stands out as this volcano-shaped secondary formed CW (around 10 DAP) at the center of MSC (**Figure 1.12**). It is thought to serves as an anchor for mucilage structuring polyssacharides like cellulose, although MSC from species lacking columella can also present structured mucilage (Viudes et al., 2021). The columella is primarily made of cellulose, although its exact composition is unclear (Macquet et al., 2007). Some CW proteins like RUBY, a galactose oxidase (Šola et al., 2019b) and PMEI6 which regulates mucilage methylesterification (Saez-Aguayo et al., 2013; Ezquer et al., 2016) were found apically positioned around or center of the columella.Yet, it is likely that additionnal CW proteins are present in the columella to mediate its connectivity with adjacent adherent mucilage and overhead primary wall.

1.3.1.3. The primary wall

On the surface, MSC primary wall exhibits traditional properties. Yet, it encompasses a subcellular CW remodeling which is critical for proper mechanical release of the mucilage (**Figure 1.12B**). Around 8 DAP, PMEI6 activity on unknown PME/PMEs results in a partial methylesterification pattern in HG at the top of the radial wall (Saez-Aguayo et al., 2013). This pattern was shown to allow for PRX36 anchoring in this CW microdomain and subsequent local primary wall loosening, possibly through ROS generation although this was never formely demonstrated (Francoz et al., 2019b). Lack of either PRX36 or PMEI6 resulted in defect in primary wall rupture and subsequent defect in mucilage release (Saez-Aguayo et al., 2013; Kunieda et al., 2013). Is it unknown if parallel CW stiffening events take place in adjacent wall, although primary wall-columella linkage remaining after mucilage release (**Figure 1.12B**) is likely to involve local CW stiffening.

Combined with aforementioned MSC dynamics, precise PRX36 anchoring in its CW microdomain highlighted the importance of this cell layer as a model to study local CW remodeling events.

1.4. Context and objectives

This work is part of the ANR project "Cell wall Microdomain molecular scaffolds control plant cell Wall dynamics" (Microwall) between three main partners (i) Vincent Burlat (LRSV, Toulouse), (ii) Jérôme Pelloux (BIOPI, Amiens) and (iii) Marie-Christine Ralet (BIA, Nantes) which aims to further understand the dynamics of PMEI6-PRX36 microdomain and evaluate the relevance of the paradigm in other CW microdomains.
As such, my objectives were to identify additional partners of this molecular scaffold. Which PME is inhibited by PMEI6 activity? Are there other molecular determinants required for PRX36 anchoring? Are there other spatially confined PRXs responsible for MSC CW dynamics?

As such, my experimental work is separated in three chapters.

Chapter 2: First, I aimed to screen additional candidates and evaluate their putative involvement in both mucilage release and PRX36 anchoring in its CW microdomain. I put particular emphasis on putative HG remodeling enzymes though other leads were explored.

Chapter 3: Then, I intended to functional characterize one particular actor (TBL38) which stood up after initial screening. I investigated its molecular function and discussed its activity and positionning with PRX36-PMEI6 molecular scaffold.

Chapter 4: Finaly, I meant to initiate first steps in the assessement of the recurrence of such microdomain in MSCs. I screened five additional MSC expressed *CIII-PRXs* and tried to correlate the localization and function of one promising candidate (PRX56) with other CW remodeling event akin to stiffening.

With regards to the data spreaded across these parts, and to improve overall clarity of my work, each chapter was designed and written in an hybrid form between manuscript and journal article. As such, results are compiled and discussed in this manner, although it mostly fits the functional characterization of a promising candidate in Chapter 3. The methods and bibliography sections are more traditionnaly gathered at the end of the thesis.

2. Chapter two: *PRX36-PMEI6* seed coat co-expression network is enriched in MSC-expressed genes and CW microdomain co-accumulating proteins

The work included in this Chapter is the result of my personal work started during a Master's internship and further completed during my PhD.

MSC dynamics have been described across multiples species and developmental stages and studies on *A. thaliana* led to a so called "MSC toolbox" encompassing large amounts of gene involved in this process in this species, many of which were specific to MSCs (Francoz et al., 2015a; Viudes et al., 2021). These previously described actors were classified in general roles varying from transcriptional factors, mucilage synthesis/secretion/stabilization, CW modification… Recently, PRX36 and PMEI6, two CW proteins were found to be part of the same molecular scaffold necessary for mucilage release via a CW microdomain modification (Saez-Aguayo et al., 2013; Kunieda et al., 2013; Francoz et al., 2019b). The first part of this work consisted in identifying additional molecular actors involved in the PRX36-PMEI6 molecular scaffold.

2.1. Generating a co-expression network focused on PEROXIDASE36 expression

Precise remodeling of the CW microdomain localized to the top of MSC radial primary walls by PRX36 is done thanks to PRX36 anchoring to the PMEI6-dependant homogalacturonan specific methylesterification pattern during embryogenesis (Francoz et al., 2019b). This is related to a tight spatio-temporal co-expression of both genes using the tissue-specific seed developmental kinetics GSE12404 dataset (Belmonte et al., 2013; Francoz et al., 2019b). We reanalyzed the co-expression network centered on *PRX36* in which each gene was assigned a Pearson correlation coefficient and a rank (**Figure 2.1A**). Originally, *PMEI6* came as the first hit initiating the previous parallel study of both genes products leading to the conclusion that both enzymes were eventually involved in the same CW microdomain molecular scaffold (Francoz et al., 2019b). Adopting similar logic, we isolated five putative candidates based on their overall ranking and predicted molecular function (**Figure 2.1A**). Little is known about *DUF1191* (At4g01140) which is predicted to be a transmembrane protein except that a rice DUF1191 domain-containing gene was found to be upregulated in heat stress (Lv et al., 2019). *TRICHOME-BIREFRINGENCE-LIKE38* (At1g29050) belongs to a multigenic family (46 members in *A. thaliana*) of acetyl-transferases, some of which influence the degree of acetylation of wall polymers. We selected *PME16/PMEPCRD* (At2g43050) and *PME6/HMS* (At1g23200) as putative interacting candidates with PMEI6. Interestingly, PME6 was described as HIGHLY METHYL ESTERIFIED SEEDS as *pme6* seeds were unable to properly release their mucilage (Levesque-Tremblay et al., 2015). Finally, we selected *CASP-LIKE PROTEIN 2A1* (At1g17200) to assess the possibility that a CASPL-mediated transmembrane

A

RK	PCC	Gene Symbol	pre-globular stage							globular stage							heart stage							linear-cotyledon stage							bending cotyledon stage							mature green stage						
			pg EP	pg MOE	pg PEN	pg CZEN	pg CZSC	pg SC	pg WS	g EP	g SUS	g MOEN	g PEN	g CZEN	g CZSC	g SC	g WS	h EP	h MOEN	h PEN	h CZEN	h CZSC	h SC	h WS	lc EP	lc MOEN	lc PEN	lc CZEN	lc CZSC	lc SC	lc WS	bc EP	bc PEN	bc CZEN	bc CZSC	bc SC	bc WS	mg EP	mg MOEN	mg PEN	mg CZEN	mg CZSC	mg SC	mg WS
1	1.0000	*PRX36*	15	27	4	11	8	8	2	4	2	13	2	12	8	2	4	3	3	3	15	14	3	9	4	5	9	12	405	1522	554	1	2	27	992	29	20	7	1	11	3	53	65	9
2	0.9474	*PMEI6*	2	15	7	8	2	1	6	2	1	2	1	2	2	6	6	2	8	8	4	10	6	13	10	54	54	1	52	423	236	6	34	14	232	65	52	29	11	19	25	37	93	34
3	0.9145	*DUF1191*	2	11	14	11	7	12	3	0	9	11	10	7	6	5	7	5	5	22	11	13	60	83	6	3	1	14	181	656	101	3	5	9	196	160	19	19	1	6	5	34	27	9
13	0.8160	*TBL38*	9	11	25	34	2119	876	1094	10	5	61	26	2	2076	1003	1508	8	9	8	55	1064	1790	1012	16	47	7	17	1274	5537	2991	44	1	1	2731	894	312	1262	10	31	9	582	135	476
44	0.6962	*PME16/PMEPCRD*	6	18	14	26	2	2	8	9	16	4	4	5	6	12	12	8	3	19	19	14	3	7	13	44	12	31	27	2340	390	16	43	16	44	1338	366	12	2	30	21	69	318	95
376	0.4519	*PME6/HMS*	20	5	25	3	10	14	11	13	12	5	8	10	3	9	12	4	4	18	18	42	46	182	8	33	11	11	70	3096	1674	14	41	15	607	5134	1431	16	41	31	12	432	1513	322
1619	0.2713	*CASPL2A1*	17	3	40	30	124	838	650	111	223	12	19	11	15	686	997	235	42	24	9	139	1578	817	187	30	7	10	235	944	407	194	21	5	237	329	140	214	26	13	8	36	176	207
12571	-0.0591	*ACT2*	475	316	726	490	175	272	249	491	159	349	537	474	72	205	426	654	1003	909	643	150	267	426	554	387	1517	503	73	550	694	715	627	447	98	159	790	356	190	287	247	147	96	408

B

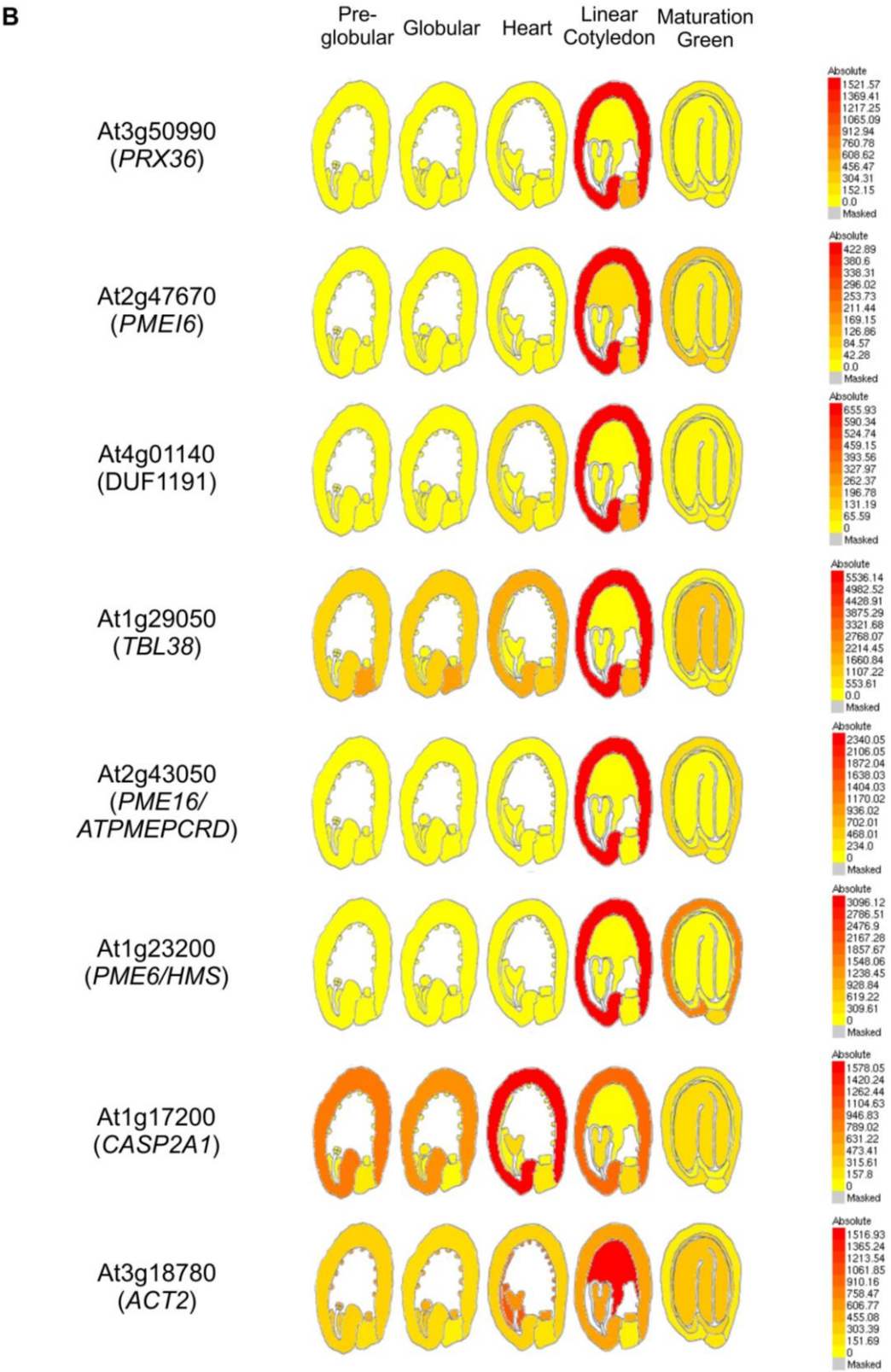

platform could be necessary for PRX36 anchoring in a similar fashion as the CASP1-PRX64 model in root endodermis (Lee et al., 2013). In this example, CASP define the future Casparian Strip territory before PRX64 positionning and activity (see published review in the introduction for more details).

Therefore, we selected *CASPL2A1* not for its rank in the network but for its high seed coat expression peaking before *PRX36* and *PMEI6.* Altogether, we data mined available tissue-specific transcriptomic data to select diverse putative actors of the PRX36-PMEI6 molecular scaffold, all of which show peak expression in the seed coat of developing seed similar to *PRX36* (**Figure 2.1A and B**).

Figure 2.1: Selection of candidate genes in *PRX36* and *PMEI6* co-expression network for further functional genomics study. **(A)** *PMEI6* is the first hit of the *PRX36* co-expression network using the tissue-specific seed developmental kinetics GSE12404 dataset (Belmonte et al., 2013). Mutants from both genes labeled in pink have similar mucilage phenotype (Kunieda et al., 2013; Saez-Aguayo et al., 2013) and a molecular link has been established to explain the similar phenotype: PMEI6 activity enables to produce a homogalacturonan specific methylesterification pattern necessary for PRX36 anchoring to a cell wall microdomain of mucilage secretory cells. The accurately positioned PRX36 further loosens the CW microdomain to enable correct mucilage release upon seed imbibition (Francoz et al., 2019b). In an effort to search new proteins involved in this cell wall microdomain molecular scaffold, five genes labeled in green have been selected for functional genomic study. These encode for: (i) a proteins of unknown function (DUF) closely co-expressed, (ii) a member of TBL family possibly involved in CW polysaccharide acetylation, (iii) 2 PME candidates that could be the target of PMEI6 (Note that *pme6/hms* has a mucilage phenotype; Levesque-Tremblay et al (2015)), and (iv) a CASP-like protein belonging to a multigenic family whose funding member CASP1 has been demonstrated to enable positioning of PRX64 to another CW microdomain in another biological context [formation of lignified Casparian strip of root endodermis, Lee et al (2013)]. The profile of *ACT2* used as a "house keeping" gene in this study is shown as well. RK, rank ; PCC, Pearson Correlation Coefficient ; EP, embryo proper ; SUS, suspensor ; MCE, micropylar endosperm ; PEN, peripheral endosperm ; CZEN, chalazal endosperm ; CZSC, chalazal seed coat ; SC, seed coat ; WS, whole seed. **(B)** expression profiles of the candidate genes in five out of the six developmental stages according to http://bar.utoronto.ca/efp/cgi-bin/efpWeb.cgi.

2.2. The expression of four candidate genes is restricted to the MSCs

Although the tissue-specific expression data used here gave crucial information for building an accurate co-expression network, additional precision was needed to assess MSC-specific expression of the candidate genes. Indeed, *A. thaliana* seed coat is made of 5 layers with MSCs being the outer-most layer named outer integument 2 (Debeaujon et al., 2003). Therefore, the expression data from Belmonte et al. did not give gene expression information from MSCs specifically but rather from a 5-layers thick seed coat tissue including MSCs. Acknowledging this, we generated digoxigenin-labeled RNA probes specific to each candidate and performed *in situ* RNA hybridization on wild-type paraffin sections of developing seeds (**Figure 2.2A**). No antisense probe could be generated for *CASPL2A1* which is not included in the Figure. The serial sections of the tissue-arrays and the facilitated analysis of the scans allowed comparison of the signal on serial sections of the exact same seeds for each gene. The specific hybridization signal appears in purple/violet over the overall brownish nonspecific background and natural pigmentation of the seed coat. The signal/background ratio can be further appreciated by comparing the antisense (AS) and corresponding sense (S) columns for each gene. The seed-coat specificity of the studied genes appeared with the whole seed view (**Figure 2.2A**) while the MSC-specific RNA-localization was better appreciated for *PRX36* and the four candidate genes (**Figure 2.2B**). The whole seed view also showed that the signal was weaker/absent in the chalazal seed coat zone at the bottom of each image (**Figure 2.2A**), in agreement with the transcriptomic data (**Figure 2.1A, B**). With regards to the background level of sense probe, the signal was the highest for seeds at the early linear and bending cotyledon stages (**Figure 2.2A**) in accordance with the co-expression data (**Figure 2.1A**). We were able to roughly correlate signal intensity with the expression kinetics of these genes, particularly for *DUF1191* which only showed faint signals (**Figure 2.1; Figure 2.2.A**).

Altogether, *DUF1191*, *TBL38*, *PME6* and *PME16* were specifically co-expressed with *PRX36* in the MSC particularly at the late heart/early linear cotyledon stages while *CASP2A1* could not be studied.

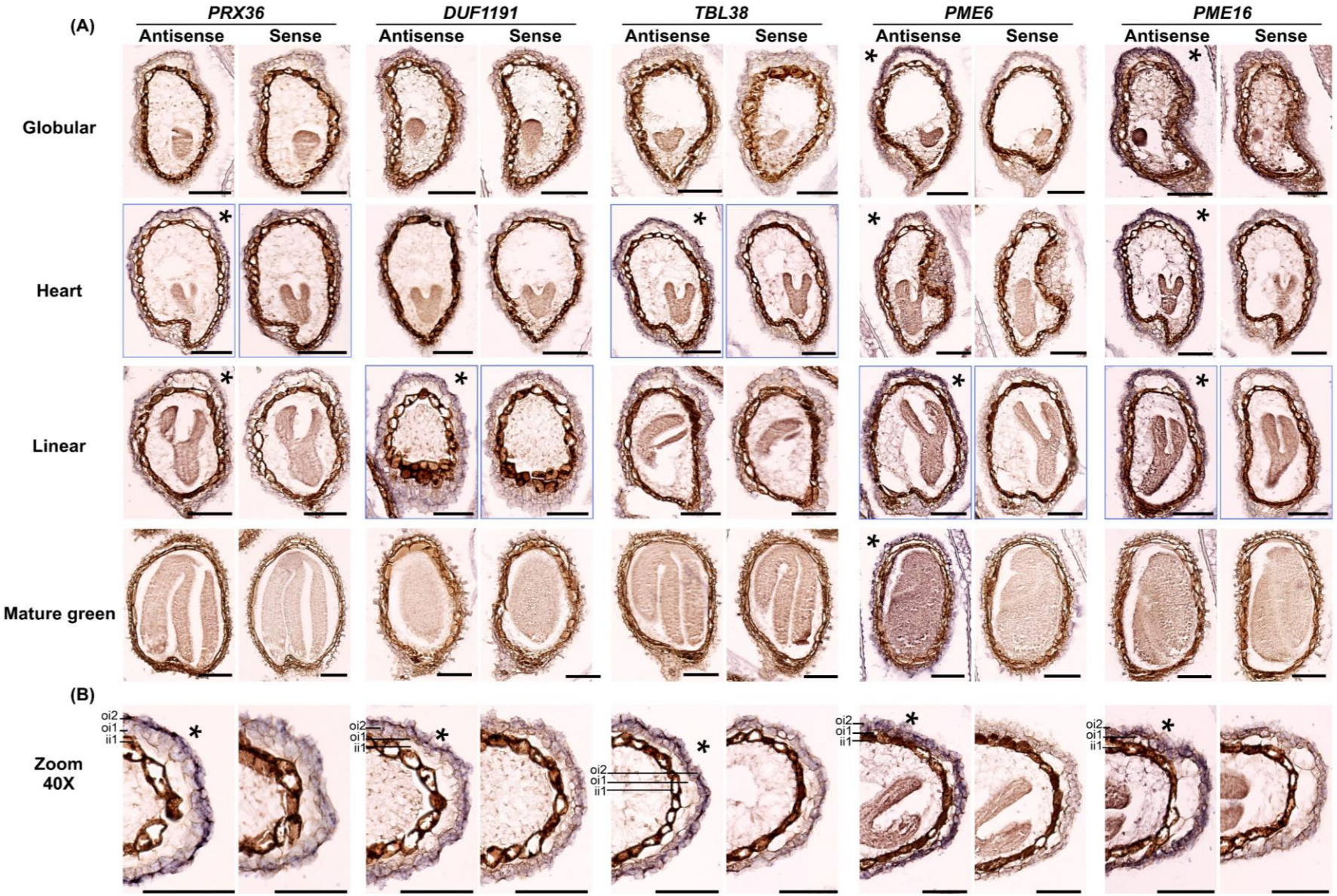

Figure 2.2: Transcript localization of four seed coat-expressed candidate genes is tied to the mucilage secretory cells (outer integument2). *In situ* RNA hybridization performed on serial sections of developing seeds. The seed coat is composed of five cell layers, the MCS corresponding to the outer most outer integument2 (oi2) while the inner most inner integument1 layer shows the typical natural brown pigmentation of the seed. **(A)** Kinetics of hybridized sections show gene expression across seed development. Sections were hybridized with gene-specific antisense (AS) probes which labeled the mucilage secretory oi2 cells of each seeds. The sense (S) probes correspond to the background level observed on a serial section of the same seed. The intensity of the signal observed in this column must be subtracted from the first column to determine the specificity of the signal. **(B)** 40X zoom of the apical zone of images highlighted in a blue box in (A). Signals were better observed at the early / linear cotyledon stage, although faint for *DUF1191*. Sections displayed for the 5 genes are taken from the same seed. Such contrasted signals were observed on multiple seeds. *, hybridization signal; Bars: 100 µm.

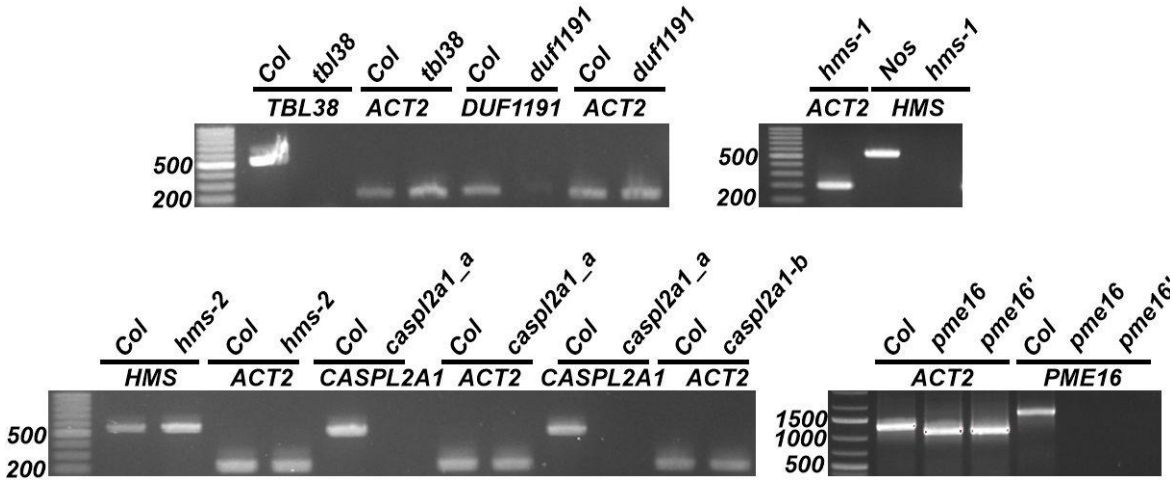

Sup. Fig. S2.1: Most TDNA-insertion lines for the 5 candidate genes are knock-out mutants. RT-PCR amplification was performed with 40 cycles to challenge the putative residual low expression levels in mutants. Gel should be read by grouping 4 lanes (studied gene in WT vs mutant, *ACTIN2* (*ACT2*) in WT vs mutant as loading controls, respectively) except for Nos where *ACT2* is missing. The second lane of each group indicates that all mutant lines expect *hms-2* are knock-out mutants while expression of *ACTIN2* remained unchanged. Note that PME16 expression in Col-0 was studied on genomic DNA which does not represents actual gene expression in wild-type. Similar result was found on cDNAs prepared from two independent sampling of 6 to 8 DAP old siliques.

2.3. Mucilage release assays show contrasted phenotypes

First, we isolated knock-out mutants for each candidate using high number of PCR cycles (**Sup. Fig. S2.1**). A very faint residual *DUF1191* expression was observed in *duf1191* and a strong *HMS* expression was observed in *hms-2*. In all the other mutants, no specific gene expression was observed and we selected these KO lines for the following assays (**Sup. Fig. S2.1**). Mutations on either *PRX36* or *PMEI6* show similar effect on mucilage release. Namely, without pre-weakening of the microdomain at the top of radial CW that occurs in wild type, the swelling mucilage cannot effectively break the radial primary wall, resulting in erratic mucilage release (Kunieda et al., 2013; Saez-Aguayo et al., 2013). Thus, we expected that mutations on genes belonging to PRX36 molecular scaffold could result in similar defect. To test this hypothesis, dry seeds were imbibed and released adherent mucilage was stained with ruthenium red. As expected, mucilage release was found impaired in *prx36*, *pmei6* and *pme6/hms* seeds (Saez-Aguayo et al., 2013; Kunieda et al., 2013; Francoz et al., 2019b; Levesque-Tremblay et al., 2015). Note that *pme6/hms* mutation occurred in a different ecotype background (Nos-0) that by itself behave in a slightly different manner as compared to Col-0, although *PME /HMS* expression was found in both wild-types. Visually, no differences were noticed for other

mutants whose adherent mucilage formed a continuous halo around seeds (**Figure 2.3**). Quantitative analysis of various mucilage parameters combined with statistical approaches confirmed our first observations, though *tbl38* and *pme16* seed mucilage release was slightly higher than that of Col-0. With care to the interpretation of these results, no obvious release defect was observed in mutated seeds from new candidate genes (**Figure 2.3**). However, mucilage release defects can be complex to assess, particularly if the protein actors only contribute for a portion of the process. Thus, we investigated the putative effects that mutation of the candidate genes could have on the PMEI6-dependent HG methylation pattern formation.

2.4. Generating specific MSC wall surface-enriched fractions

Initially, we sought to develop a quick and reliable way of extracting MSC CW from dry seeds to perform various analysis. MSC as a study model presents many benefits and we took advantage of two of them: direct accessibility of the surface of the seed and sturdiness. Collectively, this meant that MSC CW mechanical enrichment could be achieved if done in a controlled manner. To test this, a home-made abrasion system was developed in the team during a previous M2 internship (Trezel, 2018, See Methods; **Figure 6.11**) which allowed for precise MSC surface CW enrichment. Multiple parameters related to seed amount, sandpaper width or shaking speed were tested to obtain homogenous MSC surface CW.

Genotype	Col	*prx36*	*pmei6*	*duf1191*	*tbl38*
Preview	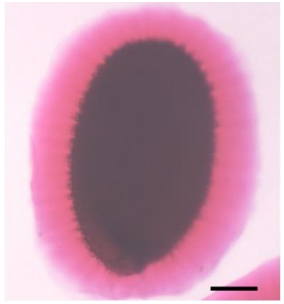	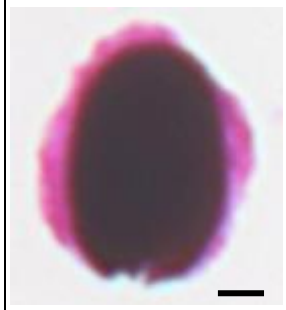	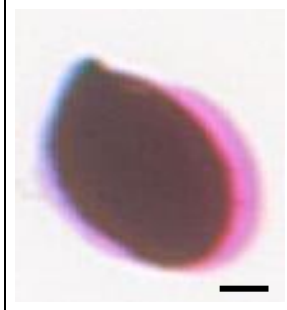	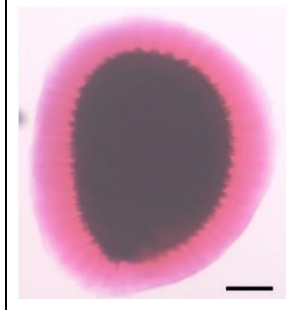	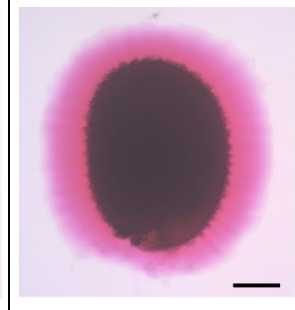
Mucilage area (µm²)	126145	55238	18881	124093	138428
Mucilage area (% of Col)	100	42	15	95	106
± SD (% of Col, µm²)	22	11	19	25	20
p-value (WT)		8,6905E-256	1,2502E-276	0,012102509	2,68836E-34
Genotype	*pme16*	*caspl2a1-a*	*caspl2a1-b*	*Nos*	*hms-1*
Preview	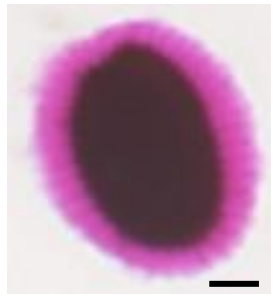	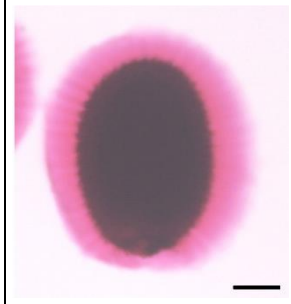	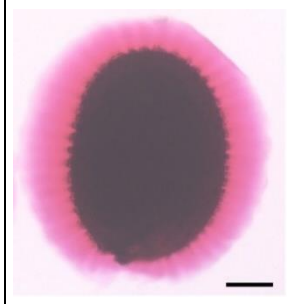	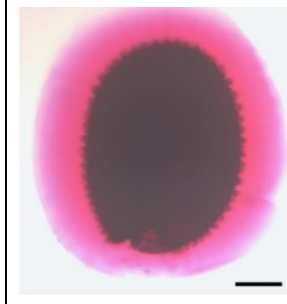	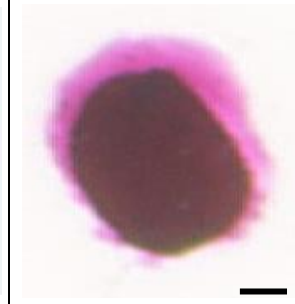
Mucilage area (µm²)	170564	94283	133516	103675	89547
Mucilage area (%)	131	73	103	80	69
(+/-) SEM (µm²)	24	23	31	19	50
p-value (WT)	4,46288E-59	4,1258E-31	0,147164435	2,07316E-41	3,29668E-05

Figure 2.3: None of the new candidates displays an obvious defect in mucilage release similar to those of *prx36* and *pmei6*. Ruthenium Red (RR) staining assays under aqueous shaking condition shows no obvious mucilage release abnormalities in mutants from new candidate genes as compared to previously studied mutants. The adherent mucilage area was presented as absolute values, % and following a red (max) to yellow (min) heatmap. Note the similar phenotype for *prx36* and *pmei6* as previously described (Francoz et al., 2019b). *hms-1* seeds consistently released little to no mucilage as compared to its wild type control Nos-0, as previously reported (Levesque-Tremblay et al., 2015) while other genotypes were similar to their Col-0 wild type common control. N = 157-571 seeds; SD: standard deviation expressed as % of Col-0; bar: 100 µm.

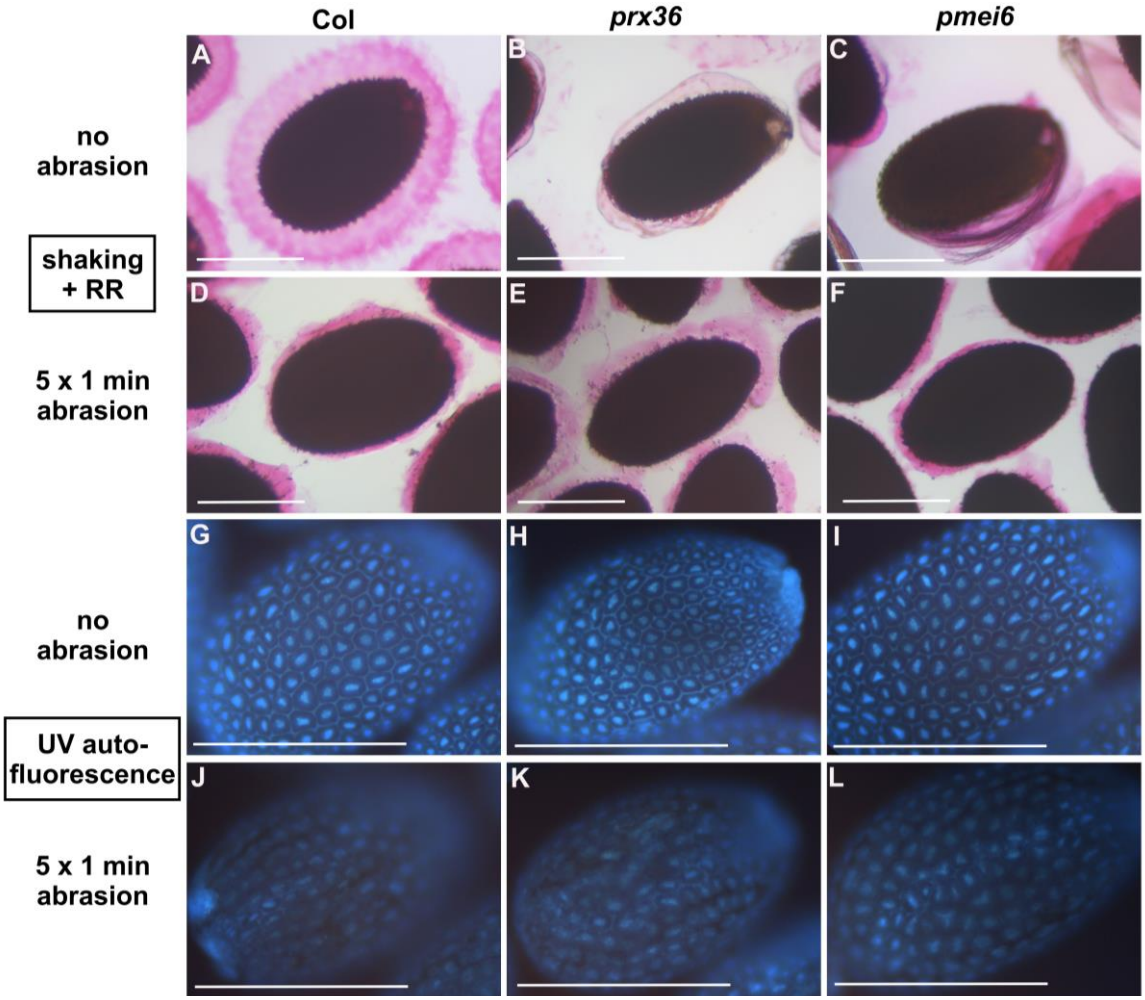

Figure 2.4: Mucilage release phenotype of *prx36* and *pmei6* seeds and efficiency of dry seed abrasion. Dry seeds from Col-0, *prx36* and *pmei6* before and after abrasion were **(A-F)** stained with ruthenium red (mucilage release efficiency), **(B-L)** observed under UV (MSC surface morphology). Note the remaining thin layer of adherent mucilage and the loss of autofluorescence of MSC radial walls and the decrease of autofluorescence of columella in the three genotypes Scale bars: 300 µm. (Adapted from Trezel, 2018).

Ruthenium red staining performed on abraded seeds from different genotypes could still label leftover mucilage suggesting that the abrasion only occurred at the surface of MSCs (**Figure 2.4 A-F**). Additionally, we used the MSC autofluorescence occurring at the radial CW and columella to assess the abrasion effect. The autofluorescence of the radial CW was essentially lost while that occurring at the columella was not fully lost in abraded seed (**Figure 2.4 G-L**). Further analysis (scanning electron microscopy, histochemistry, immunofluorescence) will be presented in the chapter 3 focused on TBL38 (**Sup. Fig. S3.1**). Taken together, these results indicated that the enrichment was specific to the surface of MSC CW with no contaminants from another cell. Samples were already grounded as a powder which was stable for weeks and could be used as such for further extraction and molecular analysis.

2.5. Immunodotblots on MSC surface wall extracts show TBL38 involvement in HG remodeling - Immunofluorescence on paraffin sections shows HG methylation status on a spatial scale

The specific HG methylation pattern necessary for PRX36 anchoring can be labeled by both JIM7 and LM20 monoclonal antibodies (Francoz et al., 2019b). In the literature, both are described as labeling HG with a relative high degree of methylesterification, and have often being used in pair (Verhertbruggen et al., 2009). Therefore, we performed DotBlot using both antibodies on MSC surface abrasive wall extracts to assess putative changes in the methylesterification status of MSC surface HG in mutated background. No changes in JIM7 labeling was observed aside from *pmei6* (**Figure 2.5A**) which was expected (Saez-Aguayo et al., 2013; Francoz et al., 2019b). Semi-quantitative measurements and analysis confirmed that no other significant changes occurred in other genotypes (**Figure 2.5A**). The same decrease of signal was observed with LM20 for *pmei6* (**Figure 2.5B**) as expected (Saez Aguayo; Francoz 2019). Surprisingly, significant changes were observed in *tbl38* as well, whose LM20 signal decrease was statistically similar to that of *pmei6* (**Figure 2.5B**). While JIM7 and LM20 recognition epitopes are partly different (Clausen et al., 2003; Verhertbruggen et al., 2009), loss of only one labeling in the context of this HG methylation pattern was unexpected since both antibodies behave similarly in previous studies as they did in *pmei6*. While other genotypes did not display any significant difference in both JIM7 and LM20 signal, dot blot assays did not consider the spatial distribution of the HG-ME pattern.

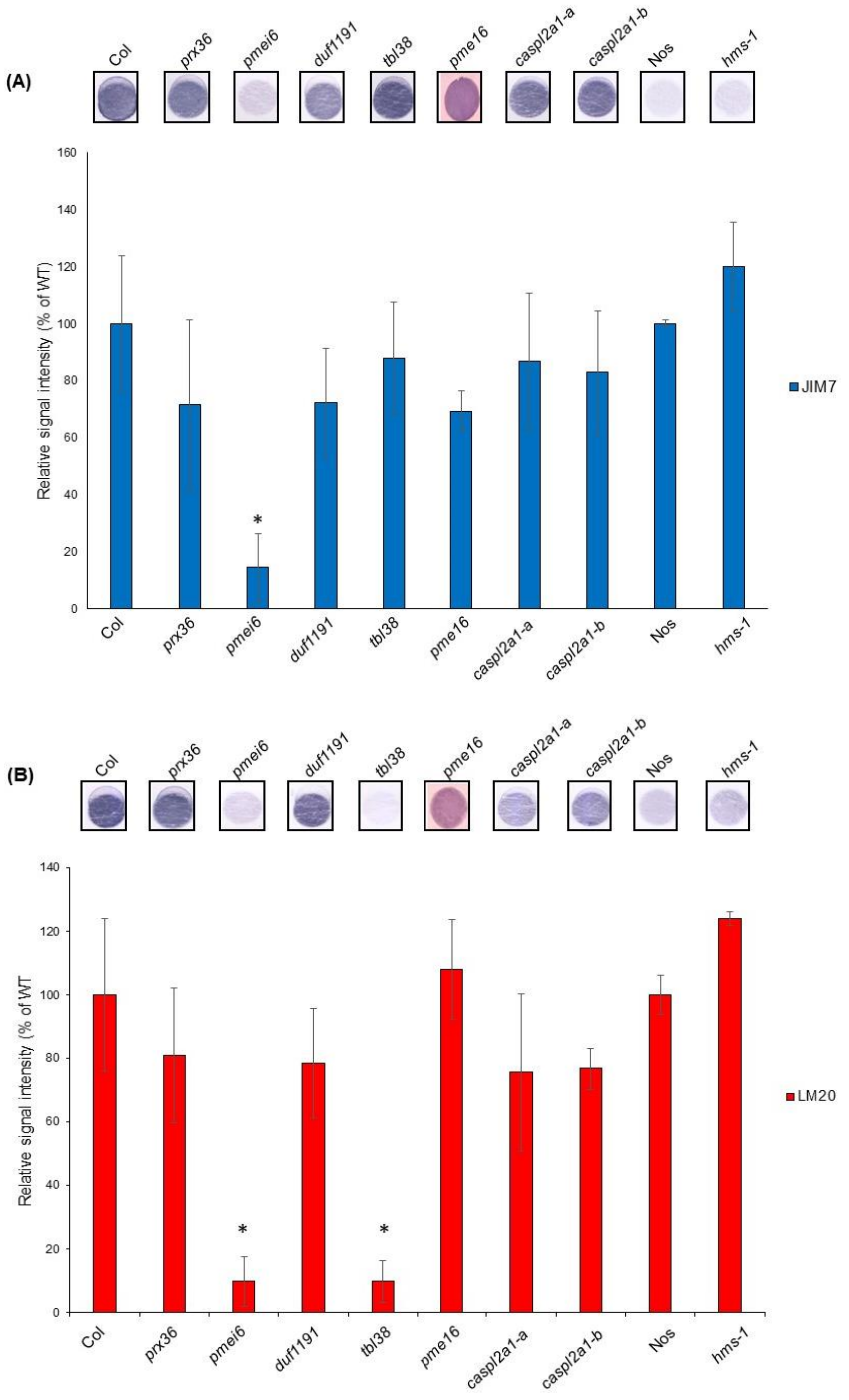

Figure 2.5: Immuno dot blots of MSC fractions show modifications in partially methylesterified HG labeled by JIM7 and LM20. (A) JIM7 Immuno dot blots of MSC enriched fractions show that *pmei6* is the only genotype having a phenotype (nearly 90% decrease of labeling). Individual dot examples were cropped out of the same nitrocellulose membrane showing a representative view of at least 2 biological replicates. **(B)** LM20 immuno dot blots highlight a similar 90% decrease of labeling for *pmei6* but a surprising additional 90% decrease of labeling for *tbl38* whose JIM7 labeling was unmodified. Note that the resultas are expressed as % of Col-0 or % of Nos-0. Statistical tests were performed to assign groups of values relative to Col-0 or Nos-0 for $p < 0.01$:
JIM7 p-value for Col-0 = (7.16E-2; 1.15E-5; 1.80E-2; 4.13E-2; 1.33E-4; 1.40E-1; 8.21E-2); for Nos-0 = 1.97E-2)
LM20 p-value for Col-0 = (3.30E-1; 2.73E-9; 2.70E-1; 4.50E-9; 2.89E-2; 2.60E-1; 1.24E-1); for Nos-0 = 1.82E-1).

Because such factors are equally as important for the PRX36 positioning, precise information on both signals was obtained at the sub-cellular level by immunofluorescence of JIM7 and LM20 on paraffin sections of tissue arrays encompassing developing seeds from the various genotypes. JIM7 signal in Col-0 was visible after 6 to 8 DAP at the onset of columella formation. They formed a pattern at the top of the radial primary CW which was consistent even at later developmental stages (**Figure 2.6**) in agreement with previous results (Francoz et al., 2019b). Although overall signal intensity could vary between genotype, signal intensity on section cannot be accurately quantified. As such, no significant changes in JIM7 labeling was observed in any genotypes aside from loss of JIM7 labeling on sections of *pmei6* as previously shown (Francoz et al., 2019b). Larger kinetics also confirmed that *pme6/hms* did not impact the MSC labeling for JIM7 at any developmental stage despite the strong defect in mucilage release (**Sup. Fig. S2.2**) as previously shown (Levesque-Tremblay et al., 2015). The positioning and loss of LM20 labeling in MSC CW microdomain was similar to JIM7 in Col-0 and *pmei6*, respectively (**Figure 2.7**). Like JIM7, the LM20 labeling was not significantly modified in most genotypes (**Figure 2.7; Sup. Fig. S2.2**). However, while *tbl38* displayed a JIM7 labeling in the microdomain located at the top of radial primary CW, the corresponding LM20 labeling was specifically lost, in agreement with dot blot results (**Figure 2.7**).

Altogether, this immunofluorescence and dot blots survey provided spatial and semi-quantitative results that confirmed the phenotype of *pmei6* (Saez-Aguayo et al., 2013; Francoz et al., 2019b) and the absence of phenotype of *prx36* (Francoz et al., 2019b) and *pme6/hms* (Levesque-Tremblay et al., 2015). This combined approach also showed the absence of phenotype of *pme16*, *duf1191* and *casp2a1* and more importantly it revealed the intriguing LM20 phenotype for *tbl38*.

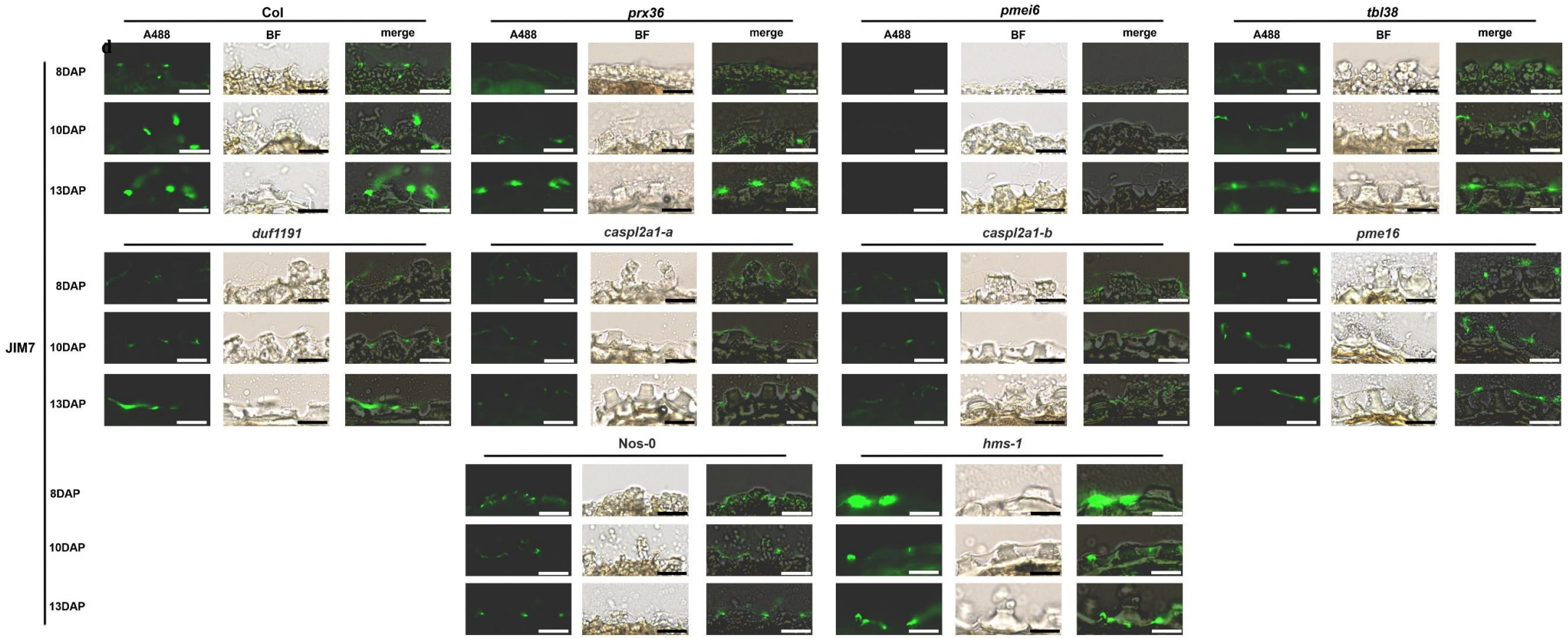

Figure 2.6 : JIM7 labeling shows no difference in epitope positionning in selected new mutants. Partially methylesterified HG are primarily deposited broadly in the periclinal primary CW before columella formation (8 DAP) and then at the top of the radial primary CW in the MSC microdomain of mature seeds (10-13DAP) in Col-0. Previously studied mutants used as controls show loss of JIM7 signal in *pmei6* and no difference as compared to Col-0 in *prx36*. In new selected mutants, JIM7 signal localization is similar across each genotype and developmental stages analyzed despite signals of apparent lower intensity in some genotypes (e.g. *caspl2a1*). Each genotype was studied under the Col-0 background except *hms-1* which was under the Nos-0 background which on average, produced smaller columella.
40 x scans of fluorescence channel, brightfield as well as the merge were taken on siliques labeled at 3 development stages and embeded in paraffin. The same parameters were used to analyze each image. Images are representative of n > 50 MSCs. Bars: 25µm

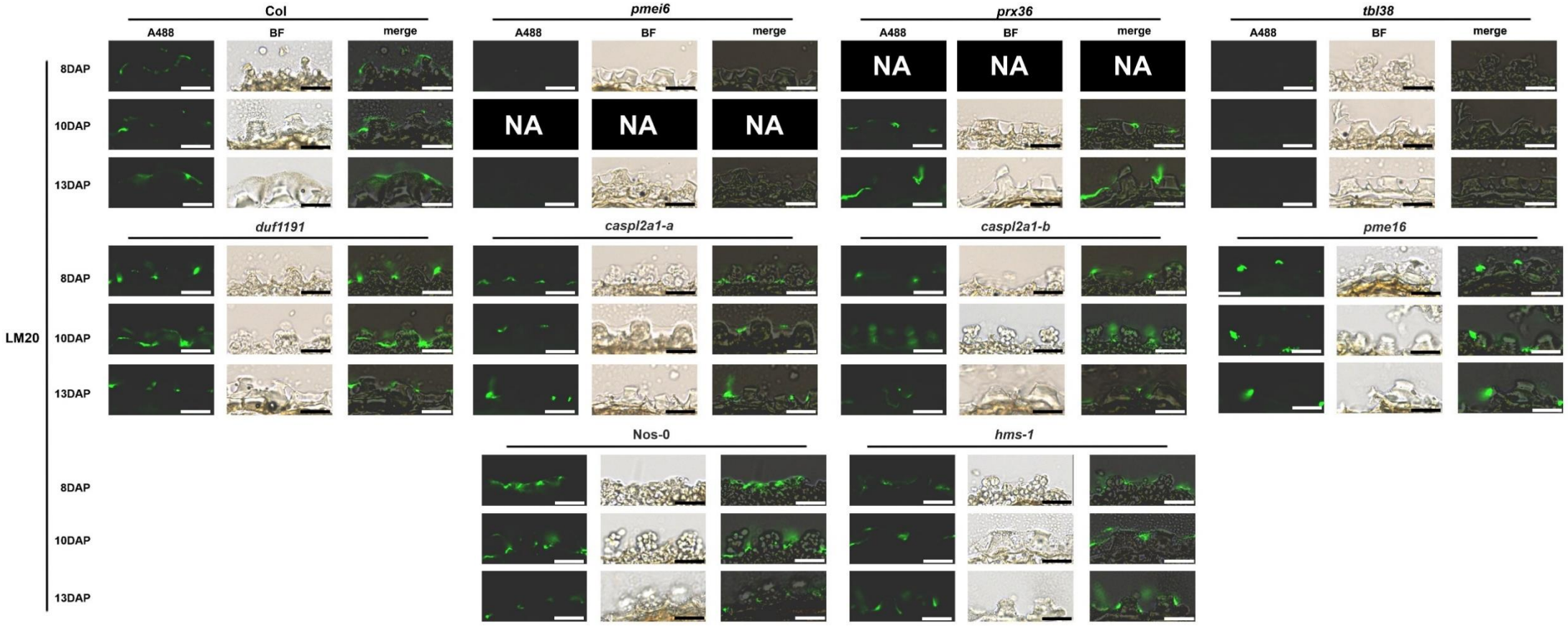

Figure 2.7 : LM20 labeling reveals TBL38 as a putative new actor of HG methylesterification. Partially methylesterified HG are broadly deposited at 8 DAP before columella formation but deposited at 10 and 13 DAP at the top of the radial primary CW in the MSC microdomain of more mature seeds. Previously studied mutants used as controls show loss of LM20 signal in *pmei6* and no difference as compared to Col-0 in *prx36*. In new selected mutants, LM20 signal is consistent to JIM7 signal across each genotype analyzed with the notable exception of *tbl38* which does not show any LM20 signal in mature seeds. NA, non available samples. Each genotype was studied under the Col-0 background except *hms-1* which was under the Nos-0 background. On average, both Nos-0 and *hms-1* produced smaller columella.
40 x scans of fluorescence channel, brightfield as well as the merge were taken on siliques labeled at 3 development stages and embeded in paraffin. The same parameters were used to analyze each image except for Nos-0 and hms-1 whose signals were amplified (A488 channel 200%) for better visual representation without altering signal quality. Images are representative of n > 50 MSCs. Bars: 25µm

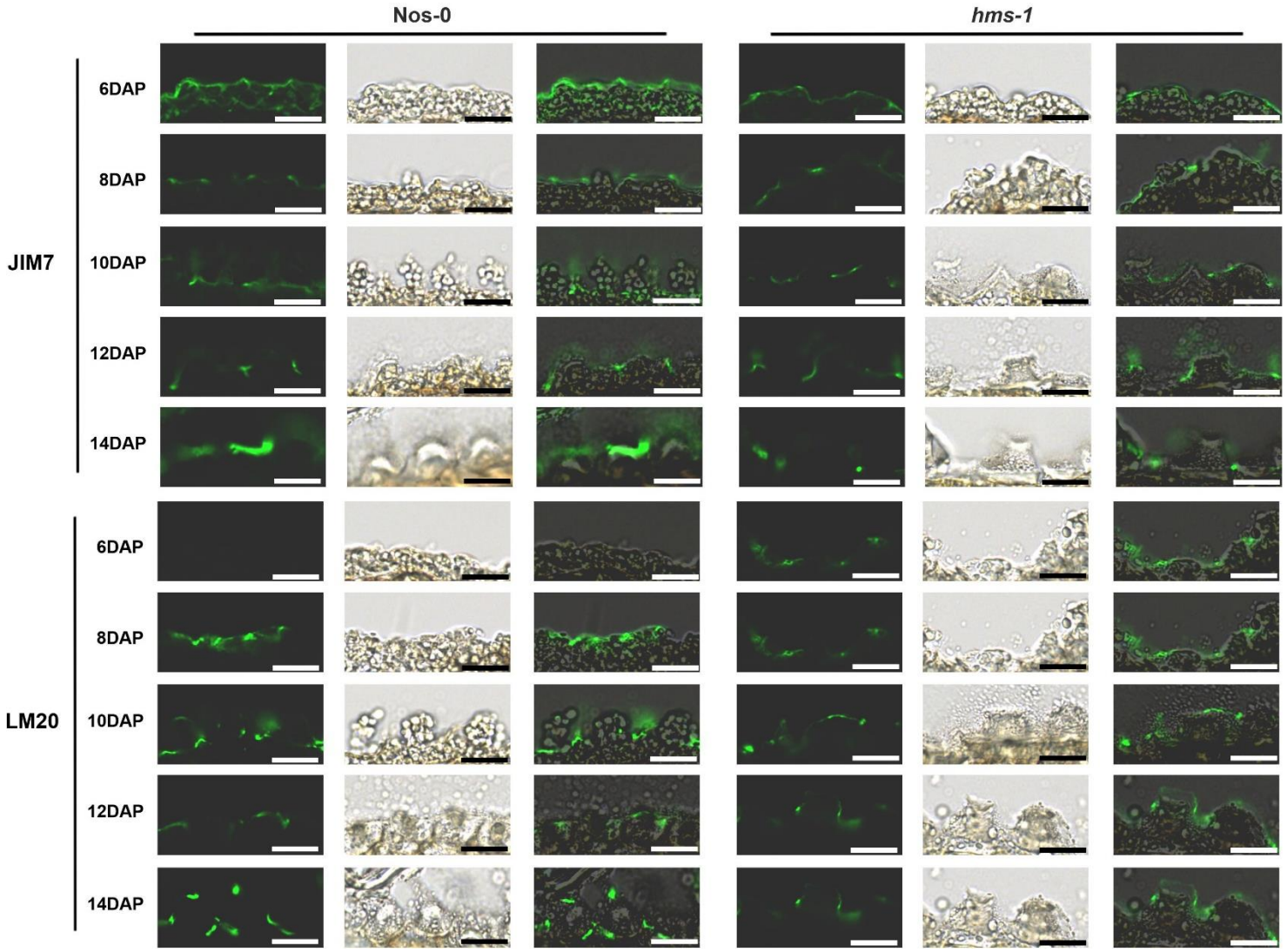

Sup. Fig. S2.2 : JIM7 and LM20 labeling show that HMS activity does not influence HG methylesterification patterns at the surface of the MSC primary CW. Partially methylesterified HG labeled by JIM7 and LM20 were equally found in Nos and *hms-1* genotypes. Signals were similar throughout seed development kinetics. Before columella formation at 6-8 DAP, signals were absent or broadly placed on periclinal primary CW. Most signal after 10 DAP was observed at the top of the radial primary CW. 40 x scans of fluorescence channel, brightfield as well as the merge were taken of siliques labeled at 5 development stages and embedded in paraffin tissue arrays. Images are representative of n > 50MSCs. Bars: 25µm

2.6. PRX36 localization is unaffected in candidate gene mutants

The rationale of JM7/LM20 screening was intended to identify possible relationships between the candidate genes and the formation of PRX36 anchoring platform since JIM7/LM20 labeling has been related to this platform in the CW microdomain (Francoz et al., 2019b). As the last step of our screen, we sought to investigate PRX36 localization itself in mutated backgrounds to evaluate a possible mislocalization in mutants from candidate genes as it occurred in *pmei6* (Francoz et al., 2019b). Immunofluorescence labeling with anti-PRX36 polyclonal antibody was consistently performed on all genotypes and proPRX36::PRX36-TagRFP localization was studied in *pmei6*, *tbl38* and *pme16* selected backgrounds under spinning disk confocal microscopy. Unfortunately, we could not get the corresponding transformant for *pme6/hms-1* yet. Anti-PRX36 signal was detected on most genotype excepted *prx36* and *pmei6* used as controls (Francoz et al., 2019b), Nos-0 and *hms-1* (**Figure 2.8A**). At later developmental stage, the signal was barely seen in most genotypes including Col-0 or lost in *casp2a1_a* (**Figure 2.8A**, data not shown) which could be associated with putative natural protein degradation rather than mislocalization. TagRFP fusion of selected protein yielded similar preliminary results, as no obvious difference was observed between Col-0 and other genotypes (**Figure 2.8B**). PRX36-TagRFP signals was the weakest in *pmei6* background and overall protein mislocalization to the mucilage was the highest in this condition fitting with previous results (Francoz et al., 2019b). For *tbl38*, two lines were compared. Taken together, these results indicated that PRX36 localization was not affected in a significant way in any of the new studied genotypes, including *tbl38* despite its LM20 phenotype. The loss of anti-PRX36 immunofluorescence in *hms-1* cannot be accounted for a mislocalization since the signal is absent also from the Nos-0 background control. The plants expressing PRX36-TagRFP in Nos-0 and *hms-1* are yet missing to clearly conclude on a possible role of PME6/HMS for PRX36 localization.

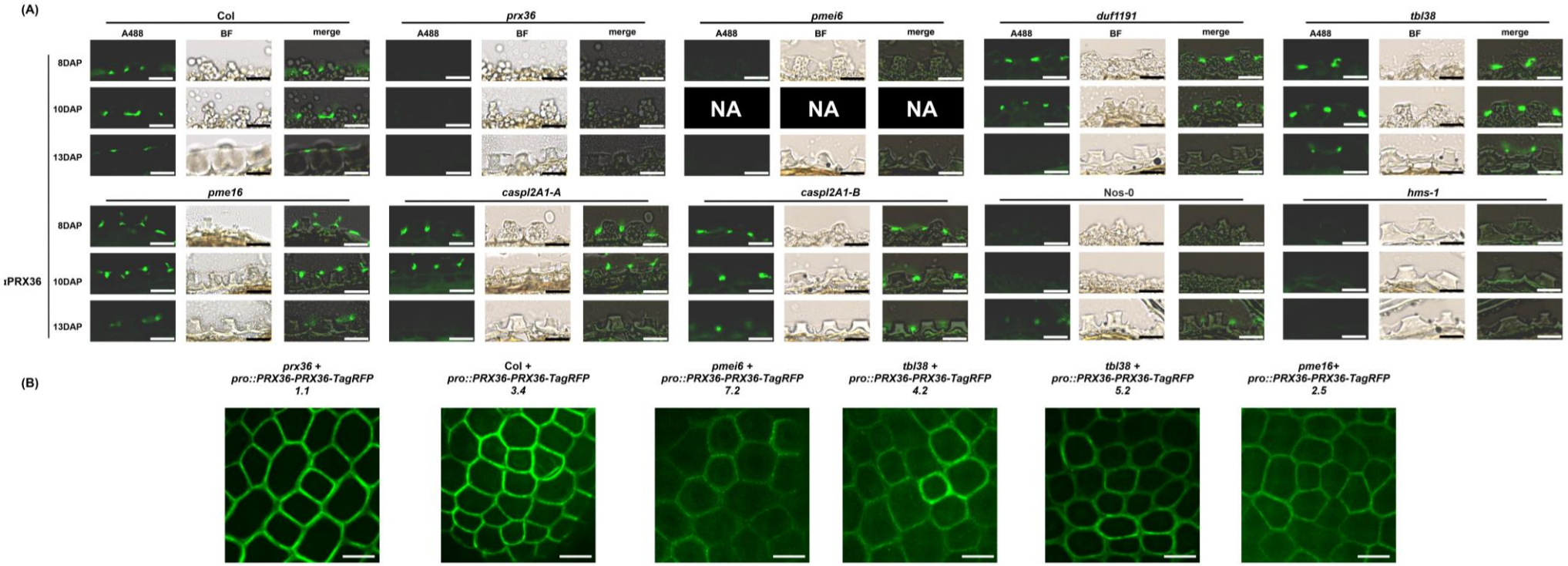

Figure 2.8: PRX36 localization is not affected in new studied mutant backgrounds. **(A)** αPRX36 signal was first observed after the onset of columella formation (6-8 DAP) at the top of the radial primary CW microdomain. As MSC development progressed (10-13 DAP), clear signals were found alternating between each columella. As seeds matured, αPRX36 labeling was weakened in most genotypes including Col-0 or lost *in casp2a1_a* at 13 DAP and later lost in all genotypes (data not shown). As expected, no signal was detected in both *pmei6* and *prx36* mutants. Interestingly, faint of no labeling could be observed both in Nos-0 and *hms-1*, suggesting either lack of protein accumulation or peptide recognition in the Nos-0 genetic background. NA, non available result. Each genotype was studied under the Col-0 background except *hms-1* which was under the Nos-0 background. **(B)** PRX36-TagRFP signal was observed on seeds at 8 DAP under spinning confocal microscopy. Compared to *prx36* background, the presence of endogenous PRX36 in other genotypes led to additional faint signals not localized in the CW microdomain indicating a competition between the non labeled endogenous and the labeled exogenous PRX36 as previously shown (Francoz et al., 2019b). TagRFP signal additional mislocalization to the mucilage was mostly observed in *pmei6* background.
40 x scans of fluorescence channel, brightfield as well as the merge were taken of siliques labeled at 3 development stages and embeded in paraffin. The same parameters were used to analyze each image. Images are representative of (n > 50MSCs). Bars: 25µm

2.7. Tag-RFP fusions of PMEI6, TBL38, PME6 and PME16 co-localized with PRX36 in this CW microdomain

MSC development leads to an increasingly smaller cytosol as this space is taken up by the mucilage and the columella, and mature MSCs are mainly composed of three distinct CW material, namely, the primary CW, the columella and the mucilage (**See Chapter 1 Introduction; Figure 1.12**). Because PRX36 is only found in the CW microdomain located at the top of the radial primary CW, precise localization of candidate proteins is therefore needed to further assess the relevancy or not of candidates in the PRX36 molecular scaffold. To this end, we generated Tag-RFP fusions of four selected proteins and observed developing seeds under spinning confocal microscopy (**Figure 2.9**). Indeed, considering the lack of phenotype for the mutants of the two membrane predicted proteins DUF1191 and CASPL2A1, we rather concentrated our effort on the CW-predicted PMEI6, PME6/HMS, PME16 and the membrane predicted TBL38 whose mutant displayed an intriguing LM20 phenotype. Note that these constructs were generated under the control of the *PRX36* promoter in the corresponding mutant backgrounds except PME6/HMS which was expressed in Nos-0 for technical reason (The hygromycin resistance of the transgene was the same as those of *hms* T-DNA). We detected Tag-RFP signal for PRX36 and PME6/HMS similar to what was previously published (Levesque-Tremblay et al., 2015). The signal that appeared in the primary CW surrounding the MSC on face views (**Figure 2.9A-B**) turned out to be located at the top of radial CW as revealed by orthogonal projections (**Figure 2.9C**). We also detected PMEI6-TagRFP strongly in the PRX36 CW microdomain but faint signals around the columella were observed in later developmental stages (Data not shown). It is unclear if this is the result of protein de-localization or increasing background level as what was observed in every line presented, abnormally including PRX36, while grown in imperfect conditions. Regardless, we did not observe signals at the surface of the columella as previously described (Saez-Aguayo et al., 2013; Ezquer et al., 2016). Subtle differences in the MSC CW microdomain signal appeared for PMEI6-TagRFP with alternating punctuated intensities and for PME6/HMS-TagRFP with higher intensity in the tri cellular junctions (**Figure 2.9A-B, Figure 2.10**). Indeed, fluorescence profile analysis along CW between two successive tri-cellular junctions showed signal frequencies distinct from other constructs (**Figure 2.10A-B**). Yet, we also showed that PME16-TagRFP was a CW proteins co-localizing with PRX36 in its CW microdomain, and we show another intriguing result for TBL38-TagRFP also colocalizing in this CW microdomain despite a previously reported common Golgi localization of other TBLs. This last result will be

developed and discussed in details in the following chapter concerning the exhaustive characterization of TBL38.

Altogether, despite the subtleties observed for PMEI6 and PME6/HMS, five proteins whose encoding genes are closely co-expressed, end up in the same subcellular compartment consisting in the PRX36-PMEI6 CW microdomain, when co-expressed under the control of *PRX36* promoter.

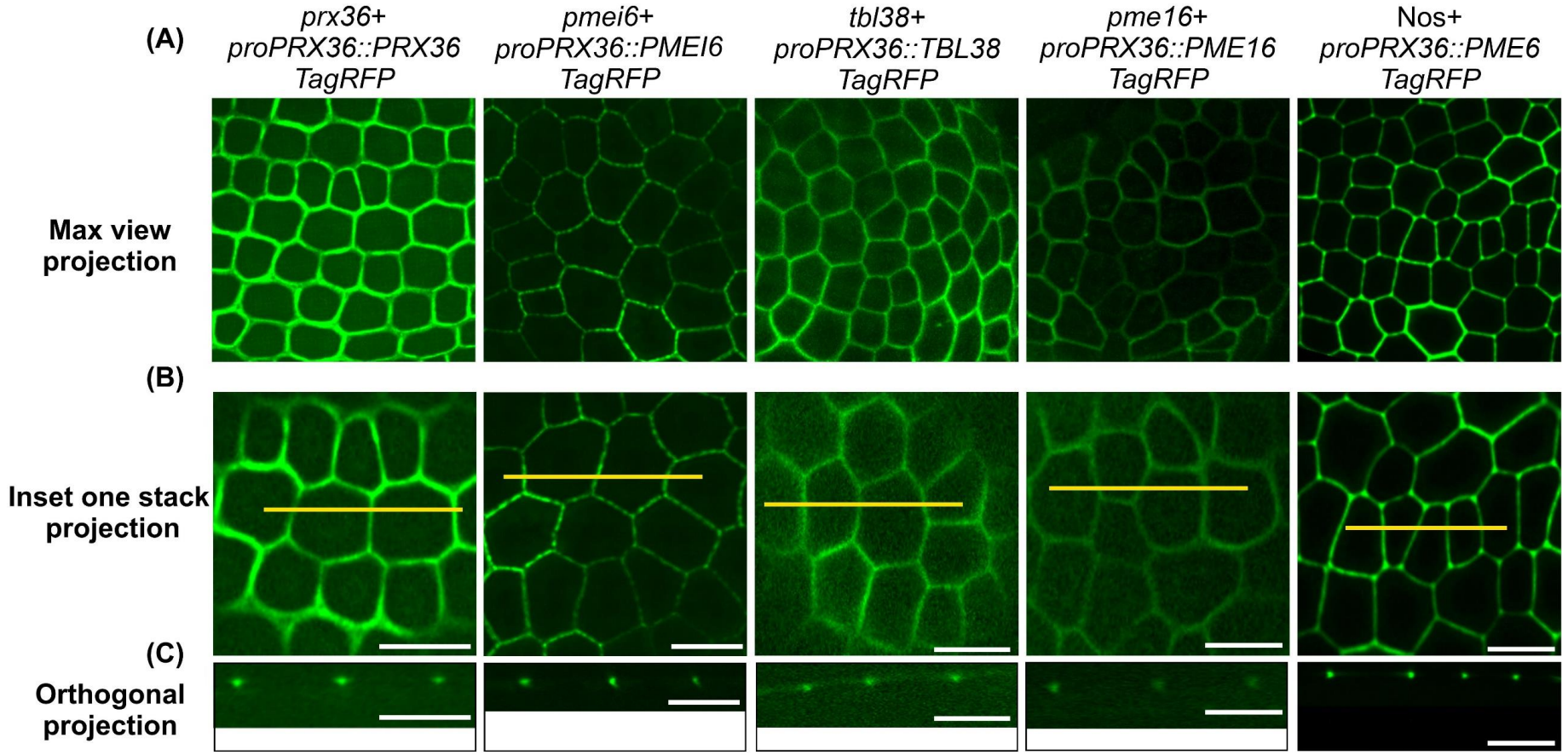

Figure 2.9: Tag-RFP fusions of PMEI6, TBL38, PME16 and PME6 co-localized with PRX36 in top of radial primary CW microdomain. Seeds were extracted from siliques aged between 8-10 DAP and the Tag-RFP signal was directly observed under confocal spinning microscopy. Faint signals encircling the columella could be observed in later developmental stages in the non-optimal plant growth conditions (not shown). **(A)** Maximum projection views of at least 30 z stacks. **(B)** Close up of a single confocal image in the highest intensity plan. **(C)** Orthogonal projection view along the yellow axis displayed in (B) illustrating the position of the CW microdomain in a MSC virtual cross-section. Bar: 200 µm

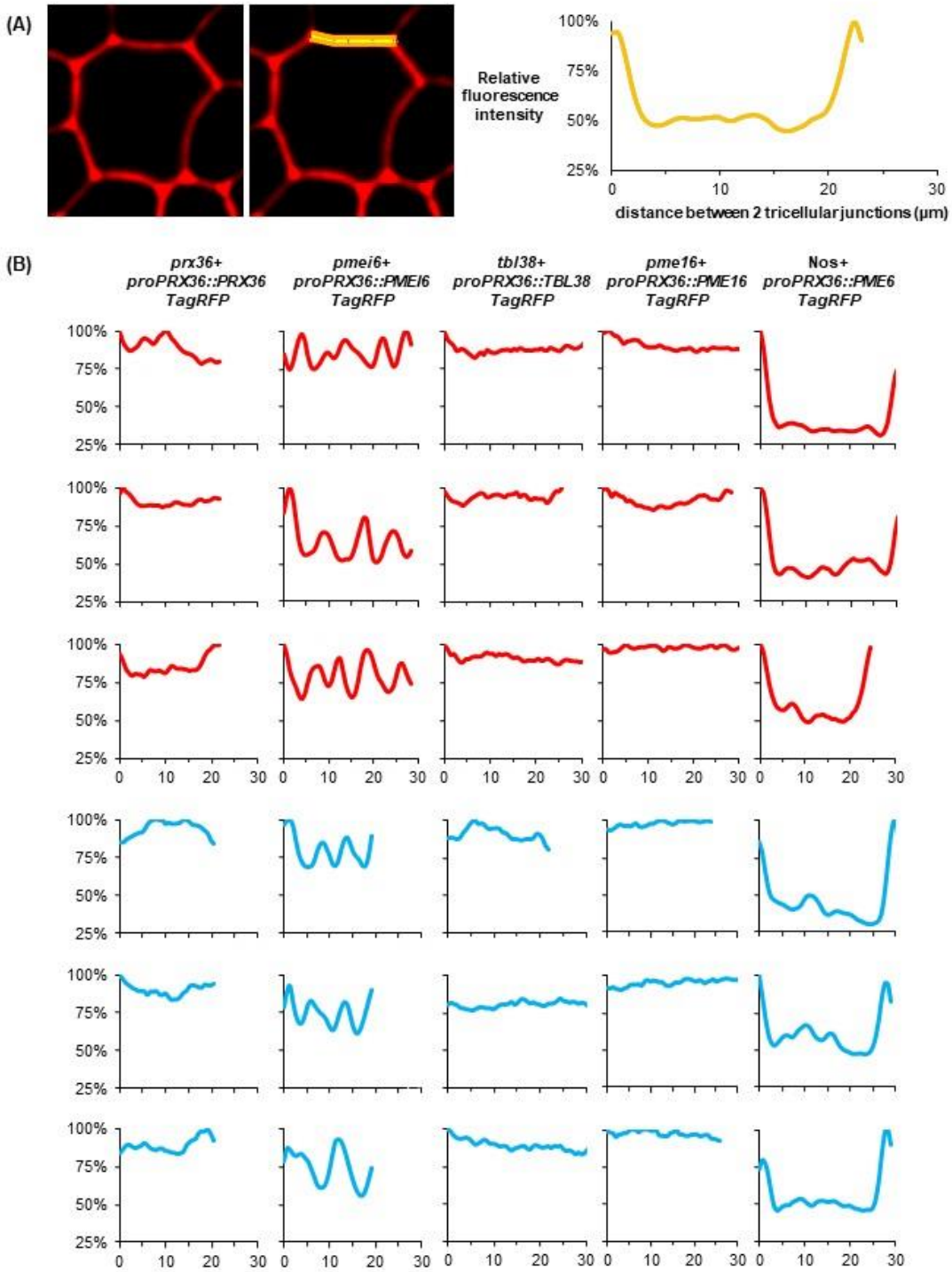

Figure 2.10 : Semi-quantitative analysis of fluorescence intensity profiles highlights PMEI6-TagRFP and PME6/HMS-TagRFP subtle distribution patterns within the MSC CW microdomain. (A) Left image shows an example of image to be analyzed (Z projection of 30 slices processed with the sum slice mode); the middle image shows an example of region of interest (ROI) defined along the primary CW between two successive tricellular junctions (orange segmented line) and the graph on the right shows the corresponding relative fluorescence intensity profile along the ROI. **(B)** For the five genetic backgrounds (labeled on the top), the individual profile taken from three ROIs on two separated 8-to-10 DAP seeds (red and blue lines, respectively) are shown. Note that the Y and X axis scales are the same for each plot [see detailed legend in (A)]. Note the nearly sinusoidal profile of PMEI6-TagRFP and the profile of PME6/HMS-TagRFP peaking at both extremities of the ROI, corresponding to punctuated and spots of higher intensity in tricellular junction, respectively. The three other constructs display more homogeneous profiles, corresponding to more homogeneous distribution of the fluorescence along the ROIs. See Figure 2.10 for fluorescence images of the five genetic backgrounds.

2.8. Discussion

2.9.1. The *PRX36*/*PMEI6* co-expression network is enriched in MSC-specific candidate genes.

Initial selection of candidate genes was done considering the similarity of their spatio-temporal expression to those of *PRX36* and *PMEI6*. Accordingly, the *PRX36* co-expression network built with tissue-specific transcriptomic data along seed development (Belmonte et al., 2013) was enriched in seed coat specific candidate genes (**Figure 2.1**). Despite this level of precision in spatial expression, additional information was needed. Indeed, Arabidopsis seed coat is subdivided in 5 layers of cells, respectively named (from inside to outside): ii1 (inner integument), ii1', ii2, oi1 (outer integument) and oi2, which is commonly addressed here as MSCs (Debeaujon et al., 2003; Francoz et al., 2015a). Each layer has its own particular cellular activity. Therefore, we could not exclude that the candidate genes were expressed in a different layer than the MSCs. Thus, we performed *in situ* hybridization on embedded developing seeds to directly pinpoint specific transcripts in the distinguishable layers of the seed coat. Hybridization of probes systematically resulted in a purple signal covering the MSCs (**Figure 2.2**). Separation between each layer can be difficult to identify, depending on the seed morphology and quality of sections. Indeed, as seeds mature, ii1 and oi2 are the easiest seen layers, the three other cell layers being compressed. Yet, with regards to the localization of the signal in the outer-most side of the seed coat, we can accurately differentiate the outer integument from the inner integument. Outside of *CASPL2A1*, whose expression could not be studied due to failure to generate anti-sense probes, all candidate genes were expressed in the MSC with the exception of the chalazal seed coat zone. The lack of signal in this tissue was also in good agreement with the transcriptomic data with the exception of *TBL38* for which we did not observed signals.

2.9.2. Different scale phenotyping provides complementary results though it did not identify clear actors of PRX36 molecular scaffold.

The candidate genes being expressed in the MSCs, the first screening step consisted in evaluating whether mutants for these genes displayed similar mucilage release defect phenotype to those of *prx36* and *pmei6*. Standardized protocol allowed studying mucilage release by measuring the adherent mucilage area in a high throughput manner. So far, mutation on *PRX36* or *PMEI6* was enough to prevent a correct mucilage release following water imbibition. Ruthenium red assay was then a quick and easy way of evaluating a gene contribution to the mucilage release. In this study, most KO mutants for candidate genes did not have a defect in

their mucilage release, with the exception of *hms-1* as previously reported (Levesque-Tremblay et al., 2015) (**Figure 2.3**). Lack of phenotype for *hms-2* is explained by the presence of transcript level comparable to the wild type found in RT-PCR (**Sup. Fig. S2.1**). The insertion was reported at -29 bp from the + 1 site (**See Methods; Figure 6.1**) and the normal expression was previously reported (Levesque-Tremblay et al., 2015).

The second round of screening concerned the spatial and semi-quantitative labeling of partially methylesterified HG epitopes recognized by JIM7 and LM20 monoclonal antibodies that were necessary for PRX36 anchoring (Francoz et al., 2019b). Regardless of a clear mucilage release defect, analysis of the HG-ME pattern with JIM7 and LM20 in dot blots revealed intriguing results (**Figure 2.5; Figure 2.6; Figure 2.7**). (i) Three knock out lines (*duf1191_a*, *casp2a1_a*, *casp2a1_b*) did not show any significant difference in JIM7 and LM20 signal intensity, which, combined with ruthenium red assays, further suggested that these two candidate genes are disconnected from a direct role in mucilage release related to PRX36/PMEI6 molecular scaffold. (ii) Contrary to *pmei6* for which the loss of JIM7/LM20 labeling was related to abnormal mucilage release, no direct relationship could be made for *hms-1* between the abnormal mucilage release phenotype and the unchanged JIM7/LM20 labeling similarly found in *pme16*. (iii) However, significant lack of LM20 signal in *tbl38* extracts indicates a peculiar change in pectin properties. While databases information indicates that these antibodies are highly similar (https://plantcellwalls.leeds.ac.uk/science/a ntibodies/rat-mabs/) in agreement with their similar labeling patterns in Col-0, *prx36* and *pmei6* MSC CW domain (Francoz et al., 2019b), slight differences in labeling patterns observed in other contexts may separates LM20 from JIM7 (Verhertbruggen et al., 2009). Indeed, while it is commonly accepted that both antibodies labels “highly / partially methylesterified HG” which is often described as a percentage of methylation, this does leave several parameters unchecked. Namely, spatial distribution of methylationand HG acetylation. Clausen et *al* highlighted that particular patterns of methylation may be equally important as overall methylation level for JIM7 labeling (Clausen et al., 2003). The characterized members of TBL multigenic family are involved in CW polysaccharide *O*-acetylation, the effects of *O*-2 / *O*-3-acetylation on galacturonic acid residues of HGs are still largely unknown but could prevent labeling via spatial structure HG changes (Pérez et al., 2000). The exact pattern of HG-ME required for LM20 binding is unknown, although *in vitro* dot blot assays suggested that it could bind on a peculiar ME pattern in HGs different from those recognized by JIM7. To our knowledge, our results are one of the first case of clear distinction between these antibodies in this CW domain. Thus, *TBL38*

mutation might affect the HG-ME subtly but sufficiently to completely alter the LM20 specific pattern in MSC CW domain. Further analysis to explore and completement these ideas will be developed in Chapter 3 of this work.

The third round of screening concerned the putative effect of mutation of candidate genes on PRX36 localization itself. Taken together, our results suggest that mutation in candidate genes did not disturb (or not disturb enough) HG methylation, leading to mostly unaffected PRX36 localization in its CW microdomain (**Figure 2.8**). As a consequence, mucilage release was for the most part unaffected in candidate mutant aside from *hms-1* (**Figure 2.8**). Although it is unlikely that PME6/HMS is involved in PRX36 localization due to the conservation of JIM7 and LM20 labeling in *pme6*, we could not get proper anti-PRX36 labeling in Nos-0 or *pme6/hms* background (**Figure 2.8**). It could be that, regardless of *PME6* expression, PRX36 positioning and dynamics are different in Nos-0 background, as Nos-0 MSC morphology was different than Col-0. Indeed, we observed smaller columella, possibly due to slower development than in Col-0. However, PRX36-TagRFP in Nos-0 background could be localized in the usual CW microdomain (**Figure 2.9**), suggesting that both PRX36 and the determinants for its positioning in Col-0 are also present in Nos-0. Because the anti-PRX36 antibody was originally designed based on PRX36 sequence in Col-0, we compared the protein sequences in Col-0 and Nos-0 to identify putative mutation in the immunogenic peptide sequence. In Nos-0, 6 SNPs were found in PRX36 sequence, yet these were not positioned in the immunogenic peptide (**Figure 2.11**). However, because spatial structure could affect Anti-PRX36 binding, we built a structural model on PRX36, both from Col-0 and Nos-0, based on PRX53 crystallographic data (Østergaard et al., 2000). Highlight of key residues showed that out of 6 modifications, 2 were adjacent to the immunogenic peptide which could prevent binding of anti-PRX36 (**Figure 2.11**). Although TagRFP fusion protein in *pme6/hms* would provide answer to the aforementioned hypothesis, no successful transformant were obtained as of yet.

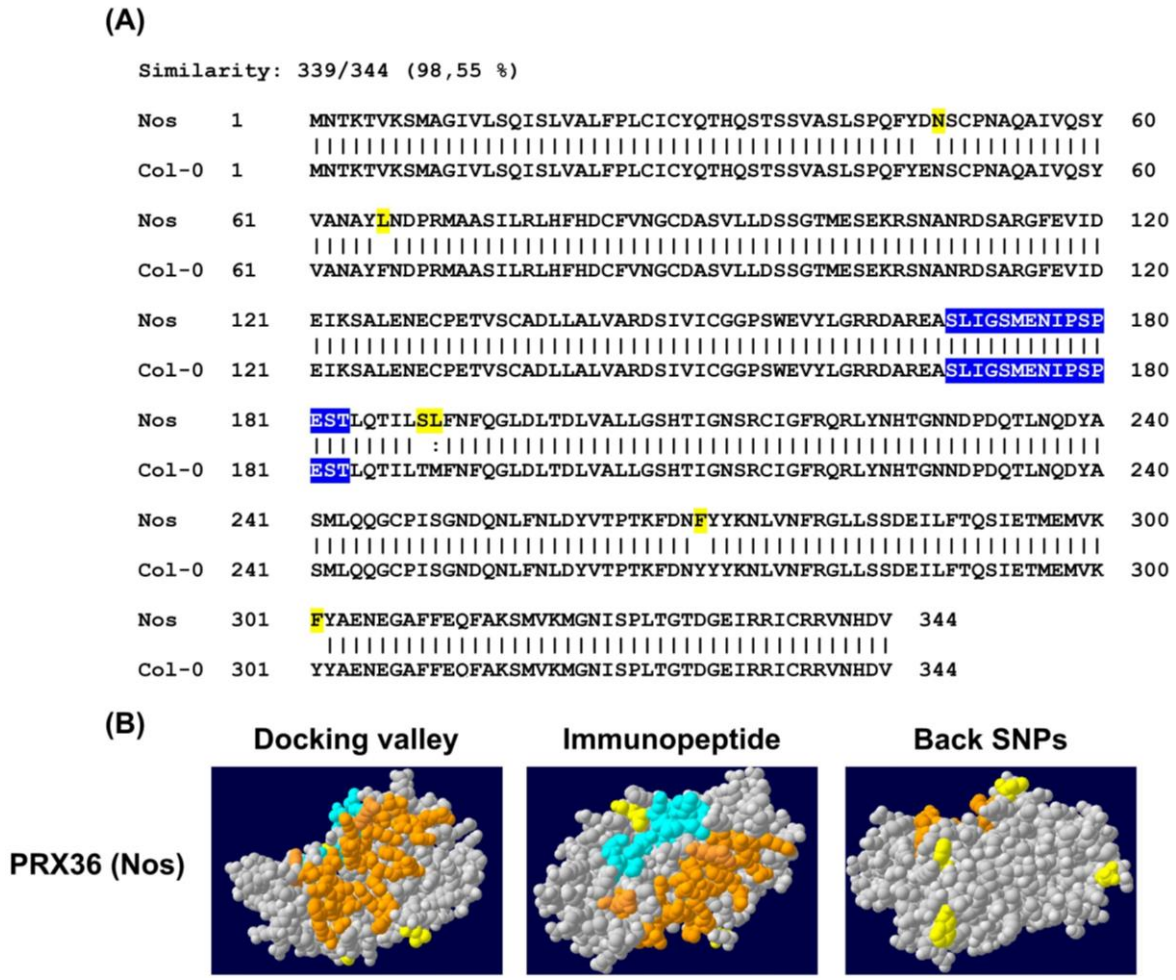

Figure 2.11: PRX36 SNPs in Nos-0 background may explain lack of binding of Anti-PRX36. (A). Alignment of PRX36 protein sequence from Nos-0 and Col-0 background. In total, 7 SNPs were detected including 6 responsible for missense mutations which were highlighted in yellow. The immunogenic peptide from which the Anti-PRX36 was designed is highlighted in blue and is identical in both genotypes. **(B)** Homology model for PRX36 (Nos-0) built with the Phyre2 server (Kelley et al., 2015). PRX36 docking valley (Francoz et al 2019b) was represented in orange and is not modified in Nos-0. Out of the 6 SNPs colored in yellow, two are adjacent to the immunogenic peptide showed in blue. Modifications of the spatial environment near the recognition site (Threonine-Methionine into Serine-Leucine) could prevent binding of Anti-PRX36. The other 4 SNPs are located in the back of the protein and should impact minimally -if any- both sites. The PRX36 (Nos-0) structural model used in this study was the Phyre2 prediction with the highest-ranking score (Confidence: 100.0%; Coverage: 88%). The template was the crystallographic structure (X-Ray diffraction, 1.45 A°) of *A. thaliana PRX53* (At5g06720; Protein Data Bank no. 1PA2) (Ostergaard et al., 2000).

2.9.3. The *PRX36*/*PMEI6* co-expression network is enriched in proteins colocalizing with PRX36 to the MSC CW microdomain

Finally, for selected co-expressed candidate genes, we evaluated the subcellular localization of TagRFP fusion proteins (PME6/HMS, PME16, PMEI6, TBL38) and compared it to those of PRX36 in MSC. The rationale of commonly using the *PRX36* promoter was related to (i) convenience, (ii) its demonstrated efficiency (Francoz et al., 2019b; Mcgee et al., 2019) and (iii) to the fact that it should spatiotemporally mimick the promoter of the coexpressed selected candidate genes. Interestingly, the four selected fusion proteins displayed a similar CW microdomain localization as PRX36-TagRFP (**Figure 2.9**). The colocalization of PMEI6-TagRFP with PRX36-TagRFP is in agreement with the relationship between these two proteins (Francoz et al., 2019b). Yet, we observed differences in PMEI6 positionning compared to previous studies. So far, PMEI6 has been localized either using a 35S::PMEI6-GFP (Saez-aguayo et al., 2013) or endogenous proPMEI6::PMEI6-GFP (Ezquer et al., 2016). In both instances, the GFP signal was observed in the primary wall and at the top of the columella. Although we did see PMEI6-TagRFP signals appearing around the columella in later developmental stage (12-14DAP), we associated it to natural protein misslocalization as what was observed in PRX36-TagRFP case (Francoz et al., 2019b). Still, we never observed signal on top of the columella as Ezquer and colleague did. Such difference could be due to intrinsic properties of the GFP and TagRFP. Indeed, the TagRFP pKa is lower (<3.8) than GFP, which makes it a more suitable fluorescent protein for studying the more acidic environment of the CW (Stoddard and Rolland, 2019). Notably, previous work using a proPRX36::PRX36-GFP showed the GFP signal fading in seeds as early as 10 DAP (**Sup. Fig. S2.3**). Thus, we propose that difference in protein localization may be due to stability of the fluorescent protein. The subtle differences that appear (punctuated signal for PMEI6 and continuous signal for PRX36 may explain why PRX36 was not fully delocalized in *pmei6* (Francoz et al., 2019b), or in other words, may indicate that PMEI6 is necessary but not sufficient for PRX36 anchoring. Additionally, PME6/HMS-TagRFP also showed particular positionning as signal were particularly intense in cell corners (**Figure 2.10B**). Although subtle differences in protein positionning were never discussed in their study, this result was also observed in HMS characterization (Levesque-trembley et al., 2015). However, this result does not explain the absence of relationship of PME6/HMS, PME16 or TBL38 with PRX36

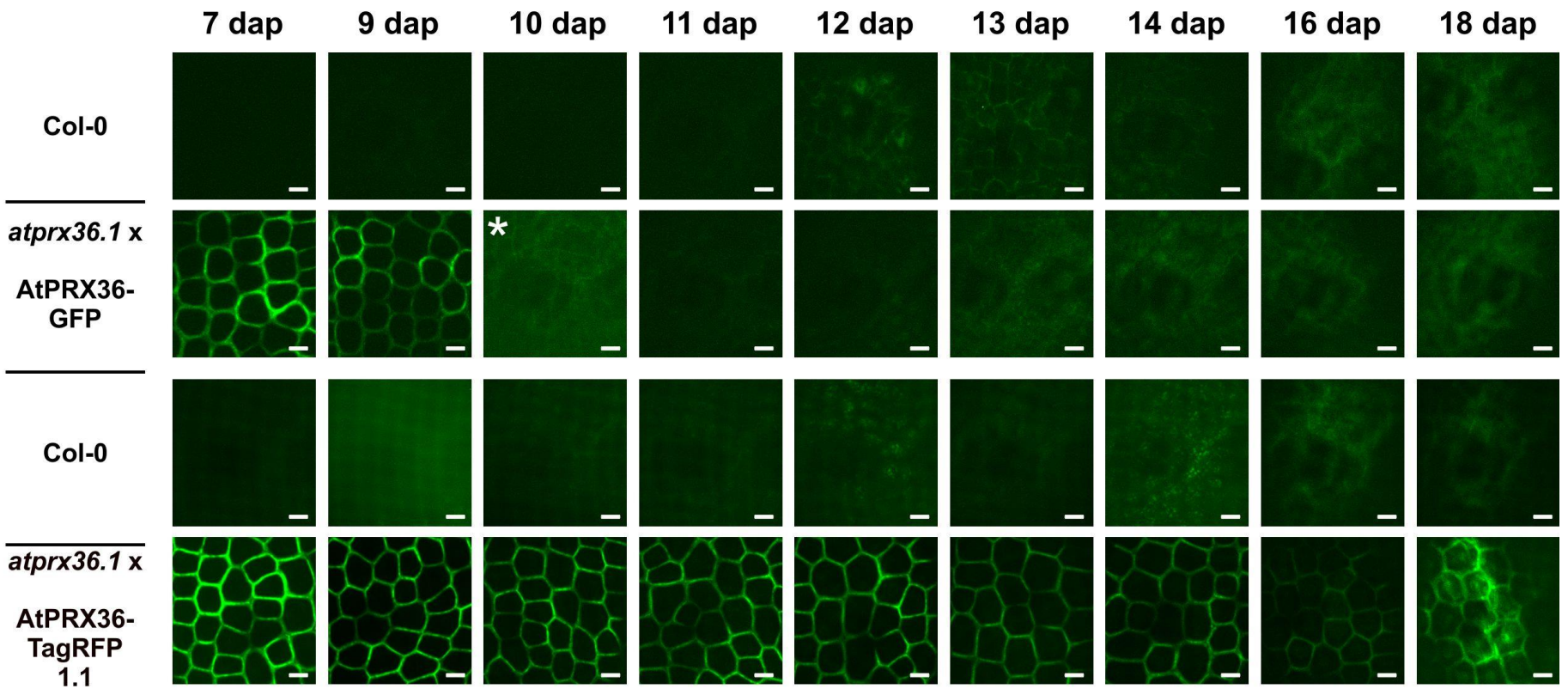

Sup. Fig. S2.3: TagRFP fluorescent signal show higher stability than GFP in developing MSC. Confocal spinning disk observations were made of developing seeds expressing either PRX36-GFP or PRX36-TagRFP under the proPRX36 promoter. For each construct, similar images of Col-0 were taken using the respective GFP and RFP settings to appreciate overall background level. PRX36-GFP signal correctly accumulated at the top of the radial primary CW but was lost in early developmental stage (9 DAP). Comparatively, PRX36-TagRFP could still be observed around 14-to-16 DAP at which point the signal faded in profit of background noise. Such contrasted observations are most likely due to differences in the GFP and TagRFP pka (5.9 and 3.8, respectively). Bars: 20 µm.

anchoring, suggesting additional distinct or redundant roles for these proteins in the CW microdomain. Because the co-expression network was built using *PRX36* as a bait whose expression was tied to the MSCs (Kunieda et al., 2013; Francoz et al., 2015a), the possibility that most genes spatially and temporarily co-expressed with *PRX36* systematically led to proteins co-accumulating in the MSC CW microdomain was plausible. This could be reinforced by the common use of *PRX36* promoter. In such an hypothesis, polarized protein secretion could be simply due to the natural polarization of the cell machinery in a spatiotemporal frame corresponding to *PRX36* promoter activity. Indeed, although it is difficult to study MSC organelle and cytoskeleton dynamics due to the rapid expansion of the CW, early apical accumulation of starch granule is observed during seed development (Francoz et al., 2015a) suggesting polarization of MSC. Logically, this would mean that using the *PRX36* promoter, any CW protein CDS would be sent to this CW microdomain. However, counter-examples of different localization of expressed CW protein driven by the PRX36 promoter can be found in the literature. Reportedly, both proPRX36::PRX50-TagRFP or proPRX36::MUM2-Citrine were mostly found in the mucilage (Francoz et al., 2019b; McGee et al., 2019). Alternatively, protein positioning could be achieved through determinants present in the protein sequences, either common or specific to each protein. Notably, targeted mutagenesis on PRX36 showed that without the key residue responsible for its anchoring, the protein was mislocalized and in turn, possibly degraded (Francoz et al., 2019b). Although this only explains PRX36 localization, similar or parallel determinant could explain the colocalization of PMEI6, PME6/HMS, PME16 and TBL38 in this CW microdomain. Conversely, protein positioning could be achieved through determinants present in the CW microdomain itself, either common or specific to each protein, as demonstrated with the HG methylesterification pattern controlled by PMEI6 that is necessary for PRX36 anchoring. The study of how precise CW protein localization is achieved has led to contrasted example explaining this (Dauphin et al., 2022). CASP transmembrane protein anchoring peroxidases (Lee et al., 2013), localized PMEI endocytosis (Dardelle et al., 2010) or built-in HG anchoring platform (Francoz et al., 2019b), all of which could be one of the possible explanations for such systematic co-localization.

It could be interesting, although time consuming, to systematically evaluate the localization of the candidate fusion proteins in the various candidate gene mutants to identify possible determinants as it has been performed for PRX36 in *pmei6* (Francoz et al., 2019b).

2.9.4. Integrated analysis of results and literature for each candidate gene/mutant and perspectives

DUF1191 and CASPL2A1

Despite its near-perfect co-expression with *PRX36*, mutation in *DUF1191* showed no difference with Col-0 in our assays. At4g01140 is the sole *DUF1191*-gene expressed in MSC (**Table 2.1A**), thus functional redundancy cannot explain lack of phenotype. In the literature, information on DUF1191 containing domain proteins is sparse. Interestingly, when Lv and colleagues overexpressed such protein in *E. coli*, resistance to heat stress improved, possibly due to enhancement in catalase, superoxide dismutase and peroxidase activities which should lead to overall decrease in free radial species (Lv et al., 2019). If such hypothesis held true in Arabidopsis, DUF1191 could act as a negative regulator of ROS in MSC by promoting expression of various genes including peroxidases. Thus, insight on ROS accumulation in *duf1191* seeds could provide clues as to its role in MSC, particularly when a large number of peroxidases are expressed in this cell-type.

Similarly, *caspl2a1* seeds did not show any significant role in this scaffold. Unfortunately, we still lack the *in situ* hybridization to know whether or not *CASPL2A1* is expressed in MSCs. Initially, we selected this gene to test the possibility of a CASP-PRX36 model in MSC, similar to the root endodermis (Lee et al., 2013). Conceptually, CASPL2A1 would create a zone of junction between the plasma membrane and the CW early on during MSC development. This would lead to accumulation of PRX36 and PMEI6 in the primary CW specifically in this region. As MSC development advances, the PW would separate from the PM leaving the PRX36 anchored to the HG demethylesterified pattern. Yet, no experimental evidence supporting this was found. Despite some work associating CASP-like in developmental processes (Roppolo et al., 2014; Yang et al., 2015), the root endodermis remains the unique tissue in which CASP were responsible for CW proteins anchoring in a particular domain so far. Still, *casp1* single mutation was not enough to disturb Casparian strip formation due to functional redundancy with *CASP3* (Roppolo et al., 2011). Thus, it may be that lack of PRX36 mislocalization in *caspl2a1* is due to expression of other CASP / CASP-L in MSC such as *CASPL2D1* (*At4g25830*) or *CASPL2B1* (*At2g35760*) which share similar expression profile specific to MSC (**Table 2.1B**). Clear protein localization would help evaluate the likelihood of a similar transmembrane CASP-L domain, although MSC natural dynamics may make study transmembrane protein difficult even at younger developmental stages.

Table 2.1: Selection of *DUF1191* and *CASPL1F1* from the *PRX36-PMEI6* co-expression network. **(A)** Very few information is available on DUF1191-domain containing genes, In MSC, only At4g021140 was found to be expressed, Relative expression values are colored from yellow to red. **(B)** No *CASPL* was ranked high in *PRX36* network. We initially selected *CASPL2A1* (green) based on its seed coat expression prior occurring prior to *PRX36* expression considering that it could position a domain responsible for PRX36 anchoring prior to *PRX36* expression. *CASPL2D1* and *CASPL2B1* (purple) could also be interesting candidates displaying seed coat expression earlier than *PRX36* expression. Overall relative expression values are colored from yellow to red. Expression below 50 were represented in grey and genes that never reach the cutoff were masked (*CASPL4C1*; *CASPL4A1*; *CASPL1E2*; *CASPL1B2*; *CASP2*; *CASPL1D1*; *CASPL5A2*; *CASPL3A2*; *CASP3*) and no information was available for: *CASPL1A1*; *CASPL5C3*; *CASPL5A1*; *CASPL4D2*; *CASPL3A1*; *CASPL5B2*; *CASPL1C1*; *CASPL5B1*; *CASPL4A2*. Annotations were done using the toolbox from Roppolo et al 2014. RK, rank ; PCC, Pearson Correlation Coefficient ; EP, embryo proper ; SUS, suspensor ; MCE, micropylar endosperm ; PEN, peripheral endosperm ; CZEN, chalazal endosperm ; CZSC, chalazal seed coat ; SC, seed coat ; WS, whole seed.

RK	PCC	ORF/AGI	Gene Symbol	pg EP	pg MCE	pg PEN	pg CZEN	pg CZSC	pg SC	pg WS	g EP	g SUS	g MCEN	g PEN	g CZEN	g CZSC	g SC	g WS	h EP	h MCEN	h PEN	h CZEN	h CZSC	h SC	h WS	lc EP	lc MCEN	lc PEN	lc CZEN	lc CZSC	lc SC	lc WS	bc EP	bc PEN	bc CZEN	bc CZSC	bc SC	bc WS	mg EP	mg MCEN	mg PEN	mg CZEN	mg CZSC	mg SC	mg WS
1	1	AT3G50990	*PRX36*	15	27	4	11	8	8	2	4	2	13	2	12	8	2	4	3	3	3	15	14	3	9	4	5	9	12	405	1522	554	1	2	27	992	29	20	7	1	11	3	53	65	9
3	9,15E-01	AT4G01140	*DUF1191*	2	11	14	11	7	12	3	0	9	11	10	7	6	5	7	5	5	22	11	13	60	83	6	3	1	14	181	656	101	3	5	9	196	160	19	19	1	6	5	34	27	9
11836	-4,81E-02	AT4G23720	*DUF1191*	55	50	7	5	5	2	22	12	107	2	2	10	6	4	11	9	19	5	3	24	16	13	11	89	4	17	10	17	12	6	2	11	4	3	13	3	2	3	13	13	4	9
20261	-1,72E-01	AT3G08600	*DUF1191*	42	15	143	38	17	52	30	23	21	15	52	8	11	20	40	18	11	18	17	12	25	28	15	14	42	15	8	11	18	28	14	12	10	21	28	22	13	20	9	6	5	42
21706	-2,15E-01	AT4G11950	*DUF1191*	11	34	26	32	16	7	23	15	18	45	10	25	27	15	16	5	15	9	27	19	10	7	24	7	20	12	23	6	8	19	13	19	14	14	18	39	18	20	4	9	36	20

(B)

RK	PCC	ORF/AGI	Gene Symbol	pre-globular stage							globular stage								heart stage							linear-cotyledon stage							bending cotyledon stage							mature green stage						
				pg EP	pg MCE	pg PEN	pg CZEN	pg CZSC	pg SC	pg WS	g EP	g SUS	g MCEN	g PEN	g CZEN	g CZSC	g SC	g WS	h EP	h MCEN	h PEN	h CZEN	h CZSC	h SC	h WS	lc EP	lc MCEN	lc PEN	lc CZEN	lc CZSC	lc SC	lc WS	bc EP	bc PEN	bc CZEN	bc CZSC	bc SC	bc WS	mg EP	mg MCEN	mg PEN	mg CZEN	mg CZSC	mg SC	mg WS
1	1	AT3G50990	*PRX36*	15	27	4	11	8	8	2	4	2	13	2	12	8	2	4	3	3	3	15	14	3	9	4	5	9	12	405	1522	554	1	2	27	992	29	20	7	1	11	3	53	65	9
1619	2,71E-01	AT1G17200	*CASPL2A1*	17	3	40	30	124	838	650	111	223	12	19	11	15	686	997	235	42	24	9	139	1578	817	187	30	7	10	235	944	407	194	21	5	237	329	140	214	26	13	8	36	176	207
3113	1,80E-01	AT5G54980	*CASPL4A1*	1	2	3	9	36	29	21	3	6	3	10	2	6	29	5	6	13	13	17	34	33	24	30	19	34	79	53	53	12	34	21	18	13	23	27	75	21	26	21	36	42	56
3435	1,67E-01	AT5G40300	*CASPL2B2*	199	2	46	26	677	133	133	102	254	7	33	10	491	87	149	132	186	132	20	719	203	245	88	140	116	35	518	117	128	64	53	86	499	161	112	63	185	115	161	506	208	107
5138	1,02E-01	AT2G36330	*CASP5*	48	57	71	94	501	106	119	70	137	129	38	34	250	86	214	65	115	121	133	654	216	137	75	128	142	144	459	78	150	77	177	356	407	71	92	125	201	136	488	546	70	132
7103	4,65E-02	AT4G25830	*CASPL2D1*	17	6	38	26	106	1664	1101	5	2	59	38	21	65	2095	2518	3	10	43	32	275	4858	2762	6	4	5	8	349	943	465	5	2	18	302	24	28	24	11	9	47	52	14	3
8749	7,68E-03	AT3G55390	*CASPL1D2*	34	17	105	43	500	265	386	79	17	46	104	10	227	229	264	164	145	204	17	482	452	287	178	103	231	119	245	142	93	45	42	221	190	84	80	23	22	31	218	194	139	53
10294	-2,31E-02	AT4G20390	*CASP1*	4	12	11	38	1	13	6	11	12	18	5	39	12	10	1	12	7	7	16	13	5	11	3	13	10	10	15	7	19	4	11	14	10	22	14	10	18	26	24	110	692	18
10408	-2,48E-02	AT5G44550	*CASPL1E1*	3	44	9	5	6	4	17	14	8	8	7	11	6	12	11	1	4	4	31	20	11	9	1	11	8	1	11	5	6	5	5	12	20	28	8	16	25	24	12	39	312	17
12200	-5,36E-02	AT2G35760	*CASPL2B1*	25	11	38	57	491	1218	1083	13	9	26	6	31	242	587	877	7	15	9	21	702	1463	1182	11	39	21	9	509	139	100	14	26	19	156	18	41	114	232	209	73	85	113	102
12619	-5,98E-02	AT3G50810	*CASPL5B3*	29	173	38	39	141	34	48	22	71	237	34	35	86	41	29	23	41	25	65	111	60	38	31	47	11	87	71	38	27	14	47	41	48	32	35	30	35	42	33	35	31	36
13081	-6,56E-02	AT2G38480	*CASPL4D1*	28	4	16	465	32	13	33	25	13	32	27	681	47	31	44	10	22	7	881	81	33	62	37	23	61	53	40	59	44	17	59	34	29	67	63	46	64	64	47	49	229	100
13900	-7,53E-02	AT2G27370	*CASPL4B1*	6	2	2	5	2	2	12	10	12	3	5	12	10	1	5	4	5	1	12	11	4	0	4	33	7	7	11	1	13	3	2	8	7	15	11	12	291	43	50	13	29	28
14246	-7,91E-02	AT4G15630	*CASPL5C2*	7	3	10	10	8	4	10	3	1	8	1	15	2	4	2	29	25	5	15	11	6	12	160	15	21	13	7	7	87	413	10	12	6	9	243	1145	10	47	7	11	65	610
14940	-8,72E-02	AT4G25040	*CASPL4A3*	19	2	189	313	5	1	31	4	5	6	31	323	22	17	28	0	25	12	149	36	8	10	1	2	2	1	8	15	11	1	4	1	5	6	2	15	3	10	1	2	90	6
18583	-1,40E-01	AT4G16442	*CASPL1C2*	72	8	6	13	68	198	111	67	54	16	7	27	27	50	117	160	39	8	15	75	77	100	69	123	34	7	34	43	105	157	92	22	27	14	131	267	293	255	101	57	29	299
19131	-1,50E-01	AT2G28370	*CASP4*	59	37	30	33	30	27	19	55	37	87	38	27	2	13	26	78	108	62	16	7	13	72	46	73	62	58	21	38	72	67	68	56	17	36	80	82	93	80	111	5	52	84
20813	-1,85E-01	AT3G11550	*CASPL2A2*	12	11	19	18	10	32	34	2	16	14	12	20	7	85	52	2	11	1	14	10	16	16	8	28	12	16	2	4	14	9	10	2	1	5	11	3	15	6	2	5	10	4

PME6/HMS, PME16, PMEI6

To our knowledge, experimental proof of a PMEI-PME *in vivo* interacting duo was only given once in the context of Arabidopsis apical pollen tube growth (Dardelle et al., 2010; Mollet et al., 2013). Given the relatively low number of expressed PME in MSCs (7), we decided to study PME6/HMS and PME16 as putative partner to PMEI6 as their expression was the highest in MSC. Previous work has described PME6 as playing a role in embryo development (Levesque-Tremblay et al., 2015), thus expression outside of MSC is possible. This is also corroborated by PME6 specific positioning in MSC and embryo (**Figure 2.9**, Levesque-Tremblay et al., 2015). PME16 spatial accumulation was similar in MSC, although its functions remain unknown

With regards to our experimental results, we propose several ideas for lack of evidence towards the involvement of candidate PMEs in PRX36/PMEI6 scaffold:

(1) Obviously, it may be that putative PMEI6 interactant is encoded by another *PME* expressed in MSCs (**Table 2.2**). Although we focused on *PME16* and *PME6/HMS*, other *PMEs* were present in the co-expression network. Notably *At5g53370* (*PME61*, rank 100 but relatively low expression level) for which no mutated line was available. It may also be that the expression data used showed incorrectly below-significance expression level for MSC-expressed *PMEs* which would have resulted in their exclusion from the network. Indeed, *PME7* (At1g44980, rank 6553) and *PME45* (At4g33230, rank 6534) were experimentally found expressed in the seed coat (Levesque-Tremblay et al., 2015) but not in the expression data (Belmonte et al., 2013, **Table 2.2**). Based on Belmonte data, we know that *PME19*, *PME42*, *PME44* and *PME58* are also highly expressed in the seed coat with a similar time-frame as *PRX36* (**Table 2.2***)*. Although PME58 localization is missing, it was found to be involved in mucilage modification leading to a mucilage release phenotype but not in its ability to release it (Turbant et al., 2016). No information is known for *PME19*, *PME42*, *PME44*, *PME52* and *PME63*

(2) Because *pmei6* lacks JIM7 and LM20 signals, we assume mutation on the gene encoding the interacting PME would result in similar changes in the ME status. However, conceptionally, we cannot exclude that *pme6/hms* or *pme16* mutation could lead to changes to overall *PME* and/or *PMEI* expression, which could alter HG ME status unexpectedly or could lead to compensation phenomenon.

(3) Functional redundancy between multiple PMEs can also be considered. Although maximum expression of *PME16* should be lower than *PME6/HMS* (**Figure 2.1, Figure 2.2**), their

expression level at the linear-cotyledon stage are similar. Moreover, we observed that PMEI6, PME16 and PME6/HMS are spatially co-localized to the CW microdomain giving some credit to putative functional redundancy between PME16 and PME6/HMS. Although PMEI-PME are sometimes thought to work as a specific duo, clear evidence supporting this hypothesis is still lacking, particularly when PMEIs were shown to inhibit multiple PMEs *in vitro* depending on pH conditions (Lionetti et al., 2007).

(4) Subtle differences in colocalization may explain the absence of relationship between these proteins. PME6-TagRFP localization in the CW microdomain appeared more intense in the tri-cellular junction than in the intermediate primary CW (**Figure 2.9**). For technical reasons, this construct was expressed in Nos-0 rather than in *pme6/hms*, so we cannot exclude that the exogenous labeled protein is in competition with the endogenous non-labeled protein, somehow impairing the localization pattern.

Table 2.2: *PME* selection from the *PRX36-PMEI6* co-expression network. Out of the 36 seed expressed *PMEs*, only a few show expression patterns similar to *PRX36* in the seed coat. Based on this, *PME16* and *PME6/HMS* (green) were selected for their high expression profile at the linear-cotyledon stage. Other interesting candidates which could have been selected for their seed coat expression are in purple. Relative expression values are colored from yellow to red. Expression below 50 were represented in grey and genes that never reach the cutoff were masked (*PME5*, *PME15*, *PME47*, *PME11*, *PME43*, *PME25*, *PME50*, *PME67*, *PME30*, *PME28*, *PME45*, *PME26*, *PME38*, *PME66*, *PME24*, *PME56*) and no information was available for: *PME52*; *PME63*. PME annotation was done using the toolbox from Scheller et al 2015. RK, rank ; PCC, Pearson Correlation Coefficient ; EP, embryo proper ; SUS, suspensor ; MCE, micropylar endosperm ; PEN, peripheral endosperm ; CZEN, chalazal endosperm ; CZSC, chalazal seed coat ; SC, seed coat ; WS, whole seed,

RK	PCC	ORF/AGI	Gene Symbol	pre-globular stage							globular stage								heart stage							linear-cotyledon stage							bending cotyledon stage							mature green stage						
				pg EP	pg MCE	pg PEN	pg CZEN	pg CZSC	pg SC	pg WS	g EP	g SUS	g MCEN	g PEN	g CZEN	g CZSC	g SC	g WS	h EP	h MCEN	h PEN	h CZEN	h CZSC	h SC	h WS	lc EP	lc MCEN	lc PEN	lc CZEN	lc CZSC	lc SC	lc WS	bc EP	bc PEN	bc CZEN	bc CZSC	bc SC	bc WS	mg EP	mg MCEN	mg PEN	mg CZEN	mg CZSC	mg SC	mg WS
1	1	AT3G50990	*PRX36*	15	27	4	11	8	8	2	4	2	13	2	12	8	2	4	3	3	3	15	14	3	9	4	5	9	12	405	1522	554	1	2	27	992	29	20	7	1	11	3	53	65	9
44	6,96E-01	AT2G43050	*PME16*	6	18	14	26	2	2	8	9	16	4	4	5	6	12	12	8	3	19	19	14	3	7	13	44	12	31	27	2340	390	16	43	16	44	1338	366	12	2	30	21	69	318	95
100	6,21E-01	AT5G53370	*PME61*	2	5	13	5	3	3	20	3	7	3	2	13	49	28	90	4	4	15	9	70	38	80	1	6	20	26	134	113	21	2	10	5	114	68	28	17	4	2	10	58	6	9
214	5,28E-01	AT2G47550	*PME20*	13	6	24	14	11	14	7	11	9	20	12	17	13	9	7	7	13	10	48	20	10	17	9	13	12	8	48	12	158	8	7	13	151	20	25	15	10	17	16	30	33	17
376	4,52E-01	AT1G23200	*PME6/HMS*	20	5	25	3	10	14	11	13	12	5	8	10	3	9	12	4	4	18	18	42	46	182	8	33	11	11	70	3096	1674	14	41	15	607	5134	1431	16	41	31	12	432	1513	322
417	4,39E-01	AT1G11580	*No number*	2	12	8	22	10	21	196	1	2	5	5	10	14	16	35	1	2	1	8	73	3	34	8	20	5	3	34	50	45	11	5	15	269	44	19	33	12	5	13	159	2	28
2500	2,12E-01	AT1G11590	*PME19*	12	38	32	21	5	1270	464	18	7	276	10	11	5	2181	1234	1	5	106	13	23	4584	1253	8	41	29	17	76	2123	428	9	69	33	17	735	118	13	11	13	2	25	216	39
3383	1,69E-01	AT5G49180	*PME58*	17	69	27	36	235	3132	2746	3	28	121	76	21	101	3669	4769	9	20	39	34	356	5781	3834	10	42	26	16	836	3063	938	5	89	16	384	2008	412	161	167	111	94	130	645	94
3707	1,55E-01	AT4G03930	*PME42*	30	74	42	22	13	901	501	35	38	49	22	44	20	1941	349	46	23	68	23	26	2473	901	83	62	24	38	62	1118	138	52	142	27	30	241	71	71	40	72	35	24	139	75
4407	1,28E-01	AT3G59010	*PME35*	6	10	6	16	971	19	422	7	9	14	1	5	439	23	318	4	12	1	6	831	7	140	5	8	11	19	514	23	71	5	5	12	532	21	27	2	4	9	11	772	21	56
5112	1,03E-01	AT1G02810	*PME7*	6	10	4	2	2	8	1	59	78	5	1	5	4	1	10	82	62	19	7	7	2	17	80	26	21	40	57	37	40	56	23	8	8	9	18	31	22	11	3	3	2	37
5408	9,39E-02	AT3G29090	*PME31*	140	132	461	132	383	262	327	192	289	179	439	45	270	224	274	302	198	342	151	320	382	225	208	135	84	261	325	252	215	232	289	445	362	101	168	373	244	283	200	257	122	239
5958	7,70E-02	AT3G49220	*PME34*	150	4	25	24	2378	889	1044	26	205	19	4	7	1092	164	306	16	6	2	14	1361	87	118	14	4	6	12	894	14	27	36	15	19	955	23	25	41	10	6	7	499	29	59
6463	6,26E-02	AT4G33230	*PME45*	5	3	5	18	6	2	1	4	2	8	2	26	15	6	7	1	2	7	15	12	2	2	5	1	8	25	18	5	11	2	9	18	8	2	4	2	6	2	10	3	7	6
7153	4,52E-02	AT5G09760	*PME51*	187	488	388	269	702	291	398	80	181	549	272	179	543	123	457	143	302	646	264	910	279	274	194	249	128	156	590	114	258	294	145	233	759	187	309	287	518	574	203	954	191	396
7327	4,11E-02	AT2G45220	*PME17*	1	8	16	14	13	6	11	8	5	18	6	18	12	12	13	11	10	1	11	12	5	2	11	3	4	13	5	16	26	4	14	1	31	9	12	4	17	10	15	293	24	20
7372	4,01E-02	AT3G14310	*PME3*	2	5	2	9	132	73	40	17	2	13	7	24	89	19	13	24	10	14	8	69	4	20	23	10	178	16	71	12	38	16	66	3	59	24	12	33	4	12	68	39	14	9
7921	2,65E-02	AT1G53840	*PME1*	23	42	6	20	130	209	233	41	7	5	14	12	68	206	166	62	15	29	16	71	217	194	72	54	51	13	91	166	263	347	162	26	38	170	190	331	312	306	188	157	168	384
7999	2,46E-02	AT2G26450	*PME66*	7	5	8	29	6	4	9	13	5	13	19	3	10	19	23	18	23	6	13	12	10	14	37	30	116	52	17	17	37	14	57	12	29	25	39	40	18	17	24	3	13	30
8909	4,10E-03	AT5G20860	*PME54*	7	10	8	3	11	3	2	5	3	29	7	10	1	1	2	1	2	2	5	9	3	4	7	2	8	11	5	3	5	0	10	13	35	14	8	3	12	11	39	240	148	18
9298	-3,87E-03	AT5G07420	*PME49*	13	34	4	6	8	8	6	2	10	1	7	5	6	11	4	2	8	7	8	9	3	1	5	5	15	324	10	5	7	1	2	18	33	6	2	2	1	2	7	2	9	10
9517	-8,13E-03	AT5G07430	*PME50*	9	6	12	15	1	2	1	2	5	5	2	2	5	39	3	3	3	1	6	7	5	7	28	2	71	285	9	6	1	4	6	16	41	10	7	17	10	1	21	20	19	9
10333	-2,38E-02	AT3G24130	*PME29*	14	17	12	219	17	24	22	29	20	20	16	166	23	34	32	8	17	2	51	26	9	19	16	24	10	18	29	33	8	16	28	7	23	13	25	14	22	19	34	25	42	18
10490	-2,62E-02	AT3G62170	*PME37/VGDH2*	5	2	1	1	2	2	2	10	5	3	1	2	3	17	1	1	4	6	2	7	1	3	61	1	87	329	4	1	2	0	1	1	32	2	2	2	5	1	1	6	8	5
11042	-3,49E-02	AT2G47040	*PME4*	24	16	15	36	11	15	19	26	22	3	16	16	18	74	5	5	11	13	7	144	2	7	507	3	549	963	22	7	4	4	3	12	140	12	10	13	4	15	5	12	8	12
11099	-3,61E-02	AT2G26440	*PME12*	1	2	18	17	668	58	167	70	11	4	6	1	307	60	115	118	23	3	14	512	48	75	142	899	222	10	407	132	210	187	767	23	98	121	376	266	459	523	225	116	96	377
11116	-3,63E-02	AT3G05620	*PME22*	8	2	1	8	279	1	28	1	5	2	2	7	31	1	12	1	1	3	6	8	2	0	1	2	4	0	8	8	1	0	4	9	7	9	1	1	6	7	1	3	7	1
11135	-3,67E-02	AT1G69940	*PME1*	3	12	1	2	0	1	2	6	1	13	1	3	1	13	1	3	1	1	13	1	3	1	23	7	55	284	2	2	1	1	1	1	19	4	2	7	6	1	1	3	1	3
12055	-5,12E-02	AT5G51490	*PME59*	1	9	2	2	12	3	1	1	1	3	1	1	1	12	18	4	14	29	6	12	206	235	4	842	55	5	48	209	88	11	361	29	14	113	134	20	1598	1503	1218	139	237	329
12408	-5,67E-02	AT2G19150	*PME10*	17	1447	6	22	1	9	28	14	120	584	9	18	5	19	6	3	9	11	13	9	7	2	5	9	3	11	5	2	3	4	9	17	14	6	1	2	1	2	3	2	4	8
12474	-5,76E-02	AT3G43270	*PME32*	21	4	23	35	566	5	292	2	4	10	1	7	324	20	154	7	7	6	8	411	3	62	58	35	17	4	360	16	44	126	110	7	280	27	129	673	1145	958	1029	343	232	552
13163	-6,65E-02	AT5G55590	*PME62*	2	2	24	556	4	1	5	8	5	4	32	3770	148	9	56	5	7	2	4664	72	4	181	7	31	11	130	43	22	10	9	76	2	22	9	5	2	3	4	3	14	12	3
13257	-6,77E-02	AT3G60730	*PME65*	7	20	8	7	11	8	18	12	8	8	1	1	8	14	9	2	13	2	5	15	6	1	6	12	2	19	5	6	11	2	9	19	14	1	14	1270	24	575	160	4	13	23
13617	-7,17E-02	AT4G02300	*PME39*	52	642	15	33	6	9	29	4	124	566	8	8	4	1	17	5	9	9	13	14	12	1	5	4	1	6	2	3	1	2	2	19	11	3	2	11	4	4	6	1	4	2
16584	-1,09E-01	AT5G64640	*PME64*	24	101	52	21	28	20	40	40	77	87	34	41	39	43	55	57	86	91	20	30	57	40	39	50	19	31	24	51	72	67	23	112	18	19	77	87	79	82	44	39	40	117
16826	-1,12E-01	AT5G47500	*PME68*	14	13	7	7	56	35	27	11	9	20	5	5	15	1	9	15	6	4	18	17	6	11	75	13	23	7	13	1	45	162	7	4	5	2	92	29	9	5	22	5	3	75
19700	-1,61E-01	AT5G19730	*PME53*	14	8	4	9	144	27	85	2	5	1	5	12	62	33	54	9	3	7	1	58	40	33	54	1	18	9	6	8	19	98	13	2	4	3	61	211	15	15	28	28	3	158
20263	-1,72E-01	AT4G33220	*PME44*	1032	93	22	29	219	1594	923	610	1023	18	42	43	82	1411	2081	539	146	6	41	104	2685	872	848	81	24	2	49	31	284	773	20	12	21	10	595	217	31	22	10	24	21	571

However, in such a case, the higher exogenous fluorescence in tri cellular junctions could indicate a lower abundance of the endogenous protein in this location, leading to a similar mirror conclusion that PME6/HMS is not evenly distributed in the CW microdomain as PRX36 or PME16 are.

Although attempts to study total PME positioning in Col, *pme16* and *pme6* using an Anti-PME antibody (courtesy of Jerome Pelloux) gave interesting preliminary results clear, assessments of signals were difficult to make at this stage on 10 µm paraffin sections (data not shown). Ultimately, while systematic TagRFP positioning of expressed PME in MSC can give cues on their function, this work highlights the potential for PME functional redundancy in this context. While a *pme16 x pme6* mutant could give appropriate answer, the different background in which these genotypes were obtained (Col-4 and Nos-0, respectively) as well as the difference observed between both prevented us to generate this line yet. Regardless, FRET-FLIM analysis between PMEI6 and candidate PME would help resolve the putative interaction between these actors.

TBL38

The intriguing results obtained for TBL38 will be discussed in detail in Chapter 3 focused on the characterization of this protein.

Technical interlude: growth condition and effect of temperature.

The fundamental basis of my work comes from *PRX36* and *PMEI6* parallel study that was done in the team (Francoz et al., 2019b) during which plants were grown under constant light at 22 °C. In this work, due to structural changes in the growth chambers, plants had to be grown instead on a long day/night cycle (16h day/8h night; See material, 6.1.1.2) at similar temperatures then transferred at the onset of flowering in the greenhouse which sometimes led to unwanted biotic (pests) and abiotic (rises in temperature) stress on the plants. Under normal conditions, we first verified that the data we present here was consistent with previous finding in the team (PRX36-TagRFP positionning, *prx36* / *pmei6* seed mucilage release phenotype). Naturally, we eliminated from our analysis batches of plants and seeds that did not meet these standards. We then proceeded with further analysis while keeping our respective control to assess the impact of said stresses. As such, the data we presented are the representative results of experiments performed on healthy plants, with regards to their respective genotype.

Thankfully, these problems were not necessarily met in each generation of plants, which gave us the ability to confidently produce data with a high degree of reproducibility. However, particular issues were encountered this last summer, as exterior temperature rose to alarming values, sometimes leading to growth chamber breakdown or uncontrolled greenhouse parameters. This corresponded with our analysis of *proPRX36::TBL38-RFP* in *A. thaliana* which will be developed as preliminary results in Chapter 3, pending complete kinetics of the fluorescence pattern.

The effects of such issues were mainly observed under the confocal spinning microscope when studying TagRFP localization of key proteins.

PRX36, which served us as a great control, has being localized multiple times in previous studies or in this work at the top of the primary wall in MSC using either fluorescent proteins or polyclonal antibody (Kunieda et al., 2013, Francoz et al., 2019b, Chapter 2). Using the Tag-RFP, we could see the onset of its expression all the way to its decline. In later developmental stages, PRX36-TagRFP is progressively getting misslocalized as signals around the columella could be observed (Francoz et al., 2019b, **Figure 3.0, Sup. Fig. 2.3**). However, when plants were submitted to heat stresses during silique development, we saw severe modifications in PRX36-TagRFP behavior (**Figure 3.0**). First, we could not observe the onset of *proPRX36::PRX36-TagRFP* expression, as signals could be observed even in the youngest

developed siliques. There, PRX36-TagRFP was observed in the mucilage and the radial primary wall until 7 to 8 DAP (**Figure 3.0**).

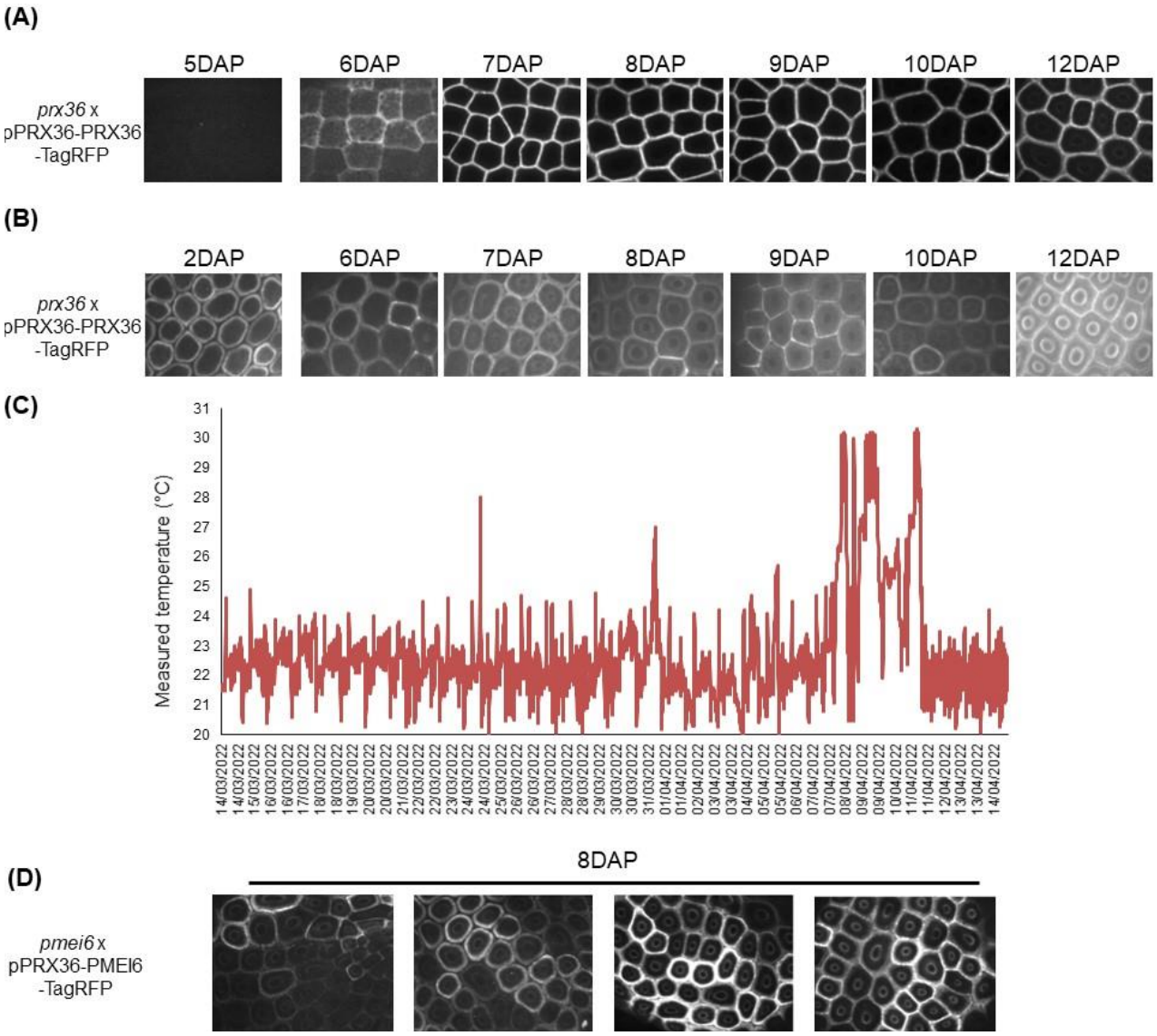

Figure 3.0: Heat stresses have drastic effects of PRX36/PMEI6-TagRFP signal behaviour. (A) Developmental kinetics of PRX36-TagRFP in MSC under normal growth condition. PRX36-TagRFP accumulates at 6 DAP in the radial primary wall and gradually fades as seed maturation progresses. Faint but detectable signals can be observed around the columella at later stages. **(B)** PRX36-TagRFP kinetics under heat stress. The onset of *PRX36* expression is not visible even at 2 DAP and protein accumulates in the mucilage early on. It is also misslocalized around the columella even at younger (7-10 DAP) stages. **(C)** Temperature report of the growth chamber in which the plants shown in (B) grew. **(D)** Misslocalization of PMEI6-TagRFP under heat stress. PMEI6 has been positioned in previous studies at the top of the radial primary wall (Ezquer et al., 2016; Chapter 2) and possibly at the top of the columella (Saez-aguayo et al., 2013). Yet, we saw high intensity signals in seed mucilage and around the columella.

Even then, signals could also be observed around the columella with high intensity, which never occurred in normal conditions. Such changes corresponded to an average increase of 3°C during silique development with peaks exceeding a 10°C increase (**Figure 3.0C**).

Although previous work positioned PMEI6 at the top of the radial primary wall (Ezquer et al., 2016) and even at the top of the columella (Saez-Aguayo et al., 2013; Ezquer et al., 2016), we could observe similar mislocalization of *proPRX36::PMEI6-TagRFP* when cultivated in similar conditions (**Figure 3.0A and D**). Interestingly, we still never observed a clear signal covering the top of the columella. Regardless, this made clear that drastic changes in growth conditions would lead to equally drastic changes in studied protein localization (**Figure 3.0**).

Unfortunately, final localization and complementation of *proPRX36::TBL38-TagRFP* in *tbl38* was done under worse condition than stated above. During siliques development, an average of 26.5°C with peak temperature exceeding 36°C were measured. Considering the consequences observed for PRX36-TagRFP (**Figure 3.0B**), it is difficult to give conclusions as to the precise kinetics of TBL38 localization in MSC. Therefore, Chapter 3 will only present such result as preliminary data needing further analysis for accurate kinetics of the localization.

Overall, we were able to generate and experiment on healthy seeds for each genotype presented in each chapter. In particular, molecular analysis were always performed on multiple plants from multiple generation which ensure stable and reproductible results. Yet, for clarity and avoid any misunderstanding of our results and conclusions, we highlight here and hereafter in the following chapters every time it is necessary to take additional care when interpreting the presented data.

Chapter three: TBL38 is an atypical homogalacturonan acetylesterase with a peculiar cell wall microdomain localization

The work included in this Chapter corresponded to the major part of my PhD conducted in the frame of the ANR MicroWall project. Particular collaborations were developed with colleagues in BIA, Nantes and BIOPI, Amiens for the mass spectrometry analysis and with Philippe Ranocha in the Lab for *in silico* molecular docking prediction and protein modelisation.

3. Introduction

Throughout every step of their development, plant cells specifically synthesize, design and constantly remodel their cell wall (CW) to better suit their needs. Such dynamics led to an impressive diversity in cell wall structure/function, related to specific composition and properties. At the molecular scale, accumulating evidence of modifications of chemical groups on particular polysaccharides involved in key developmental processes can be found in the literature. For instance, methylation of pectins is a well-documented field while acetylation of hemicelluloses and pectins has been increasingly studied over the years. The importance of pectin methylesterification dynamics has been largely studied, particularly for homogalacturonans (HGs). In the Golgi apparatus, HGs are methylated on the COOH through methyl-transferase activity (Driouich et al., 2012) and later undergo additional remodeling once in the CW. Methyl groups can be deesterified through pectin methyl esterase (PME) activity which in turn can be suppressed by their inhibitor (PMEIs). Examples of the consequences of such interaction have been described in large amounts of processes (See Chapter 1 Introduction). Additionally, *O*-acetylation of CW polymers such as pectins and hemicelluloses in the Golgi lumen has been described on multiple studies highlighting 3 groups of proteins involved in this process (Gille and Pauly, 2012). (i) As the sole member of its family in *A. thaliana*, ALTERED XYLOGLUCAN 9 (AXY9) was found to be a responsible for the non-specific acetylation of different hemicelluloses like xyloglucans and xylans (Schultink et al., 2015) leading to overall smaller plants when mutated. (ii) In *A. thaliana*, the REDUCED WALL *O*-ACETYLATION (RWA) family has 4 members which are also involved in *O*-acetylation of xylans, mannans, xyloglucans and pectins, although precise polysaccharides were not disclosed (Manabe et al., 2011, 2013). (iii) Finally, TRICHOME-BIREFRINGENCE-LIKE (TBLs) is the third and largest family made of 46 members separated in 4 phylogenetic clades in *A. thaliana* which has been increasingly studied (**Figure 3.1; Sup. Table S3.1**). Originally named after changes in the birefringence properties of *tbr* CWs, an impressive number of TBLs have been characterized for their *O*-acetyltransferase activity (Potikha and Delmer, 1995). Indeed, the 21 *TBLs* that have been characterized so far are involved in *O*-acetylation of various CW polysaccharides including the xyloglucan backbone and side chains, xylans, mannans, rhamnogalacturonan I (RG-I) and HGs (**Figure 3.1; Sup. Table S3.1**, reviewed in Gille and Pauly 2012; Pauly and Ramirez 2018). These activities may be highly clade-specific as 9 TBLs belonging to the similar clade displayed xylan-acetyltransferase activity (**Figure 3.1, Sup. Table S3.1**).

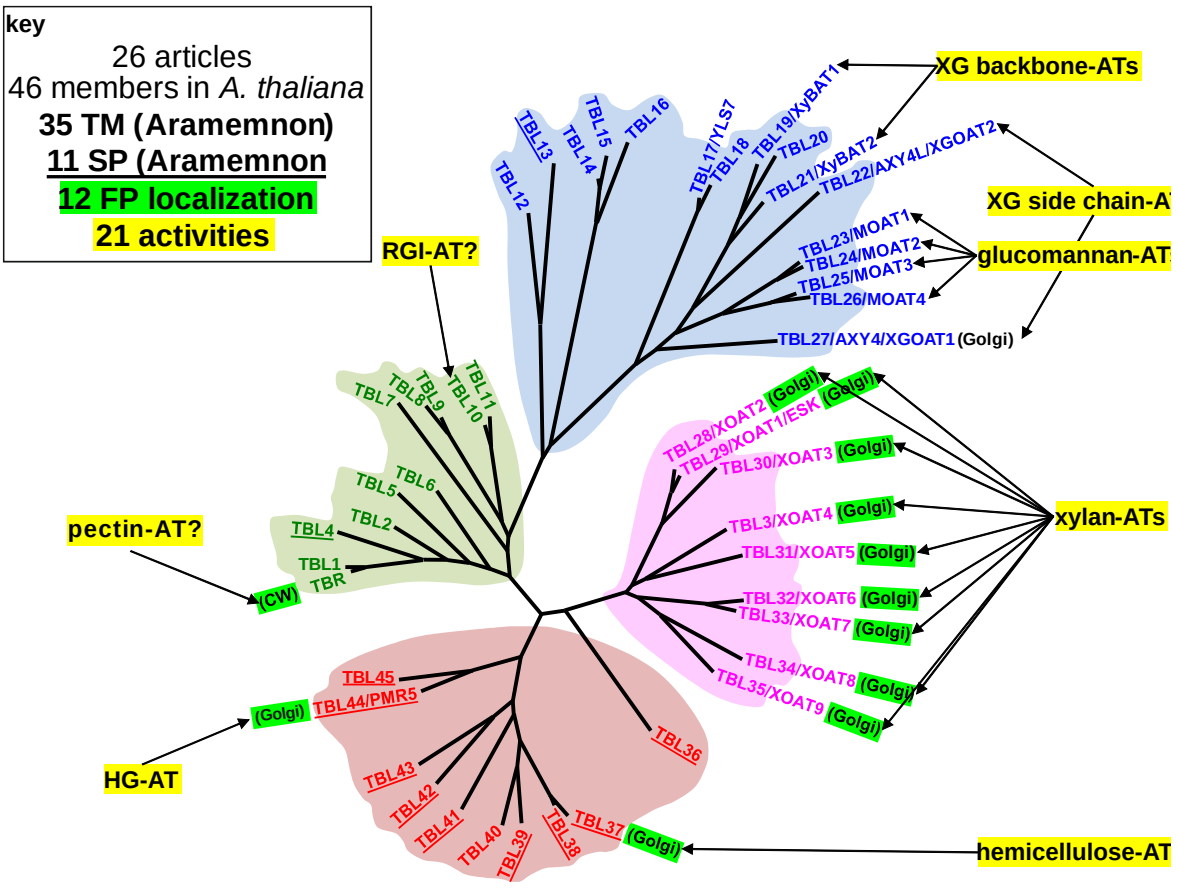

Figure 3.1: TBL gene family is primarily made of Golgi-localized acetyltransferases specifically acting on various CW polymers. The 46 members show high sequence homology and two conserved GDSL and DXXH motif which may be associated with esterase activities. However, previous works have described multiple TBLs as participating in *O*-acetylation of a wide range of CW polymers in the Golgi with the notable exception of TBR which was positioned in the CW (21 recombinant enzymatic activities and 12 fluorescent protein (FP) localization reported). Aramemnon predicts that the N-terminus hydrophobic domains either acts as a transmembrane domain (35 non underlined proteins) or as a cleaved signal peptide (11 underlined proteins). So far, each TBL or TBL phylogenetic clu seems to specifically act on a CW polysaccharide which assumes various role in development. See **Sup. Table S3.1** for detailed information. The phylogenetic tree was adapted from Bischoff et al., (2010).

TBL10 and TBL44/PMR5 were found responsible for RG-I and HG acetylation, respectively making them the only TBL targeting pectins (Stranne et al., 2018; Chiniquy et al., 2019; Yuan et al., 2016, **Figure 3.1, Sup. Table S3.1**). Mutations on particular *TBL* led to defect in CW structure and plant overall development as observed in *tbr, tbl03, tbl29, tbl37* (Bischoff et al., 2010; Lefebvre et al., 2011; Sun et al., 2020) although increased resistance to drought stress (Stranne et al., 2018) or pathogen (Chiniquy et al., 2019) was also observed in *tbl10* and *tbl44/pmr5*, respectively (**Sup. Table S3.1**). Like AXY9, TBLs have the conserved GDSL domain which is typically associated with esterase activity/lipase (Lai et al., 2017; Zhang et al., 2017; Akoh et al., 2004), and a DXXH motif found in a rhamnogalacturonan acetylesterase of *Aspergillus aculeatus*, although no such activity was ever described for TBLs (Mølgaard and Larsen, 2004). Out of the 23 characterized TBLs, 12 have been localized to the Golgi, supporting their role of *O*-acetyltransferase alongside AXY9 and RWAs (**Figure 3.1, Sup. Table S3.1**). Interestingly, TBR was localized to the CW in roots, contrasting with other TBLs (Sinclair et al., 2017) or similar acetyltransferases. Yet, although its precise activity is still unknown, an overall decrease in pectin acetylation was observed, even if the existence of a CW-localized acetyl donor is unclear (Sinclair et al., 2017). *In silico* prediction of the targeting function of the N-terminal hydrophobic sequence sorted the 46 TBLs in two groups (35 transmembrane anchoring and 11 cleaved signal peptide) and 6 TBLs have been reported in CW-enriched fractions without direct relationship with the predictions (**Sup. Table S3.1**). Overall, experimental evidence depicts TBLs as acetylesterase of various polymers in the Golgi lumen while unexplained rare association of some TBLs with the CW exist.

Initially, we set out to screen genes involved in *A. thaliana* seed mucilage release with particular interest on candidates that could modify the esterification status of HGs. The mucilage is a pectin hydrogel synthesized by the seed mucilage secretory cells (MSC) at the outer most layer of the seed coat (**See Chapter 1 Introduction; Figure 1.12**). During seed maturation, HGs methylesterification status is modified through PECTIN METHYLESTERASE INHIBITOR6 6 (PMEI6) activity on an unknown PME in a CW microdomain at the top of the radial primary wall, leading to a methylesterified pattern in HGs (Saez-Aguayo et al., 2013; Francoz et al., 2019b). This pattern acts as an anchoring platform for PEROXIDASE36 (PRX36) which then induces local loosening of the primary wall microdomain (Kunieda et al., 2013; Francoz et al., 2019b). After seed inhibition, the swelling mucilage breaks the pre-weakened primary wall and is extruded around the seed. Co-expression network centered around *PRX36* revealed that both *PRX36* and *PMEI6* had striking similarity in their spatio-temporal expression pattern (**Figure 3.2A**), thus additional proteins involved in their molecular scaffold could present similar gene

expression profile. On this basis, we identified *TBL38* (At1g29050) for its high co-expression with *PRX36* in the seed coat (**Figure 3.2A-B**). Based on the literature cited above, we first hypothesized TBL38 to be a Golgi localized protein acting as an acetyltransferase on CW polymers possibly including HG, considering its co-expression with *PMEI6*. Hereafter, we examined TBL38 positioning, activity and putative role in MSCs and uncovered that TBL38 is an atypical CW-localized HG acetylesterase Although TBLs are not thought to influence the methylesterification status of CW polymers, we investigated the putative indirect role of HG *O*-acetylation on methylation status and PRX36 anchoring, and discuss fine tuning of HG remodeling during plant development.

3.1. Results

3.1.1. *TBL38* is co-expressed with *PRX36* and *PMEI6* in mucilage secretory cells at intermediate developmental stages of seed development.

Precise loosening at MSCs surface of the radial primary wall requires tight spatio-temporal coordination of *PRX36* and *PMEI6* during seed coat development (Francoz et al., 2019b). On that basis, we built a co-expression data centered around *PRX36* in which *PMEI6* came as the second hit, using the tissue-specific seed developmental kinetics GSE12404 dataset (Belmonte et al., 2013). From this data, information on *TBL* expression was available for 37 out of the 46 *TBLs*, although only 26 were above the detection limit (**Figure 3.2A-B; Sup. Table S3.2**). Co-expression with *PRX36* was the highest for *TBL38* which was ranked 13 in this network due to specific and strong seed coat expression at the linear cotyledon stage (**Figure 3.2A-B; Sup. Table S3.2**). From there, we could not discriminate expression specific to a particular layer (**Figure 3.2A-B**). Indeed, the seed coat expression data encompasses 5 layers of cells which are referred to as (from inside to outside): ii1 (inner integument), ii1', ii2, oi1 (outer integument) and oi2, commonly addressed here as MSCs (Debeaujon et al., 2003; Francoz et al., 2015a). Therefore, we verified MSC specific expression using *in situ* hybridization on tissue array paraffin sections encompassing the whole developmental kinetics of wild-type seeds. Hybridized anti-sense probes displayed a clear purple/violet signal, particularly between the early linear and early bending cotyledon developmental stages (**Figure 3.2C**).

(A)

RK	PCC	ORF/AGI	globular stage								heart stage								linear-cotyledon stage								bending cotyledon stage								mature green stage							
			g EP	g SUS	g MGEN	g PEN	g CZEN	g CZSC	g SC	g WS	h EP	h MGEN	h PEN	h CZEN	h CZSC	h SC	h WS	lc EP	lc MGEN	lc PEN	lc CZEN	lc CZSC	lc SC	lc WS	bc EP	bc PEN	bc CZEN	bc CZSC	bc SC	bc WS	mg EP	mg MGEN	mg PEN	mg CZEN	mg CZSC	mg SC						
1	1	*PRX36*	4	2	13	2	12	8	2	4	3	3	3	15	14	3	9	4	5	9	12	405	1523	554	1	2	27	992	29	20	7	1	11	3	53	65						
2	9,47E-01	*PMEI6*	2	1	2	1	2	2	6	6	2	8	8	4	10	6	13	10	54	54	1	52	423	236	6	34	14	232	65	52	29	11	19	25	37	93						
13	8,16E-01	*TBL38*	10	5	61	26	2	2076	1003	1508	8	9	8	55	1064	1790	1012	16	47	7	17	1274	5537	2991	44	1	1	2731	894	312	1262	10	31	9	582	135						

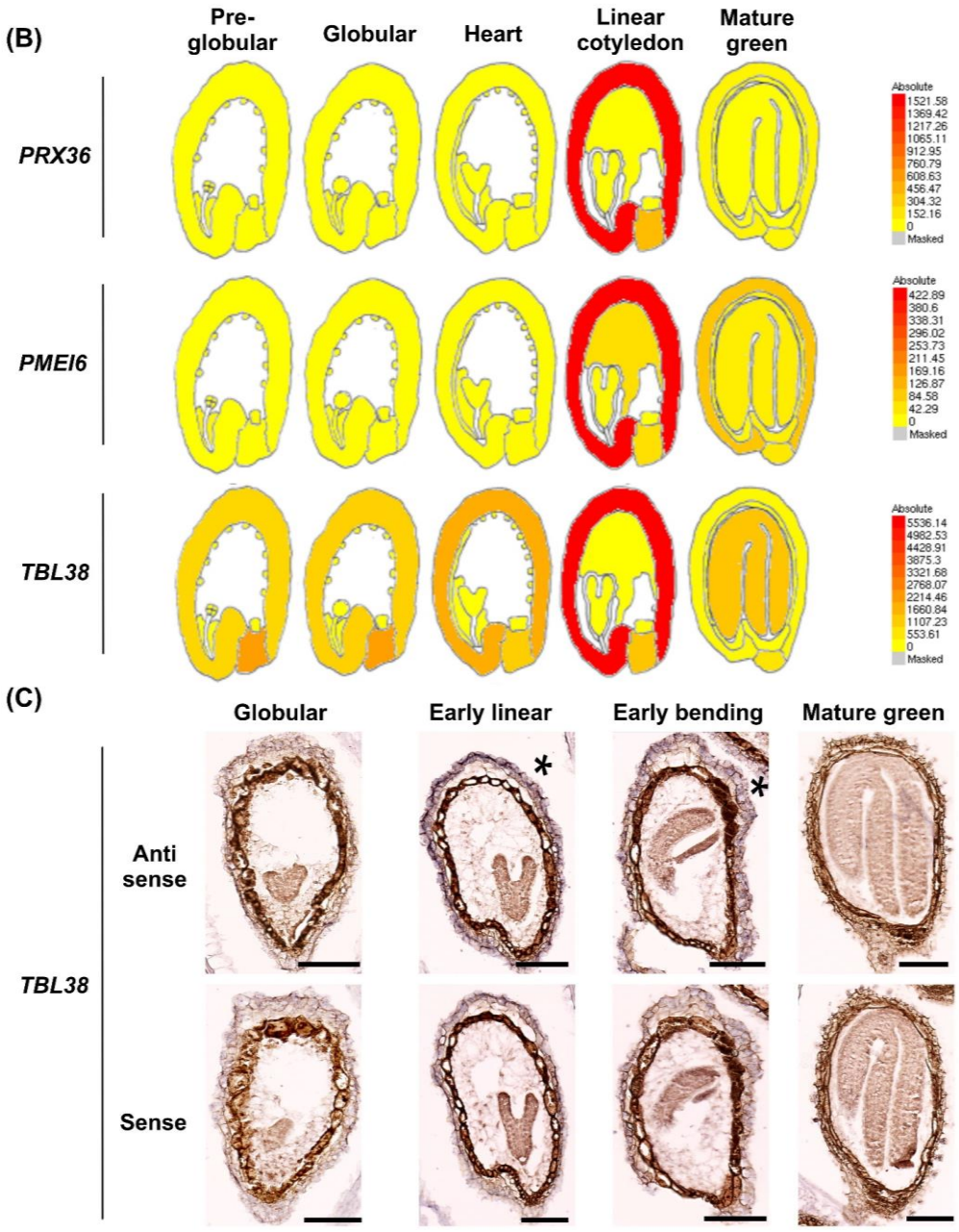

Figure 3.2: *TBL38* is coexpressed with *PRX36 and PMEI6* and transcript localization of *TBL38* is tied to the mucilage secretory cells (outer integument 2). (A) PRX36 co-expression network highlighting the similar profile of *PRX36*, *PMEI6* and *TBL38* (see Sup Table S3.2 for details). **(B)** eFP browser pictogram displaying the similarity in the spatiotemporal expression of *PRX36*, *PMEI6* and *TBL38* in *A. thaliana* seed coat. Absolute tissue-specific expression level is represented in color variation from yellow (lowest) to red (highest). Adapted from http://bar.utoronto.ca/efp/cgi-bin/efpWeb.cgi. **(C)** *In situ* hybridization of dig-labeled RNA probes targeting *TBL38* on paraffin sections of developing wild-type seeds. Anti-sense probes showed highest purple signal in the outermost layer corresponding to MSCs of seeds between the early linear and early bending developmental stages. These signals should be subtracted from the overall background obtained on serial sections of the same exact seeds with the sense probe control. Bars: 200 µm.

Contrasting with the earlier and later stages and with the sense probe control showing overall background level, we could associate the specific anti-sense probe signal in MSC excluding the chalazal tissues, in agreement with the transcriptomic data (**Figure 3.2A-C**). Still, we refined *TBL38* seed coat expression to MSC specific expression.

3.2. TBL38-TagRFP is localized to the PRX36-PMEI6 outer periclinal/radial cell wall microdomain

So far, except TBR which was positioned to the CW (Sinclair et al., 2017), 12 of out the 13 localized TBLs have been found in the Golgi lumen (**Figure 3.1; Sup. Table S3.1**). We generated a *pro35S::TBL38-TagRFP* construct which was transiently transformed *in N. benthamiana* leaves. Fluorescence was observed between 48 to 54h after transformation under confocal microscopy. TBL38-TagRFP fluorescence did not colocalize with a Golgi-YFP marker, but rather displayed a cellular delineation (**Figure 3.3**). To attribute the TagRFP fluorescence signal to the CW or the plasma membrane, we expressed both TBL38-TagRFP and a plasma membrane-YFP marker. Under plasmolysis condition, we could clearly see YFP signals separating from the TBL38-TagRFP CW signal as the PM was receding. However, although plasmolysis resulted in overall lower intensity signals, CWs were still labeled by TBL38-TagRFP (**Figure 3.3**). Thus, we concluded that TBL38 was a CW-localized protein similarly to TBR and contrarily to the 12 other Golgi-localized TBLs (**Figures 3.1 and 3.3**, Sinclair et al 2017).

As seed development advances, MSCs become mostly made of different CWs, namely the primary wall, the mucilage and the columella (**See Chapter 1 Introduction; Figure 1.12**). Increasing evidence have positioned CWs protein only in one or two types of wall (Francoz et al., 2019b; Šola et al., 2019b; McGee et al., 2019) or in sub-layer (microdomain) of one CW (Francoz et al., 2019b). As such, we needed additional precision on TBL38 localization in *A. thaliana* MSCs. For this, we generated a *proPRX36::TBL38-TagRFP* construct which was transformed in *tbl38* plants. Although additional experiments are needed to bring a definitive conclusion on the precise kinetics (**See Interlude**), we localized TBL38-TagRFP in the radial primary wall of MSC in early developmental stages (**Figure 3.3B**). Orthogonal projection allowed to refine TBL38-positonning at the top of the primary wall, corresponding to the CW microdomain harboring PRX36.

Both transient and stable expression of TBL38-TagRFP show an unexpected CW localization making TBL38 the second TBL positioned in the CW with TBR. Because its localization was

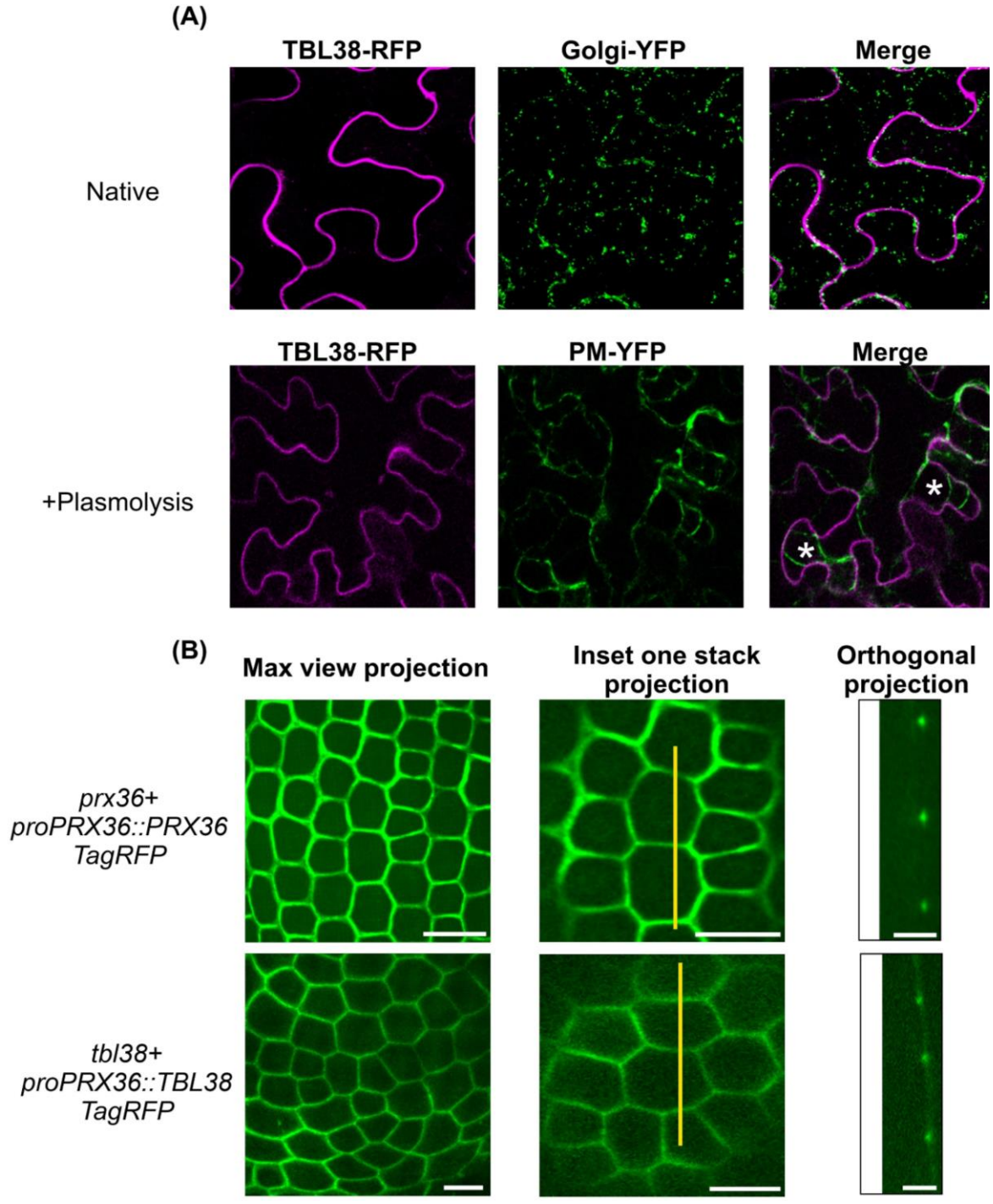

Figure 3.3: TBL38 is a cell wall protein localized to the radial primary wall of MSCs. (A) Confocal microscopy visualization of both TBL38-TagRFP and a Golgi-YFP markers transiently overexpressed in *N. benthamiana* leaves indicates that, contrary to most TBL proteins, TBL38 is not a Golgi localized protein. Under plasmolysis, the TagRFP signal and the plasma membrane-YFP marker signal are separated, indicating the association of TBL38-TagRFP to the cell wall. First row images are extracted from a maximum projection of 17 stacks. Second row images are a representative view of a single confocal plan. **(B)** Confocal spinning disk observations of PRX36-TagRFP and TBL38-TagRFP in *A. thaliana* developing seeds at 8 DAP. TBL38-TagRFP fluorescence was positioned similarly to PRX36-TagRFP in the radial primary wall of MSC. Orthogonal projection refined this localization to the CW microdomain consisting in the top of the radial primary wall. Max view projections were done using similarly sized projection of Z >30stacks with no singular edition. Bars: 50 µm.

strikingly similar to PRX36, we investigated TBL38 involvement in the PRX36-PMEI6 molecular scaffold and particularly its influence on HG modification.

3.3. The mucilage release and anchoring of PRX36 are not significantly modified in *tbl38*

Mutation in either *PRX36* or *PMEI6* resulted in impaired mucilage release because the primary wall failed to break upon seed imbibition. Because *TBL38* gene products had similar spatio-temporal expression and positioning as *PRX36,* we assessed whether or not mucilage release was affected in mutated seeds. We isolated a homozygous KO line for *tbl38* (**see Chapter 2 and methods**) and released its non-adherent mucilage through 1 hour vigorous shaking in solution. Subsequent ruthenium red mucilage staining was done on released adherent mucilage which was quantified for various parameters. Visually, we did not observe any differences between WT and *tbl38* seeds, particularly when compared to *prx36* or *pmei6* (**Figure 3.4A**). Statistically, *tbl38* mucilage area was on average slightly larger than WT, though only by a few percent (**Figure 3.4**). We did not see any obvious changes in mucilage staining intensity as was sometimes observed in mutated background responsible for mucilage modification (Turbant et al., 2016). Since proper mucilage release is the consequence of PRX36 anchoring to a specific HG platform subsequently enabling wall loosening, we investigated PRX36 positioning in *tbl38.* For this, we hybridized the αPRX36 polyclonal antibody on paraffin sections of developing seeds. As previously shown (Francoz et al., 2019b), αPRX36 labeled the top of the primary wall in Col-0 but not in *prx36* or *pmei6* (**Figure 3.4B**). We could also label PRX36 in *tbl38* in the same CW microdomain of the primary wall. In our experiments, αPRX36 behaved similarly in Col-0 or *tbl38* at all developmental stages (**Figure 3.4B**). To reinforce this result, we generated a *proPRX36::PRX36-TagRFP* construct which we transformed in *prx36* and *tbl38* background. Observation of TagRFP signal were made on developing seeds aged from 6-to-14 DAP which encompass the onset of the PRX36 promoter activity as well as the downfall of the PRX36-TagRFP signal (**Figure 3.4C**). In *prx36,* PRX36-TagRFP could be seen accumulating at the top of the radial primary wall in seeds as young as 6 DAP with some signals inside MSC which was associated with trafficking vesicles (**Figure 3.4C** see 6 DAP). Then, the signal accumulated only to the CW microdomain around 8 DAP and stayed consistent until 12-14 DAP after which we could observe overall decline of TagRFP fluorescence (**Figure 3.4C** see 14 DAP). For the most part, PRX36-TagRFP showed similar localization in *tbl38* and *prx36.* Differences in signal intensity were noted around 6 DAP as signals were consistently more

intense in *tbl38* (**Figure 3.4C** see 6 DAP). This could be associated with a slightly better protein anchoring at early stages although additional work is needed to confirm this subtle result.

So far, the particular PMEI6-specific HG methylation pattern occurring at the top of the radial primary wall linked proper mucilage release with PRX36 anchoring (Francoz et al., 2019b). Our results did not show such obvious relationship between TBL38, mucilage release and PRX36 positioning, suggesting that no changes in this HG methylation pattern should occur in *tbl38*. However, TBL38 could be involved in acetylation of wall polymers similarly to other described TBLs. Because changes in CW polymer acetylation could lead to different methylesterification status, possibly through indirect PME induction or hindering the dimerization of pectin chains (Kohn and Furda, 1968; Ralet et al., 2003), we studied the HG methylation pattern in *tbl38*.

3.2.4. The partially methylated homogalacturonan JIM7 epitope corresponding to the PRX36-PMEI6 cell wall microdomain are maintained in *tbl38*, while the corresponding LM20 epitopes are surprisingly lost

The specific HG platform enabling PRX36 anchoring, is generated through the inhibition of an unknown PME by PMEI6 leading to a partially methylesterified pattern in HGs at the top of the radial primary wall. Previous work determined that this molecular pattern could be labeled by both JIM7 and LM20, two monoclonal antibodies routinely used to characterize partially methylesterified HGs (Francoz et al., 2019b). Thus, we took advantage of this and hybridized JIM7 and LM20 on paraffin sections of developing seeds from *tbl38* and control backgrounds.

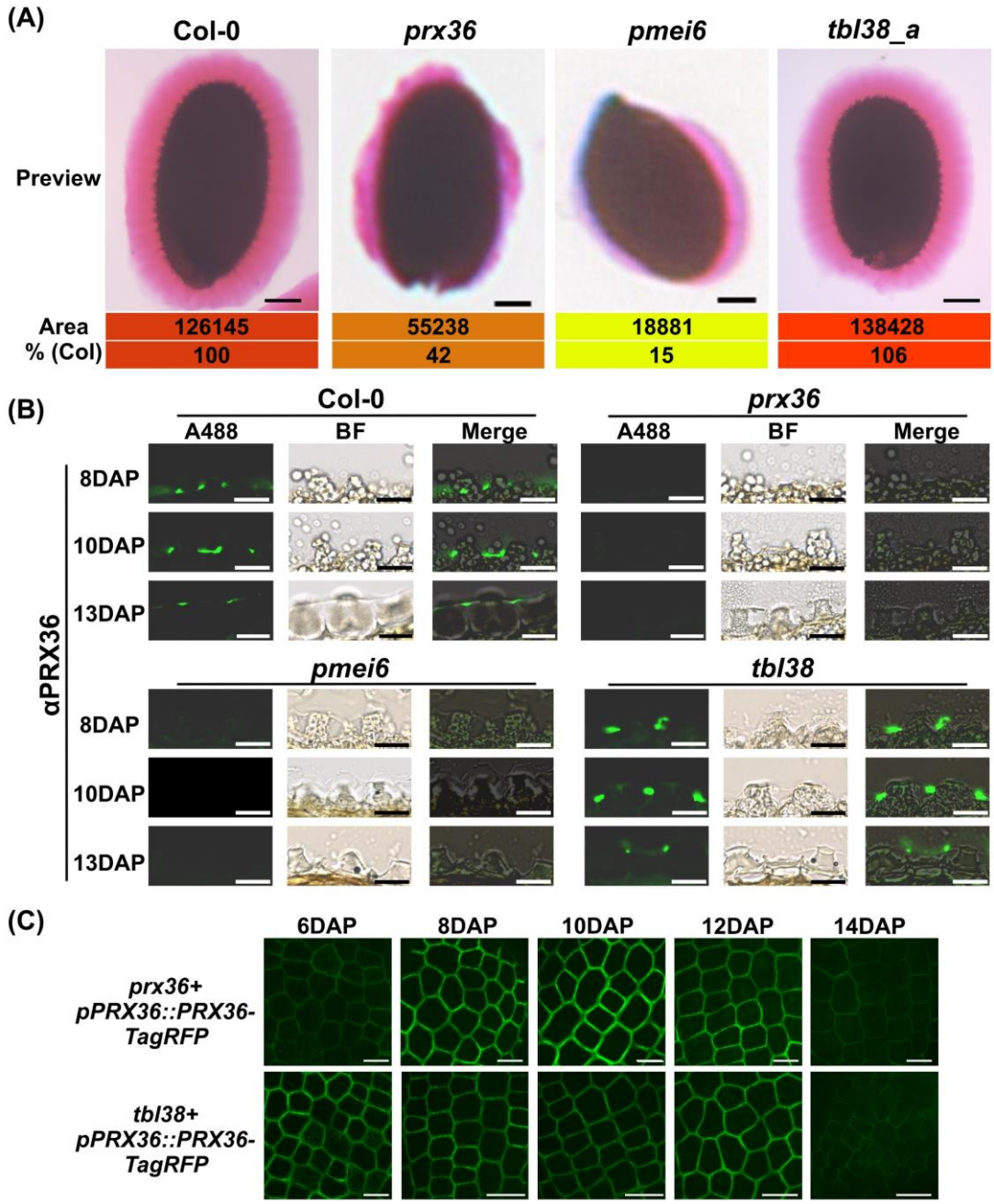

Figure 3.4: *tbl38* seeds show no defect in mucilage release and accordingly no obvious consequence in PRX36 anchoring (A) Ruthenium red staining of released adherent mucilage shows similar defect only in *prx36* and *pmei6* as previously shown (Kunieda; Saez; Francoz et al. 2019). *tbl38* mucilage shape and area size is similar to those in Col-0. Bars: 100 µm. **(B)** αPRX36 labeling of paraffin sections correctly positioned PRX36 at the top of radial primary cell wall from MSC in both Col-0 and *tbl38* contrary to the loss of labeling in *prx36* and *pmei6* controls. Bars: 25 µm. **(C)** PRX36-TagRFP localization is not affected in *tbl38* developing seeds. Confocal spinning disk observations of stable *proPRX36::PRX36-TagRFP* in *A. thaliana* reveal no obvious mislocalization of the signal in *tbl38*. Similar protein accumulation at 6 DAP and loss of signal at 14 DAP were seen in both genotypes. Images are the result of a maximum projection of similar stacks (Z>30) which were not edited. Bars: 50 µm.

First, we saw JIM7 signals correctly positioned at the top of the radial primary wall in Col-0 and *prx36*, particularly as MSC development advanced to later stages (**Figure 3.5A**). In *pmei6*, lack of inhibition of putative PMEs likely resulted in unesterified HG which was not labeled by JIM7 as previously shown (Francoz et al., 2019b). However, neither loss of signal or topological arrangement were observed in *tbl38* (**Figure 3.5A**). Similar observations were made with LM20 control genotypes: although sometimes patchier, signals were positioned at the top of the primary wall in Col-0, *prx36* but not in *pmei6*. To our surprise, LM20 signals were missing in *tbl38* (**Figure 3.5B**). While both antibodies are generally used in parallel to label partially methylesterified HG, their recognized epitopes are somehow different (Clausen et al., 2003; Verhertbruggen et al., 2009). Still, it is one of the first time that such a clear case was illustrated in MSC, particularly for PRX36 microdomain which we did not expect. To verify that loss of LM20 signals was due to mutation in *tbl38*, we transformed *tbl38* plants with a *proPRX36::TBL38-TagRFP* construct and hybridized again LM20 on paraffin sections of complemented lines. To make sure we did not miss key points in seed development, we expanded our kinetic to include every silique harvested between 6 DAP to 10 DAP. Regardless of the developmental stages, we confirm the loss of LM20 signals in *tbl38* as compared to Col-0 (**Figure 3.6A-B**). Interestingly, LM20 signal was overall restored in *proPRX36::TBL38-TagRFP* lines which display a similar labeling pattern as Col-0 (**Figure 3.6C**).

Overall, we concluded that mutation of *tbl38* resulted in lack of LM20 signal but not JIM7, possibly through a putative activity on HGs. Yet, it is still unclear if this was due to changes in the acetylation of HG which prevented LM20 binding through steric hindrance or changes in the methylation of HG due to a putative indirect effect of acetylation. Regardless, we sought to investigate TBL38 biochemical function in MSCs.

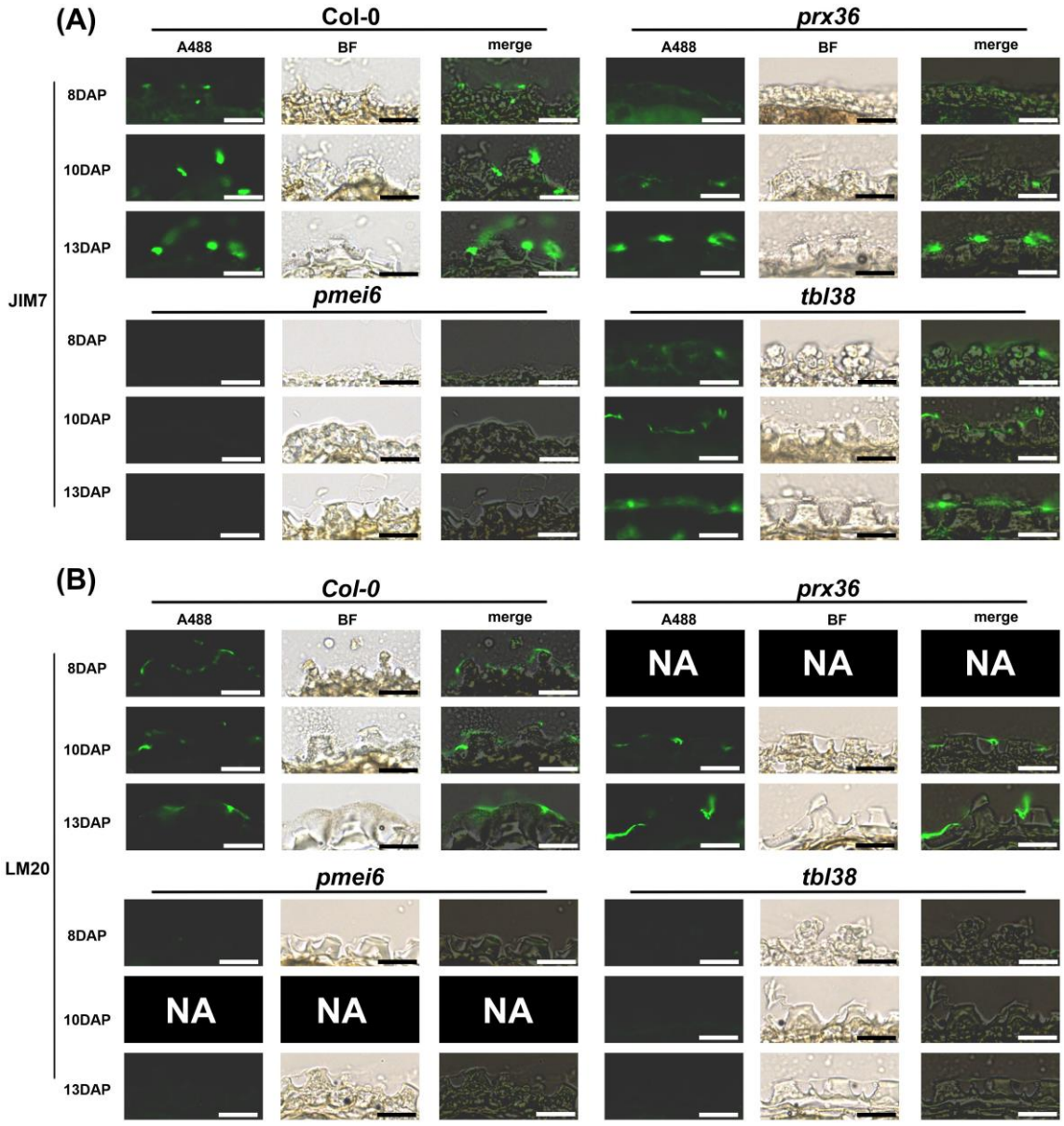

Figure 3.5: LM20 labeling reveals TBL38 as a putative new actor of HG methylesterification. (A) JIM7 labeling of partially methylesterified HG is deposited as early as 8 DAP at the top of the radial primary CW in the MSC microdomain of more mature seeds. No differences were observed except for *pmei6* used as a negative control. **(B)** The LM20 was previously though to bind to similar epitopes than JIM7 in MSC. Yet, we observed similar lack of binding in *pmei6* and surprisingly in *tbl38*, which the latter did not show lack of JIM7 binding. NA, non-available samples. Each genotype was studied under the Col-0 background. 40 x scans of fluorescence channel, brightfield as well as the merge were taken on paraffin-sections of seeds labeled at 3 development stages. The same parameters were used to analyze each image which are a representative of n > 50 MSCs. Bars: 25µm

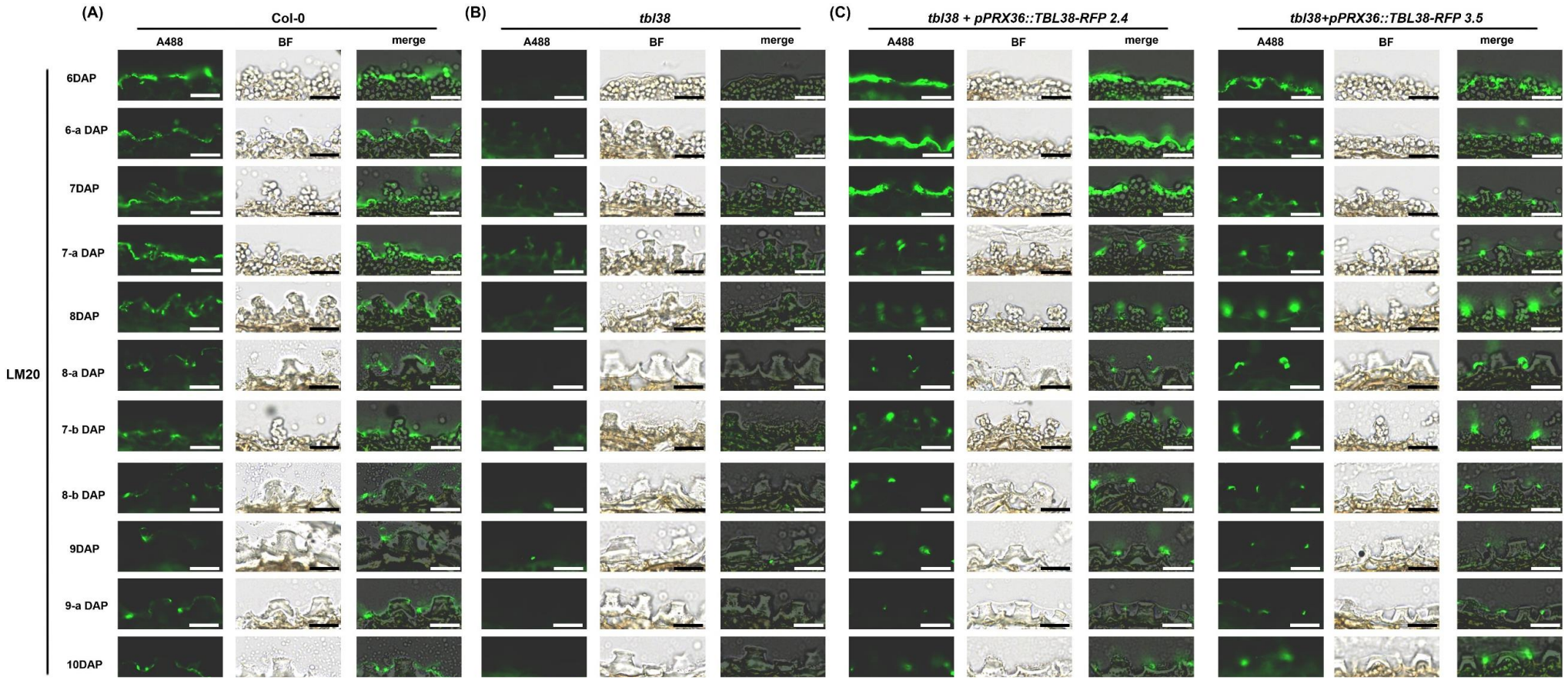

Figure 3.6 : Complemented *tbl38* lines transformed with *proPRX36::TBL38-TagRFP* show rescue of LM20 signal at the top of the radial primary wall. **(A)** In Col-0, LM20 epitopes are broadly distributed in the periclinal primary wall before columella formation between 6 to 8 DAP. Note the precise positioning in the CW microdomain as MSC development advances. **(B)** *tbl38* mutants displays complete lack of LM20 labeling in MSC even at 6 DAP. Signals could still be found in premature stages before *TBL38* expression or in the Chalazal zone (data not shown) due to absence of *TBL38* expression, in agreement with the *in situ* hybridization. **(C)** and **(D)** Expression of *TBL38-TagRFP* driven by *proPRX36* is enough to rescue LM20 phenotype in two homozygous complemented *tbl38* lines. Both LM20 signal intensity and localization were similar across each sample.
40 x scans of fluorescence channel, brightfield as well as the merge were taken on paraffin-sections of seeds labeled at 5 development stages. Additional siliques growing between labeled ones were also analyzed and additionally annotated with arbitrary letters. The minimum number of unlabeled siliques was selected to homogenize the variability in silique production of each plants. The same parameters were used to analyze each image which are representative of n > 50MSCs. Bars: 25µm.

3.2.5. Analysis of dry seed surface-enriched abrasion cell wall fractions indicates that TBL38 displays an atypical acetylesterase activity towards CW polymers rather than the canonical acetyltransferase activity observed in other studied TBLs

We took advantage of MSC accessibility and sturdiness to generate MSC surface-enriched cell wall abrasion fractions from dry seed using home-made abrasion columns (**see methods**). We used sand paper approximately 1:10 of seed size to scrape the surface of dry seeds, the resulting homogeneous powder being collected through a nylon mesh and subsequently analyzed (**Sup. Fig. S3.1A-F**). We confirmed that the abrasion process was restricted to MSC surface as MSC CW autofluorescence was strongly impaired but could still be barely observed in abraded seeds (**Sup. Fig. S3.1G-H**) which released residual amount of adherent mucilage when imbibed (**Sup. Fig. S3.1I-J**). Although overall MSC morphology was affected, we could still position each wall structure in this cell type (**Sup. Fig. S3.1M-N**) and we successfully abraded a surface extract containing the top of the primary wall, as both LM20 and JIM7 signals were lost in abraded seeds (**Sup. Fig. S3.1K-L**). Thus, we used theses fractions to advance in our study of TBL38 biochemical function. First, we verified that the immunological phenotype observed in *tbl38* MSC paraffin sections was also found in abrasion fractions using dot blot experiments. Semi quantitative analysis of dots membrane showed almost total loss of LM20 in *pmei6* and *tbl38* and loss of JIM7 only in *pmei6* (**Figure 3.7**). However, *proPRX36::TBL38-TagRFP* transformation partially rescued wild type phenotype in *tbl38* as dot signals were significantly different from *tbl38,* though not as intense as in Col-0 (**Figure 3.7**). Despite the aforementioned limitations in plant growth conditions (**see interlude**) that may impact dotblot quantification analysis, we succeeded in generating CW fractions which encompassed the CW material at the MSC surface to further explore TBL38 biochemical function with the presented partially completemented lines (**Figure 3.7**).

So far, every described TBL were either directly characterized as acetyltransferase or associated with lower acetylation content of CW polymers in mutated backgrounds (**Sup. Table S3.1**). Therefore, following the Stranne et al protocol which described TBL10 activity, we used an enzymatic kit to quantify the acetic acid content of our surface enriched fractions. Samples were chemically de-esterified and released acetic acid content was subsequently determined. Surprisingly, calculated amounts of acetic acid were significantly higher in *tbl38* compared to Col-0 (**Figure 3.8A**). This suggested that TBL38 activity was akin to an acetylesterase rather than the traditionally described acetyltransferase in this gene family. However, increase in acetylation phenotype was partially restored in *proPRX36::TBL38-TagRFP* lines which

showed partial complementation (about 40% rescue) similarly to dot blot results (**Figure 3.8A**). We still miss measurement of transcript levels to decipher whether the partial complementation could be related to unsufficient expression of *TBL38* under the control of *PRX36* promoter. To solve this, we engaged similar constructs using putative endogenous TBL38 promoter with / without TagRFP to also evaluate a putative negative impact of the TagRFP. Although we could associate TBL38 with de-acetylation of MSC enriched fractions, we could not measure acetylation level of specific polymers using this method. Because the increased acetylation level in *tbl38* could be achieved through acetylation of multiple polymers, we sought to identify TBL38 substrate in these fractions.

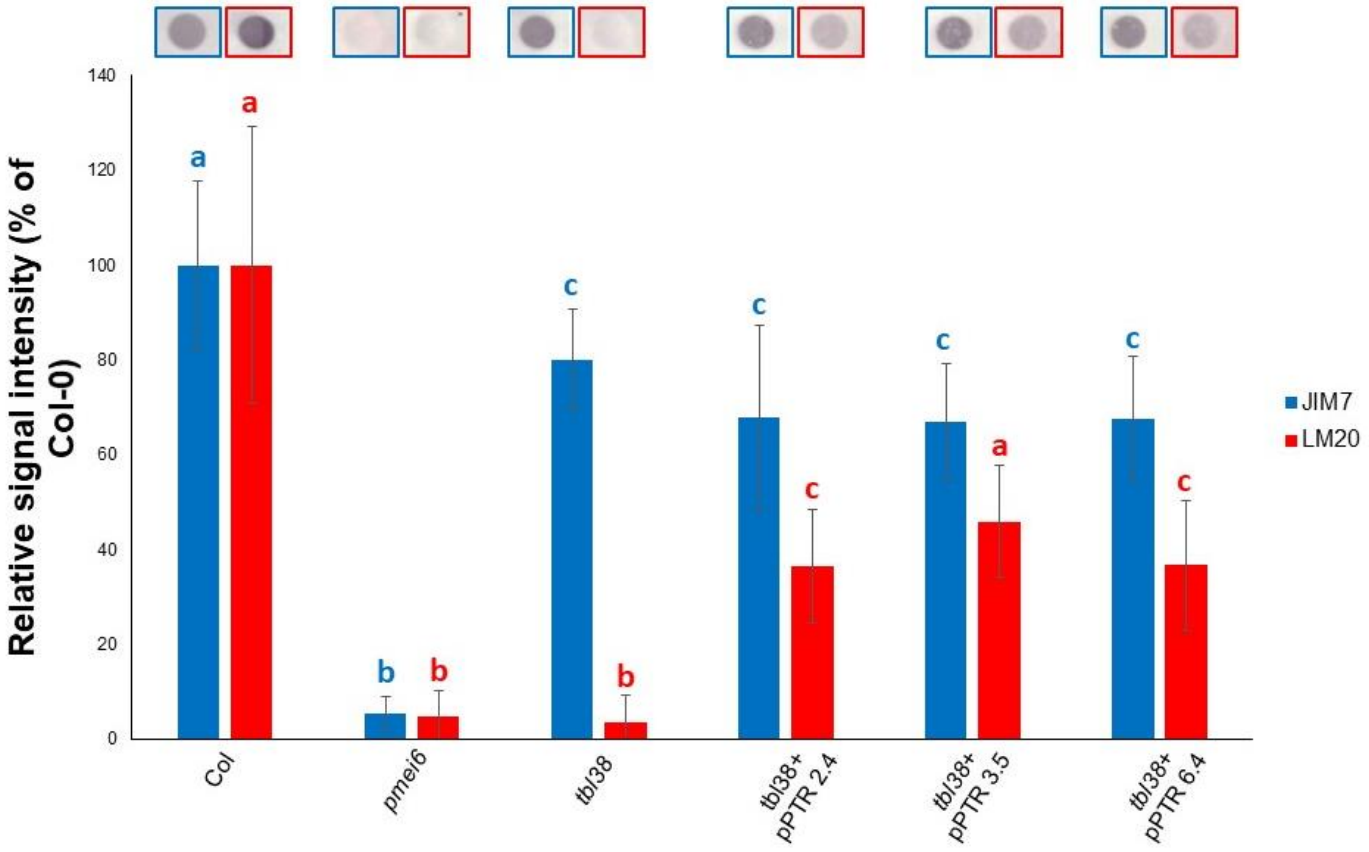

Figure 3.7: A partial complementation of *tbl38* is achieved through *proPRX36::TBL38-TagRFP* (*pPTR*) expression. (A) Immuno dotblot of MSC CW enriched fraction suggests a restoration of LM20 signal and no difference of JIM7 signal in complemented lines. Individual dots were cropped out of the same nitrocellulose membrane showing a representative view of 3 biological replicates spread across at least 10 technical replicates. **(B)** Semi-quantitative analysis of immuno dotblot signals reveals a partial complementation (35-45% ± SD) of LM20 signals relative to Col-0. Statistical tests were performed to assign groups of values relative to Col-0 for $p < 0.01$ (respective JIM7 p-value = 6.97E-11; 3.81E-3; 2.76E-4; 2.77E-5; 4.42E-5; LM20 p-value = 2.06E-6; 1.58E-06; 4.05E-3; 3.81E-2; 4.92E-3).

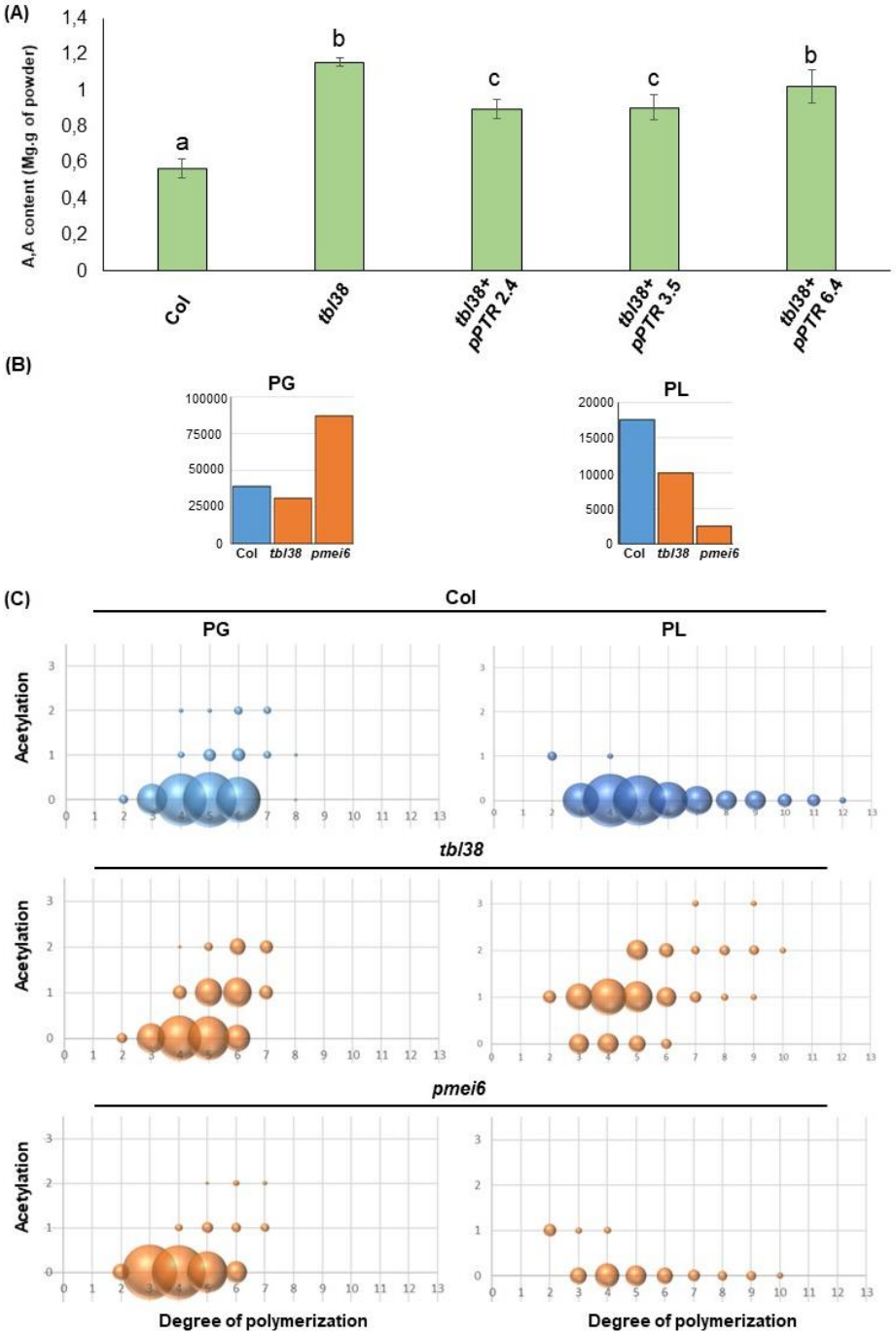

Figure 3.8: TBL38 is an acetylesterase working on HGs of both low and high degree of methylation (DM). **(A)** The acetic acid content of MSC enriched fractions was determined using an enzymatic kit and normalized according to sample mass. Note the partial complementation of *tbl38* which was statistically significant at the 5% cutoff (respective p-value: 3.53E-05; 6.09E-3; 5.02E-3; 3.20E-3). Mean results +/- SD were obtained using 3 biological replicates each composed of 3 technical replicates. **(B)** Mass spectrometry analysis of oligogalacturonates (OGAs) obtained using PG and PL, two HG cleaving enzymes with affinity towards poorly and highly methylesterified HGs, respectively, yielded contrasted amount of species in the three genotypes. The high number of species with PG and low number with PL observed for *pmei6* is in agreement with the low degree of HG methylesterification (DM) occurring in *pmei6* due to lower inhibition of PME activities (Saez-Aguayo et al., 2013). **(C)** Plot view of mass spectrometry analysis of samples degree of acetylation (DA) according to their degree of polymerization (DP) which correspond to the number of GalA in this species. Note the difference between Col-0 and *tbl38* which show higher acetylation level and acetylated GalA diversity. This representation is the representative view of 10 replicates spread across 2 biological replicates. The area of the circle reflects the sum of peak areas of species of a iven DA/DP combination (the isomers were not chemically determined). DA: degree of acetylesterifcation, DP: degree of polymerization, GalA: Galacturonic acid, PG: polygalacturonase, PL: pectin lyase.

3.2.6. TBL38 is a cell wall localized homogalacturonan acetylesterase

Abrasion fractions were enzymatically hydrolyzed in parallel with a polygalacturonase (PG) or a pectin lyase (PL), displaying specificity toward poorly and highly methylesterified HGs, respectively. The resulting oligogalacturonates (OGAs) from Col-0, *tbl38* and *pmei6* used as an additional control could then be analyzed in mass spectrometry which allowed for the triple analysis of the degree of polymerization (DP), degree of methylation (DM) and degree of acetylation (DA). Using a PG which has a higher affinity for HG with a lower DM, no obvious difference was observed in the total number of identified oligosaccharide species (mainly OGAs and some RGI oligosaccharides; data not shown) when comparing Col-0 to *tbl38* while the number of species drastically increased for *pmei6* (**Figure 3.8B**). This illustrates the specificity of PG since the lack of PME inhibition in *pmei6* leads to higher PME activities and consequently to a lower DM of HGs (Saez-Aguayo et al., 2013). Conversely, using a PL which has a higher affinity for HG with a high DM, comparable amounts of species were detected for Col-0 and *tbl38*, but we only detected a small fraction of species in *pmei6* as expected (**Figure 3.8B**). Altogether, the parallel approach with PG and PL allowed a better coverage of the variety of OGAs and particularly of DM diversity in the three genotypes to be compared. Then, the integration of peak area for the different isomers covering given numbers of acetyl (DA) for a given number of galacturonic acid (DP) were summed and plotted (**Figure 3.8C**). Remarkably, among the comparable amount of OGA species with relatively low DM obtained following PG hydrolysis (**Figure 3.8B**), a drastic increase in the abundance of OGA species of DA 1 and DA 2 and a correlated decrease of OGA species of DA 0 was observed in *tbl38* MSC fractions compared to Col-0 (**Figure 3.8C**). The phenotype was clearly observed at the acetylation level (DA) rather than at the DP level. This first result reinforced the high acetylation phenotype of *tbl38* (**Figure 3.8A**) and demonstrated that the targeted CW polymer included HGs. Using PL, despite the lower number of OGA species with relatively high DM occurring in *tbl38* (**Figure 3.8B**), a similar higher DA phenotype appeared for *tbl38* as compared to Col-0 (**Figure 3.8C**). Combined together, these results indicated that a higher DA phenotype occurred in *tbl38* for OGAs of both relatively low and high DM, respectively, demonstrating that TBL38 was an acetylesterase targeting HGs with various level of DM.

No such high DA phenotype occurred in *pmei6* (**Figure 3.8C**) demonstrating the specificity of the *tbl38* phenotype and suggesting that the HG acetylesterase activity of TBL38 was independent from the PMEI6 activity. The relatively higher and lower total number of species

obtained in *pmei6* with PG and PL, respectively (**Figure 3.8B**) was also observed in the detailed DA/DP plot as compared to Col-0 and *tbl38* (**Figure 3.8C**).

Taken together, these results were consistent with our previous finding associating TBL38 as an acetylesterase, but allowed us to refine TBL38 substrate as targeting HG with either low of high degree of methylesterification.

3.2.7. Simultaneous analysis of acetylation and methylation status gives insight in HG molecular fine-tuning

Conjointly with mass spectrometry analysis of the acetylation status of enriched MSC fractions, we obtained similar data concerning the degree of methylesterification (DM) observed on OGAs of each DP. Using PG (targeting HG of low DM), no drastic difference in the number of identified species was previously observed (**Figure 3.8B**). No shift in HG free carboxylic group, mirroring the methylation status, was observed between Col-0 and *tbl38* whose profiles were quantitatively but also qualitatively similar (**Figure 3.9**). This confirmed the absence of obvious methylation phenotype discussed in the previous section and reinforced the specificity of the acetylation phenotype for *tbl38* (**Figure 3.9**). In agreement with the higher number of identified species observed for *pmei6* as compared to Col-0 and *tbl38* (**Figures 3.8B**, the abundance of the individual OGAs of various DM (various number of free COOH) and DP was collectively larger for *pmei6* as compared to the two other genotypes (**Figure 3.9**). However, despite this overall quantitative difference the profiles were qualitatively similar, i.e. nearly all the isomers were more abundant in *pmei6* and we did not observe clear appearance or disappearance of given OGAs as it was the case while considering the DA for *tbl38* vs Col-0. Using PL (targeting HG of higher DM), once again the quantitative differences previously discussed (**Figure 3.8B**) were distributed among all the OGAs, regardless the DM (mirroring the number of free COOH) or DP while comparing the three genotypes (**Figure 3.9**). The Col-0 profile was quantitatively higher and somehow qualitatively similar as compared to those of *tbl38* (**Figure 3.9**). Similarly, the even lower amount of total species observed in *pmei6* was evenly distributed following a similar qualitative profile as those of Col-0 and *tbl38* with a general lower abundance of each species (**Figure 3.9**). Taken together, these results indicated that *pmei6* mutation does not have substantial effects on the DM diversity of HG in our samples, but rather contributed to the relative proportion of low vs high methylesterified OGAs retrieved with PG and PL, respectively (**Figure 3.8B**).

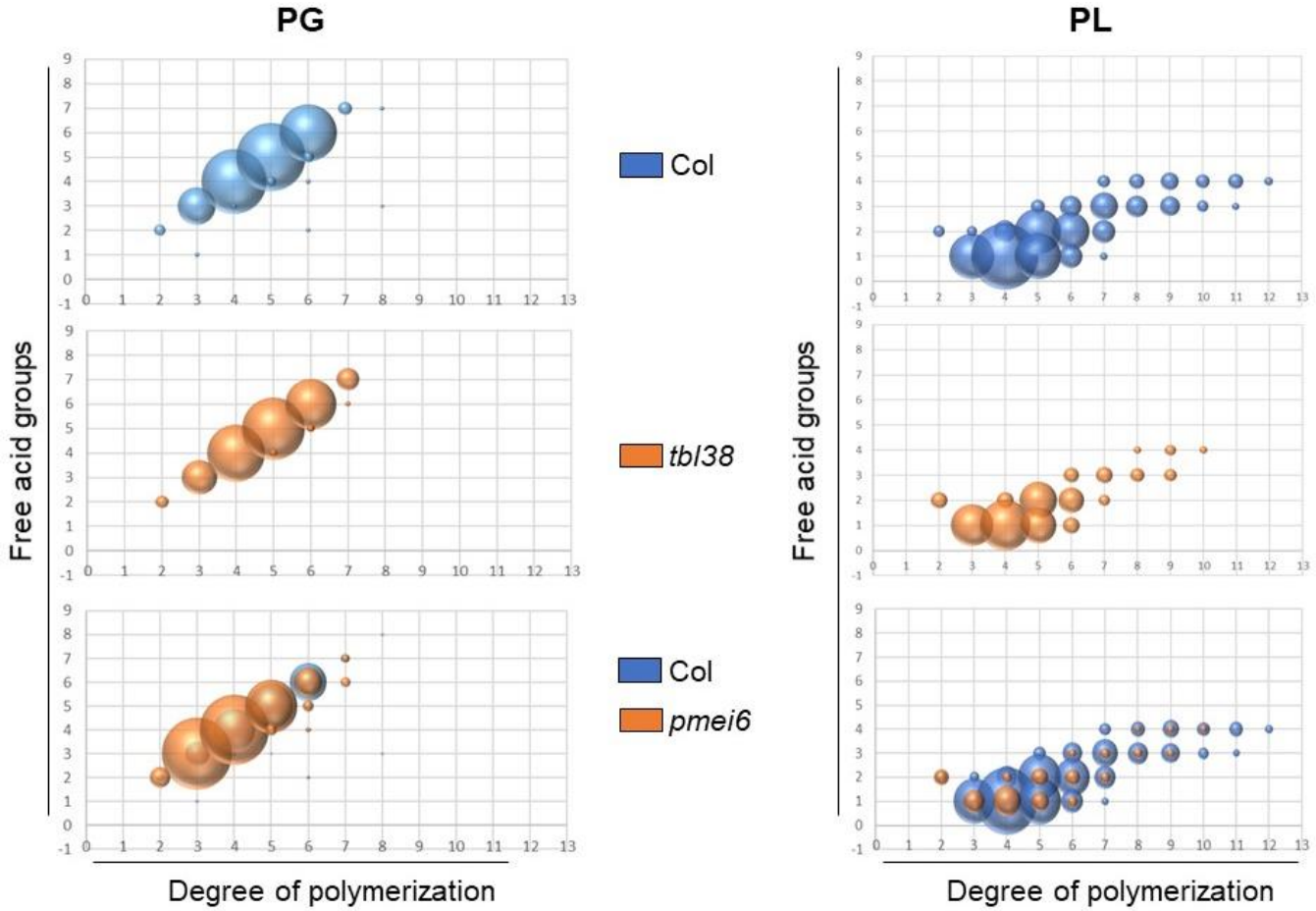

Figure 3.9: HG methylesterification does not seem affected in *tbl38*. Mass spectrometry analysis of MSC enriched fractions was done using a PG and PL which preferentially cleave HG with a low and a high DM, respectively. For instance, 4 free acid groups on a -DP6 would indicate that 6-4 = 2 methyl group would be found on a chain of 6 GalA. We mostly identified species in *pmei6* using PG, no drastic enrichment or diminution of the major species were observed. Similar results were found in *tbl38*, although we could see enhancement of some species using PL. DM: degree of methylesterification, DP: degree of polymerization, GalA: Galacturonic acid, PG: polygalacturonase, PL: pectin lyase

However, it is intriguing that the lower amount of total identified species retrieved following hydrolysis with PL in *tbl38* as compared to Col-0 (**Figure 3.8B**) was observed at the DA level (**Figure 3.8C**) as well as at the DM level (**Figure 3.9**). While this could be related to a possible lower activity of PL towards HGs with relatively high DA (Zeuner et al., 2020), this sparked the question of the natural relationship between acetylation and methylation. Because we had now mutations on two genes that were linked directly or indirectly with HG deacetylation and demethylation, we used these backgrounds to relate overall HG methylation to acetylation. The specificity of PG and PL for HG of relatively low and high DM, respectively, was clearly illustrated while comparing the DM profiles of the OGA produced by both enzymes (**Figure 3.10**). As a whole, Col-0 fractions were mostly deacetylated, as the DA was close to 0 regardless of the absence (PG; **Figure 3.10A)** or presence (PL; **Figure 3.10B**) of methyl groups. Overall HG acetylation was higher in *tbl38* even at higher DM further illustrating the acetylesterase activity of TBL38. However, the profile of *pmei6* fractions was similar to those of Col-0, suggesting lack of interplay between acetylation and methylation (**Figure 3.10**). Interestingly, although HG can be *O*-acetylated in two positions (2-*O* or 3-*O*) but methylated in only one (COOH), we always observed a higher DM than DA suggesting that HGs present in MSC surface walls are rather deacetylated and partially demethylated (**Figure 3.10**).

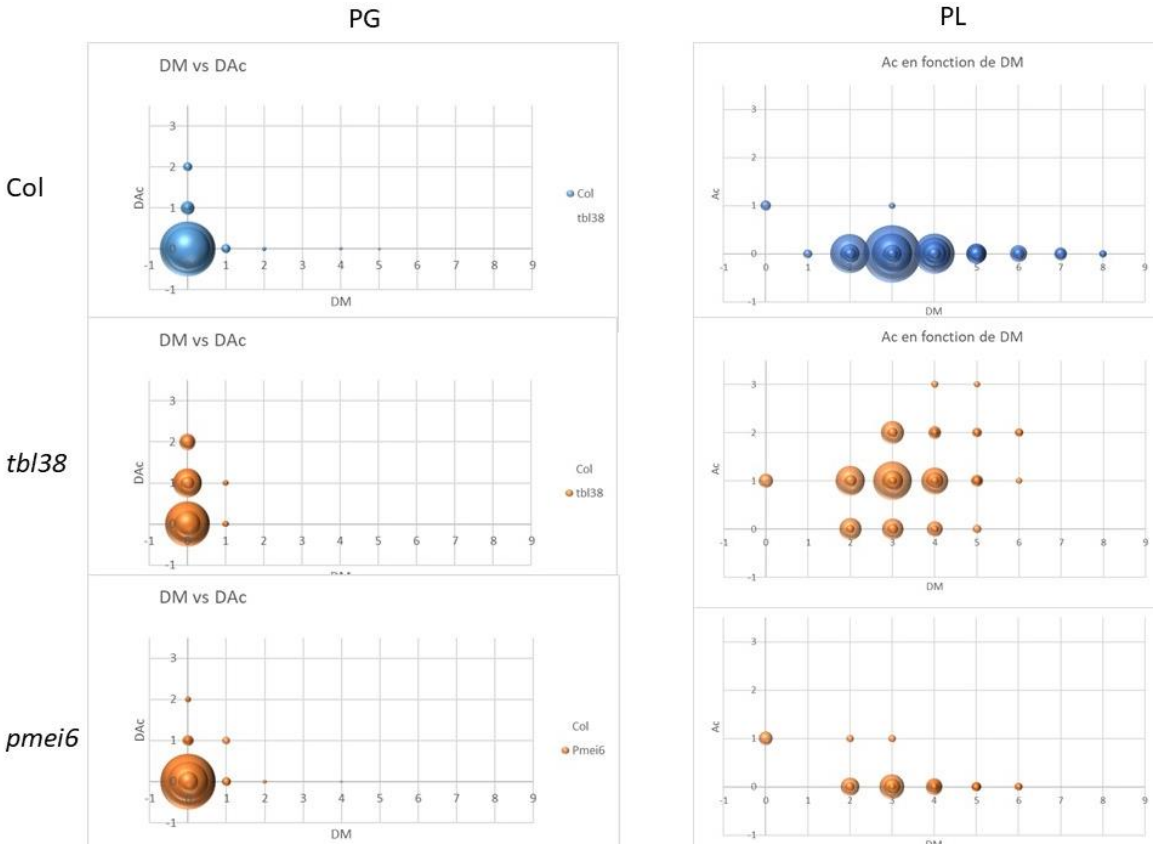

Figure 3.10: Methyl and Acetyl parallel study give clues to HG fine tuning in MSC fractions. The relative abundance of species of various DA and DM previously described according to their DP in Figures 3.8 and 3.9 were here represented according to one-another regardless of the DP. **(A)** Combined results obtained with the PG clearly illustrates the specificity of PG for OGAs of low DM and shows the limited acetylation of species in Col-0 and *pmei6*, although *tbl38* showed more acetylated GalA for similar DM. **(B)** The PL specificity for HGs of higher DM is clearly illustrated. Using the PL on Col-0 and *pmei6* fractions revealed that increased methylation level did not correlate with DA since the OGAs were weakly acetylated. Consistent with previous results, the DA/DM balance was increased in *tbl38* which showed higher acetylation, particularly on OGAs with a DM of 2-to-4. DA: degree of acetylation, DM: degree of methylesterification, DP, degree of polymerization; GalA: Galacturonic acid, PG: polygalacturonase, PL: pectin lyase.

3.3. Discussion

3.3.1. TBL38 is atypically positioned in the PRX36/PMEI6 cell wall microdomain of MSCs

Originally, we searched for genes involved in PRX36-PMEI6 molecular scaffold with a particular interest in HG remodeling enzymes. Using spatio-temporal similarity in gene expression with *PRX36*, we selected *TBL38* for its putative role in HG acetylation. Previously described TBLs were for the most part found anchored to the Golgi membrane (**Sup Table S1**) with the exception of TBR (Sinclair et al., 2017). Although the authors did not refute the possibility of some TBR-GFP signal in the Golgi, they concluded that TBR was a CW protein. Granting that N-ter sequence analysis of TBLs predicts either transmembrane (which would be akin to a Golgi-localized protein) or a signal peptide (akin to a secreted CW protein), experimental evidences sometimes contradicts targeting predictions (**Sup Table S1**). Indeed, the Golgi experimental localization matches with the TM prediction for 10 TBLs (TBL27, 28, 29, 30, 03, 31, 32, 33, 34, 35) while Golgi-localized TBL37 is predicted with a cleaved signal peptide and TBR that has been localized to the CW is predicted with a transmembrane domain (**Sup Table S1**). Six TBLs including TBL38 have been identified in cell wall proteomes but these proteins did not match perfectly to the targeting prediction (good match with signal peptide prediction for TBL9, 38, 39 and 45 ; bad match with transmembrane domain prediction for TBL15 and TBL40) (**Sup Table S1**). As such, we did not necessarily consider TBL38 predicted signal peptide and presence in a CW proteome as proof of secretion outside of the Golgi. Yet, we localized TBL38-TagRFP in *N. benthamiana* and *A. thaliana* to resolve conflicting information.

Unexpectedly, both constructs positioned TBL38 in the CW of tobacco leaves or *A. thaliana* MSCs (**Figure 3.4**). As stated, is still unclear as to why both TBL38 and TBR behave differently than other TBLs. It could be that predictions of addressing do not accurately account for hidden motif in the sequence. To test this, we replaced the 100 bp N-ter portion of TBL38 sequence with that of TBL27 which was localized to the Golgi (Gille et al., 2011) to build p35S Nter-TBL27 Cter-TBL38 Tag-RFP T-Nos and did the opposite to build Nter-TBL38 Cter-TBL27 (See **Table 6.11** Methods). Although additional experiments are needed, first results showed mislocalization of both chimeric proteins in *N. benthamiana* leaves (data not shown). Therefore, the atypical targeting of TBL38 to the CW is supported by TagRFP experiments in two model plants, in agreement with its localization in a cell wall proteome and the predicted signal peptide. In MSCs, this targeting is restricted to the CW microdomain harboring the

HG/PMEI6/PRX36 molecular scaffold even though final kinetics of localization are missing yet.

3.3.2. TBL38 as an CW acetylesterase of HG

Sequence analysis of the TBL family highlighted the conservation of the characteristic domains found in every protein. The most notable domain are the GDS and DXXH motifs commonly found in esterases (Akoh et al., 2004; Mølgaard and Larsen, 2004). Detailed analysis of ESK1/XOAT1/TBL29 including crystallography work and site mutagenesis pointed to the spatial reunion of these two domains including the conserved Ser-His-Asp catalytic site, The Ser coming from GDS and the His and Asp coming from DXXH (Lunin et al., 2020). Based on the crystallography of TBL29, we built an *in silico* model of TBL38 to verify the position of said amino acids. In our model, the predicted catalytic site was correctly positioned, although the putative polysaccharide docking valley was not as open in TBL38 (**Figure 3.11**). In the Lunin study, mutation of a nearby Arg which stabilizes the catalysis resulted in loss of transfer of acetyl groups for the acetyl transferase activity. We verified that similar Arg was present in TBL38 at the R193 position (**Figure 3.11**). So far, every described TBLs have been associated with a Golgi-localized acetyltransferase activity, either on hemicelluloses or pectins (**Figure 3.1; Sup. Table S3.1**). Therefore, the question arose on whether the CW-localization of TBL38 could lead to similar activity. Yet, both enzymatic assay of acetic acid and mass spectrometry analysis rather put TBL38 as an acetylesterase targeting acetylated homogalacturonans as opposed to other TBLs (**Figure 3.8-3.10**). The presented *in silico* study of TBL38 suggests that TBL38 does not have a particular motif or conformation which could explain such opposite activity. Thus, we propose that the opposite activity of TBL38 is related to its CW localization. Indeed, polysaccharide acetylation is done in two consecutive steps: formation of the acyl-enzyme intermediate which hydrolyses the acetyl group, followed by transfer of the *O*-acetyl moiety to its target. To our knowledge, neither acetyl CoA or a putative acetyl donor is present in the CW, which could prevent a CW localized TBL38 to complete the first step of the reaction and the enzyme could then rather function as a direct acetylesterase on acetylated HGs. Such esterase activity was also measured on $TBL29_{219A}$ which could only achieve esterification of its acetyl donor substrate. (Lunin et al., 2020). It should be noted that such results were not observed

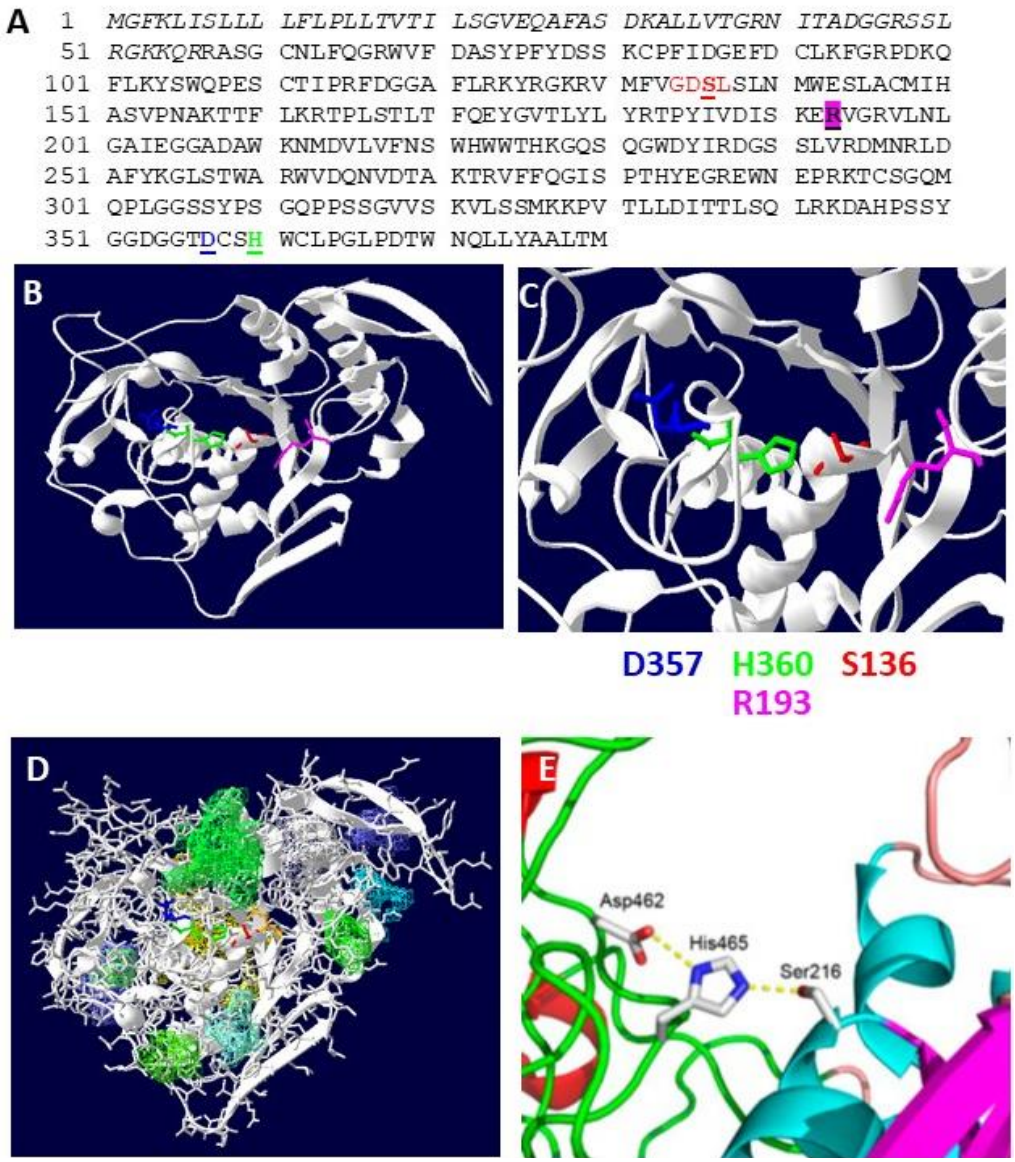

Figure 3.11: Molecular modeling of TBL38 displaying its putative catalytic triad and substrate binding pocket. **(A)** Amino acid sequence of TBL38 (At1g29050). The putative signal peptide is underlined. The amino acids in italic correspond to the 15% of the protein not covered by the molecular modeling performed in (B). GDS and DxxS tetrads that are conserved among the 46 DUF231 (TBR/TBLs) including TBL38 (Bischoff et al., 2010) are highlighted. The amino acids participating to the putative catalytic triad S136-H369-D357 appear in bold underlined. **(B)** Homology model for TBL38 (At1g29050) was built with the Phyre2 server (Kelley et al., 2015). The TBL38 structural model used in this study was the Phyre2 prediction with the highest-ranking score (Confidence: 100.0%; Coverage: 85%). The template was the crystallographic structure (X-Ray diffraction, 1.85 Å) of *A. thaliana* TBL29/ESK1/XOAT1 (At3g55990; PDB 6CCI; Phyred2 c6cciA) (Lunin et al., 2020). **(C)** Zoom on the putative catalytic triad S136-H369-D357 originally identified in Ser proteases and classically found in several dissimilar enzymes and protein folds that cleave amide or ester bonds via nucleophilic attack (Dodson and Wlodawer, 1998), and necessary for the acetyl transferase activity of TBL29 (Lunin et al., 2020). The Arg residue present near the catalytic site has been described as critical for transferase activity in TBL29/ESK1/XOAT1 **(D)** Visualization of the wide grooves including the wider green groove located on the top of the catalytic triad corresponding to the putative substrate binding pocket. **(E)** TBL29/ESK1/XOAT1 catalytic triad for comparison (Lunin et al., 2020).

in TBR despite its CW positioning. *tbr* was associated with lower acetylation level of HG (the opposite phenotype of *tbl38*), possibly through TBR-mediated protection of HG from pectin acetyl esterases (Sinclair et al., 2017). Although is it unclear how such a mechanism could play out, it is difficult to explain such differences in measured acetylation levels. Recombinant TBL38 production was initiated in *P. pastoris* by the J. Pelloux team for *in vitro* activity test at different pH. The preliminary results show that TBL38 displays an acetylesterase activity on artificial substrates. Deeper ongoing characterization will help understanding the putative dual-activity of TBL38.

3.3.3. HG fine tuning of esterification is affected in *tbl38*

Although HG acetylation and methylation is achieved through different protein actors, proof of the direct and indirect interplay between both chemical groups was given. Indeed, HG acetylation could inhibit PME activity by steric hindrance (Celus et al., 2018; Kohn and Furda, 1968). Additionally, methyl ester groups are preferentially added on non-acetylated galacturonic acid, which may explain the overall low level of acetylation in most plants and in our results with Col-0 (Pérez et al., 2000, **Figures 3.8 and 3.10**). Although we did not quantify HG methylesterification, the total number of identified species was particularly lower in *tbl38*, when using PL with affinity for highly methylesterified HG (**Figures 3.9; 3.10**). Considering lack of LM20 labeling, this could be associated with reduced HG methylesterification in *tbl38*. It should be noted, however, that the combined use of PG/PL might not give the full representation of HG species, particularly for a DM of 50%. Additionally, the similar antibody JIM7 could still hybridize sections of *tbl38* seeds suggesting that lack of LM20 binding might rather be due to steric hindrance caused by HG acetylation, rather than changes in the pattern of methylesterification. Therefore, LM20 could display a specificity for relatively highly methylesterified HGs with low acetylation, while JIM7 would be specific for relatively highly methylesterified HGs regardless of the acetylation status. Evaluation of both *PME* expression and PME activity in *tbl38* developing MSCs could give clues as to TBL38 indirect influence on HG methylesterification.

Regardless of the DM, our results confirmed increased amounts of HG acetylation in *tbl38* fractions. Contrary to methylesterification, acetylation should not influence the charge density and therefore cation binding capacity of HG (Dronnet et al., 1996; Ralet et al., 2003). However, experimental evidences have consistently associated high acetylated HG with reduced affinity to cations binding such as Ca^{2+} (Ralet et al., 2003; Celus et al., 2018). Conceptually, this could be due to direct influence of acetylation on conformation, access or cations binding properties

but also indirect effect on the PME activity as stated above (Renard and Jarvis, 1999; Oosterveld et al., 2000). *In vivo*, negatively charged HG can be crosslinked with Ca^{2+} to form so-called "egg-boxes" structures which is generally related to CW stiffening. Indeed, mucilage release is impaired in a $CaCl_2$ solution but improved with EDTA which is known to chelates Ca^{2+}. Interestingly, during additional mucilage release assays performed in 20mM $CaCl_2$, we observed a significantly improved release in *tbl38* compared to Col-0 and *prx36* (**Sup. Fig. 3.2**). This is consistent with previous finding, as the higher HG acetylation in *tbl38* would lead to decreased cations affinity and thus overall reduced Ca^{2+}-induced CW stiffening eventually leading to facilitated mucilage release. We could also observe smaller mucilage halo compared to water conditions, either suggesting partial release or densification of the mucilage halo due to influence of Ca^{2+} (**Sup. Fig. 3.2**). Still, further experiments are required, particularly on complemented lines for which this work was not done yet.

3.3.4. Increased HG acetylation may benefit PRX36 anchoring

So far, our results have identified TBL38 as a CW localized HG acetylesterase which mutation caused increase acetylation level and thus lower Ca^{2+} binding affinity with no obvious effects on PRX36 positioning, despite colocalization in the same CW microdomain. Previous work has demonstrated that PRX36 binding in HG was dependent on Ca^{2+} as the PRX36-TagRFP was severely impacted using EDTA (Francoz et al., 2019b). Hence, we aimed to investigate the implication of acetylated HG on PRX36 docking using an *in silico* model based on PRX53 crystallographic data (Oosterveld et al., 2000). The previous in silico study tested the five OGAs of DP6 used by Clausen et al to define JIM7 specificity (Clausen et al. Francoz et al., 2019b). It turned out that the three OGAs (so called Clausen 3, 4 and to a lesser extend 5) that were the best recognized by JIM7 could be used for in silico docking on a PRX36 valley that was validated by site directed mutagenesis (Francoz et al., 2019b). Here, we first randomly screened *in silico* PRX36 anchoring on 124 OGAs representing all the combinations of methylesterification from DP2 to DP6 **(Sup Table S3.3**). The *in silico* models consisted in 9 poses of decreasing affinity (increasing energy level). To rationalize the distribution of these poses on the protein surface, we systematically measured the root mean square deviation (RMSD) showing the distance between the best pose and the 8 other poses.

(A)

RK with ac	RK	Clausen et al 2013	OGAs (code and structure)	DP	DM	DA	Σ EL/ Σ RMSD (RANKED)	Σ EL	Affinity EL = Energy level (kcal/mol) 9 poses of docking vs all surface of PRX36									Σ RMSD	Distance RMSD (Root-mean-square deviation) 9 poses of docking vs all surface of PRX36								
									1	2	3	4	5	6	7	8	9		1	2	3	4	5	6	7	8	9
1		Clausen 4 *O*2-ac	063b-ó8888ó	6	50%	50%	-1.2099	-54.9	**-6.8**	**-6.6**	**-6.3**	**-6.1**	**-6.1**	-5.9	**-5.8**	**-5.7**	-5.6	45.4	**0.0**	**3.3**	**2.7**	**5.3**	**4.6**	30.8	**6.2**	5.3	29.2
2	1	Clausen 4	063-o8888o	6	67%	0%	-1.1306	-51.3	**-6.7**	**-6.2**	**-5.7**	**-5.6**	**-5.6**	**-5.4**	**-5.4**	-5.4	**-5.3**	45.4	**0.0**	**2.1**	**2.6**	**2.9**	**2.2**	**4.3**	**2.0**	27.4	**1.9**
3		Clausen 4 *O*3-ac	063c-ò8888ò	6	50%	50%	-1.0667	-48.4	**-5.7**	**-5.4**	-5.4	-5.4	**-5.3**	**-5.3**	-5.3	**-5.3**	-5.3	45.4	**0.0**	**2.2**	16.4	16.5	**4.5**	**4.5**	19.2	**3.2**	16.4
4	2	Clausen 3	047-oo888o	6	50%	0%	-1.0269	-53.8	**-6.7**	**-6.3**	**-6.2**	**-6.1**	**-5.9**	**-5.8**	**-5.7**	**-5.6**	-5.5	52.4	**0.0**	**6.1**	**4.9**	**4.2**	**5.0**	**7.0**	**1.8**	**4.6**	18.8
98		Clausen 3 *O*2-ac	047b-óó888ó	6	50%	50%	-0.3459	-62.8	-7.1	**-7.1**	**-7.1**	**-7.0**	**-7.0**	-7.0	-6.9	**-6.9**	-6.7	181.6	20.4	**0.0**	**16.9**	**17.1**	**9.8**	30.8	35.1	**17.1**	34.4
122		Clausen 3 *O*3-ac	047c-òò888ò	6	50%	50%	-0.2731	-61.0	**-7.0**	-6.9	**-6.9**	-6.8	-6.8	**-6.7**	-6.7	-6.6	-6.6	223.4	**0.0**	30.8	**18.3**	26.5	31.4	**19.2**	31.4	34.6	31.0

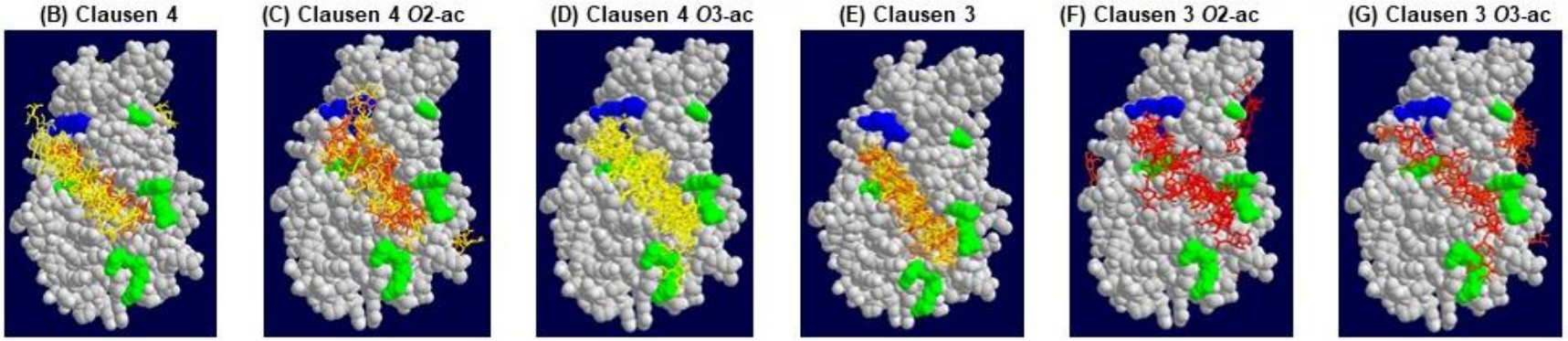

Figure 3.12: The acetylation of the best oligogalacturonate hit for PRX36 docking does not impair the docking prediction. (A) The two best hits obtained following random systematic screening of molecular docking of PRX36 on 124 OGAs (DP6-D2) covering all theoretical demethylesterification patterns correspond to two OGA of DP6 constituting the epitope of JIM7 (**Sup Table S3.3**). These two OGAs named Clasusen 3 and Clausen 4 (Francoz et al. 2019) were further acetylated *in silico* in their non methylated galacturonic acids either in *O*-2 or *O*-3 positions. The molecular docking performed on the whole PRX36 surface was compared between the non acetylated and acetylated OGAs using autodock vina showing the 9 best poses including their individual energy level (EL) and Root-mean-square deviation (RMSD) indicating the affinity of the interaction (the lower, the better) and the distance in Angstrom of the 9 poses for a given oligogalacturonate (the lower, the shorter), respectively. (i) Data mining was performed as detailled in **Sup Table S3.3** and methods and the oligogalacturonates were sorted according to SEL/SRMSD used to integrate the affinity and the distance (the lowest, the highest affinity and shorter distance). Red-to-yellow and blue-to-yellow heatmaps were drawn for EL and RMSD, respectively. The EL or RMSD values appearing in bold underlined frames correspond to poses fitting to the PRX36 valley previously demonstrated (Francoz et al 2019) to accomodate the hexagalacturonates Clausen 3, 4 and 5 (047-oo888o, 063-o8888o and 027-8o8o8o) that are recognized by JIM7 monoclonal antibody (Clausen et al 2003). **Note that the docking specificity of the best hit (Clausen 4) is not significantly modified between the non acetylated and the two acetylated versions whereas the docking of the second best hit (Clausen 3) is strongly impaired following acetylation. (B-G)** visualization of the docking models for the six combinations of hexagalacturonates. Key: RK, rank; DP, degree of polymerization; DM, degree of methylation; DA, degree of acetylation; OGA, oligogalacturonate; o, demethylesterified galacturonic acid, ó, O2-acetylated demethylesterified galacturonic acid,ò, O3-acetylated demethylesterified galacturonic acid, 8, methylated galacturonic acid.The red and blue amino acids in **(B-G)** correspond to polar positive and hydrophe amino acids from the OGA docking valley whose experimental mutation impaired PRX36 localization (Francoz et al 2019). The OGAs in **(B-G)** were color coded following the energy level heat map shown in **(A)**

We integrated the sum of energy levels and sum of RMSD for each OGA as a proxy of affinity and distances (**Sup Table S3.3**; see methods). The 124 OGAs could then be sorted in a rationale -though of course imperfect manner- for their ability to bind PRX36 valley. This strongly reinforced the previous docking experiments made with apriori with Clausen1-5 OGAs (Francoz et al., 2019b) since Clausen 4 and Clausen 3 ranked 1 and 2 **(Figure 3.12**; **Sup Table S3.3**). Finally, we tested the impact of the addition of 2-*O* or 3-*O* acetyl on the non methylated galacturonic acids of Clausen 3 and 4 (**Figure 3.12**). The addition of acetyl to the hit number 2 (Clausen 3) strongly impaired the docking capacity which did not fit with the observed results (no obvious modification of PRX36 anchoring and no mucilage release phenotype in *tbl38*). However, the addition of acetyl on the number 1 hit (Clausen 4) did not had a strong impact on the docking capacity (**Figure 3.12**). In turn, this is consistent with immunolocalization of αPRX36 and confocal imaging of PRX36-TagRFP in *tbl38* background (**Figure 3.4**) which did not show any obvious mislocalization of PRX36.

In light of our results, we conclude that TBL38 acts as an HG acetyltransferase in the CW microdomain harboring PRX36 with no deleterious effect observed in *tbl38* mutant contrary to *pmei6*. The uncommon acetylesterase activity could be related to the localization to the CW were acetyl-CoA is absent so we could hypothesize that TBL38 could have the opposite activity if artificially targeted in a different environment such as the Golgi considering the presence of all the canonical amino acids required for acetyl transferase activity. The increased acetylation observed in *tbl38* leads to decreased HG Ca^{2+} binding which might affect surface primary wall properties independently of PRX36. Rather, PRX36 docking could be unaffected or even improved as an indirect effect of *tbl38* mutation, thus facilitating mucilage release, as suggested by the even better docking score of Clausen 4 with 2-*O* acetylation of the two non methylated galacturonic acids. Additional work is needed to confirm such a subtle phenotype, notably transcriptomic analysis of relevant genes in *tbl38*, as well as defining the ultra-structural and mechanical properties of *tbl38* MSC cell wall microdomain. Beyond this case study, this may pave the way for further understanding of the role of fine tuning of complex cell wall polysaccharides.

Supplemental data

Sup Table S3.1: Phylogeny, subcellular-localization and activity of TBL multigenic family members in *A. thaliana*.

Phylogeny			Subcellular localization					Activity and function[g]	*In vitro* Assay			Reverse genetic			Miscellaneous	Reference
Name	Gene ID	Clade[a]	Arame-mnon Topo-logy[b]	WP DB[c]	Subcell Loc[d]	Fluo Tag[e]	Species[f]		Recom-binant Protein[h]	Substrate[i]	Product[j]	Biochemical Phenotype[k]	Develop-mental Phenotype[l]	Comple-mentation[m]		
TBR	At5g06700	A	TM?		CW	GFP	*A.th.*	Pectin-AT or protection of *O*-acetylated pectin from de-acetylation by pectin acetyl-esterases in the CW				Reduced secondary wall cellulose (cristalline) content; Increased PME activity; Reduced pectin acetylation; Increased pectin methyl-esterification	Absence of secondary wall in trichomes; Reduced etiolated hypocotyl elongation	Full, with 35S promoter and native promoter		Potikha and Delmer (1995) Plant J Bischoff et al (2010) Plant Physiol Sinclair et al (2017) Curr Biol
TBL01	At3g12060	A	TM?													
TBL02	At1g60790	A	TM?													
TBL04	At5g49340	A	SP?													
TBL05	At5g20590	A	TM?													
TBL06	At3g62390	A	TM?													
TBL07	At1g48880	A	TM?													
TBL08	At3g11570	A	TM?													

TBL09	At5g06230	A	TM?	etiolated hypo-cotyls												Feiz et al (2006) Plant Methods
TBL10	At3g06080	A	TM?				*A.th.*	Putative RGI-AT				Reduced acetylation of RGI in rosette leaves	enhanced drough tolerance	Two independant KO mutants		Stranne et al (2018) Plant J
TBL11	At5g19160	A	TM?													
TBL12	At5g64470	B	TM?													
TBL13	At2g14530	B	SP?													
TBL14	At5g64020	B	TM?													
TBL15	At2g37720	B	TM?	leaves												Duruflé et al (2019) Data Brief
TBL16	At5g20680	B	TM?													
TBL17/YLS7	At5g51640		TM?												yellow-leaf-specific gene	Yoshida et al (2001) Plant Cell Physiol
															Causal candidate gene underlying the QTL4 for root length in drougth GWAS	El-Soda et al (2015) Plant Cell Environ
TBL18	At4g25360	B	TM?													

TBL19/XyBAT1	At5g15900	B	TM?					xyloglucan (XG) backbone AT (XyBAT)	human HEK293F cells (secreted form)	Cello-hexaose	acetyl groups onto 6-*O* of Glc residues in cellohexaose (XG backbone)	Heterologous expression of a rice XG backbone AT (XyBAT) in Arabidopsis led to a severe reduction in cell expansion and plant growth and a drastic alteration in xyloglucan xylosylation pattern with the non classical acetylation of XG backbone: XGG, XGGG, XXGG, XXGG, XXGGG and XXGGG (G, non acetylated Glc; G acetylated Glc; X, xylosylated Glc)			TBL19,20,21 are orthologs from rice and tomato XyBAT acetylating XG backbone. TBL19 and 21 activity is intriguing since acetylation of XG backbone is reported only in grasses and solanaceae. It might exist in specialized cells. In planta, the XG backbone might be first acetylated and then xylosylated	Zhong et al (2020) Plant Cell Physiol
TBL20	At3g02440	B	TM?					no	human HEK293F cells (secreted form)	Cello-hexaose	no activity					Zhong et al (2020) Plant Cell Physiol
TBL21/XyBAT2	At5g15890	B	TM?					xyloglucan (XG) backbone AT (XyBAT)	human HEK293F cells (secreted form)	Cello-hexaose	acetyl groups onto 6-*O* of Glc residues in cellohexaose (XG backbone)					Zhong et al (2020) Plant Cell Physiol
TBL22/AXY4L/XGOAT2	At3g28150	B	TM?					xyloglucan (XG) side chain AT and weak esterase activity	human HEK293F cells (secreted form)	Fucosylated Gal of XG side chain	acetyl groups onto 6-*O* (3-*O*, 4-*O* and 4,6-di-*O*) of fucosylated Gal residues	Drastic reduction of acetylated XG in seeds				Gille et al (2011) Plant Cell Zhong et al (2018) Planta

											on XG side chains.					
TBL23/MOAT1	At4g11090	B	TM?					gluco-mannan AT	human HEK293F cells (secreted form)	Manno-hexaose	acetyl groups onto 2-*O* and 3-*O* of Man residues on Mannohexaose side chains.	Simultaneous RNAi inhibition of the expression of MOAT1, 2, 3 and 4 leads to a drastic reduction in glucomannan acetylation in Arabidopsis floral stem	None detected			Zhong et al (2018) Plant Cell Physiol
TBL24/MOAT2	At4g23790	B	TM?					gluco-mannan AT	human HEK293F cells (secreted form)	Manno-hexaose						Zhong et al (2018) Plant Cell Physiol
TBL25/MOAT3	At1g01430	B	TM?					gluco-mannan AT	human HEK293F cells (secreted form)	Manno-hexaose						Zhong et al (2018) Plant Cell Physiol
TBL26/MOAT4	At4g01080	B	TM?					gluco-mannan AT	human HEK293F cells (secreted form)	Manno-hexaose						Zhong et al (2018) Plant Cell Physiol
TBL27/AXY4/XGOAT1	At1g70230	B	TM?		Golgi	GFP	*N. bentha.*	xyloglucan (XG) side chain AT and weak esterase activity	human HEK293F cells (secreted form)	Fucosylated Gal of XG side chain	acetyl groups onto 6-*O* (3-*O*, 4-*O* and 4,6-di-*O*) of fucosylated Gal residues on XG side chains.	drastic reduction of acetylated XG in seedlings, roots, leaves			TBL27 acts down-stream of MYB103 to affect Al sensitivity through XG *O*-acety-lation	Gille et al (2011) Plant Cell Zhong et al (2018) Planta Zhu et al (2014) Plant Physiol Wu et al (2022) Plant J
TBL28/XOAT2	At2g40150	C	TM?		Golgi	m-Cherry	*N. bentha.*	xylan AT	human HEK293F cells (secreted form)	Xylan (Xyl6)	**Xyl-2Ac**; Xyl-3Ac;		No obvious secondary wall phenotype			Zhong et al (2017) Plant Cell Physiol

										Xyl-2,3Ac					
TBL29/XOAT1/ESK1	At3g55990	C	TM?		Golgi	YFP	N/A	xylan AT necessary for correct xylan substitution enabling correct interaction with cellulose microfibrils	human HEK293F cells (secreted form)	Xylan (Xyl6)	**Xyl-2Ac; Xyl-3Ac; Xyl-2,3Ac**	The recombinant protein activity is confirmed in *esk1* stems	collapsed vessels	Various patterns of complementation with *ESK1*, *TBL28* or *TBL30*	Crystal structure allowing molecular modeling of other TBLs	Lefebvre et al (2010) Plos One Xiong et al (2013) Mol Plant Yuan et al (2013) Plant Cell Physiol Zhong et al (2017) Plant Cell Physiol Grantham et al (2017) Nature Plants Lunin et al (2020) Plant Cell
TBL30/XOAT3	At2g40160	C	TM?		Golgi	m-Cherry	*N. bentha.*	xylan AT	human HEK293F cells (secreted form)	Xylan (Xyl6)	Xyl-2Ac; **Xyl-3Ac**					Zhong et al (2017) Plant Cell Physiol
TBL03/XOAT4	At5g01360	C	TM?		Golgi	YFP	*A.th.* proto.	xylan AT	human HEK293F cells (secreted form)	Xylan (Xyl6)	**Xyl-2Ac; Xyl-3Ac**; Xyl-2,3Ac	Decreased cellulose, Ara, Gal Rha, Fuc and uronic acid content; Increased PME activity	Reduced inflorescence stem elongation			Bischoff et al (2010) Plant Physiol Yuan et al (2016)

															Plant Cell Physiol Zhong et al (2017) Plant Cell Physiol
TBL31/XOAT5	At1g73140	C	TM?		Golgi	YFP	*A.th.* proto.	xylan AT	human HEK293F cells (secreted form)	Xylan (Xyl6)	Xyl-2Ac; **Xyl-3Ac**; Xyl-2,3Ac				Yuan et al (2016) Plant Cell Physiol Zhong et al (2017) Plant Cell Physiol
TBL32/XOAT6	At3g11030	C	TM?		Golgi	YFP	*A.th.* proto.	xylan AT	human HEK293F cells (secreted form)	Xylan (GlcA)Xyl4	**Xyl-3Ac-2GlcA**				Yuan et al (2016) Plos One Zhong et al (2017) Plant Cell Physiol
TBL33/XOAT7	At2g40320	C	TM?		Golgi	YFP	*A.th.* proto.	xylan AT	human HEK293F cells (secreted form)	Xylan (GlcA)Xyl4	**Xyl-3Ac-2GlcA**				Yuan et al (2016) Plos One Zhong et al (2017) Plant Cell Physiol
TBL34/XOAT8	At2g38320	C	TM?		Golgi	YFP	*A.th.* proto.	xylan AT	human HEK293F cells (secreted form)	Xylan (Xyl6)	**Xyl-2Ac; Xyl-3Ac**; Xyl-2,3Ac				Yuan et al (2016) Plant Sci Zhong et al (2017) Plant Cell Physiol
TBL35/XOAT9	At5g01620	C	TM?		Golgi	YFP	*A.th.* proto.	xylan AT	human HEK293F cells	Xylan (Xyl6)	**Xyl-2,3Ac**				Yuan et al (2016) Plant Sci

									(secreted form)							Zhong et al (2017) Plant Cell Physiol
TBL36	At3g54260	D	SP?													
TBL37	At2g34070	D	SP?		Golgi	GFP	*N. bentha.*	Hemicellulose-AT Stem and leaves				Reduced poly-saccharide (hemicellulose) acetylation	Dwarf, collapsed vessels, reduced secondary CW thickening in fibers, reduced mesophyll cell size	Full, pTBL37::TBL37	Directly activated by MYC2 Enhances herbivore resi-stance	Sun et al (2020) Plant Physiol
TBL38	At1g29050	D	SP?	leaves ; stems	CW	Tag RFP	*A. th.; N. bentha.*	Homo-galacturonan-AE Localized to a CW microdomain of seed mucilage secretory cells	*P. pastoris*	HG		Increase in *O*-acetylation of homogalacturonan; Loss of LM20 but not JIM7 epitopes		Partial, pPRX36::TBL38-TagRFP		Duruflé et al (2019) Data Brief ; This study
TBL39	At2g42570	D	SP?	roots												Nguyen-Kim et al (2016) Proteomics
TBL40	At2g31110	D	TM?	roots												Nguyen-Kim et al (2016) Proteomics
TBL41	At3g14850	D	SP?													
TBL42	At1g78710	D	SP?													

TBL43	At2g30900	D	SP?												
TBL44/PMR5	At5g58600	D	SP?		Endo-membranes?	GFP	*A.th.*	Homogalactu-ronan-AT	*E. coli*	Oligo-Galactu-ronides	Acetylated oligo-galacturonides	Altered pectin, decreased acetate and decreased cellulose contents	Increased pathogen resistance	Full, pTBL44::TBL44-GFP	Alteration of pathogen resi-stance	Chiniquy et al (2019) Plant J
TBL45	At2g30010	D	SP?	inflorescence		N/A	*A.th.*									Xu et al. (2016) Mol Cell Proteomics

[a] Phylogeny according to Bischoff et al (2010) Plant Physiol. The clade letters were added here for sake of clarity ; [b] Prediction of transmembrane anchoring (TM?) or signal peptide clivage (SP?) according to http://aramemnon.uni-koeln.de/ ; [c] Occurrence in cell wall proteomes (http://www.polebio.lrsv.ups-tlse.fr/WallProtDB/) ; [d] Experimentally assessed subcellular localization (CW, cell wall) ; [e] Fluorescent tag used for subcellular localization ; [f] Species in which the localization was performed (*A. th.*, *A. thaliana*; proto., protoplast; *N. bentha.*, *N. benthamiana*); [g] Summary of enzymatic activity and function (AT, acetyl transferase; AE, acetyl esterase) ; [h] Heterologous system used for recombinant protein production; [i] Polysaccharide oligomer used as a substrate for *in vitro* activity ; [j] *In vitro* product ; [k] Biochemical phenotype observed in KO mutant, RNAi lines or overexpressors ; [l] Developmental phenotype observed in KO mutant, RNAi lines or overexpressors; [m] Construct used for complementation assay. "Full" indicates a full complementation. N/A, non available.

Sup Table S3.2: Selection of *TBL38* in *PRX36*/*PMEI6* co-expression network for further functional genomics and biochemical studies. *PMEI6* is the first hit of the *PRX36* co-expression network using the tissue-specific seed developmental kinetics GSE12404 dataset (Belmonte et al., 2013). Mutants from both genes have similar mucilage phenotype (Kunieda et al (2013); Saez-Aguayo et al (2013) and a molecular link has been established to explain the similar phenotype: PMEI6 activity enables to produce a homogalacturonan specific methylesterification pattern necessary for PRX36 anchoring to the cell wall microdomain of mucilage secretory cells (Francoz et al 2019). The accurately positioned PRX36 further loosens the CW microdomain to enable correct mucilage release upon seed imbibition. In an effort to search new proteins involved in HG remodeling, TRICHOME BIREFRINGENCE-LIKE38 labeled in green has been selected for functional genomic study. Relative expression values are colored from yellow to red. Expression below the 45-cutoff were represented in grey and genes that never reach the cutoff were masked (*TBL23/MOAT1;TBL18; TBL21/XyBAT2; TBL17/YLS7; TBL07; TBL19/XyBAT1;TBL03/XOAT4;TBL20; TBL44/PMR5; TBL27/AXY4/XGOAT1; TBL34/XOAT8*). No information was available for: *TBL02; TBL04; TBL08; TBL09; TBL14; TBL24/MOAT2; TBL29/XOAT1/ESK1; TBL31/XOAT5; TBL33/XOAT7*. RK, rank ; PCC, Pearson Correlation Coefficient ; EP, embryo proper ; SUS, suspensor ; MCE, micropylar endosperm ; PEN, peripheral endosperm ; CZEN, chalazal endosperm ; CZSC, chalazal seed coat ; SC, seed coat ; WS, whole seed.

RK	PCC	ORF/AGI	pre-globular stage							globular stage								heart stage							linear-cotyledon stage							bending cotyledon stage						mature green stage					
			pg EP	pg MCE	pg PEN	pg CZEN	pg CZSC	pg SC	pg WS	g EP	g SUS	g MCEN	g PEN	g CZEN	g CZSC	g SC	g WS	h EP	h MCEN	h PEN	h CZEN	h CZSC	h SC	h WS	lc EP	lc MCEN	lc PEN	lc CZEN	lc CZSC	lc SC	lc WS	bc EP	bc PEN	bc CZEN	bc CZSC	bc SC	bc WS	mg EP	mg MCEN	mg PEN	mg CZEN	mg CZSC	mg SC
1	1	AtPrx36	15	27	4	11	8	8	2	4	2	13	2	12	8	2	4	3	3	3	15	14	3	9	4	5	9	12	405	1522	554	1	2	27	992	29	20	7	1	11	3	53	65
2	9,47E-01	PMEI6	2	15	7	8	2	1	6	2	1	2	1	2	2	6	6	2	8	8	4	10	6	13	10	54	54	1	52	423	236	6	34	14	232	65	52	29	11	19	25	37	93
13	8,16E-01	TBL38	9	11	25	34	2119	876	1094	10	5	61	26	2	2076	1003	1508	8	9	8	55	1064	1790	1012	16	47	7	17	1274	5537	2991	44	1	1	2731	894	312	1262	10	31	9	582	135
5198	1,00E-01	TBL40	5	32	5	25	104	3	70	1	2	13	3	1	64	11	27	3	6	2	17	166	9	15	1	7	1	1	95	2	10	1	1	3	67	4	1	6	10	10	1	57	9
6959	4,98E-02	TBL06	46	12	8	50	88	237	243	69	20	84	8	2	54	184	98	52	38	27	3	56	232	81	124	37	23	1	35	129	70	94	38	4	26	77	56	101	78	37	42	10	61
6994	4,90E-02	TBL45	197	49	22	25	41	203	171	107	437	19	14	8	21	271	260	100	36	14	14	28	663	272	74	262	1	41	51	224	114	25	20	103	30	88	53	19	12	5	61	60	291
7753	3,06E-02	TBL10	96	113	103	50	169	123	70	79	344	490	159	28	276	162	90	108	294	252	27	286	159	186	50	44	610	23	383	82	132	39	199	111	204	47	69	19	13	26	80	152	40
7844	2,85E-02	TBL30/XOAT3	13	14	13	30	26	61	50	10	11	48	11	9	10	95	38	12	17	21	2	18	119	47	10	9	11	12	19	44	30	9	11	43	16	25	21	22	15	6	13	17	239
9223	-2,56E-03	TBL13	48	16	36	13	31	51	55	51	35	7	20	4	49	46	68	72	46	65	12	48	42	68	105	55	72	3	23	53	51	61	47	40	42	55	55	45	68	58	51	40	64
10258	-2,24E-02	TBL12	53	65	91	45	49	50	48	43	57	154	58	53	36	42	51	41	60	79	104	34	45	106	69	58	57	148	56	77	46	75	91	46	40	49	84	49	17	44	32	48	48
12225	-5,41E-02	TBL28/XOAT2	15	21	9	9	15	10	16	1	1	4	16	15	5	9	9	26	11	1	20	6	11	21	32	85	5	4	13	25	61	42	31	9	6	9	37	195	203	145	78	2	15
12396	-5,65E-02	TBL22/AXY4L/XGOAT2	10	2	9	28	77	58	42	6	120	51	17	13	25	39	24	88	911	160	17	35	39	162	22	693	697	93	33	151	142	74	430	269	93	24	168	480	90	140	590	53	61
13137	-6,62E-02	TBL35/XOAT9	156	8	40	9	67	108	86	99	142	27	22	3	25	48	70	85	23	13	27	60	127	47	84	22	13	188	26	48	56	52	26	232	51	22	38	18	45	75	78	31	44
13339	-6,87E-02	TBL43	8	25	28	2625	56	10	54	4	2	15	36	2277	68	21	70	4	4	7	270	5	1	3	2	2	3	2	5	17	7	2	2	17	3	17	10	2	7	3	6	3	5
13378	-6,91E-02	TBL15	599	10218	162	204	14	8	391	95	1403	5370	7	598	12	20	238	2	33	8	82	13	5	6	3	9	4	2	4	1	7	1	8	2	1	2	4	5	5	9	2	4	13
14329	-8,00E-02	TBL42	480	7881	1079	856	2	32	252	55	850	3336	679	643	5	13	107	0	22	33	217	9	7	18	2	11	2	7	3	5	2	4	1	12	6	10	5	2	6	4	2	2	14
14985	-8,76E-02	TBR	81	10	45	11	162	160	205	80	23	27	38	17	159	155	105	105	146	77	33	126	192	129	133	238	72	25	131	98	105	114	172	32	71	147	105	162	479	294	232	86	111
15156	-8,97E-02	TBL39	105	20	14	23	81	75	26	258	16	21	16	24	42	47	45	123	51	42	29	87	18	36	90	34	11	2	64	6	62	114	14	41	50	17	93	51	14	16	19	22	2
15766	-9,78E-02	TBL41	2225	19267	1673	10135	183	164	1631	72	2266	7572	69	8757	423	16	476	9	30	5	2234	83	22	53	5	16	16	19	75	36	17	9	10	126	119	5	11	13	9	2	22	85	14
16074	-1,02E-01	TBL36	4	4	1	5	13	2	12	56	5	3	2	4	15	14	2	105	4	2	3	1	1	30	114	50	6	2	1	4	46	73	6	1	2	2	53	164	379	3	7	1	7
16513	-1,08E-01	TBL01	65	11	18	34	32	29	30	68	91	7	4	23	37	19	11	109	48	25	19	31	19	33	185	48	24	4	35	18	57	162	11	13	23	9	64	140	9	17	22	16	21
17654	-1,24E-01	TBL37	13	19	6	14	10	160	71	76	6	9	10	10	16	110	98	31	13	9	20	28	98	42	25	3	3	16	14	11	40	41	6	8	9	15	24	102	1	8	5	13	12
17817	-1,27E-01	TBL25/MOAT3	9	49	19	23	42	453	227	23	3	25	7	19	23	246	193	12	15	24	8	29	177	45	69	72	143	5	12	43	53	92	181	22	24	43	122	87	59	76	56	2	11
18136	-1,32E-01	TBL32/XOAT6	656	790	533	178	658	1020	675	927	979	1326	1002	538	1043	1719	344	786	1432	1023	164	599	667	749	732	649	1571	879	825	731	452	566	1059	732	590	1182	381	937	763	657	1284	433	1008
21035	-1,91E-01	TBL16	42	221	16	24	1	36	25	43	40	104	28	68	15	42	16	43	22	43	2	5	10	10	40	66	38	11	15	10	31	62	46	62	9	21	34	58	37	65	64	34	29

Sup. Table S3.3: Random systematic screening of molecular docking of PRX36 on 124 oligogalacturonates (DP6-D2) covering all theoretical demethylesterification patterns highlights the specific interaction of PRX36 with the two hexagalacturonates constituting the epitope of JIM7. For each oligogalacturonate, the molecular docking performed on the whole PRX36 surface using autodock vina enabled retrieving the 9 best poses including their individual energy level (EL) and Root-mean-square deviation (RMSD) indicating the affinity of the interaction (the lower, the better) and the distance in Angstrom of the 9 poses for a given oligogalacturonate (the lower, the shorter), respectively. (i) Data mining was performed by calculating the sum of the EL (ΣEL) reflecting the global affinity of each oligogalacturonate for PRX36 and the sum of RMSD (ΣRMSD) reflecting the dispersion vs concentration of the 9 poses on the protein surface.(ii) Then, the oligogalacturonates were sorted according to ΣEL/ΣRMSD used to integrate both parameters (the lowest, the highest affinity and shorter distance). Red-to-yellow and blue-to-yellow heatmaps were drawn for EL and RMSD, respectively. The EL or RMSD values appearing in bold underlined frames correspond to poses fitting to the PRX36 valley previously demonstrated (Francoz et al., 2019) to accommodate the hexagalacturonates clausen 3, 4 and 5 (047-oo888o, 063-o8888o and 027-8o8o8o) that are recognized by JIM7 monoclonal antibody (Clausen et al., 2003). o, demethylesterified galacturonic acid, 8, methylated galacturonic acid. Note that the docking specificity is neither related to the degree of polymerization (DP) nor to the degree of methylation (DM), but rather relies on a peculiar demethylesterification bar code.

Rank	Clausen et al 2013	Oligo-galacturonates (code and structure)	DP	DM	Σ EL / Σ RMSD	Σ EL	EL = Energy level (kcal/mol) 9 poses of docking vs all surface of PRX36									Σ RMSD	RMSD (Root-mean-square deviation) 9 poses of docking vs all surface of PRX36								
							1	2	3	4	5	6	7	8	9		1	2	3	4	5	6	7	8	9
1	Clausen 4	063-o8888o	6	67%	-1.1306	-51.3	-6.7	-6.2	-5.7	-5.6	-5.6	-5.4	-5.4	-5.4	-5.3	45.374	0.00	2.13	2.62	2.85	2.25	4.26	1.98	27.36	1.94
2	Clausen 3	047-oo888o	6	50%	-1.0269	-53.8	-6.7	-6.3	-6.2	-6.1	-5.9	-5.8	-5.7	-5.6	-5.5	52.390	0.00	6.05	4.88	4.20	5.03	7.04	1.75	4.60	18.84
3		038-ooo8o8	6	33%	-0.8588	-54.4	-6.2	-6.1	-6.1	-6.1	-6.0	-6.0	-6.0	-6.0	-5.9	63.341	0.00	3.74	5.06	3.26	1.76	20.64	4.23	4.99	19.66
4		040-ooo888	6	50%	-0.8098	-51.7	-6.0	-5.9	-5.8	-5.7	-5.7	-5.7	-5.7	-5.6	-5.6	63.839	0.00	6.51	2.99	20.97	2.35	2.93	20.10	1.57	6.42
5		041-oo8ooo	6	17%	-0.8022	-54.9	-6.8	-6.4	-6.2	-6.0	-6.0	-5.9	-5.9	-5.9	-5.8	68.434	0.00	19.41	3.13	20.53	9.12	4.92	1.76	7.48	2.10
6		024-8oo888	6	50%	-0.7954	-50.6	-5.7	-5.7	-5.7	-5.7	-5.6	-5.6	-5.6	-5.5	-5.5	63.615	0.00	21.83	4.18	2.49	15.39	3.41	2.66	2.22	11.44
7		106-ooo8	4	25%	-0.7944	-49.7	-5.9	-5.7	-5.7	-5.5	-5.5	-5.4	-5.4	-5.3	-5.3	62.56	0.00	4.09	6.78	2.83	1.99	2.66	16.15	23.98	4.09
8		069-88ooo	5	40%	-0.7804	-62.4	-7.2	-7.1	-7.1	-7.1	-7.0	-6.8	-6.7	-6.7	-6.7	79.96	0.00	19.49	9.15	18.24	5.91	18.59	2.26	3.83	2.49
9		008-888o88	6	83%	-0.7742	-58.3	-6.7	-6.7	-6.6	-6.5	-6.4	-6.4	-6.4	-6.3	-6.3	75.30	0.00	0.51	1.61	12.10	17.42	8.63	8.07	10.57	16.40
10		065-88888	5	100%	-0.7498	-51.5	-5.9	-5.8	-5.8	-5.7	-5.7	-5.7	-5.7	-5.6	-5.6	68.68	0.00	2.13	5.57	2.41	1.94	15.26	11.17	16.66	13.56
11		107-oo8o	4	25%	-0.7421	-49.8	-5.7	-5.6	-5.6	-5.6	-5.5	-5.5	-5.5	-5.4	-5.4	67.11	0.00	17.69	7.42	7.22	2.83	3.67	17.19	7.77	3.33
12		101-8ooo	4	25%	-0.7365	-51.2	-6.4	-5.9	-5.8	-5.7	-5.5	-5.5	-5.5	-5.5	-5.4	69.52	0.00	15.52	15.52	3.18	2.36	15.06	2.17	1.73	13.98
13		099-88oo	4	50%	-0.6895	-52.9	-6.5	-6.3	-5.9	-5.8	-5.8	-5.7	-5.7	-5.7	-5.5	76.73	0.00	3.02	3.84	14.30	15.55	4.10	15.57	15.61	4.74
14		096-o8888	5	80%	-0.6427	-52.0	-6.1	-5.9	-5.8	-5.7	-5.7	-5.7	-5.7	-5.7	-5.7	80.91	0.00	3.48	4.72	14.74	16.89	4.48	15.79	4.00	16.81
15		023-8oo88o	6	50%	-0.5895	-54.6	-7.0	-6.3	-6.1	-5.9	-5.9	-5.9	-5.9	-5.8	-5.8	92.63	0.00	8.55	9.69	8.92	2.04	21.14	18.82	7.62	15.86
16	Clausen 5	027-8o8o8o	6	50%	-0.5806	-50.9	-6.3	-6.1	-5.8	-5.8	-5.7	-5.4	-5.3	-5.3	-5.2	87.67	0.00	2.58	2.41	3.03	2.97	4.85	25.48	14.61	31.75
17		028-8o8o88	6	67%	-0.5750	-54.5	-6.7	-6.4	-6.1	-6.0	-5.9	-5.9	-5.9	-5.8	-5.8	94.78	0.00	1.72	3.46	1.86	11.11	12.55	22.19	20.89	20.99
18		009-88oooo	6	33%	-0.5662	-54.2	-6.4	-6.4	-6.2	-6.0	-5.9	-5.9	-5.8	-5.8	-5.8	95.72	0.00	21.24	3.50	21.34	11.17	21.66	3.27	8.83	4.71

19		012-88oo88	6	33%	-0.5633	-48.4	-5.6	-5.6	-5.4	-5.4	-5.4	-5.4	-5.3	-5.2	-5.1	85.93	0.00	7.63	26.74	1.81	1.83	1.86	11.13	27.92	7.02
20		059-o88o8o	6	50%	-0.5596	-54.4	-6.5	-6.2	-6.2	-6.1	-6.1	-5.9	-5.8	-5.8	-5.8	97.21	0.00	3.11	5.21	20.24	20.24	21.47	22.00	1.77	3.18
21		108-oo88	4	50%	-0.5584	-51.8	-6.7	-5.8	-5.7	-5.7	-5.7	-5.6	-5.6	-5.6	-5.4	92.76	0.00	4.90	5.54	17.32	5.07	17.01	12.68	17.56	12.67
22		060-o88o88	6	67%	-0.5569	-51.5	-5.9	-5.8	-5.8	-5.7	-5.7	-5.7	-5.7	-5.6	-5.6	92.48	0.00	6.52	3.61	26.08	2.06	3.48	18.50	25.88	6.35
23		112-o888	4	75%	-0.5485	-51.5	-6.5	-5.8	-5.8	-5.8	-5.7	-5.5	-5.5	-5.5	-5.4	93.90	0.00	16.72	3.27	14.42	1.58	3.23	24.93	14.47	15.28
24		097-8888	4	100%	-0.5415	-51.7	-6.5	-5.8	-5.8	-5.8	-5.7	-5.6	-5.5	-5.5	-5.5	95.47	0.00	3.44	1.66	1.66	15.42	15.75	15.30	14.67	27.58
25		064-o88888	6	83%	-0.5366	-52.9	-6.6	-6.2	-5.9	-5.8	-5.7	-5.7	-5.7	-5.7	-5.6	98.58	0.00	3.09	2.34	3.46	20.90	21.42	5.16	20.56	21.65
26		031-8o888o	6	67%	-0.5304	-54.6	-6.8	-6.2	-6.1	-6.0	-6.0	-5.9	-5.9	-5.9	-5.8	102.94	0.00	21.38	13.80	6.25	21.46	12.06	1.77	19.83	6.40
27		015-88o88o	6	67%	-0.5291	-53.6	-6.8	-6.0	-5.9	-5.9	-5.9	-5.9	-5.8	-5.7	-5.7	101.30	0.00	1.24	5.77	5.08	20.34	19.86	21.25	13.46	14.30
28		089-o8ooo	5	20%	-0.5258	-48.7	-5.9	-5.6	-5.5	-5.4	-5.3	-5.3	-5.3	-5.2	-5.2	92.63	0.00	25.06	4.10	11.43	1.37	10.61	25.04	9.99	5.02
29		037-ooo8oo	6	17%	-0.5218	-55.6	-7.0	-6.5	-6.2	-6.2	-6.1	-6.0	-5.9	-5.9	-5.8	106.55	0.00	1.61	2.90	21.13	13.80	4.44	21.03	20.45	21.20
30		093-o88oo	5	40%	-0.5175	-50.5	-5.8	-5.7	-5.7	-5.7	-5.6	-5.5	-5.5	-5.5	-5.5	97.59	0.00	11.20	6.85	10.54	1.38	6.32	11.08	25.14	25.08
31		075-8oo8o	5	40%	-0.5172	-53.9	-6.4	-6.3	-6.1	-6.0	-6.0	-5.9	-5.8	-5.7	-5.7	104.21	0.00	5.06	6.26	3.79	20.87	5.07	20.24	30.76	12.15
32		029-8o88oo	6	50%	-0.5124	-54.8	-7.0	-6.2	-6.1	-6.0	-6.0	-5.9	-5.9	-5.9	-5.8	106.96	0.00	1.59	2.07	11.61	21.19	25.43	2.35	21.00	21.72
33		051-o8oo8o	6	33%	-0.5093	-56.4	-6.7	-6.5	-6.5	-6.3	-6.2	-6.2	-6.0	-6.0	-6.0	110.73	0.00	8.64	8.21	6.03	1.66	31.52	21.20	12.54	20.93
34		007-888o8o	6	67%	-0.5085	-53.8	-6.6	-6.3	-6.0	-5.9	-5.9	-5.8	-5.8	-5.8	-5.7	105.80	0.00	1.80	1.74	5.49	20.29	11.85	21.14	21.33	22.17
35		049-o8oooo	6	17%	-0.5047	-57.8	-6.8	-6.8	-6.6	-6.5	-6.3	-6.3	-6.2	-6.2	-6.1	114.52	0.00	11.27	11.06	1.71	12.66	25.87	24.95	2.75	24.25
36		061-o888oo	6	50%	-0.4987	-53.6	-6.6	-6.3	-5.9	-5.9	-5.9	-5.8	-5.8	-5.7	-5.7	107.47	0.00	3.11	21.94	14.05	22.31	4.30	20.18	8.91	12.67
37		044-oo8o88	6	50%	-0.4965	-54.7	-6.8	-6.6	-6.0	-5.9	-5.9	-5.9	-5.9	-5.9	-5.8	110.16	0.00	1.65	5.47	11.60	20.45	34.00	20.99	14.14	1.87
38		050-o8ooo8	6	33%	-0.4929	-52.8	-6.1	-6.0	-6.0	-5.9	-5.8	-5.8	-5.8	-5.7	-5.7	107.13	0.00	25.36	24.45	14.90	2.05	14.84	1.64	6.71	17.18
39		052-o8oo88	6	50%	-0.4861	-52.5	-6.1	-5.9	-5.9	-5.8	-5.8	-5.8	-5.8	-5.7	-5.7	108.01	0.00	21.22	5.15	4.51	5.62	30.04	29.19	6.67	5.60
40		016-88o888	6	83%	-0.4778	-51.5	-6.7	-5.8	-5.7	-5.6	-5.6	-5.6	-5.6	-5.5	-5.4	107.78	0.00	6.19	3.55	21.40	22.74	11.81	4.08	29.24	8.77
41		039-ooo88o	6	33%	-0.4730	-56.2	-6.4	-6.3	-6.3	-6.3	-6.2	-6.2	-6.2	-6.2	-6.1	118.81	0.00	24.80	6.47	20.28	11.98	24.25	1.57	24.03	5.42
42		062-o888o8	6	67%	-0.4719	-54.1	-6.5	-6.1	-6.1	-6.0	-5.9	-5.9	-5.9	-5.9	-5.8	114.64	0.00	6.58	5.79	2.73	21.78	5.24	21.36	29.20	21.96
43		013-88o8oo	6	50%	-0.4711	-53.9	-6.7	-6.0	-6.0	-5.9	-5.9	-5.9	-5.9	-5.8	-5.8	114.40	0.00	20.85	20.88	6.11	32.21	21.21	4.58	3.02	5.56
44		105-oooo	4	0%	-0.4702	-53.8	-6.6	-6.1	-6.0	-6.0	-5.9	-5.9	-5.8	-5.8	-5.7	114.43	0.00	14.38	15.32	4.12	15.29	15.40	20.67	14.92	14.34
45		036-oooo88	6	33%	-0.4697	-53.2	-6.1	-6.0	-6.0	-5.9	-5.9	-5.9	-5.8	-5.8	-5.8	113.27	0.00	22.32	12.31	17.06	23.59	13.26	12.23	7.27	5.24
46		003-8888oo	6	67%	-0.4682	-54.7	-6.8	-6.3	-6.2	-6.0	-6.0	-5.9	-5.9	-5.8	-5.8	116.83	0.00	3.23	1.69	21.00	19.27	5.32	14.67	20.44	31.21

47		048-oo8888	6	67%	-0.4663	-56.3	-6.8	-6.7	-6.2	-6.2	-6.2	-6.1	-6.1	-6.0	-6.0	120.74	0.00	1.69	20.64	21.06	1.20	20.97	21.75	20.26	13.17
48		114-88o	3	67%	-0.4578	-48.3	-5.9	-5.7	-5.4	-5.3	-5.3	-5.3	-5.2	-5.1	-5.1	105.50	0.00	26.87	10.33	3.09	1.40	32.61	3.48	25.98	1.74
49		068-888o8	5	80%	-0.4552	-49.4	-5.6	-5.6	-5.5	-5.5	-5.5	-5.5	-5.4	-5.4	-5.4	108.52	0.00	11.32	11.34	1.95	25.09	25.10	30.14	1.41	2.18
50		082-oooo8	5	20%	-0.4543	-49.2	-5.7	-5.7	-5.6	-5.5	-5.4	-5.4	-5.3	-5.3	-5.3	108.31	0.00	1.02	2.52	24.77	10.83	1.63	10.48	32.34	24.72
51		033-oooooo	6	0%	-0.4509	-60.3	-7.0	-6.9	-6.8	-6.8	-6.8	-6.6	-6.5	-6.5	-6.4	133.74	0.00	2.89	21.53	32.23	12.16	14.92	22.69	5.14	22.19
52		006-888oo8	6	67%	-0.4508	-51.7	-6.1	-5.9	-5.8	-5.7	-5.7	-5.7	-5.6	-5.6	-5.6	114.67	0.00	11.77	23.48	2.99	26.64	28.46	1.71	2.03	17.59
53		081-ooooo	5	0%	-0.4435	-55.1	-6.3	-6.2	-6.2	-6.2	-6.2	-6.0	-6.0	-6.0	-6.0	124.25	0.00	13.79	1.34	5.11	1.78	25.34	25.63	25.91	25.35
54		021-8oo8oo	6	33%	-0.4388	-55.3	-6.9	-6.3	-6.2	-6.1	-6.0	-6.0	-6.0	-5.9	-5.9	126.02	0.00	6.23	20.93	3.69	6.08	31.83	20.92	5.66	30.70
55		014-88o8o8	6	67%	-0.4382	-54.1	-6.8	-6.3	-6.1	-6.0	-6.0	-5.8	-5.8	-5.7	-5.6	123.46	0.00	7.60	21.70	4.04	21.49	11.62	12.12	22.06	22.83
56		076-8oo88	5	60%	-0.4360	-48.7	-5.9	-5.6	-5.5	-5.4	-5.3	-5.3	-5.3	-5.2	-5.2	111.70	0.00	5.89	7.04	25.20	25.16	1.44	10.62	30.88	5.47
57		070-88oo8	5	60%	-0.4342	-49.5	-5.7	-5.6	-5.5	-5.5	-5.5	-5.5	-5.4	-5.4	-5.4	113.99	0.00	10.88	3.95	30.97	2.76	24.26	10.90	5.79	24.50
58		042-oo8oo8	6	33%	-0.4325	-55.9	-6.8	-6.4	-6.2	-6.1	-6.1	-6.1	-6.1	-6.1	-6.0	129.23	0.00	11.75	19.87	21.03	21.17	1.84	12.87	20.40	20.30
59		055-o8o88o	6	50%	-0.4253	-54.9	-6.6	-6.2	-6.1	-6.0	-6.0	-6.0	-6.0	-6.0	-6.0	129.07	0.00	5.90	11.80	3.64	20.30	22.22	21.43	22.04	21.74
60		085-oo8oo	5	20%	-0.4246	-51.8	-5.9	-5.8	-5.8	-5.8	-5.8	-5.7	-5.7	-5.7	-5.6	122.01	0.00	26.40	26.24	15.79	3.65	16.06	26.73	1.55	5.60
61		054-o8o8o8	6	50%	-0.4214	-54.3	-6.5	-6.1	-6.0	-6.0	-6.0	-6.0	-5.9	-5.9	-5.9	128.85	0.00	2.97	8.87	21.78	22.44	23.17	24.11	21.32	4.21
62		011-88oo8o	6	50%	-0.4206	-55.4	-6.5	-6.3	-6.3	-6.2	-6.1	-6.0	-6.0	-6.0	-6.0	131.70	0.00	31.56	21.44	21.48	21.19	4.10	20.26	8.48	3.21
63		002-88888o	6	67%	-0.4200	-52.7	-6.7	-6.1	-5.9	-5.9	-5.8	-5.7	-5.6	-5.5	-5.5	125.49	0.00	3.04	19.07	3.00	8.36	20.12	31.68	19.94	20.28
64		034-oooo8	6	17%	-0.4197	-51.3	-5.8	-5.8	-5.8	-5.7	-5.7	-5.7	-5.6	-5.6	-5.6	122.24	0.00	27.17	16.78	28.87	13.51	2.34	2.72	28.67	2.19
65		078-8o8o8	5	60%	-0.4165	-51.9	-5.9	-5.9	-5.9	-5.8	-5.8	-5.7	-5.7	-5.6	-5.6	124.61	0.00	15.10	9.12	22.44	1.61	28.94	1.73	23.24	22.42
66		030-8o88o8	6	67%	-0.4139	-50.9	-5.9	-5.9	-5.7	-5.6	-5.6	-5.6	-5.6	-5.5	-5.5	122.97	0.00	11.16	26.63	10.87	1.77	12.01	28.25	4.07	28.21
67		102-8oo8	4	50%	-0.4091	-48.5	-5.8	-5.6	-5.4	-5.4	-5.4	-5.3	-5.3	-5.2	-5.1	118.55	0.00	14.92	1.82	24.67	32.21	32.31	1.69	5.23	5.71
68		109-o8oo	4	25%	-0.4085	-51.5	-6.5	-6.0	-5.9	-5.8	-5.7	-5.6	-5.4	-5.3	-5.3	126.07	0.00	1.45	3.12	20.13	14.24	28.62	26.38	14.29	17.86
69		045-oo88oo	6	33%	-0.4052	-55.0	-6.9	-6.2	-6.1	-6.0	-6.0	-6.0	-6.0	-5.9	-5.9	135.72	0.00	1.57	22.21	11.35	14.20	20.52	23.00	21.02	21.85
70		115-8oo	3	33%	-0.4046	-51.5	-6.4	-6.3	-5.9	-5.7	-5.5	-5.5	-5.5	-5.4	-5.3	127.29	0.00	1.33	13.92	3.57	25.05	11.75	23.03	23.18	25.46
71		019-8ooo8o	6	33%	-0.4046	-55.9	-7.0	-6.3	-6.2	-6.1	-6.1	-6.1	-6.1	-6.0	-6.0	138.18	0.00	3.29	30.95	21.66	2.05	31.59	20.85	21.87	5.92
72		090-o8oo8	5	40%	-0.4041	-49.8	-5.9	-5.8	-5.8	-5.5	-5.5	-5.4	-5.3	-5.3	-5.3	123.25	0.00	30.52	25.25	24.96	8.85	8.45	9.62	8.08	7.51
73		025-8o8ooo	6	33%	-0.4014	-54.1	-6.8	-6.4	-6.0	-5.9	-5.9	-5.9	-5.8	-5.7	-5.7	134.78	0.00	3.29	31.55	22.53	5.47	23.32	20.54	21.13	6.95
74		092-o8o88	5	60%	-0.4012	-49.7	-5.7	-5.6	-5.6	-5.6	-5.5	-5.5	-5.4	-5.4	-5.4	123.87	0.00	3.99	14.85	14.56	5.42	24.33	31.36	5.32	24.06

75		057-o88ooo	6	33%	-0.4010	-51.8	-6.0	-5.9	-5.9	-5.8	-5.8	-5.6	-5.6	-5.6	-5.6	129.18	0.00	24.35	24.43	24.07	24.29	12.22	5.06	1.85	12.92
76		005-888ooo	6	50%	-0.3864	-52.2	-6.3	-6.1	-5.9	-5.8	-5.7	-5.6	-5.6	-5.6	-5.6	135.08	0.00	21.63	21.60	3.07	11.25	18.52	31.32	12.51	15.19
77		058-o88oo8	6	50%	-0.3817	-56.0	-6.4	-6.4	-6.3	-6.2	-6.2	-6.2	-6.2	-6.1	-6.0	146.73	0.00	27.21	25.33	4.39	13.96	25.32	2.02	23.18	25.32
78		095-o888o	5	60%	-0.3807	-50.2	-5.8	-5.8	-5.6	-5.6	-5.6	-5.5	-5.5	-5.4	-5.4	131.85	0.00	7.69	7.38	11.98	20.97	23.48	21.65	35.96	2.74
79		080 - 8o888	5	80%	-0.3778	-52.2	-6.1	-6.0	-5.9	-5.8	-5.8	-5.7	-5.7	-5.6	-5.6	138.15	0.00	25.61	24.34	5.49	1.77	24.05	15.16	25.50	16.23
80		017-8ooooo	6	17%	-0.3754	-53.3	-6.2	-6.1	-6.1	-6.0	-5.9	-5.8	-5.8	-5.7	-5.7	141.97	0.00	8.51	14.95	23.72	15.89	22.56	23.70	10.37	22.28
81		022-8oo8o8	6	50%	-0.3721	-52.5	-6.8	-6.0	-5.8	-5.7	-5.7	-5.7	-5.6	-5.6	-5.6	141.09	0.00	5.24	20.48	18.84	19.52	20.56	3.41	21.11	31.95
82		066-8888o	5	80%	-0.3718	-53.6	-6.3	-6.0	-6.0	-6.0	-6.0	-5.9	-5.8	-5.8	-5.8	144.16	0.00	5.01	22.36	23.77	21.07	18.42	23.64	23.95	5.93
83		111-o88o	4	50%	-0.3692	-48.9	-5.8	-5.6	-5.5	-5.5	-5.4	-5.3	-5.3	-5.3	-5.2	132.45	0.00	14.72	14.75	34.39	9.55	15.27	22.02	2.76	18.99
84		087-oo88o	5	40%	-0.3655	-50.0	-5.7	-5.7	-5.6	-5.5	-5.5	-5.5	-5.5	-5.5	-5.5	136.81	0.00	7.39	15.02	25.59	5.45	15.36	27.59	12.90	27.53
85		083-ooo8o	5	20%	-0.3644	-52.2	-6.0	-5.9	-5.9	-5.8	-5.8	-5.8	-5.7	-5.7	-5.6	143.25	0.00	25.41	1.79	20.69	12.40	17.52	15.80	16.63	33.01
86		074-8ooo8	5	40%	-0.3610	-48.9	-5.7	-5.6	-5.6	-5.5	-5.5	-5.4	-5.4	-5.1	-5.1	135.46	0.00	1.80	15.11	2.70	2.12	26.52	34.85	26.67	25.71
87		067-888oo	5	60%	-0.3607	-54.7	-6.4	-6.3	-6.2	-6.1	-6.0	-6.0	-5.9	-5.9	-5.9	151.66	0.00	22.89	30.59	24.53	15.13	14.97	31.48	1.25	10.83
88		056-o8o888	6	67%	-0.3572	-53.8	-6.1	-6.1	-6.0	-6.0	-6.0	-6.0	-5.9	-5.9	-5.8	150.60	0.00	25.16	14.54	26.90	1.63	26.46	24.08	6.06	25.77
89		046-oo88o8	6	50%	-0.3544	-54.7	-6.8	-6.3	-6.1	-6.0	-5.9	-5.9	-5.9	-5.9	-5.9	154.35	0.00	21.38	21.13	6.75	20.38	19.81	21.72	21.08	22.11
90		020-8ooo88	6	50%	-0.3528	-53.6	-6.4	-6.1	-6.0	-6.0	-5.9	-5.8	-5.8	-5.8	-5.8	151.91	0.00	1.75	1.16	24.26	25.76	24.26	24.72	24.85	25.16
91	Clausen 2	010-88ooo8	6	50%	-0.3528	-49.4	-6.1	-5.8	-5.7	-5.6	-5.3	-5.3	-5.3	-5.2	-5.1	140.03	0.00	32.68	23.11	2.37	32.30	14.93	10.36	5.33	18.96
92		043-oo8o8o	6	33%	-0.3515	-54.8	-6.2	-6.2	-6.2	-6.1	-6.1	-6.1	-6.0	-6.0	-5.9	155.91	0.00	23.81	27.20	27.36	23.24	25.20	1.94	3.69	23.50
93		032-8o8888	6	83%	-0.3506	-52.5	-6.7	-5.8	-5.8	-5.7	-5.7	-5.7	-5.7	-5.7	-5.7	149.75	0.00	6.12	21.21	31.92	3.27	21.31	5.23	30.80	29.91
94		072-88o88	5	80%	-0.3484	-48.6	-5.9	-5.8	-5.5	-5.3	-5.3	-5.3	-5.2	-5.2	-5.1	139.51	0.00	11.11	5.18	11.60	10.17	21.59	32.54	24.50	22.84
95		122-8o	2	50%	-0.3461	-48.8	-6.1	-5.8	-5.5	-5.4	-5.3	-5.3	-5.2	-5.1	-5.1	140.99	0.00	2.90	2.91	14.85	30.71	16.53	16.98	31.32	24.80
96		103-8o8o	4	50%	-0.3442	-51.9	-6.4	-6.0	-5.8	-5.8	-5.7	-5.6	-5.6	-5.5	-5.5	150.78	0.00	25.54	10.03	24.51	3.33	25.49	11.47	17.79	32.64
97		124-o8	2	50%	-0.3438	-50.4	-6.2	-6.1	-5.8	-5.6	-5.4	-5.4	-5.3	-5.3	-5.3	146.60	0.00	47.24	12.82	12.54	24.50	1.33	13.16	23.84	11.17
98		113-888	3	100%	-0.3401	-45.4	-5.6	-5.2	-5.1	-5.0	-5.0	-5.0	-5.0	-4.8	-4.7	133.47	0.00	3.17	3.08	3.41	29.64	30.83	29.94	3.38	30.03
99		035-oooo8o	6	17%	-0.3349	-57.3	-6.6	-6.5	-6.5	-6.4	-6.4	-6.4	-6.2	-6.2	-6.1	171.10	0.00	11.35	25.39	24.74	21.06	14.74	23.67	24.48	25.67
100		110-o8o8	4	50%	-0.3316	-48.9	-5.7	-5.5	-5.5	-5.5	-5.4	-5.4	-5.3	-5.3	-5.3	147.45	0.00	14.78	32.44	28.20	15.67	5.33	22.74	23.30	4.99
101		100-88o8	4	75%	-0.3298	-48.3	-5.7	-5.5	-5.4	-5.4	-5.4	-5.3	-5.2	-5.2	-5.2	146.44	0.00	3.01	15.71	15.61	28.20	29.83	11.01	15.25	27.81
102		084-ooo88	5	40%	-0.3277	-50.6	-6.1	-5.8	-5.8	-5.6	-5.5	-5.5	-5.5	-5.5	-5.3	154.40	0.00	16.99	17.56	1.47	27.17	7.39	24.51	28.23	31.08

103		026-8o8oo8	6	50%	-0.3168	-49.2	-5.8	-5.7	-5.7	-5.5	-5.4	-5.4	-5.3	-5.2	-5.2	155.28	0.00	5.68	31.34	20.20	29.67	22.10	4.93	25.01	16.36
104		077-8o8oo	5	40%	-0.3159	-57.8	-6.7	-6.7	-6.5	-6.4	-6.4	-6.3	-6.3	-6.3	-6.2	182.98	0.00	17.34	23.09	24.11	31.12	30.36	24.84	14.55	17.58
105		088-oo888	5	60%	-0.3158	-50.2	-5.6	-5.6	-5.6	-5.6	-5.6	-5.6	-5.6	-5.5	-5.5	158.97	0.00	21.31	41.43	17.44	15.93	28.79	29.05	1.59	3.45
106		094-o88o8	5	60%	-0.3140	-51.0	-6.1	-5.9	-5.7	-5.6	-5.6	-5.6	-5.5	-5.5	-5.5	162.41	0.00	20.65	16.33	21.63	13.52	20.61	34.56	21.13	13.99
107		104-8o88	4	75%	-0.3125	-48.0	-5.8	-5.6	-5.4	-5.4	-5.3	-5.2	-5.2	-5.1	-5.0	153.61	0.00	3.03	15.07	20.49	20.30	15.90	33.89	15.79	29.15
108		004-8888o8	6	83%	-0.3121	-50.6	-6.0	-5.7	-5.7	-5.7	-5.6	-5.6	-5.5	-5.4	-5.4	162.10	0.00	24.14	24.58	17.00	28.74	32.70	12.88	6.53	15.52
109		079-8o88o	5	60%	-0.3040	-50.9	-5.8	-5.7	-5.7	-5.7	-5.6	-5.6	-5.6	-5.6	-5.6	167.44	0.00	3.98	19.78	20.76	7.62	20.85	28.56	29.91	35.98
110		091-o8o8o	5	40%	-0.3014	-48.9	-5.8	-5.6	-5.5	-5.4	-5.4	-5.3	-5.3	-5.3	-5.3	162.24	0.00	1.47	25.46	22.66	24.37	34.68	25.35	3.75	24.50
111		071-88o8o	5	60%	-0.2991	-49.1	-5.8	-5.7	-5.5	-5.5	-5.4	-5.4	-5.3	-5.3	-5.2	164.14	0.00	10.40	10.79	4.86	22.54	25.43	22.88	42.11	25.13
112		120-o88	3	67%	-0.2951	-45.6	-5.5	-5.2	-5.1	-5.1	-5.1	-5.0	-5.0	-4.8	-4.8	154.54	0.00	11.76	31.47	5.72	12.24	24.21	2.01	35.76	31.37
113		053-o8o8oo	6	33%	-0.2950	-51.4	-6.1	-5.9	-5.8	-5.7	-5.7	-5.6	-5.6	-5.5	-5.5	174.26	0.00	8.86	33.44	30.98	18.22	16.11	16.60	16.67	33.38
114		119-o8o	3	33%	-0.2894	-46.3	-5.6	-5.4	-5.4	-5.2	-5.0	-5.0	-5.0	-4.9	-4.8	159.99	0.00	3.15	13.65	12.91	24.49	30.57	16.59	41.64	16.99
115	Clausen 1	018-8oooo8	6	33%	-0.2883	-51.8	-6.4	-6.2	-5.8	-5.7	-5.6	-5.6	-5.6	-5.5	-5.4	179.67	0.00	22.05	13.23	31.69	28.30	10.87	22.03	30.89	20.61
116		073-8oooo	5	20%	-0.2834	-48.7	-5.8	-5.7	-5.6	-5.5	-5.3	-5.2	-5.2	-5.2	-5.2	171.87	0.00	6.86	25.18	30.34	22.76	31.06	6.60	25.18	23.90
117		086-oo8o8	5	40%	-0.2790	-50.0	-5.7	-5.7	-5.7	-5.6	-5.5	-5.5	-5.5	-5.4	-5.4	179.22	0.00	27.05	24.91	10.77	25.22	25.40	24.69	26.61	14.57
118		123-oo	2	0%	-0.2760	-48.1	-6.1	-5.4	-5.4	-5.3	-5.3	-5.2	-5.2	-5.1	-5.1	174.30	0.00	1.34	47.48	24.55	22.74	23.72	28.23	1.64	24.60
119		117-ooo	3	0%	-0.2724	-47.0	-5.5	-5.4	-5.3	-5.2	-5.2	-5.2	-5.1	-5.1	-5.0	172.54	0.00	24.15	26.32	25.95	26.37	3.84	30.81	3.69	31.42
120		116-8o8	3	67%	-0.2702	-46.6	-5.6	-5.2	-5.2	-5.2	-5.1	-5.1	-5.1	-5.1	-5.0	172.45	0.00	10.12	23.02	35.26	12.68	26.05	26.12	13.35	25.85
121		098-888o	4	75%	-0.2494	-47.1	-5.4	-5.3	-5.3	-5.2	-5.2	-5.2	-5.2	-5.2	-5.1	188.86	0.00	31.47	15.30	17.07	18.76	14.94	43.72	15.75	31.86
122		118-oo8	3	33%	-0.2397	-46.7	-5.7	-5.5	-5.2	-5.2	-5.1	-5.1	-5.0	-5.0	-4.9	194.81	0.00	3.79	30.26	24.28	30.37	13.22	30.42	30.54	31.93
123		121-88	2	100%	-0.2392	-48.8	-6.0	-5.7	-5.6	-5.5	-5.4	-5.3	-5.2	-5.1	-5.0	204.03	0.00	47.13	12.46	22.31	47.45	12.69	24.48	12.27	25.23
124		001-888888	6	100%	-0.2093	-41.3	-5.6	-4.8	-4.6	-4.5	-4.5	-4.4	-4.4	-4.3	-4.2	197.36	0.00	1.68	29.33	32.80	34.84	29.77	29.46	19.68	19.80

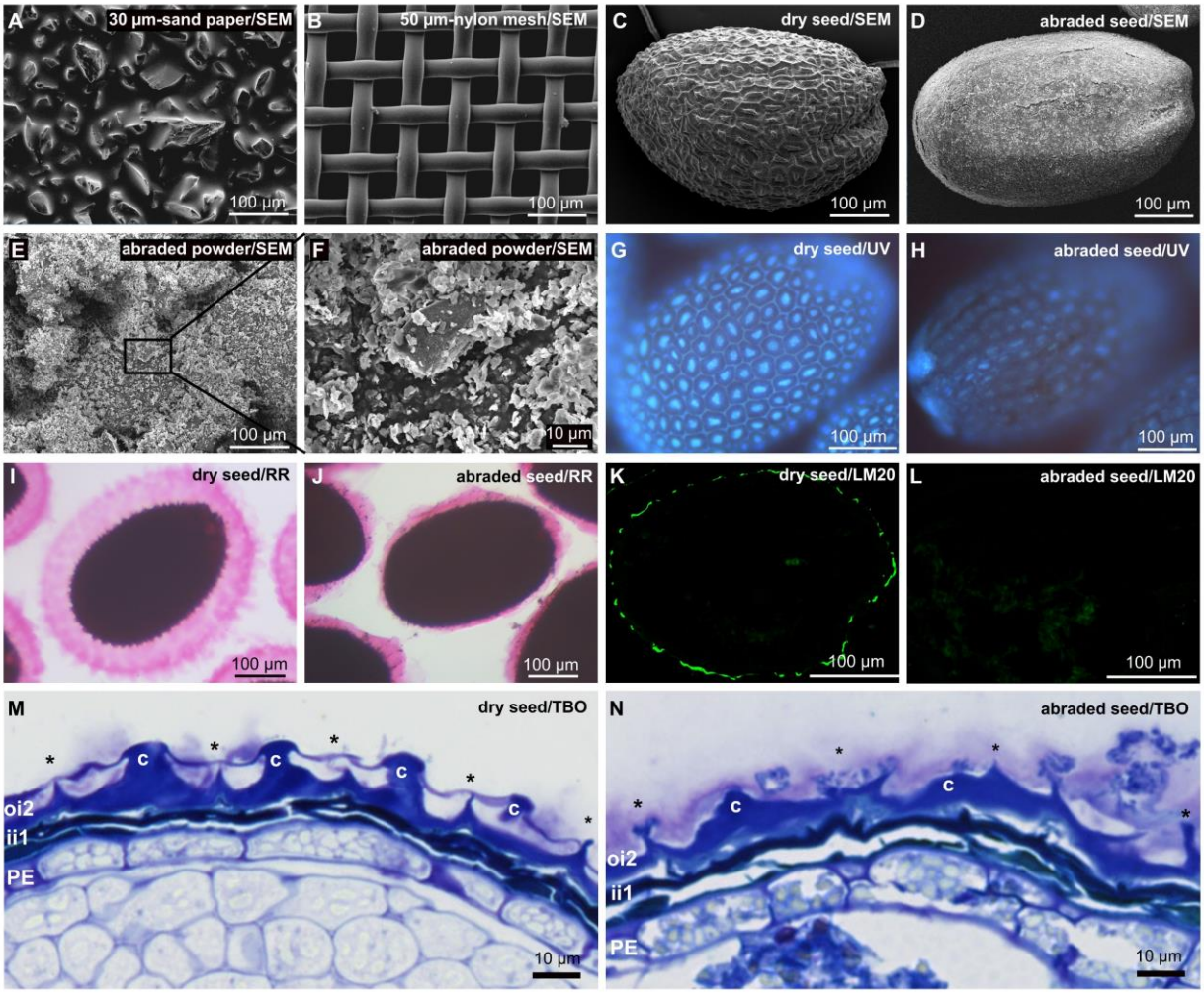

Sup. Fig. S3.1: Characterization of the abrasion process of dry seed surface to produce a mucilage secretory cell (MSC) surface-enriched fraction. Scanning electron microscopy (SEM) view of sand paper **(A)**, nylon mesh **(B)** included in the home made abrasion column (see methods), dry seed before **(C)** and after **(D)** 5 x 1 min abrasion illustrating the homogeneous etching of the dry seed surface. SEM view of the recovered MSC surface-enriched powder **(E, F)** illustrating the small size and relatively homogeneous particles. Note that the same scale is used for **A** to **E** to better compare the sizes. UV imaging of dry seed before **(G)** and after **(H)** abrasion illustrating the loss of autofluorescence of MSC radial walls and the decrease of autofluorescence of columella. Ruthenium red (RR) staining of dry seed before **(I)** and after **(J)** abrasion showing the remaining thin layer of adherent mucilage. LM20 immunofluorescence of dry seed before **(K)** and after **(L)** abrasion showing that the LM20 cell wall microdomain is abraded. Toluidine blue O (TBO) staining of dry seed before **(M)** and after **(N)** abrasion further showing that the etching occurred only at the surface of the MSC. *, radial primary wall, c, columella, oi2, outer integument 2, ii1, inner integument 1, PE, peripheral endosperm.

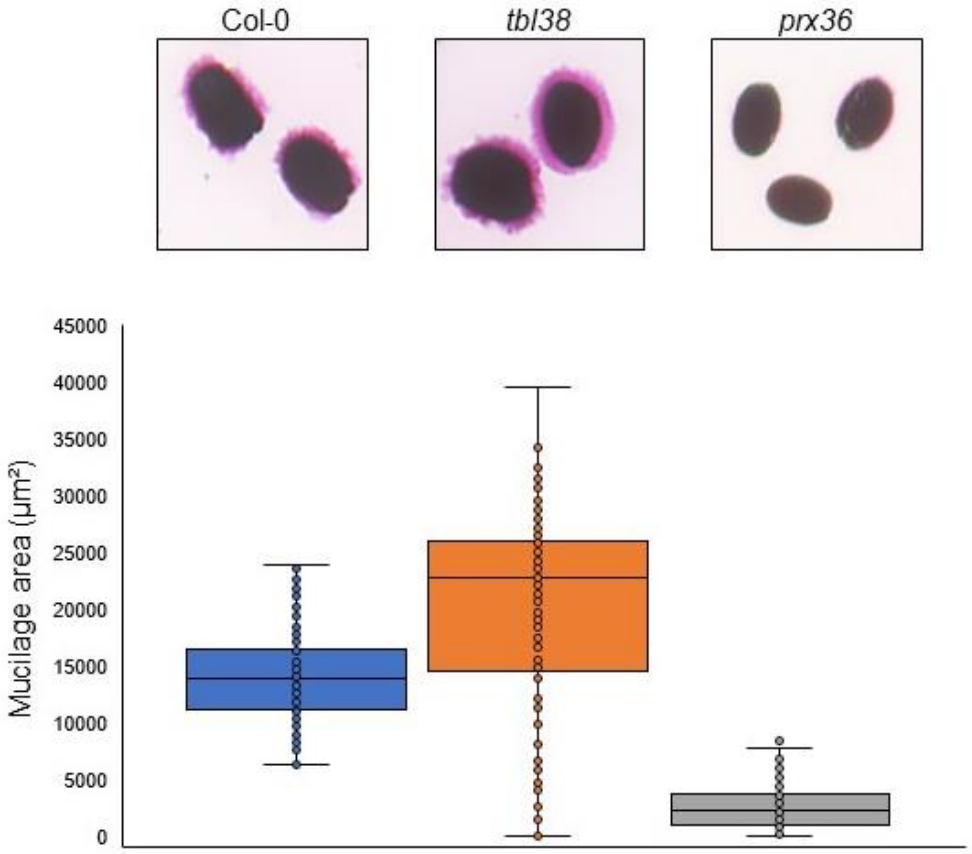

Sup. Fig. S3.2 Mucilage release is facilitated in *tbl38* with 20mM $CaCl_2$. Cell wall stiffening is induced through HG crosslinking via formation of the Ca^{2+} dependent "egg-box structure". In *tbl38*, mucilage area was found significantly larger than Col-0. Released was fully additionally impaired in prx36 seeds which hardly shown any mucilage.

4. Chapter four: Role of MSC-expressed Class III-peroxidases in remodeling of other putative CW microdomains

This part of the work was initiated during Edith Francoz PhD with mutants genotyped by P. Ranocha. This work was pursued during my PhD with a particular focus during the Internship of Fabien Nirina-Ramamonjy that I co-directed in the Lab. Part of the data are the results of our work that I further developped after his departure.P. Ranocha was also involved in the in silico molecular docking and protein modelisation

4.1. Introduction

So far, we have studied MSC surface wall CW dynamics through the lens of *PRX36* whose expression, positioning and activity was the driving force behind candidate identification, screening and characterization. In this model, PRX36 is anchored on a PMEI-dependant partially methylesterified HG and induces a local CW loosening, most likely through ROS generation, which is necessary for primal wall microdomain breakage and proper seed mucilage release in imbibed seeds(Francoz et al., 2019b). As stated in the general introduction, Class-III peroxidases (CIII-PRXs) have been associated with three major roles (i) signaling through H_2O_2 production/regulation affecting biotic/abiotic stress resistance and hormonal pathways (Laloi et al., 2004; Kim et al., 2010; Mase and Tsukagoshi, 2021), (ii) CW stiffening through ROS-mediated polymerization of aromatic compounds notably found in extensins and monolignols (Jacobowitz et al., 2019; Roppolo et al., 2011; Cannon et al., 2008) and (iii) CW loosening, presumably by ROS generation which break the covalent bond of CW polymers (Schweikert et al., 2000; Kunieda et al., 2013; Francoz et al., 2015b). How can a single protein achieve such diverse and sometimes contrary functions? Although clear *in vivo* evidence is still missing, *in vitro* experiments propose that CIII-PRXs can perform loosening or stiffening action not based on each protein specificity, but rather on their molecular environment (Francoz et al., 2015b). Coincidentally, examples of particularly positioned CIII-PRXs have emerged this last decade (Lee et al., 2013; Kunieda et al., 2013; Hoffmann et al., 2020) which suggests that multiple CIII-PRXs expressed in a single cell could participate in compartmented processes in a non-redundant manner. Similarly, mutants from 5 individual CIII-PRXs co-expressed in micropylar endosperm display individual phenotypes of either acceleration or delay of germination arguing for their non redundant roles possibly linked their –yet undetermined- distribution in remote wall microdomains from the same cell type (Jemmat et al., 2020).

The MSC offers great advantages to study parallel CW remodeling events as it undergoes several CW architectural changes during its development. Namely, mucilage secretion, columella and primary wall development including localized loosening. Large family of actors have been identified as contributing to the architectural changes of the mucilage and/or columella, most of which have been classified in a "MSC tool-box" (Francoz et al., 2015a; Viudes et al., 2021). Conceptually, it is possible that each CW remodeling event encompasses localized CIII-PRX-mediated CW remodeling at the subcellular level such as the pre-weakening of the top of radial CW (Kunieda et al., 2013; Francoz et al., 2019b). Indeed, unresolved spotted distribution of JIM12 extensin epitopes at the seed surface (Lee et al., 2012),

turned out to be localized at the top of the columella (Francoz, 2015) and JIM12 and LM1 extensin epitopes were similarly localized at this position in resin-embedded dry seeds (Jemmat et al., 2020). This suggested the occurrence of wall stiffening possibly via CIII-PRX-mediated extensin cross-linking. In an effort to evaluate this hypothesis, we selected MSC-expressed *CIII-PRXs* using data from both Belmonte tissular specific transcriptomic experiments and systematic *in situ* hybridization of the *CIII*-PRX multigenic family on wild-type seed sections (Belmonte et al., 2013; Francoz et al., 2016). Using these combined approaches, in addition to *PRX36*, 5 highly MSC-expressed *CIII-PRXs* were identified during seed development (**Figure 4.1**; Francoz et al., 2016). Out of the 5, both PRX03 and PRX17 were already described as CW CIII-PRXs involved in response to potassium deficiency and lignified CW formation, respectively (Cosio et al., 2017; Kim et al., 2010). Interestingly, *PRX50* and *PRX51* originated from tandem duplication and consequently presented high sequence homology leading to impossibility to distinguish them in transcriptomics (**Figure 4.1A**). Previous work positioned PRX50 in the mucilage pocket, although its role was not disclosed (Francoz et al., 2019b). Finally, little is known about *PRX56* aside that it is not regulated by key transcriptional factors targeting *PRX36* (Ranocha et al., 2014). Reportedly, mucilage release was impaired in *prx56* seeds (Ranocha et al., 2014), although this phenotype could not be reproduced (Francoz, 2015). Here, we selected homozygous lines of each mutants which corresponded to knock-out (*prx03, prx17, prx56,* **Sup. Fig. S4.1**) or knock-down lines (*prx50, prx51,* **Sup. Fig. S4.1**), some of which were already characterized (Courtesy of P. Ranocha; Jemmat al. 2020). We evaluated the putative role of each CIII-PRX and we particularly focused on PRX56 as a candidate for extensin polymerization at the top of the columella.

4.2. Results

4.2.1. Mucilage release is not impaired in mutated seeds

Mucilage release is a quick and reliable way to assess changes in CW dynamics which may range from pectinaceous mucilage secretion to remodeling of CW mechanical properties. Although CIII-PRXs can be linked to functions which may not be directly or indirectly associated with mucilage release, we expected mutations of key MSC-CIII-PRX genes to alter CW properties and possibly impair mucilage release as it occurred for *prx36*. Thus, we released and quantified seed mucilage of each mutant. After 1 h vigorous shaking, we did not observe obvious defect in mucilage release aside from *prx36* used as a control (**Figure 4.2, Sup. Fig. S4.1**). *prx56* seeds which were once wrongly described in the team as impaired in their mucilage

(A)

RK	PCC	Gene Symbol	pre-globular stage							globular stage							heart stage							linear-cotyledon stage							bending cotyledon stage							mature green stage						
			pg EP	pg MCE	pg PEN	pg CZEN	pg CZSC	pg SC	pg WS	g EP	g SUS	g MCEN	g PEN	g CZEN	g CZSC	g SC	g WS	h EP	h MCEN	h PEN	h CZEN	h CZSC	h SC	h WS	lc EP	lc MCEN	lc PEN	lc CZEN	lc CZSC	lc SC	lc WS	bc EP	bc PEN	bc CZEN	bc CZSC	bc SC	bc WS	mg EP	mg MCEN	mg PEN	mg CZEN	mg CZSC	mg SC	mg WS
1	1,0000	*PRX36*	15	27	4	11	8	8	2	4	2	13	2	12	8	2	4	3	3	3	15	14	3	9	4	5	9	12	405	1522	554	1	2	27	992	29	20	7	1	11	3	53	65	9
156	0,5691	*PRX56*	6	15	4	12	1	8	5	4	8	3	10	15	2	4	9	4	1	8	17	13	9	16	4	16	9	22	193	1781	526	6	16	2	264	2933	433	8	17	9	11	377	609	130
191	0,541	*PRX03*	3	15	14	40	127	1113	745	1	14	26	22	9	343	1160	1189	3	18	14	14	260	818	516	7	229	24	57	644	1355	802	3	213	40	1554	1609	603	21	34	4	41	771	145	88
205	0,5264	*PRX50 PRX51*	2	3	4	10	712	137	190	11	1	3	6	3	639	218	329	2	1	5	3	938	488	284	2	15	8	24	1104	3361	804	2	35	3	1406	4104	1190	2	24	7	16	1613	2950	493
16283	-0,213	*PRX17*	355	90	901	109	43	315	265	274	107	219	785	236	31	590	397	234	169	241	228	31	415	181	66	700	49	19	48	63	110	46	24	31	21	21	54	44	486	48	664	233	2	51

(B)

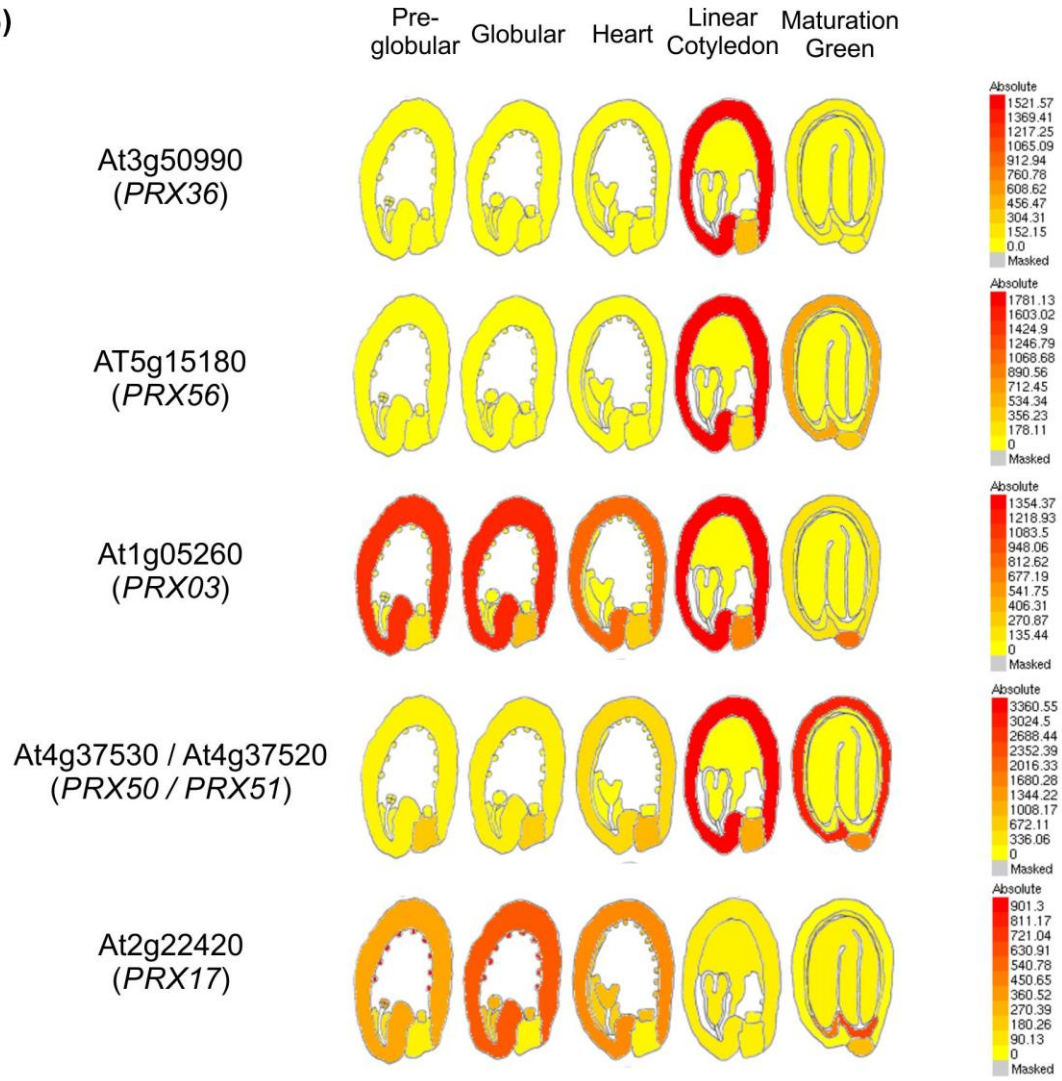

Figure 4.1: Selection of seed coat-specific *CIII-PRX* candidate genes in *PRX36* co-expression network for further functional genomics study. **(A)** *PRX36* co-expression network using the tissue-specific seed developmental kinetics GSE12404 dataset (Belmonte et al., 2013) displaying the expression profile of the 5 other seed coat-specific *CIII-PRXs*. **(B)** expression profiles of the candidate genes in five out of the six developmental stages according to http://bar.utoronto.ca/efp/cgi-bin/efpWeb.cgi. Note that *PRX50* and *PRX51* shared the same spot ID. Note also that the mucilage secretory cell (MSC)-specific expression has been previously confirmed by *in situ* hybridization for *PRX03*, *PRX17*, *PRX50* and *PRX51* (Francoz et al., 2016). RK, rank ; PCC, Pearson Correlation Coefficient ; EP, embryo proper ; SUS, suspensor ; MCE, micropylar endosperm ; PEN, peripheral endosperm ; CZEN, chalazal endosperm ; CZSC, chalazal seed coat ; SC, seed coat ; WS, whole seed.

release ability (Ranocha et al., 2014), did not show statistically difference with Col-0, in agreement with more careful examination (Francoz 2015). We could not associate either *CIII-PRX*s with putative CW loosening as was described with PRX36 (Kunieda et al., 2013). However, mucilage release can be achieved in a little as 20 s (Arsovski et al., 2009) which does not allow the appreciation of more subtle phenotype that may occurs in mutated seeds. In addition, our assay could not highlight mutation that may facilitate release at opposed to the traditional impairment found in various mutants (Arsovski et al., 2009; Kunieda et al., 2013; Saez-Aguayo et al., 2013; Levesque-Tremblay et al., 2015). Therefore, we added increasing amounts of ethanol in the solution which was shown to have negative effect on mucilage release (Francoz 2015).

First, we used 5% increments to evaluate the adequate ethanol concentration in Col-0 seeds. The rationale was to determine the ethanol concentration just below those leading to the total absence of mucilage release with Col-0, and then to assess this selected condition in mutated seeds. Stringency peaked around 30% ethanol, at which point almost no mucilage was found (**Figure 4.2B**, **Sup. Fig. 4.1B**). Thus, we selected 25% as the optimal concentration to screen for facilitated release in addition to impaired release (**Figure 4.2B**, **Sup. Fig. 4.1B**). Using these parameters, we saw complete lack of staining in *prx36* which impaired released phenotype was exacerbated. Subtle differences were quantified in *prx03*, *prx17*, *prx50* and *prx51* but most importantly, *prx56* seeds released twice as much mucilage as Col-0, suggesting that PRX56 restrained the mucilage release in wild type (**Figure 4.2B**, **Sup. Fig. 4.1B**). Indeed, under 25% ethanol, *prx56* phenotype was the opposite of *prx36* phenotype, representative of a PRX36-dependant facilitated release. Because PRX36 was described as being involved in CW loosening, we investigated PRX56 putative connection with CW stiffening.

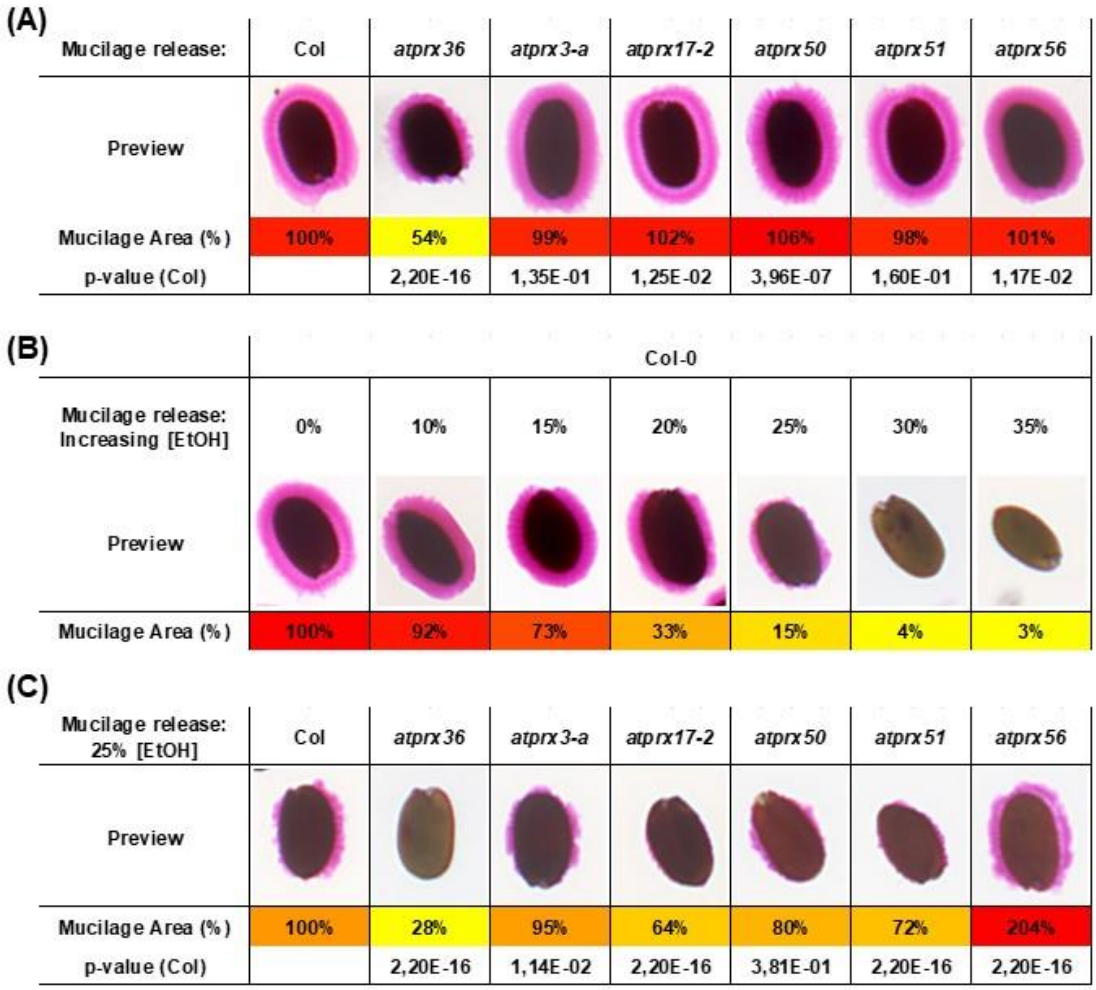

Figure 4.2 : **New *prx* candidate mutants display subtle variation of mucilage release area compared to Col-0 only under 25% ethanol conditions and *prx56* displays a strong facilitation of mucilage release phenotype under this condition. (A)** Ruthenium Red (RR) staining assays for candidate *CIII-PRX* mutants under aqueous condition show no definitive mucilage release abnormalities compared to Col-0, unlike *prx36* control which has significant (p-value < 0.01) reduction of mucilage area. **(B)** Increasing concentration of ethanol used in the RR assay on Col-0 shows that exceeding 25% ethanol leads to complete shutdown of mucilage release, therefore 25% ethanol was selected as the condition to force a significant phenotype in new candidate *prx* mutants. **(C)** Mucilage release assays in 25% ethanol shows mucilage area (relative to Col-0) subtle decrease for *atprx3-a*, *atprx17-2* and *atprx51* proven to be significant by Wilcoxon test compared to Col-0, and a significant prominent increase for *atprx56* compared to Col-0. Note that the mean values of mucilage area were expressed both in μm^2 and in %, and were displayed using a red (high values)-to-yellow (low values) heat maps for better visualization of the differences. See Figure 6.10 in the Method section for detail on the masks used for measurements. N = 609-1220 seeds per biological repeat which was repeated at least twice.

4.2.2. PRX56 is a CW protein localized around the top of the columella

CIII-PRX-mediated CW stiffening can be achieved through different processes which we described before, one of which is the cross linking of the tyrosine residue commonly found in extensins. The presence of such epitopes was demonstrated through immunolocalization using JIM12 and LM1 at the top of the columella of dry seeds in addition to the endosperm/epidermis junction **(Figure 4.3A-D**; Jemmat et al., 2020). To assess a putative extensin peroxidase role for PRX56, we undertook two separate localization strategies (i) we used an antibody raised again a PRX56 peptide and (ii) we generated a *proPRX36::PRX56-TagRFP* construct which was observed on developing *prx56* seeds under confocal microscopy (**Figure 4.3**). Unfortunately, αPRX56 signal was observed in the mucilage of both Col-0 and *prx56* in a similar manner (**Sup. Fig. S4.2**). We similarly tested anti-peptide for the other PRX candidates which turned out to also be non-specific, contrary to the anti-peptide previously raised against PRX36 (**Sup. Fig. S4.2**). Regardless to general bad plant growth condition at this time of the PhD (see interlude before Chapter 3; **Fig 3.0A**), we observed two distinct patterns of PRX56-TagRFP accumulation with the second approach. PRX56-TagRFP accumulated in the area around the top of columella and to a lesser extent, to the top of radial primary wall at early developmental stages as viewed with a maximal projection (**Figure 4.3E**), with a single confocal plan (**Figure 4.3F, H**) and with orthogonal projection of 70 stacks. (**Figure 4.3G, I**). However, this fluorescence signal surrounding the top of the columella was consistent with a putative role of PRX56 for extensin polymerization at the nearby top of the columella where the extension epitopes could be localized. Thus, we sought to investigate the extensin polymerization status in *prx56.*

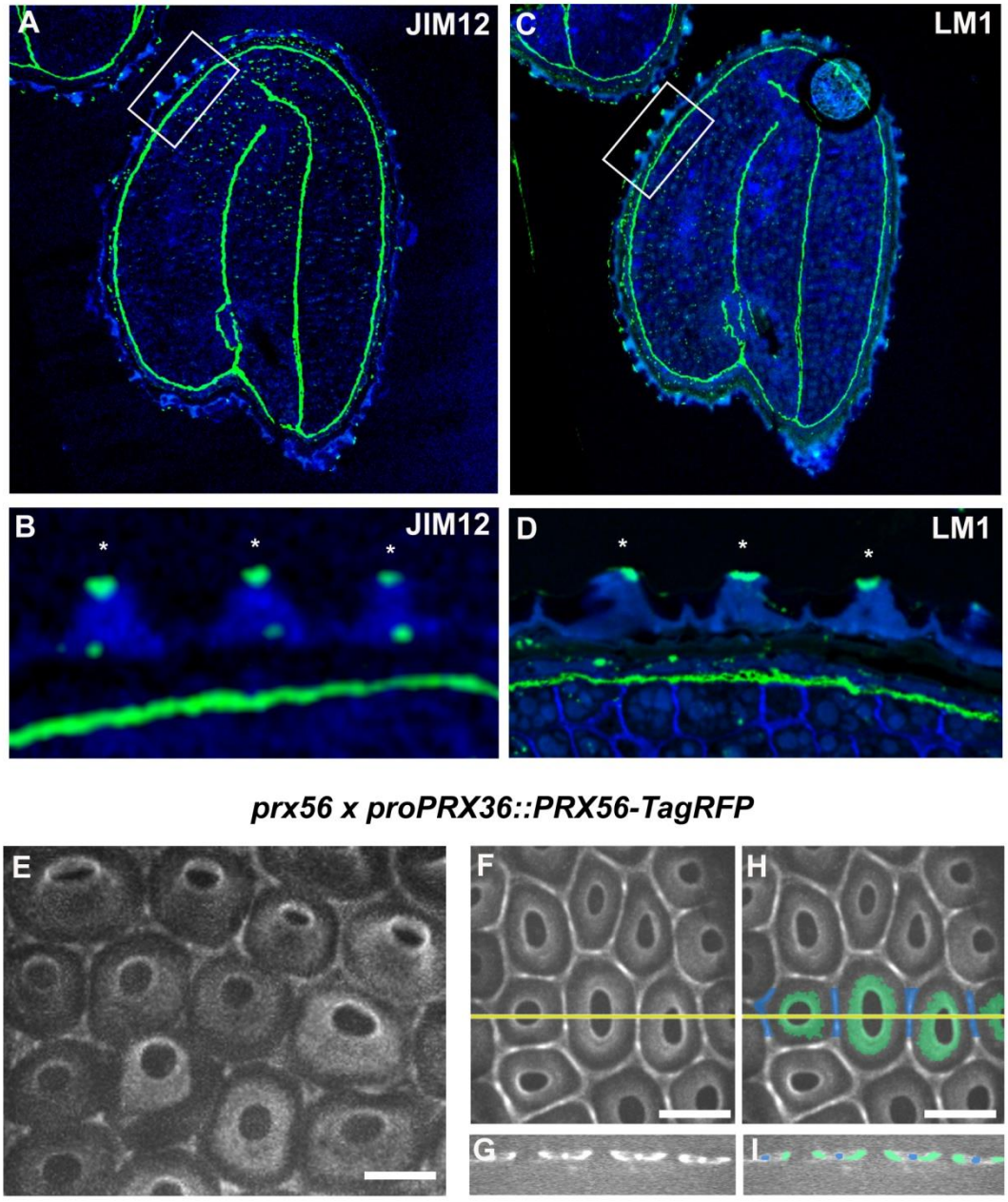

Figure 4.3: PRX56 as a putative extensin peroxidase in MSC surface walls. (A-D) Merge channel of the JIM12 **(A, B)** and LM1 **(C, D)** extensin labeling (green channel) and calcofluore/autofluorescence (blue channel) on dry seed resin serial longitudinal sections. Images in **(B)** and **(D)** are magnifications of the white frames displayed in **(A)** and **(C)** showing the labeling at the top of the columella of three successive MSCs. **(E)** Maximum projection of 70 stacks showing PRX56-TagRFP localization in the area surrounding the top of the columella and to the the top of radial primary wall. **(F-G)** Single confocal image section and orthogonal view along the yellow axis. **(H-I)** False color of images F-G, respectively. The orthogonal projection with false-colors allows for better appreciation of the signal in the mucilage around the top of columella (green) and primary wall (blue). Note that the resolution is not sufficient to decipher whether the signal surrounding the columella correspond to the external part of the columella or to inner part of the mucilage. Bars: 25 μm **(E-H)**. *, top of columella.

4.2.3. PRX56 putative involvement in extensin polymerization

First, we aimed to study immunolocalization of two anti-extensin antibody, JIM12 and LM1 which bound to similar motif (Smallwood et al., 1995) on developing Col-0 and *prx56* (data not shown). However, combined with sometimes poor resolution of paraffin sections, anti-extensin signal could not be observed in developing seeds. Unfortunately, we could not observe the JIM12/LM1 labeling in *prx56* dry seed sections yet. Thus, we focused on MSC-surface enriched fractions from dry seeds and tried to demonstrate change of JIM12/LM1 signals in Western Blot. Extensins are exported to the CW as polypeptides constituting monomers that can be further crosslinked through oxidative coupling.The monomer theoretical sizes are between 48 kDa and 73 kDa depending on glycosylation (Cannon et al., 2008). Crosslinked extensins are insoluble which usually render attempts to extract them unsuccessful explaining their poor coverage in CW proteomes (Albenne et al., 2013; Mishler-Elmore et al., 2021). As such, we tried various extraction solutions and conditions in an attempt to increase their extractability. Except low signals in the wells, almost no signal could be seen with native acetate buffer/$CaCl_2$ traditionally used to extract CW proteins (**Figure 4A-B**). We obtained highest LM1/JIM12 signal after additional extraction of the pellet in a highly denaturing solution (Kato et al 2002) complemented with $CaCl_2$ (See method section 6.2.14 for details) (**Figure 4.4C-D**). However, we could not see any difference between Col-0, *prx56* and *prx36* repeated lanes regardless the % of SDS enabling to resolve relatively medium molecular weights (**Figure 4.4C-D**), or higher molecular weights (**Figure 4.4E-H**). In both cases, the smears were mostly of very high molecular weight including signal appearing in the stacking gel zone and even in the well zone. This is in agreement with highly polymerized forms of these extension epitopes. However, faint lower molecular weight bands appearing below 72 kDa (**Figure 4.4C-D**) or above 95 kDa (**Figure 4.4E-F**) show no difference of intensity between the samples. The expected electromobility shift assay result corresponding to a clear extension polymerization role for PRX56 would have been an increase of low molecular weight bands (possibly monomers) for *prx56*. The intriguing weak JIM12 signal in *prx36* was attributed to lower protein content as shown in Ponceau red (**Figure 4.4G-H**). The ponceau red also illustrates the very low protein abundance in these dry samples in agreement with the low protein coverage of mucilage proteomes rendering this type of analysis very challenging (Tsai et al., 2017).

Preliminary results pointed to monomeric forms only found in *prx56*, however we were not able to replicate similar extraction procedure with current biological samples as of yet (**Sup. Fig. 4.3**).

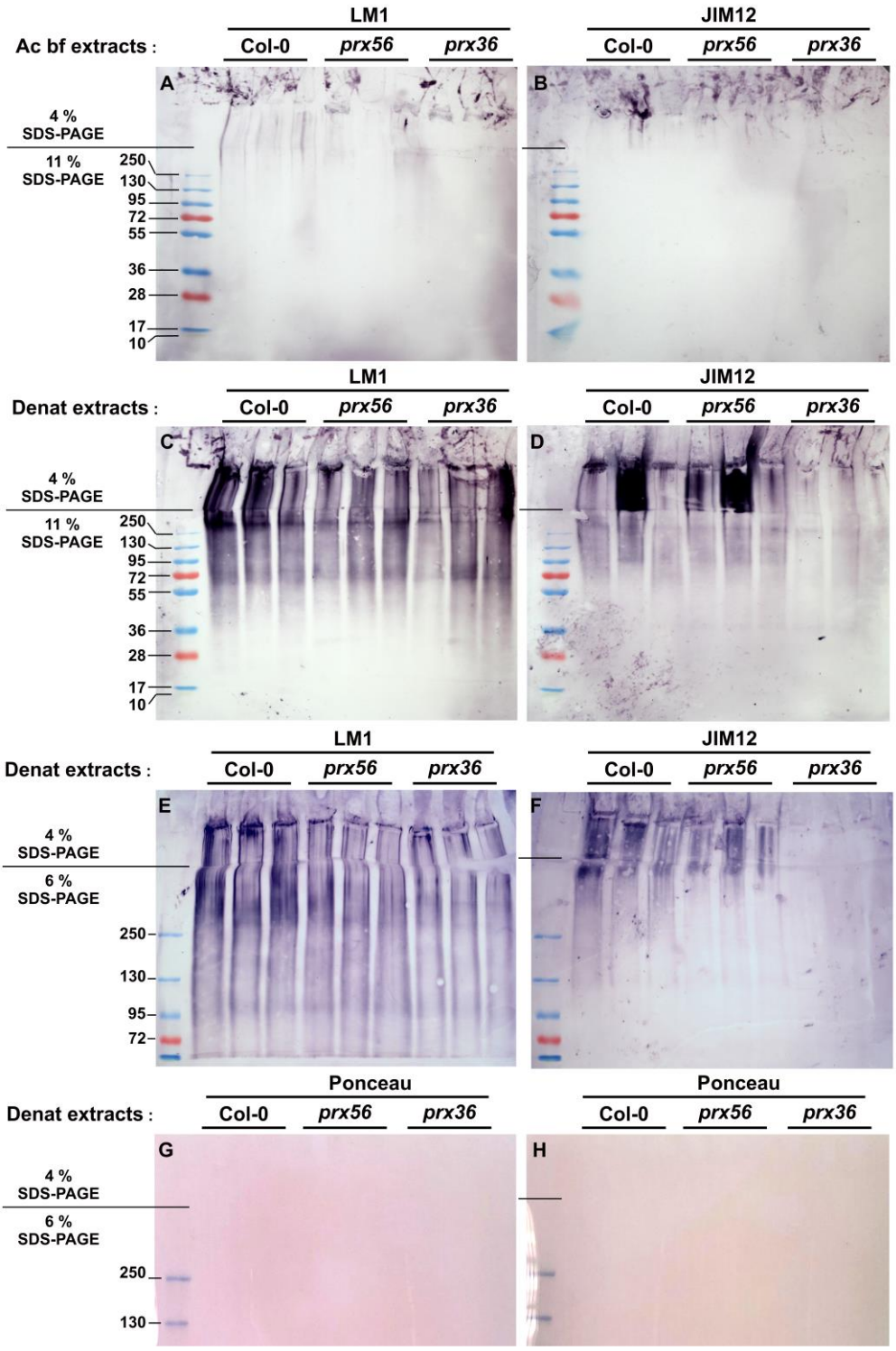

Figure 4.4: Western blot analysis of JIM12 and LM1 extensin epitopes among the genotype constitute an electromobility shift assays (EMSA) used to assess the extensin polymerization putative function of PRX56. MSC surface-enriched powders from dry seeds from Col-0, *prx56* and *prx36* were used for protein extraction with various conditions, SDS-PAGE and western bloting with JIM12 and LM1 as labeled on the figure. **(A-B)** acetate buffer/$CaCl_2$ extracts led to the absence of extension extraction. **(C-F)** highly denaturing solution (see methods) enabled visualization of high molecular weight extensin smears that were resolved with 11% **(C-D)** or 6% **(E-F)** SDS-PAGE. **(G-H)** loading control of membranes **(E-F)** using Ponceau Red shows the low protein abundance. Three parallele abrasions were made for each genotype and no clear differences could be seen between the genotypes. Note that the intriguing low JIM12 signal abundance for *prx36* has to be related to an unexplained lower protein extraction according to the Ponceau red. Ac bf extracts, extracts obtained with acetate buffer and 0.2M $CaCl_2$ only; Denat extracts, extracts obtained following a second extraction with a denaturing solution (The extraction protocols (1) and (2) were used; see Methods section 6.2.14 for details).

4.3. Discussion

4.3.1. PRX56 may stiffen walls at the top of the columella

Advancements in cell biology have led to increasing understanding on CIII-PRX targeting to both the primary and secondary cell wall. Because CIII-PRXs can be associated with both loosening and stiffening of the wall, it can be critical to assess their -putative- subtle localization to understand how they may regulate nearby wall properties.

Parallel transcriptomic data mining and *in situ* hybridization previously done in the team allowed for refined expression map of numerous seed *CIII-PRXs* (Francoz et al., 2016). Based on this, we sought to understand if, in addition to PRX36, five other MSC-expressed CIII-PRXs could be linked to the mucilage extrusion process by participating in CW properties critical for mucilage release. As traditional ruthenium red staining failed to discern subtle phenotype which may be observed in mutated seeds, we determined optimal ethanol concentration at which mucilage release was almost fully impaired in Col-0. We ended up using a final concentration of 25% ethanol, which was consistent with previous findings both in the team and in the recent literature (Dean et al., 2020). In these conditions, *prx56* seeds were twice as less affected than Col-0 seeds. Mucilage release impairment due to increased concentration of ethanol is likely due to its dehydration properties which would limit imbibition efficiency. Thus, mucilage swelling would be reduced / prevented which would not break the primary wall as efficiently. This implied that *prx56* walls could be weaker compared to Col-0, meaning that PRX56 could be linked to a CW stiffening activity. Because maturing MSCs are mostly made out of different wall material, protein localization was critical to try to associate it with stiffening activity of particular regions in MSC.

To test this, we visualized PRX56-TagRFP expressed under the control of *proPRX36* at numerous stages of seed development. The choice of this promoter was made for convenience and was relevant considering the relatively high co-expression profile of *PRX36* and *PRX56* (**Figure 4.1A**). We found some signal in the primary wall, as well as in the area surrounding the top of the columella **(Figure 4.3**) which was found consistently in multiple experiments, despite the lack of clear whole developmental kinetics so far. Such localization resembled previous parallel findings in the team (Francoz 2015). Indeed, Edith Francoz work has highlighted peroxidase activity using a fluorescent chromogenic peroxidase substrate (HPF) on globular and mature green stage seed. Using a whole mount setup, she could not see peroxidase activity at earlier stages (**Figure 4.5**). However, mature green seeds did show activity at the surface of primary wall, as well as across and around the columella (**Figure 4.5**) (Francoz,

2015). Primary wall fluorescence was expected, as it is the site of PRX36 accumulation (Kunieda et al., 2013; Francoz et al., 2019b) but the columella signal was strikingly similar to our observation of PRX56-TagRFP (**Figure 4.3, Figure 4.5**). Both Francoz and this study show clear accumulation of fluorescent signal not at the top, but around the columella which reinforces the feasibility that PRX56 could be active in this CW microdomain. In Francoz study, she reported no visible difference in fluorescent between Col-0 and *prx36* which suggested other that other CIII-PRXs may be positioned in a similar manner. Because PRX56-TagRFP has a similar localization in radial primary walls as PRX36, similar study on *prx36* x *prx56* may give interesting results as to subcellular distribution of peroxidase activity in MSCs. Interestingly, even though PRX50-TagRFP was positioned in the mucilage (Francoz et al., 2019b), little to no CIII-PRX activity was observed in the mucilage, which sparks the question of its activity.

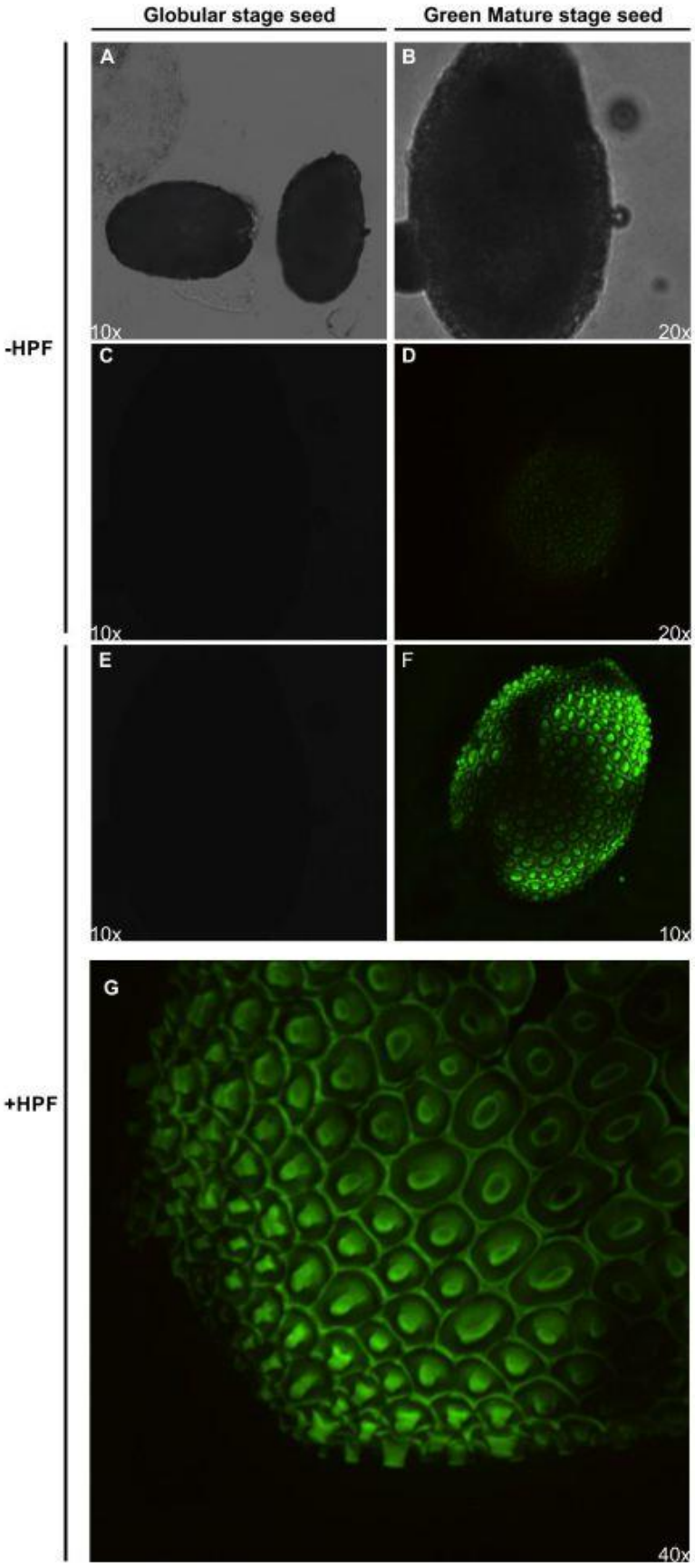

Figure 4.5: evidence of in situ peroxidase activity in mature seeds (extracted from Francoz PhD, 2015). Early developed seeds (A, C, E) or matured (B, D, F, G). -HPF: seeds before HPF treatment (A-D). +HPF: seeds after treatment. (E-G). Brightfield view (A, B) or confocal microscopy view of HPF fluorescence (C-G). Images were taken using similar setting C-G. Seed developmental stage was determined through embryo dissection after seed observation. HPF: chromogenic Class-III peroxidases substrate and endogenous H_2O_2.

4.3.2. PRX56 may be an extensin peroxidase

CW stiffening can be achieved through many different pathways including, CIII-PRX-mediated stiffening due to aromatic compounds crosslinking through ROS generation. MSCs are not lignified, but tyrosine residues of extensin can also be crosslinked to form a supramolecular complex array which is associated with wall stiffening. This has been nicely shown through in vitro assays establishing the relationship between the positioning of Tyrosine residues on EXT3/RSH and the CIII-PRX-dependant generation of pucherosine (linkages between one Tyr on a polypeptide and two Tyr separated by another amino acid on another polypeptide) explaining an elongation of the supramolecular polymerized extensin in agreement with its structural function (Cannon et al., 2008). In the case of MSC, JIM12/LM1 extensin labeling was indeed observed at the top of the columella (Francoz 2015, Jemmat 2020, **Figure 4.3**). It should be noted that even immunolabeled resin section may not give the accurate resolution to differentiate columella contour and submit, although such separation would not prevent extensin crosslinking. Although no perfect spatiotemporal colocalization of JIM12/LM1 epitopes (top of columella found on sections from mature developing seeds or dry seeds) and PRX56-TagRFP (surrounding of the top of the columella found in younger developing seeds so far) was observed, ROS such as H_20_2 are able to diffuse and be utilized by peroxidases to crosslink aromatic compounds remotely of the peroxidase localization (Lee et al., 2013; Swanson and Gilroy, 2010). Traditionally, we associate NADPH oxidases (RBOH) as plasma membrane bound protein generating H_20_2 which could diffuse in the apoplast at relatively long distances up to intercellular traffic (Ros Barceló, 2005). With regards to MSC composition, such properties would be critical for ROS positioning near the top of the columella. Indeed, as MSCs mature, additional wall material is deposited (mucilage, columella) which distances the plasma membrane from extensin deposition site. Thus, ROS diffusion would be absolutely necessary for peroxidase-mediated extensin polymerization. This is also consistent with PRX36 which requires ROS for targeted CW loosening in its microdomain (Kunieda et al., 2013; Francoz et al., 2019b). It could be argued that H_20_2 production takes place in early developmental stages, when the plasma membrane still makes up for the majority of MSC subspace. This however, is not fully in line with transcriptomic data. Indeed, only RBOH-F and RBOH-D are expressed in MSC, both having seed coat expression profile either coinciding with PRX36 or in mature green seeds, respectively (Francoz et al. 2015). Thus, this rather supports H_20_2 production and utilization by CIII-PRXs in later developmental stage. However, the repeated EMSA western blots did not enable to demonstrate the appartition of low molecular

weight/monomeric extensin polypeptides in *prx56*, so far. Additional tests with different extraction conditions will be necessary to further investigate this issue.

Another interesting question relies on which extensin could be crosslinked by PRX56. Based on the transcriptomic data, a good candidate could be *RSH/EXT3* which is the EXT displaying the strongest expression in the seed coat with highest expression level at the green mature stage (Belmonte et al 2013; Francoz 2015). The MSC-specific expression of this gene (in addition to the embryo and the endosperm) was further established through in situ hybridization (Francoz et al. 2015). While *PRX56* expressions fades at this developmental stage, CIII-PRXs are extremely resilient proteins which may stay in the CW way past their expression window. In our context, two separate experimental evidences confirmed this statement. (i) *proPRX36::PRX36-TagRFP* signal could still be observed at 14 DAP (Francoz et al. 2019) and (ii) PRX36 was found in a mucilage proteome study, most likely as contaminant from the fragmented primary wall (Tsai et al., 2017). Thus, PRX56 may be targeted at the top of the columella before extensin deposition and catalyzes their polymerization in late developmental stages. Since we possees only one allelic *prx56* mutant, it remains to see if *proPRX36::PRX56-TagRFP* transformation in *prx56* enables restoring the wild type phenotype of mucilage release with 25 % EtOH. Interestingly, we identified in 1001 genomes the Loz-0 ecotype from Spain which possesses a deletion in PRX56 coding sequence leading to a frameshift and early stop codon. However, we were so far unable to have this line flowering, likely due to particular growth condition that Loz-0 requieres.

So far, EXT3/RSH functional study has highlighted its critical role at very early developmental stages (2 cell stages of the zygote following fecundation) and plant germination as knocked-out displayed a lethal phenotype (Hall and Cannon, 2002). This impaired our ability to easily test whether *rsh* mutant could phenocopy *prx56* phenotype of facilitated mucilage release and to test whether the JIM12/LM1 epitopes observed at the top of the columella and on the western blot analysis could be related to EXT3/RSH. However, very recent work indicates that *rsh/ext3* is not the causality of the lethal phenotype initially observed. Indeed various *CRISPER*-Cas9 lines targeted on *RSH/EXT3* could not associate *EXT3/RSH* with any developmental phenotype, likely to due functional redundancy with similar proteins or unidentified lethal mutation additionally present in the original RSH/EXT3 activation tag transposon line (Doll et al., 2022). Thus, this opens a very interesting perspective and PRX56-EXT3 parallel study of the subtle phenotypes observed in MSCs may help assessing the relevancy of their proposed relationship. These lines could also be used to see if JIM12/LM1 epitopes are related to EXT3.

4.3.3. Prospect of a PRX56 docking valley

Our results highlighted the existence of another MSC-expressed CIII-PRX which may regulate wall properties in a different manner and position than PRX36. In this scenario, PRX56 would have opposite role as participating in CW stiffening rather than loosening. Previously, we stated that CIII-PRXs could perform both types of wall remodeling through generation/regulation of local ROS. From a catalytic domain standpoint, both PRX36 and PRX56 possesses conserved amino acid residues required for proper activity, meaning that in this scenario, possible differences in activity would be due to the microenvironment (wall microdomain) in which each protein is positioned. Until few years ago, subtle CIII-PRX localization in similar cell layer could only be explained by protein determinant like CASP which may explain this anchoring, although recent data actually suggest limited implication (Lee et al., 2013; Barbosa et al., 2022). However, i*n vitro* study of CIII-PRX structure and affinity led to the PRX36 model in which particular amino acid residues -some of which have been identified- could anchor the protein to specific homogalacturonan (HG) polymers (Carpin et al., 2001; Francoz et al., 2019b). Although this does not implicate that each CIII-PRX could present similar features, we wanted to confront the idea of another subtly positioned CIII-PRX due to anchoring to specific HG. While this represents very speculative future prospect that will have to be done in parallel to investigation of PRX56 putative crosslinking of extensin, we still evaluated this using *in silico* docking models.

Initially, in silico modeling of PRX36 pointed to a docking valley which was constituted of various polar and hydrophobic residues. While the initial docking models were made following an apriori scenario testing five oligogalacturonates (OGAs) previously used to test JIM7 specificity, we saw in the previous chapter that the without apriori approach reinforced the initially obtained results. Using similar parameters discussed in Chapter 3, we built a model for PRX56 and tried to identify possible similar valley on the protein surface. We randomly screened 64 OGAs of DP6 covering all the possibilities of methylesterification patterns, for their docking potential to PRX56 and ranked them using the same (imperfect) proxy used for PRX36 (**Table 4.1; Sup. Table S4.1, S4.2**). Interestingly the pattern of OGA ranking was clearly different between both proteins. Accordingly, the best hit predicted for PRX56 docking was a different OGA than those for PRX36, supporting that both proteins might need differently ME patterned HG (**Table 4.1; Sup. Table S4.1, S4.2**). Then, we used the best matching OGA for each protein to highlight similarity -or lack thereof- in the amino acid environment on both PRX36 (**Figure 4.6A, C**) and PRX56 (**Figure 4.6B, D**) surface, i.e. highlighting the amino

acids that were positioned at less than 5 Å from the best poses. We observed a putative PRX56 valley on similar face of the protein as PRX36 valley although it was tilted (**Figure 4.6A-C**). While the 33amino acids constituting these valleys shared some similarities, these were mostly different between both proteins. The tilt observed between the positioning of the two predicted specific OGAs in the two specific predicted valleys could be related to some putative specificity. Indeed, it was previously shown that site directed mutagenesis on amino acids in PRX36 predicted valley did not significantly impair the generic peroxidase activity of PRX36m but rather led to a tilt of predicted anchoring of the same OGA in PRX36m that was related to the mislocalization of PRX36m outside of the wall microdomain and consequently to its inability to complement *prx36* phenotype (Francoz et al., 2019b). While the best predicted OGA hit of PRX36 corresponded to the epitope of JIM7 which facilitated further functional studied and particularly to the demonstration that this OGA methylesterification pattern was related to PMEI6 activity, to our knowledge, the best predicted OGA of PRX56 does not correspond to the epitope of any antibody from the available collection of antibodies that show varying affinity toward HG with higher/lower DM. We were neither able to specifically label the top of the columella while screening all the Plant probes HG-specific antibodies (Jemmat et al., 2020). As such, future studies targeted on the reality of this OGA will be rather difficult. However, two types of experiments are feasible: (i) chemical de-esterification of HG and/or treatment with EDTA to assess the putative mislocalization of PRX56-TagRFP from its wall microdomain and while perturbating HGs (ii) targeted mutagenesis on amino acids from the PRX56 predicted valley to study PRX56m-TagRFP putative mislocalization and putative inability to complement subtle *prx56* phenotype. Both approaches were successfully used for PRX36 (Francoz et al., 2019b).

Altogether, PRX56 is a good candidate for extensin polymerization at the top of the columella and EXT3 is a good candidate for such a role. Extensin polymerization at this wall microdomain might explain why the top of the broken primary wall remains attached to the top of the columella during mucilage release while the adjacent PRX36/PMEI6 wall microdomain at the top of radial cell wall is broken.

Table 4.1 : Random systematic screening of in silico molecular docking of PRX36 (top Table) and PRX56 (bottom Table) on 64 oligogalacturonates (OGA) of DP6 covering all theoretical demethyesterification patterns highlights the specific interaction of PRX36 with the two OGAs constituting the best epitope of JIM7 and propose a different OGA candidate for similar docking of PRX56. For each OGA, the molecular docking performed on the whole PRX36 or PRX56 surface using autodock vina enabled retrieving the 9 best poses including their individual energy level (EL) and upper bound Root-mean-square deviation (RMSD) indicating the affinity of the interaction (the lower, the better) and the distance in Angstrom of each pose from pose 1 (the lower, the shorter), respectively. **(i)** Data mining was performed by calculating the sum of the EL (ΣEL) reflecting the global affinity of each OGA for PRX36 or PRX56 and the sum of RMSD (ΣRMSD) reflecting the dispersion vs concentration of the 9 poses on the protein surface. **(ii)** Then, the OGAs were sorted and ranked according to ΣEL/ΣRMSD used to as a proxy to integrate both parameters (the lowest, the highest affinity and shorter distance). Red-to-yellow and blue-to-yellow heatmaps were drawn for EL and RMSD, respectively. The EL or RMSD values appearing in bold underlined frames correspond to poses fitting to the PRX36 valley previously demonstrated (Francoz et al 2019) to accommodate the OGAs clausen 4, 3 and 5 (063-o8888o, 047-oo888o and 027-8o8o8o) that are recognized by JIM7 monoclonal antibody with decreasing affinity, respectively (Clausen et al 2003). o, demethylesterified galacturonic acid, 8, methylated galacturonic acid. Note that the docking specificity is not related to the degree of methylation (DM), but rather relies on a peculiar demethylesterification bar code. See **Sup Tables S4.1 and S4.2** to see the full data for PRX36 and PRX56, respectively.

PRX36 Rank	Clausen et al 2013	OGA (code and structure)	DP	DM	ΣEL/ ΣRMSD (ranked)	ΣEL	EL = Energy level (kcal/mol) 9 poses of docking vs all surface of PRX36									ΣRMSD	RMSD (Root-mean-square deviation) 9 poses of docking vs all surface of PRX36								
							1	2	3	4	5	6	7	8	9		1	2	3	4	5	6	7	8	9
1	Clausen 4	063-o8888o	6	67%	-1.1306	-51.3	-6.7	-6.2	-5.7	-5.6	-5.6	-5.4	-5.4	-5.4	-5.3	45.4	0.0	2.1	2.6	2.9	2.2	4.3	2.0	27.4	1.9
2	Clausen 3	047-oo888o	6	50%	-1.0269	-53.8	-6.7	-6.3	-6.2	-6.1	-5.9	-5.8	-5.7	-5.6	-5.5	52.4	0.0	6.1	4.9	4.2	5.0	7.0	1.8	4.6	18.8
9	Clausen 5	027-8o8o8o	6	50%	-0.5806	-50.9	-6.3	-6.1	-5.8	-5.8	-5.7	-5.4	-5.3	-5.3	-5.2	87.7	0.0	2.6	2.4	3.0	3.0	4.9	25.5	14.6	31.8
34		033-oooooo	6	0%	-0.4509	-60.3	-7.0	-6.9	-6.8	-6.8	-6.8	-6.6	-6.5	-6.5	-6.4	133.7	0.0	2.9	21.5	32.2	12.2	14.9	22.7	5.1	22.2
36	#1 PRX56	021-8oo8oo	6	33%	-0.4388	-55.3	-6.9	-6.3	-6.2	-6.1	-6.0	-6.0	-6.0	-5.9	-5.9	126.0	0.0	6.2	20.9	3.7	6.1	31.8	20.9	5.7	30.7
56	Clausen 2	010-88ooo8	6	50%	-0.3528	-49.4	-6.1	-5.8	-5.7	-5.6	-5.3	-5.3	-5.3	-5.2	-5.1	140.0	0.0	32.7	23.1	2.4	32.3	14.9	10.4	5.3	19.0
63	Clausen 1	018-8oooo8	6	33%	-0.2883	-51.8	-6.4	-6.2	-5.8	-5.7	-5.6	-5.6	-5.6	-5.5	-5.4	179.7	0.0	22.1	13.2	31.7	28.3	10.9	22.0	30.9	20.6
64		001-888888	6	100%	-0.2093	-41.3	-5.6	-4.8	-4.6	-4.5	-4.5	-4.4	-4.4	-4.3	-4.2	197.4	0.0	1.7	29.3	32.8	34.8	29.8	29.5	19.7	19.8

PRX56 Rank	Clausen et al 2013	Oligo-galacturonates (code and structure)	DP	DM	ΣEL/ ΣRMSD (ranked)	ΣEL	EL = Energy level (kcal/mol) 9 poses of docking vs all surface of PRX56									ΣRMSD	RMSD (Root-mean-square deviation) 9 poses of docking vs all surface of PRX56								
							1	2	3	4	5	6	7	8	9		1	2	3	4	5	6	7	8	9
1		021-8oo8oo	6	33%	-1.8201	-62.2	-7.5	-7.2	-7	-7	-6.9	-6.9	-6.6	-6.6	-6.5	34.2	0.0	2.2	2.4	2.1	5.8	6.1	1.8	2.1	11.7
2		016-88o888	6	83%	-1.4789	-60.4	-7.1	-7	-6.7	-6.7	-6.6	-6.6	-6.6	-6.6	-6.5	40.8	0.0	1.3	9.8	1.8	11.3	2.3	2.8	2.8	8.8
4		001-888888	6	100%	-1.2004	-55.6	-6.4	-6.3	-6.3	-6.2	-6.2	-6.1	-6.1	-6	-6	46.3	0.0	1.4	1.5	1.9	4.1	16.4	1.5	2.2	17.3
7	Clausen 4	063-o8888o	6	67%	-0.8509	-64.3	-7.8	-7.3	-7.2	-7.1	-7.1	-7	-7	-6.9	-6.9	75.6	0.0	1.9	2.4	7.3	8.9	4.7	9.5	6.0	34.8
13	Clausen 3	047-oo888o	6	50%	-0.5986	-61.9	-7.1	-7.1	-7	-6.9	-6.8	-6.8	-6.8	-6.7	-6.7	103.4	0.0	30.7	2.4	5.9	1.8	31.1	18.4	6.6	6.6
15	Clausen 2	010-88ooo8	6	50%	-0.5660	-62.7	-7.6	-7.4	-7.1	-6.9	-6.8	-6.8	-6.7	-6.7	-6.7	110.8	0.0	30.6	2.1	1.2	11.4	3.0	10.1	26.3	26.1
17		033-oooooo	6	0%	-0.5569	-65.2	-7.6	-7.4	-7.4	-7.3	-7.2	-7.1	-7.1	-7.1	-7	117.1	0.0	29.7	1.9	2.1	34.9	35.0	3.7	2.6	7.3
42	Clausen 5	027-8o8o8o	6	50%	-0.3996	-62.5	-7.5	-7.1	-7.1	-7	-6.9	-6.8	-6.8	-6.7	-6.6	156.4	0.0	26.7	26.8	27.5	34.1	10.2	25.8	3.7	1.6
61	Clausen 1	018-8oooo8	6	33%	-0.2730	-66.4	-7.7	-7.7	-7.6	-7.5	-7.4	-7.2	-7.2	-7.1	-7	243.2	0.0	35.3	30.4	1.0	34.5	35.3	35.2	35.7	35.8

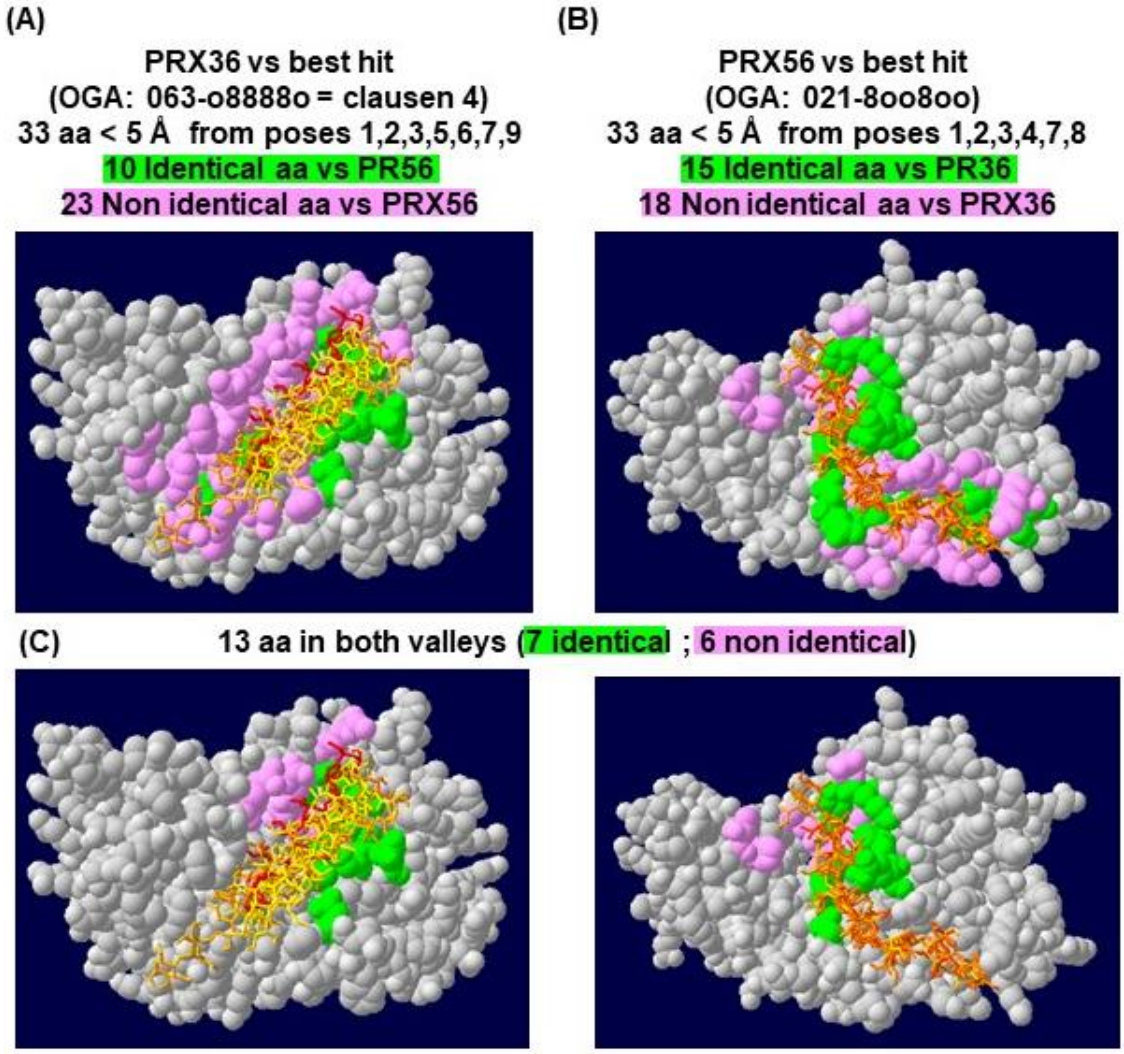

Figure 4.6 : Molecular *in silico* modeling and docking identifies putative OGA binding valley in PRX56 with a different specificity to PRX36 docking valley. (A-B) models of PRX36 and PRX56 vs their best OGA hit. The OGAs were color coded according to their relative energy levels (see legend on Figure and **Table 4.1** for detail). **(C)** The same models are show with the common amino acids to highlight that both valleys are on the same face of both proteins with almost perpendicular orientations while looking at the orientation of the respective best OGA hits.

4.4.Supplementary data

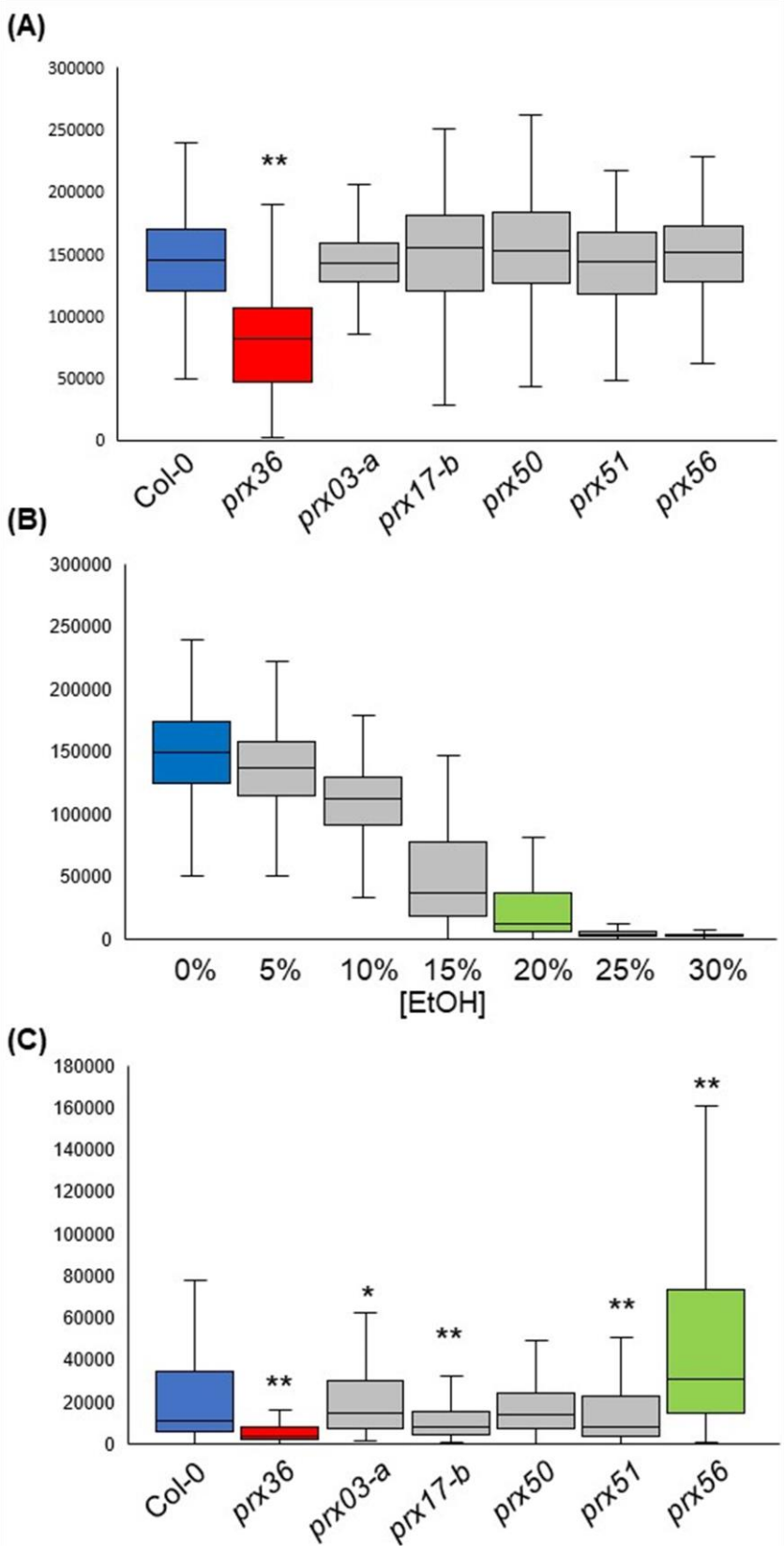

Sup. Fig. S4.1 : Box-plot view of the Figure 4.2 exploring the effect of *PRX56* mutation in mucilage release. **(A)** Ruthenium Red (RR) staining assays under aqueous condition show no definitive mucilage release abnormalities compared to Col-0 (blue), unlike *prx36 (red)* control which has significant (*p*-value < 0.01) reduction of mucilage area. Non-significative results are colored in grey **(B)** Increasing concentration of ethanol used in the RR assay on Col-0 shows that exceeding 25% ethanol leads to complete shutdown of mucilage release, therefore 25% ethanol (green) was selected as the condition to search for facilitated as well as impaired mucilage release phenotypes in *atprx* mutants. **(C)** Mucilage release assays in 25% ethanol shows mucilage area (relative to Col-0) subtle decrease for *atprx3-a*, *atprx17-2* and *atprx51* proven to be significant by Wilcoxon test compared to Col-0, and a significant prominent increase for *atprx56* compared to Col-0. N = 609-1220 seeds per biological repeat which was repeated at least twice. * show statistical significance at the 5% and ** below the 0.01% cutoff.

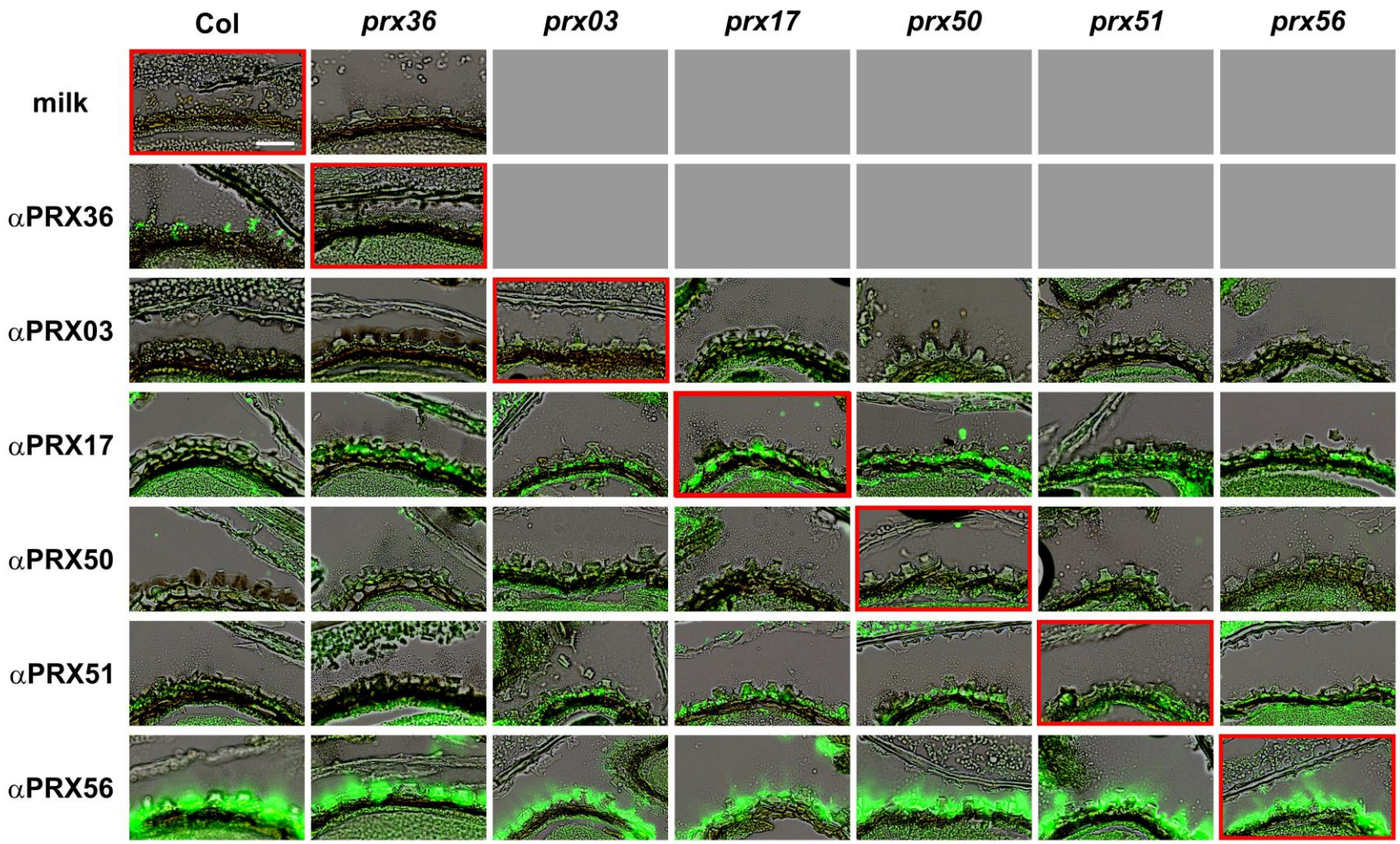

Sup. Fig. S4.2: Immunofluorescence using anti-candidate PRX antibodies on tissues arrays of developmental kinetics of all studied genotypes shows unspecific signals that are similarly present in wild type and corresponding mutants, contratry to the specific signal observed with anti-PRX36. Immunolabeling grid showing that signals, if any, observed with αPRX antipeptide do not disappear in their respective mutant MSCs. αPRX36 and *atprx36* were used as controls. Milk negative control was applied on Col-0 and *atprx36* to assess αRabbit IgG-A488 secondary antibody specificity. Grey rectangles were used for lack of data on missing experiments.

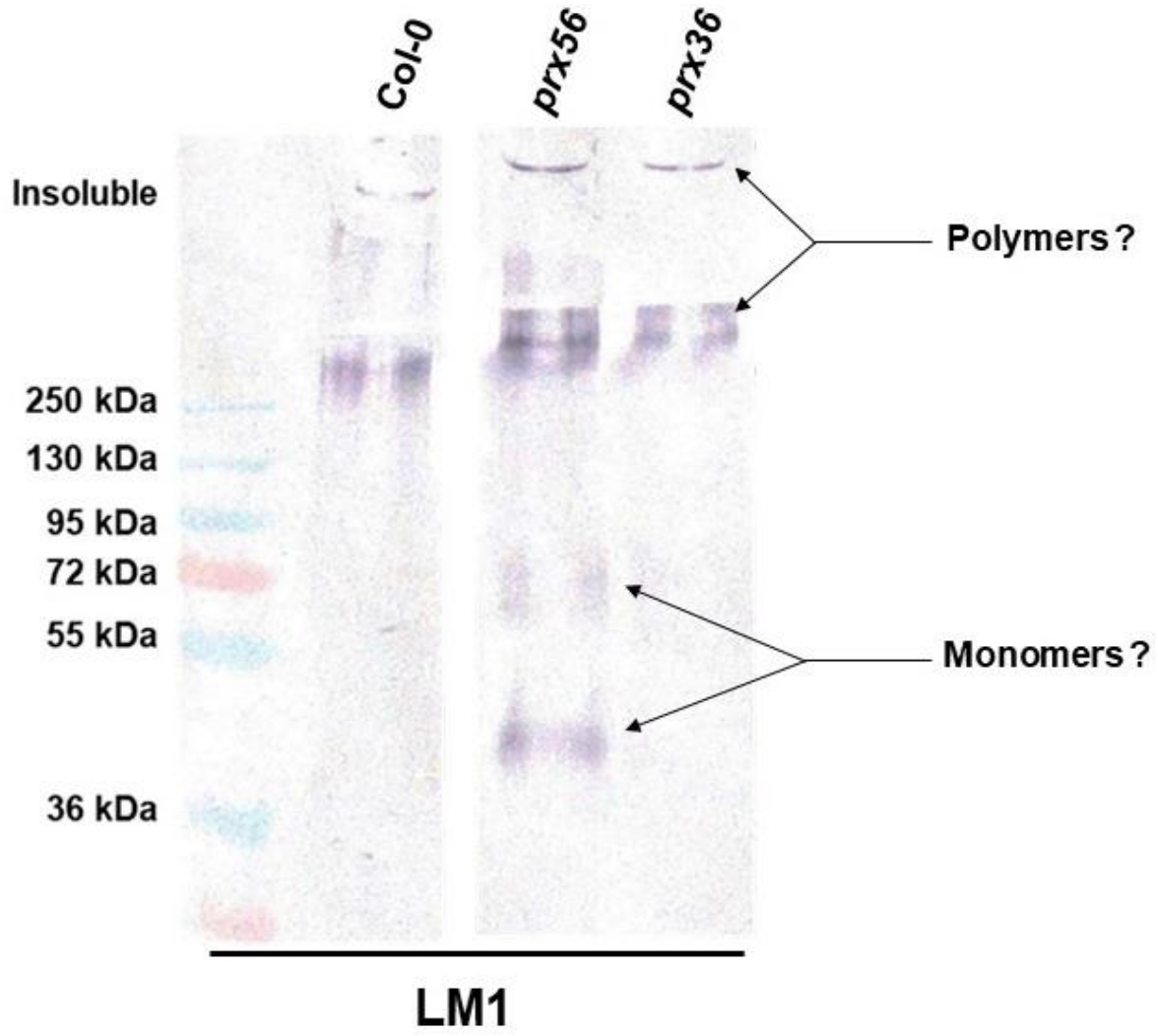

Sup. Fig. S4.3: Preliminary Western blot Electromobility Shift Assay (EMSA) using extensin specific antibody LM1 revealed striking shift in *prx56*. Extensin have varying sizes between 43 kDa and 73 kDa due to conformation changes or glycosylation. Using LM1, two additional smear/band were observed in *prx56* whose sizes corresponded with possible monomeric form of extensin while polymeric forms did not go through the stacking gel. However, this promising preliminary result was not repeated as of yet. The extraction protocol (2) was used (see Methods section 6.2.14 for details)

Sup. Table S4.1: Random systematic screening of molecular docking of PRX36 on 64 oligogalacturonates (OGA) of DP6 covering all theoretical demethyesterification patterns highlights the specific in silico interaction of PRX36 with the two hexagalacturonates constituting the epitope of JIM7. For each OGA, the molecular docking performed on the whole PRX36 surface using autodock vina enabled retrieving the 9 best poses including their individual energy level (EL) and upper bound Root-mean-square deviation (RMSD) indicating the affinity of the interaction (the lower, the better) and the distance in Angstrom of each pose from pose 1 (the lower, the shorter), respectively. **(i)** Data mining was performed by calculating the sum of the EL (□EL) reflecting the global affinity of each OGA for PRX36 and the sum of RMSD (□RMSD) reflecting the dispersion vs concentration of the 9 poses on the protein surface. **(ii)** Then, the OGAs were sorted and ranked according to □EL/□RMSD used as a proxy to integrate both parameters (the lowest, the highest affinity and shorter distance). Red-to-yellow and blue-to-yellow heatmaps were drawn for EL and RMSD, respectively. The EL or RMSD values appearing in bold underlined frames correspond to poses fitting to the PRX36 valley previously experimentally demonstrated (Francoz et al 2019) to accommodate the hexagalacturonates clausen 4, 3 and 5 (063-o8888o, 047-oo888o and 027-8o8o8o) that are recognized by JIM7 monoclonal antibody with decreasing affinity, respectively (Clausen et al 2003). o, demethylesterified galacturonic acid, 8, methylated galacturonic acid. Note that the in silico docking specificity is not related to the degree of methylation (DM), but rather relies on a peculiar demethylesterification bar code.

Rank	Clausen et al 2013	Oligo-galacturonates (code and structure)	DP	DM	ΣEL/ ΣRMSD (RANKED)	ΣEL	EL = Energy level (kcal/mol) 9 poses of docking vs all surface of PRX36									ΣRMSD	RMSD (Root-mean-square deviation) 9 poses of docking vs all surface of PRX36								
							1	2	3	4	5	6	7	8	9		1	2	3	4	5	6	7	8	9
1	Clausen 4	063-o8888o	6	67%	-1,1306	-51,3	-6,7	-6,2	-5,7	-5,6	-5,6	-5,4	-5,4	-5,4	-5,3	45,4	0,0	2,1	2,6	2,9	2,2	4,3	2,0	27,4	1,9
2	Clausen 3	047-oo888o	6	50%	-1,0269	-53,8	-6,7	-6,3	-6,2	-6,1	-5,9	-5,8	-5,7	-5,6	-5,5	52,4	0,0	6,1	4,9	4,2	5,0	7,0	1,8	4,6	18,8
3		038-ooo8o8	6	33%	-0,8588	-54,4	-6,2	-6,1	-6,1	-6,1	-6,0	-6,0	-6,0	-6,0	-5,9	63,3	0,0	3,7	5,1	3,3	1,8	20,6	4,2	5,0	19,7
4		040-ooo888	6	50%	-0,8098	-51,7	-6,0	-5,9	-5,8	-5,7	-5,7	-5,7	-5,7	-5,6	-5,6	63,8	0,0	6,5	3,0	21,0	2,3	2,9	20,1	1,6	6,4
5		041-oo8ooo	6	17%	-0,8022	-54,9	-6,8	-6,4	-6,2	-6,0	-6,0	-5,9	-5,9	-5,9	-5,8	68,4	0,0	19,4	3,1	20,5	9,1	4,9	1,8	7,5	2,1
6		024-8oo888	6	50%	-0,7954	-50,6	-5,7	-5,7	-5,7	-5,7	-5,6	-5,6	-5,6	-5,5	-5,5	63,6	0,0	21,8	4,2	2,5	15,4	3,4	2,7	2,2	11,4
7		008-888o88	6	83%	-0,7742	-58,3	-6,7	-6,7	-6,6	-6,5	-6,4	-6,4	-6,4	-6,3	-6,3	75,3	0,0	0,5	1,6	12,1	17,4	8,6	8,1	10,6	16,4
8		023-8oo88o	6	50%	-0,5895	-54,6	-7,0	-6,3	-6,1	-5,9	-5,9	-5,9	-5,9	-5,8	-5,8	92,6	0,0	8,5	9,7	8,9	2,0	21,1	18,8	7,6	15,9
9	Clausen 5	027-8o8o8o	6	50%	-0,5806	-50,9	-6,3	-6,1	-5,8	-5,8	-5,7	-5,4	-5,3	-5,3	-5,2	87,7	0,0	2,6	2,4	3,0	3,0	4,9	25,5	14,6	31,8
10		028-8o8o88	6	67%	-0,5750	-54,5	-6,7	-6,4	-6,1	-6,0	-5,9	-5,9	-5,9	-5,8	-5,8	94,8	0,0	1,7	3,5	1,9	11,1	12,6	22,2	20,9	21,0
11		009-88oooo	6	33%	-0,5662	-54,2	-6,4	-6,4	-6,2	-6,0	-5,9	-5,9	-5,8	-5,8	-5,8	95,7	0,0	21,2	3,5	21,3	11,2	21,7	3,3	8,8	4,7
12		012-88oo88	6	33%	-0,5633	-48,4	-5,6	-5,6	-5,4	-5,4	-5,4	-5,4	-5,3	-5,2	-5,1	85,9	0,0	7,6	26,7	1,8	1,8	1,9	11,1	27,9	7,0
13		059-o88o8o	6	50%	-0,5596	-54,4	-6,5	-6,2	-6,2	-6,1	-6,1	-5,9	-5,8	-5,8	-5,8	97,2	0,0	3,1	5,2	20,2	20,2	21,5	22,0	1,8	3,2
14		060-o88o88	6	67%	-0,5569	-51,5	-5,9	-5,8	-5,8	-5,7	-5,7	-5,7	-5,7	-5,6	-5,6	92,5	0,0	6,5	3,6	26,1	2,1	3,5	18,5	25,9	6,3
15		064-o88888	6	83%	-0,5366	-52,9	-6,6	-6,2	-5,9	-5,8	-5,7	-5,7	-5,7	-5,7	-5,6	98,6	0,0	3,1	2,3	3,5	20,9	21,4	5,2	20,6	21,7
16		031-8o888o	6	67%	-0,5304	-54,6	-6,8	-6,2	-6,1	-6,0	-6,0	-5,9	-5,9	-5,9	-5,8	102,9	0,0	21,4	13,8	6,2	21,5	12,1	1,8	19,8	6,4

17		015-88o88o	6	67%	-0,5291	-53,6	-6,8	-6,0	-5,9	-5,9	-5,9	-5,9	-5,8	-5,7	-5,7	101,3	0,0	1,2	5,8	5,1	20,3	19,9	21,2	13,5	14,3
18		037-ooo8oo	6	17%	-0,5218	-55,6	-7,0	-6,5	-6,2	-6,2	-6,1	-6,0	-5,9	-5,9	-5,8	106,6	0,0	1,6	2,9	21,1	13,8	4,4	21,0	20,4	21,2
19		029-8o88oo	6	50%	-0,5124	-54,8	-7,0	-6,2	-6,1	-6,0	-6,0	-5,9	-5,9	-5,9	-5,8	107,0	0,0	1,6	2,1	11,6	21,2	25,4	2,3	21,0	21,7
20		051-o8oo8o	6	33%	-0,5093	-56,4	-6,7	-6,5	-6,5	-6,3	-6,2	-6,2	-6,0	-6,0	-6,0	110,7	0,0	8,6	8,2	6,0	1,7	31,5	21,2	12,5	20,9
21		007-888o8o	6	67%	-0,5085	-53,8	-6,6	-6,3	-6,0	-5,9	-5,9	-5,8	-5,8	-5,8	-5,7	105,8	0,0	1,8	1,7	5,5	20,3	11,8	21,1	21,3	22,2
22		049-o8oooo	6	17%	-0,5047	-57,8	-6,8	-6,8	-6,6	-6,5	-6,3	-6,3	-6,2	-6,2	-6,1	114,5	0,0	11,3	11,1	1,7	12,7	25,9	25,0	2,8	24,2
23		061-o888oo	6	50%	-0,4987	-53,6	-6,6	-6,3	-5,9	-5,9	-5,9	-5,8	-5,8	-5,7	-5,7	107,5	0,0	3,1	21,9	14,1	22,3	4,3	20,2	8,9	12,7
24		044-oo8o88	6	50%	-0,4965	-54,7	-6,8	-6,6	-6,0	-5,9	-5,9	-5,9	-5,9	-5,9	-5,8	110,2	0,0	1,7	5,5	11,6	20,4	34,0	21,0	14,1	1,9
25	_	050-o8ooo8	6	33%	-0,4929	-52,8	-6,1	-6,0	-6,0	-5,9	-5,8	-5,8	-5,8	-5,7	-5,7	107,1	0,0	25,4	24,5	14,9	2,0	14,8	1,6	6,7	17,2
26	_	052-o8oo88	6	50%	-0,4861	-52,5	-6,1	-5,9	-5,9	-5,8	-5,8	-5,8	-5,8	-5,7	-5,7	108,0	0,0	21,2	5,2	4,5	5,6	30,0	29,2	6,7	5,6
27		016-88o888	6	83%	-0,4778	-51,5	-6,7	-5,8	-5,7	-5,6	-5,6	-5,6	-5,6	-5,5	-5,4	107,8	0,0	6,2	3,5	21,4	22,7	11,8	4,1	29,2	8,8
28		039-ooo88o	6	33%	-0,4730	-56,2	-6,4	-6,3	-6,3	-6,3	-6,2	-6,2	-6,2	-6,2	-6,1	118,8	0,0	24,8	6,5	20,3	12,0	24,3	1,6	24,0	5,4
29		062-o888o8	6	67%	-0,4719	-54,1	-6,5	-6,1	-6,1	-6,0	-5,9	-5,9	-5,9	-5,9	-5,8	114,6	0,0	6,6	5,8	2,7	21,8	5,2	21,4	29,2	22,0
30		013-88o8oo	6	50%	-0,4711	-53,9	-6,7	-6,0	-6,0	-5,9	-5,9	-5,9	-5,9	-5,8	-5,8	114,4	0,0	20,8	20,9	6,1	32,2	21,2	4,6	3,0	5,6
31		036-oooo88	6	33%	-0,4697	-53,2	-6,1	-6,0	-6,0	-5,9	-5,9	-5,9	-5,8	-5,8	-5,8	113,3	0,0	22,3	12,3	17,1	23,6	13,3	12,2	7,3	5,2
32		003-8888oo	6	67%	-0,4682	-54,7	-6,8	-6,3	-6,2	-6,0	-6,0	-5,9	-5,9	-5,8	-5,8	116,8	0,0	3,2	1,7	21,0	19,3	5,3	14,7	20,4	31,2
33		048-oo8888	6	67%	-0,4663	-56,3	-6,8	-6,7	-6,2	-6,2	-6,2	-6,1	-6,1	-6,0	-6,0	120,7	0,0	1,7	20,6	21,1	1,2	21,0	21,8	20,3	13,2
34	_	033-oooooo	6	0%	-0,4509	-60,3	-7,0	-6,9	-6,8	-6,8	-6,8	-6,6	-6,5	-6,5	-6,4	133,7	0,0	2,9	21,5	32,2	12,2	14,9	22,7	5,1	22,2
35		006-888oo8	6	67%	-0,4508	-51,7	-6,1	-5,9	-5,8	-5,7	-5,7	-5,7	-5,6	-5,6	-5,6	114,7	0,0	11,8	23,5	3,0	26,6	28,5	1,7	2,0	17,6
36	#1 PRX56	021-8oo8oo	6	33%	-0,4388	-55,3	-6,9	-6,3	-6,2	-6,1	-6,0	-6,0	-6,0	-5,9	-5,9	126,0	0,0	6,2	20,9	3,7	6,1	31,8	20,9	5,7	30,7
37		014-88o8o8	6	67%	-0,4382	-54,1	-6,8	-6,3	-6,1	-6,0	-6,0	-5,8	-5,8	-5,7	-5,6	123,5	0,0	7,6	21,7	4,0	21,5	11,6	12,1	22,1	22,8
38		042-oo8oo8	6	33%	-0,4325	-55,9	-6,8	-6,4	-6,2	-6,1	-6,1	-6,1	-6,1	-6,1	-6,0	129,2	0,0	11,7	19,9	21,0	21,2	1,8	12,9	20,4	20,3
39		055-o8o88o	6	50%	-0,4253	-54,9	-6,6	-6,2	-6,1	-6,0	-6,0	-6,0	-6,0	-6,0	-6,0	129,1	0,0	5,9	11,8	3,6	20,3	22,2	21,4	22,0	21,7
40		054-o8o8o8	6	50%	-0,4214	-54,3	-6,5	-6,1	-6,0	-6,0	-6,0	-6,0	-5,9	-5,9	-5,9	128,9	0,0	3,0	8,9	21,8	22,4	23,2	24,1	21,3	4,2
41		011-88oo8o	6	50%	-0,4206	-55,4	-6,5	-6,3	-6,3	-6,2	-6,1	-6,0	-6,0	-6,0	-6,0	131,7	0,0	31,6	21,4	21,5	21,2	4,1	20,3	8,5	3,2
42		002-88888o	6	67%	-0,4200	-52,7	-6,7	-6,1	-5,9	-5,9	-5,8	-5,7	-5,6	-5,5	-5,5	125,5	0,0	3,0	19,1	3,0	8,4	20,1	31,7	19,9	20,3
43	_	034-ooooo8	6	17%	-0,4197	-51,3	-5,8	-5,8	-5,8	-5,7	-5,7	-5,7	-5,6	-5,6	-5,6	122,2	0,0	27,2	16,8	28,9	13,5	2,3	2,7	28,7	2,2

44		030-8o88o8	6	67%	-0,4139	-50,9	-5,9	-5,9	-5,7	-5,6	-5,6	-5,6	-5,6	-5,5	-5,5	123,0	0,0	11,2	26,6	10,9	1,8	12,0	28,3	4,1	28,2
45		045-oo88oo	6	33%	-0,4052	-55,0	-6,9	-6,2	-6,1	-6,0	-6,0	-6,0	-6,0	-5,9	-5,9	135,7	0,0	1,6	22,2	11,3	14,2	20,5	23,0	21,0	21,8
46		019-8ooo8o	6	33%	-0,4046	-55,9	-7,0	-6,3	-6,2	-6,1	-6,1	-6,1	-6,1	-6,0	-6,0	138,2	0,0	3,3	31,0	21,7	2,0	31,6	20,8	21,9	5,9
47		025-8o8ooo	6	33%	-0,4014	-54,1	-6,8	-6,4	-6,0	-5,9	-5,9	-5,9	-5,8	-5,7	-5,7	134,8	0,0	3,3	31,6	22,5	5,5	23,3	20,5	21,1	6,9
48		057-o88ooo	6	33%	-0,4010	-51,8	-6,0	-5,9	-5,9	-5,8	-5,8	-5,6	-5,6	-5,6	-5,6	129,2	0,0	24,4	24,4	24,1	24,3	12,2	5,1	1,8	12,9
49		005-888ooo	6	50%	-0,3864	-52,2	-6,3	-6,1	-5,9	-5,8	-5,7	-5,6	-5,6	-5,6	-5,6	135,1	0,0	21,6	21,6	3,1	11,2	18,5	31,3	12,5	15,2
50		058-o88oo8	6	50%	-0,3817	-56,0	-6,4	-6,4	-6,3	-6,2	-6,2	-6,2	-6,2	-6,1	-6,0	146,7	0,0	27,2	25,3	4,4	14,0	25,3	2,0	23,2	25,3
51		017-8ooooo	6	17%	-0,3754	-53,3	-6,2	-6,1	-6,1	-6,0	-5,9	-5,8	-5,8	-5,7	-5,7	142,0	0,0	8,5	14,9	23,7	15,9	22,6	23,7	10,4	22,3
52		022-8oo8o8	6	50%	-0,3721	-52,5	-6,8	-6,0	-5,8	-5,7	-5,7	-5,7	-5,6	-5,6	-5,6	141,1	0,0	5,2	20,5	18,8	19,5	20,6	3,4	21,1	31,9
53		056-o8o888	6	67%	-0,3572	-53,8	-6,1	-6,1	-6,0	-6,0	-6,0	-6,0	-5,9	-5,9	-5,8	150,6	0,0	25,2	14,5	26,9	1,6	26,5	24,1	6,1	25,8
54		046-oo88o8	6	50%	-0,3544	-54,7	-6,8	-6,3	-6,1	-6,0	-5,9	-5,9	-5,9	-5,9	-5,9	154,4	0,0	21,4	21,1	6,8	20,4	19,8	21,7	21,1	22,1
55		020-8ooo88	6	50%	-0,3528	-53,6	-6,4	-6,1	-6,0	-6,0	-5,9	-5,8	-5,8	-5,8	-5,8	151,9	0,0	1,7	1,2	24,3	25,8	24,3	24,7	24,8	25,2
56	Clausen 2	010-88ooo8	6	50%	-0,3528	-49,4	-6,1	-5,8	-5,7	-5,6	-5,3	-5,3	-5,3	-5,2	-5,1	140,0	0,0	32,7	23,1	2,4	32,3	14,9	10,4	5,3	19,0
57		043-oo8o8o	6	33%	-0,3515	-54,8	-6,2	-6,2	-6,2	-6,1	-6,1	-6,1	-6,0	-6,0	-5,9	155,9	0,0	23,8	27,2	27,4	23,2	25,2	1,9	3,7	23,5
58		032-8o8888	6	83%	-0,3506	-52,5	-6,7	-5,8	-5,8	-5,7	-5,7	-5,7	-5,7	-5,7	-5,7	149,8	0,0	6,1	21,2	31,9	3,3	21,3	5,2	30,8	29,9
59		035-oooo8o	6	17%	-0,3349	-57,3	-6,6	-6,5	-6,5	-6,4	-6,4	-6,4	-6,2	-6,2	-6,1	171,1	0,0	11,4	25,4	24,7	21,1	14,7	23,7	24,5	25,7
60	_	026-8o8oo8	6	50%	-0,3168	-49,2	-5,8	-5,7	-5,7	-5,5	-5,4	-5,4	-5,3	-5,2	-5,2	155,3	0,0	5,7	31,3	20,2	29,7	22,1	4,9	25,0	16,4
61		004-8888o8	6	83%	-0,3121	-50,6	-6,0	-5,7	-5,7	-5,7	-5,6	-5,6	-5,5	-5,4	-5,4	162,1	0,0	24,1	24,6	17,0	28,7	32,7	12,9	6,5	15,5
62		053-o8o8oo	6	33%	-0,2950	-51,4	-6,1	-5,9	-5,8	-5,7	-5,7	-5,6	-5,6	-5,5	-5,5	174,3	0,0	8,9	33,4	31,0	18,2	16,1	16,6	16,7	33,4
63	Clausen 1	018-8ooooo8	6	33%	-0,2883	-51,8	-6,4	-6,2	-5,8	-5,7	-5,6	-5,6	-5,6	-5,5	-5,4	179,7	0,0	22,1	13,2	31,7	28,3	10,9	22,0	30,9	20,6
64		001-888888	6	100%	-0,2093	-41,3	-5,6	-4,8	-4,6	-4,5	-4,5	-4,4	-4,4	-4,3	-4,2	197,4	0,0	1,7	29,3	32,8	34,8	29,8	29,5	19,7	19,8

Sup Table S4.2: Random systematic screening of in silico molecular docking of PRX56 on 64 oligogalacturonates (OGA) of DP6 covering all theoretical demethyesterification patterns identify a candidate OGA and a docking valley. For each OGA, the in silico molecular docking performed on the whole PRX56 surface using autodock vina enabled retrieving the 9 best poses including their individual energy level (EL) and upper bound Root-mean-square deviation (RMSD) indicating the affinity of the interaction (the lower, the better) and the distance in Angstrom of each pose from pose 1 (the lower, the shorter), respectively. **(i)** Data mining was performed by calculating the sum of the EL (□EL) reflecting the global affinity of each OGA for PRX56 and the sum of RMSD (□RMSD) reflecting the dispersion vs concentration of the 9 poses on the protein surface. **(ii)** Then, the OGAs were sorted and ranked according to □EL/□RMSD used as a proxy to integrate both parameters (the lowest, the highest affinity and shorter distance). Red-to-yellow and blue-to-yellow heatmaps were drawn for EL and RMSD, respectively. Note the different profile obtained as compared to PRX36 and the very good score of OGA ranked 1: 021 (8oo800). o, demethylesterified galacturonic acid, 8, methylated galacturonic acid. Note that the *in silico* docking specificity is not related to the degree of methylation (DM), but rather relies on a peculiar demethylesterification bar code.

Rank	Clausen et al 2013	Oligo-galacturonates (code and structure)	DP	DM	ΣEL/ ΣRMSD (RANKED)	ΣEL	EL = Energy level (kcal/mol) 9 poses of docking vs all surface of PRX56									ΣRMSD	RMSD (Root-mean-square deviation) 9 poses of docking vs all surface of PRX56								
							1	2	3	4	5	6	7	8	9		1	2	3	4	5	6	7	8	9
1		021-8oo8oo	6	33%	-1,8201	-62,2	-7,5	-7,2	-7	-7	-6,9	-6,9	-6,6	-6,6	-6,5	34,2	0,0	2,2	2,4	2,1	5,8	6,1	1,8	2,1	11,7
2		016-88o888	6	83%	-1,4789	-60,4	-7,1	-7	-6,7	-6,7	-6,6	-6,6	-6,6	-6,6	-6,5	40,8	0,0	1,3	9,8	1,8	11,3	2,3	2,8	2,8	8,8
3		064-o88888	6	83%	-1,3057	-61,8	-7,6	-7,2	-7	-6,9	-6,8	-6,7	-6,6	-6,5	-6,5	47,3	0,0	1,8	1,9	3,6	11,0	3,9	2,3	8,7	14,1
4		001-888888	6	100%	-1,2004	-55,6	-6,4	-6,3	-6,3	-6,2	-6,2	-6,1	-6,1	-6	-6	46,3	0,0	1,4	1,5	1,9	4,1	16,4	1,5	2,2	17,3
5		062-o888o8	6	67%	-1,1486	-63,0	-7,5	-7,2	-7,1	-7	-6,9	-6,9	-6,8	-6,8	-6,8	54,9	0,0	1,9	10,0	4,6	4,1	2,0	10,9	11,3	10,2
6		006-888oo8	6	67%	-1,0469	-62,9	-7,7	-7,1	-7,1	-7,1	-6,9	-6,8	-6,8	-6,8	-6,6	60,1	0,0	4,2	1,8	3,1	4,7	3,0	6,7	34,6	2,0
7	Clausen4	063-o8888o	6	67%	-0,8509	-64,3	-7,8	-7,3	-7,2	-7,1	-7,1	-7	-7	-6,9	-6,9	75,6	0,0	1,9	2,4	7,3	8,9	4,7	9,5	6,0	34,8
8		059-o88o8o	6	50%	-0,8333	-64,2	-7,6	-7,6	-7,4	-7,1	-7	-7	-6,9	-6,8	-6,8	77,0	0,0	26,7	2,3	23,9	6,1	4,3	3,7	4,2	5,9
9		004-8888o8	6	83%	-0,7878	-61,9	-7,1	-7	-6,9	-6,9	-6,8	-6,8	-6,8	-6,8	-6,8	78,6	0,0	4,4	24,7	25,7	1,5	3,7	3,9	7,7	6,9
10		060-o88o88	6	67%	-0,7283	-63,8	-7,6	-7,5	-7,3	-7,2	-7,2	-7,1	-7	-6,5	-6,4	87,6	0,0	2,3	1,8	26,9	2,1	10,0	6,0	11,7	26,8
11		019-8ooo8o	6	33%	-0,6409	-61,2	-7,1	-6,9	-6,9	-6,9	-6,8	-6,7	-6,7	-6,6	-6,6	95,5	0,0	10,4	31,9	1,2	2,5	22,5	3,4	2,3	21,1
12		032-8o8888	6	83%	-0,5996	-62,3	-7,3	-7,1	-7	-7	-6,9	-6,9	-6,9	-6,6	-6,6	103,9	0,0	2,8	2,0	25,4	1,8	25,7	30,4	4,4	11,5
13	Clausen3	047-oo888o	6	50%	-0,5986	-61,9	-7,1	-7,1	-7	-6,9	-6,8	-6,8	-6,8	-6,7	-6,7	103,4	0,0	30,7	2,4	5,9	1,8	31,1	18,4	6,6	6,6
14		013-88o8oo	6	50%	-0,5702	-61,8	-7,4	-6,9	-6,9	-6,8	-6,8	-6,8	-6,8	-6,7	-6,7	108,4	0,0	2,2	7,5	4,3	8,7	34,7	1,3	14,0	35,7
15	Clausen2	010-88ooo8	6	50%	-0,5660	-62,7	-7,6	-7,4	-7,1	-6,9	-6,8	-6,8	-6,7	-6,7	-6,7	110,8	0,0	30,6	2,1	1,2	11,4	3,0	10,1	26,3	26,1
16		030-8o88o8	6	67%	-0,5603	-61,9	-7,2	-7	-7	-6,8	-6,8	-6,8	-6,8	-6,8	-6,7	110,5	0,0	26,0	6,0	22,5	7,4	7,5	25,5	7,8	7,9
17		033-oooooo	6	0%	-0,5569	-65,2	-7,6	-7,4	-7,4	-7,3	-7,2	-7,1	-7,1	-7,1	-7	117,1	0,0	29,7	1,9	2,1	34,9	35,0	3,7	2,6	7,3

18		015-88o88o	6	67%	-0,5445	-63,6	-7,2	-7,1	-7,1	-7,1	-7,1	-7,1	-7	-7	-6,9	116,8	0,0	30,1	32,0	2,3	20,5	2,0	25,9	2,3	1,8
19		042-oo8oo8	6	33%	-0,5366	-63,8	-7,7	-7,2	-7,2	-7,1	-7,1	-7	-6,9	-6,8	-6,8	118,9	0,0	30,0	2,2	10,3	4,4	3,7	4,5	34,9	28,9
20		035-oooo8o	6	17%	-0,5358	-63,5	-7,5	-7,2	-7,2	-7,1	-7	-6,9	-6,9	-6,9	-6,8	118,5	0,0	1,8	2,0	35,3	30,1	36,4	7,5	2,8	2,5
21		049-o8oooo	6	17%	-0,5313	-66,2	-7,5	-7,5	-7,4	-7,4	-7,4	-7,4	-7,2	-7,2	-7,2	124,6	0,0	23,0	1,5	19,7	33,9	7,3	34,2	2,4	2,7
22		056-o8o888	6	67%	-0,5304	-62,5	-7,3	-7,3	-6,9	-6,9	-6,9	-6,8	-6,8	-6,8	-6,8	117,8	0,0	27,0	25,4	1,1	4,5	1,8	2,6	25,0	30,4
23		023-8oo88o	6	50%	-0,5252	-61,1	-7,3	-7	-6,9	-6,8	-6,7	-6,6	-6,6	-6,6	-6,6	116,3	0,0	2,0	35,0	26,9	5,9	6,8	4,1	6,2	29,5
24		061-o888oo	6	50%	-0,5194	-64,2	-7,7	-7,3	-7,3	-7,2	-7	-7	-6,9	-6,9	-6,9	123,6	0,0	2,3	3,8	30,6	28,2	10,8	10,8	35,1	2,0
25		024-8oo888	6	67%	-0,5037	-62,4	-7,4	-7,1	-7	-7	-6,9	-6,9	-6,7	-6,7	-6,7	123,9	0,0	34,9	35,2	1,2	1,9	2,8	10,5	10,9	26,4
26		058-o88oo8	6	50%	-0,5032	-63,9	-7,8	-7,5	-7,2	-6,9	-6,9	-6,9	-6,9	-6,9	-6,9	127,0	0,0	30,5	35,1	6,1	2,6	34,9	3,1	10,7	3,9
27		051-o8oo8o	6	33%	-0,4870	-64,0	-7,6	-7,4	-7,3	-7,1	-7	-7	-7	-6,9	-6,7	131,4	0,0	27,1	1,3	23,4	16,4	19,9	1,3	8,3	33,7
28		005-888ooo	6	50%	-0,4746	-62,0	-7,4	-7,1	-7,1	-6,9	-6,8	-6,8	-6,7	-6,6	-6,6	130,6	0,0	1,9	26,6	30,3	2,0	26,5	25,6	4,6	13,2
29		031-8o888o	6	67%	-0,4741	-62,4	-7,4	-7,1	-7	-7	-6,9	-6,8	-6,8	-6,7	-6,7	131,6	0,0	1,9	34,8	2,2	34,7	2,8	5,9	14,2	35,1
30		029-8o88oo	6	50%	-0,4654	-62,5	-7,6	-7,1	-6,9	-6,9	-6,8	-6,8	-6,8	-6,8	-6,8	134,3	0,0	2,1	2,2	34,0	9,6	5,4	35,6	34,7	10,6
31		007-888o8o	6	67%	-0,4452	-62,8	-7,6	-7,1	-7,1	-7	-7	-6,9	-6,8	-6,7	-6,6	141,1	0,0	27,0	9,4	25,9	10,3	25,8	1,6	10,4	30,6
32		025-8o8ooo	6	33%	-0,4356	-64,6	-7,7	-7,6	-7,1	-7,1	-7,1	-7,1	-7	-7	-6,9	148,3	0,0	1,9	2,0	9,5	34,8	10,0	34,0	30,2	25,7
33		041-oo8ooo	6	17%	-0,4234	-66,9	-7,8	-7,7	-7,6	-7,6	-7,3	-7,3	-7,2	-7,2	-7,2	158,0	0,0	2,0	3,7	1,3	34,9	36,0	9,9	35,3	35,0
34		036-oooo88	6	33%	-0,4190	-62,7	-7,5	-7,4	-7,2	-7	-6,8	-6,7	-6,7	-6,7	-6,7	149,6	0,0	1,5	2,3	11,1	5,3	27,5	28,3	36,3	37,4
35		046-oo88o8	6	50%	-0,4163	-62,9	-7,6	-7,2	-7	-7	-6,9	-6,9	-6,8	-6,8	-6,7	151,1	0,0	30,5	2,1	35,0	34,7	35,0	3,7	4,1	6,0
36		022-8oo8o8	6	50%	-0,4129	-62,5	-7,5	-7,2	-7,2	-6,9	-6,9	-6,8	-6,8	-6,6	-6,6	151,4	0,0	1,3	35,0	9,0	34,9	23,3	6,3	7,2	34,4
37		055-o8o88o	6	50%	-0,4100	-62,9	-7,6	-7	-7	-7	-6,9	-6,9	-6,9	-6,9	-6,7	153,4	0,0	29,9	7,6	10,9	2,2	27,0	3,8	35,3	36,7
38		011-88oo8o	6	50%	-0,4091	-61,6	-7,4	-6,9	-6,8	-6,8	-6,8	-6,8	-6,7	-6,7	-6,7	150,6	0,0	26,9	13,5	25,9	7,3	34,8	2,1	4,4	35,7
39		003-8888oo	6	67%	-0,4065	-61,2	-6,9	-6,9	-6,9	-6,9	-6,8	-6,8	-6,7	-6,7	-6,6	150,6	0,0	10,4	22,7	30,2	21,6	30,3	2,0	30,8	2,6
40		002-88888o	6	83%	-0,4058	-61,0	-7,5	-7	-6,8	-6,7	-6,7	-6,7	-6,6	-6,5	-6,5	150,3	0,0	1,8	6,1	34,6	24,6	10,6	27,2	10,5	34,9
41		050-o8ooo8	6	33%	-0,4007	-63,8	-7,4	-7,3	-7,2	-7,2	-7,1	-6,9	-6,9	-6,9	-6,9	159,2	0,0	23,4	22,8	21,7	21,0	38,1	10,4	11,2	10,6
42	Clausen5	027-8o8o8o	6	50%	-0,3996	-62,5	-7,5	-7,1	-7,1	-7	-6,9	-6,8	-6,8	-6,7	-6,6	156,4	0,0	26,7	26,8	27,5	34,1	10,2	25,8	3,7	1,6
43		038-ooo8o8	6	33%	-0,3979	-63,6	-7,6	-7,3	-7,2	-7	-7	-6,9	-6,9	-6,9	-6,8	159,8	0,0	30,8	2,2	10,9	34,9	10,1	28,7	34,9	7,2
44		037-ooo8oo	6	17%	-0,3953	-61,2	-7,3	-7,2	-7	-6,8	-6,7	-6,6	-6,6	-6,5	-6,5	154,8	0,0	26,8	30,8	4,1	23,8	2,6	34,7	4,3	27,7

45		052-o8oo88	6	50%	-0,3904	-63,2	-7,4	-7,2	-7,1	-7	-7	-7	-7	-6,8	-6,7	161,9	0,0	21,3	35,6	20,0	22,5	1,9	16,6	21,0	23,0
46		008-888o88	6	83%	-0,3885	-61,0	-7,4	-6,8	-6,8	-6,8	-6,7	-6,7	-6,7	-6,6	-6,5	157,0	0,0	35,2	34,3	23,3	34,8	14,6	1,9	1,7	11,3
47		012-88oo88	6	67%	-0,3874	-60,0	-6,9	-6,8	-6,7	-6,7	-6,7	-6,6	-6,6	-6,5	-6,5	154,9	0,0	20,8	23,6	23,7	21,4	1,4	20,8	20,3	22,8
48		044-oo8o88	6	50%	-0,3822	-64,8	-7,7	-7,4	-7,3	-7,2	-7,1	-7,1	-7,1	-7	-6,9	169,5	0,0	2,2	35,1	26,3	27,3	35,0	34,8	2,3	6,5
49		026-8o8oo8	6	50%	-0,3658	-64,1	-7,5	-7,3	-7,2	-7,1	-7,1	-7,1	-7	-6,9	-6,9	175,2	0,0	1,9	34,8	34,3	35,1	2,2	32,1	6,2	28,6
50		057-o88ooo	6	33%	-0,3563	-63,9	-7,9	-7,1	-7,1	-7,1	-7	-7	-7	-6,9	-6,8	179,3	0,0	35,1	2,0	25,5	35,1	10,3	34,7	34,7	2,0
51		043-oo8o8o	6	33%	-0,3521	-61,6	-7,2	-7	-7	-6,8	-6,8	-6,7	-6,7	-6,7	-6,7	175,0	0,0	7,9	23,8	4,0	22,9	34,3	26,6	23,1	32,4
52		014-88o8o8	6	67%	-0,3517	-62,4	-7,4	-7,1	-7,1	-7,1	-6,8	-6,8	-6,7	-6,7	-6,7	177,4	0,0	34,9	30,1	1,1	34,8	32,6	28,2	6,2	9,4
53		028-8o8o88	6	67%	-0,3503	-63,4	-7,4	-7,2	-7,1	-7	-7	-7	-7	-6,9	-6,8	181,0	0,0	34,9	27,1	26,6	9,1	26,1	29,2	1,8	26,2
54		009-88oooo	6	33%	-0,3463	-63,1	-7,5	-7,4	-7,3	-7,1	-7	-6,8	-6,7	-6,7	-6,6	182,2	0,0	30,5	1,9	26,8	14,1	26,0	26,0	28,6	28,4
55		017-8ooooo	6	17%	-0,3395	-65,0	-7,6	-7,5	-7,3	-7,2	-7,1	-7,1	-7,1	-7,1	-7	191,4	0,0	2,5	30,0	2,0	26,5	35,1	34,5	34,1	26,7
56		039-ooo88o	6	33%	-0,3377	-64,6	-7,6	-7,3	-7,3	-7,2	-7,2	-7	-7	-7	-7	191,3	0,0	35,2	2,2	35,2	4,2	35,1	35,5	8,5	35,4
57		034-oooooo8	6	17%	-0,3334	-62,4	-7,4	-7,1	-7	-7	-6,9	-6,9	-6,7	-6,7	-6,7	187,2	0,0	34,9	35,2	31,1	35,2	7,6	34,7	2,0	6,4
58		045-oo88oo	6	33%	-0,3254	-64,4	-7,3	-7,3	-7,3	-7,2	-7,2	-7,2	-7	-7	-6,9	197,9	0,0	30,5	26,1	35,0	34,8	24,9	28,5	12,0	6,0
59		054-o8o8o8	6	50%	-0,3082	-60,9	-7,3	-7	-6,9	-6,8	-6,8	-6,6	-6,5	-6,5	-6,5	197,6	0,0	21,2	26,1	24,5	25,1	31,1	36,0	31,1	2,4
60		048-oo8888	6	67%	-0,2947	-64,0	-7,6	-7,4	-7,3	-7,1	-7	-6,9	-6,9	-6,9	-6,9	217,1	0,0	1,1	34,9	35,9	35,1	3,7	35,2	36,3	35,0
61	Clausen1	018-8oooo8	6	33%	-0,2730	-66,4	-7,7	-7,7	-7,6	-7,5	-7,4	-7,2	-7,2	-7,1	-7	243,2	0,0	35,3	30,4	1,0	34,5	35,3	35,2	35,7	35,8

5. Chapter five: Conclusions and perspectives

Mucilage secretory cells host a unique diversity of CW remodeling events throughout their development. Recent studies have highlighted molecular mecanisms underlying mucilage release after seed imbibition. In a local CW microdomain located at the top of the radial primary wall, PMEI6 activity on putative PME(s) creates a pattern of methylesterification in HG. This pattern is used by PRX36 to anchor itself in this CW microdomain and to induce local CW loosening, likely through ROS generation. Such molecular scaffold justifying the precise positionning of CW remodeling actors is key to understand how plants orchestrate local control of their CW properties during development. As such, we aimed to further characterize the PRX36-PMEI6 molecular scaffold and possible additional actors. Because *PRX36-PMEI6* expression patterns were similar, we selected 5 genes whose expression were either similar to that of *PRX36* or presented interesting putative functions.

In the first part, we screened each gene for (i) their specific expression in MSC, (ii) their involvement in the molecular scaffold leading to the HG methylesterified pattern, (ii) the consequence of gene mutation on PRX36 anchoring in its CW microdomain and (iv) the consequences of their mutation in mucilage release. We localized apoplastic proteins in MSC and correlated phenotype results and subcellular positionning to assess the relevancy of each candidate in our study. Early on, we dismissed DUF1191 and CASPL2A1 as they did not display any interesting phenotype in our analyses. Although it is likely that our screening methods could not exhaustively analyse the putative role of each gene, both *duf1191* and *caspl2a1* showed lack of changes in HG methylation, PRX36 anchoring and mucilage release. Similar results were obtained for PME16 which was however localized to the PRX36 CW microdomain, together with PMEI6. At this time, our experimental results cannot exclude PME6/HMS from being part of PRX36 scaffold, but combined with the Levesque- Tremblay (2015) works, it is likely that the observed mucilage release phenotype is due to defect in embryo growth rather than being related to PRX36 misslocalization. Still, we confirmed that PME6/HMS had similar positionning than aforementioned PME16/PMEI6. Therefore, it is possible that functional redundancy / putative increase in PME expression in one mutant could compensate for single *PME* mutation (**Figure 5.1**). Double *pme16 x pme6/hms* mutant would help assess this possibility, but it is possible that the correct PME candidate(s) lies in other MSC expressed *PMEs* that could not be included in this study. Moreover, while many of these proteins were similarly localized to the outer radial primary wall, subtle differences in localization may explain lack of direct relationship and/or consequences PRX36 localization. Indeed, PMEI6 punctuated localization may explain the fact that PRX36 was not fully

mislocalized in *pmei6* (Francoz et al., 2019b) and hot spots of localization of PME6/HMS in tricellular junctions do not fully correspond to PRX36 localization pattern. FRET-FLIM experiments would be also interesting to decipher more accurate proximity and possible protein-protein interaction, especially for the two PMEs vs PMEI6. Finally, our initial screen revealed TBL38 as an interesting candidate in which HG methylation status seemed altered.

In the second part, we focused on functional characterization of TBL38 as a promising candidate for HG remodeling. Historically, TBLs were mostly Golgi-localized acetyltransferase proteins (with one exception in the CW) active on multiple specific CW polysaccharides. Our results indicated that TBL38 was a CW localized protein accumulating to the PRX36/PMEI6 CW microdomain, with an atypical acetyl-esterase activity on HG (**Figure 5.1**). Although TBLs functional domain are similar to esterase proteins despite their acetyl transferase activities, TBL38 modeling did not reveal any particular changes in key amino acid residues which could explain such particular activity. As such, we hypothesized that TBL38 could be an active acetyltransferase should it be artificially localized in the Golgi (which we did not tested yet). TBL38 would act as an acetylesterase because of its environment in the CW where to our knowledge, no acetyl-CoA is present. Although TBL38 had similar localization than PRX36, we did not see major changes in PRX36 anchoring and subsequent mucilage release in *tbl38*. However, mucilage release was facilited in *tbl38* in $CaCl_2$ solution, supporting that increase HG acetylation could limit HG Ca^{2+} binding and subsequent CW stiffening. Using *in silico* modeling and docking prediction, we cautiously proposed that increased HG acetylation in *tbl38* did not change PRX36 affinity for *O*-acetylated HG but possibly subtly increased it, consistent with lack of PRX36 mislocalization in *tbl38* seeds (**Figure 5.1**). Still, we suspect the putative increase in HG pattern affinity in *tbl38* could be due to an indirect side effect of increased acetylation. Semi-quantitative measurement of PRX36 anchoring would be necessary to test this hypothesis which will be challenging. Finally, we aimed to study 5 additional MSC-expressed *CIII-PRXs* and to evaluate if other CIII-PRXs could participate in CW remodeling in other CW microdomains than PRX36/PMEI6 CW microdomain which is necessary for mucilage release. We developed an adapted mucilage release protocol which could highlight more subtle difference in release as well as putative facilitation of release using ethanol. In these conditions, we studied PRX03, PRX17, PRX50, PRX51 and PRX56. Mutation on the later showed greatly increase released phenotype in 25 % ethanol compared to Col-0 and other peroxidase mutants. This could be associated with a

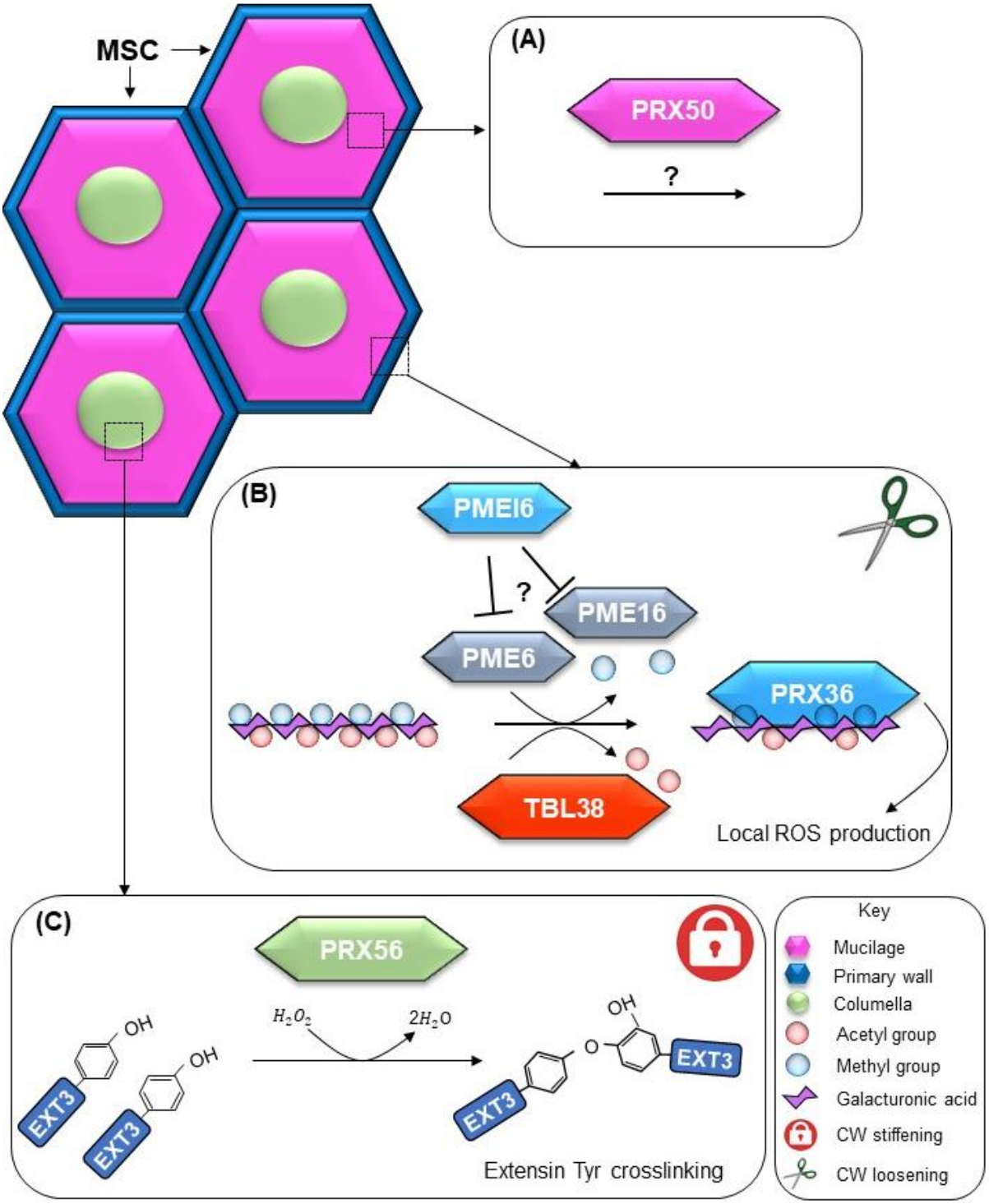

Figure 5.1 : Mucilage secretory cell CWs show unique dynamics in positionning of apoplastic molecular actors.(A) Both previous work and ours positioned PRX50 in the mucilage. It is unclear what could be its molecular function as *prx50* did not display any mucilage related phenotype, although this could be due to functional redundancy with PRX51. **(B)** At the top of the primary wall, PMEI6 may inhibit both PME16 and PME6/HMS activity (or another PME) to create a particular methylesterification pattern in HG (labeled by JIM7 and LM20). In parallel, HG is deacetylated through TBL38 activity which could indirectly affect the fine-tuning of PRX36 anchoring. **(C)** At the surrounding top of the columella, PRX56 could generate ROS which would crosslink apically positioned nearby extension epitopes (labeled by JIM12 and LM1) and reinforce the columella-primary wall surface contact. Considering extensin expression in MSCs, we propose that EXT3 could be a good candidate for crosslinkink by PRX56.

CW stiffening activity in WT that is lost in *prx56*. PRX56 also show particular MSC positionning in the adjacent and overhead wall of the to of columella. Considering the JIM12/LM1 extensin epitope recognition at the nearby top of the columella, PRX56 positionning and our initial Western blot results, we proposed that PRX56 could be an extensin peroxidase crosslinking extensin Tyr residues (**Figure 5.1**). A good extensin candidate is EXT3 which is expressed in MSCs. Phenocopy of *prx56* mucilage release phenotype and loss of JIM12/LM1 labeling in *ext3* would strengthen this hypothesis.

Overall, we demonstrated the strength of using co-expression data mining to identify genes which had MSC specific expression, as well as similar apoplastic accumulation than PRX36 in some cases. It is puzzling to imagine what is the *in muro* regulation of the PMEI/PME/TBL/PRX localized in this study. It is possible that they could belong to a sublayer of this microdomain as suggested by PMEI6 / HMS-TagRFP odd signal accumulation in developing seed. Aside from its activity which may be a byproduct of its environment, it is also intriguing to see that TBL38 is an apoplastic protein similarly to TBR. Indeed, although sequence alignment could predict putative signal peptide, examples in the literature of TBLs with similar prediction later experimentally accumulating in the Golgi are described. Future work on TBL sorting motif might explain the targeting properties of TBL38/TBR compared to other described TBLs. Still, TBL38 role in the CW is similar to PAEs which sparks the question of possible functional redundancy between these actors during CW remodeling.

We gave first clues as to the molecular function of other peroxidase in MSC as PRX56 might be an extensin peroxidase (**Figure 5.1**), although future work is needed to confirm this hypothesis. Interestingly, previous study positioned PRX50 in the mucilage which we confirmed during this work (**Figure 5.1**), although its function is unknown. It is interesting that each MSC CW microdomains has a at least a CIII-PRX (primary wall: PRX36; columella: PRX56; mucilage: PRX50; **Figure 5.1**) which further demonstrates the need for additional molecular scaffolds (similar or not to PMEI6-PRX36) to ensure proper protein accumulation specifically in each CW sublayer.

Although much work remains to be done, we believe this work further proves the relevancy of MSC in the study of CW microdomain remodeling events.

6. Chapter six: Material and Methods

6.1. Material

6.1.1. Plant material and growth conditions

6.1.1.1. *Arabidopsis thaliana* lines

Arabidopsis thaliana ecotypes and mutant genotypes were ordered from the NASC (https://arabidopsis.info/; **Table 6.1**). Homozygous lines were identified by PCR.

Table 6.1: *A. thaliana* ecotypes and genotypes used in this study. Green triangles indicate that the insertion site of T-DNA or transposon in mutant lines was verified through sequencing. Orange triangles indicate that the position of the insertion was approximated according to TAIR data (https://www.arabidopsis.org/).

Genotype	Back-ground	NASC ID	Important SNP for ecotype and genomic map for mutants	Ref
Col-0		N1093	N/A	
Nos-0		N1395	N/A	
Lossen-0 (strain 9858)		N77051	Deletion of G at position 130 of AT5G15180 (PRX56) CDS (at position 4930689 in genome) → Frame shift at Ala44 and early stop56	https://1001genomes.org/
Col-4		N933	N/A	
prx36-1	Col-0	SAIL_194_G03	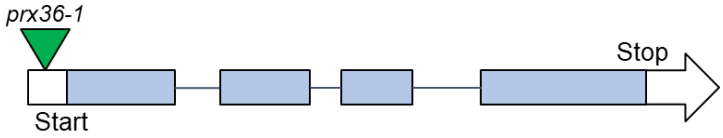	Kunieda et al (2013)
pmei6-1	Col-0	SM_3.19557	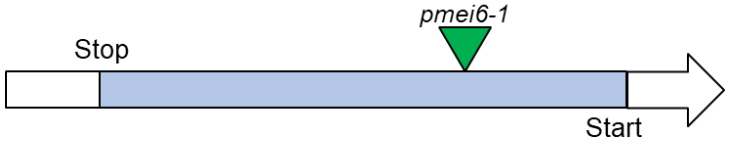	Saez-aguayo et al (2013)
tbl38	Col-0	N416808		
pme6/hms	Nos-0	N55865	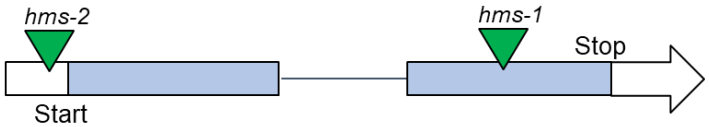	Levesque-Tremblay et al (2015)
pme16	Col-4	N55865	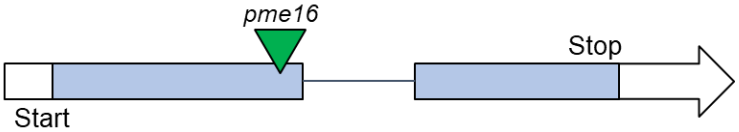	

duf1191-b	Col-0	N696258	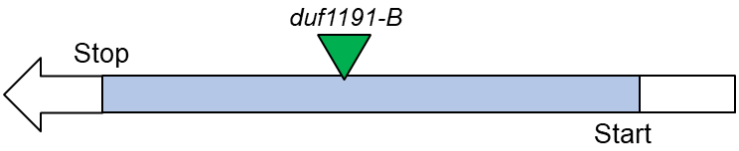	
caspl2a1-a	Col-0	N859443	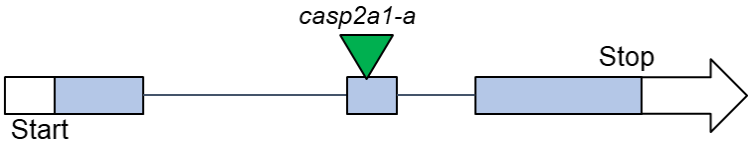	
caspl2a1-b		N482956	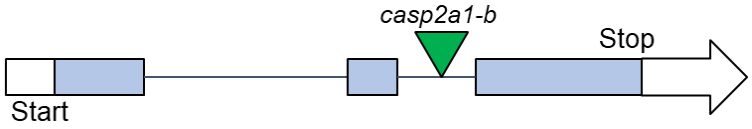	
prx03-a	Col-0	N879436	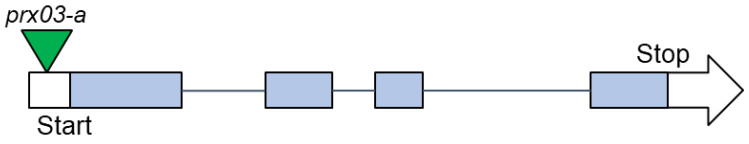	
prx03-b	Col-0	N640204	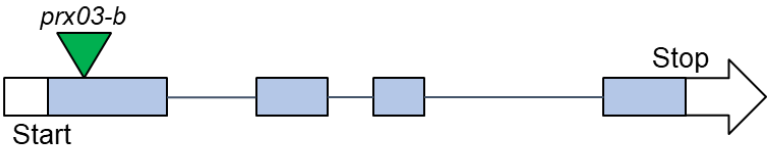	
prx17-b	Col-0	N503180	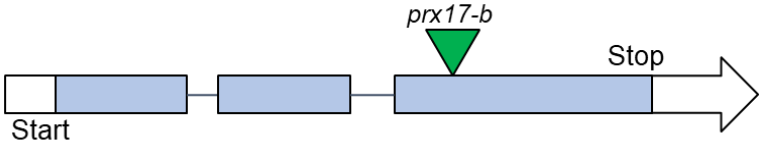	Cosio et al (2017)
prx50-b	Col-0	N563662	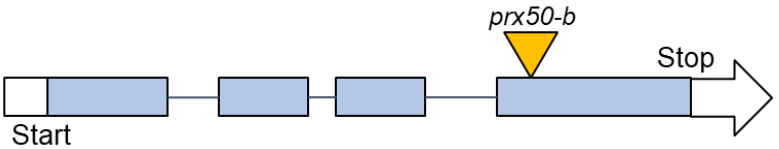	Francoz 2015
prx51-c	Col-0	GABI_888H04	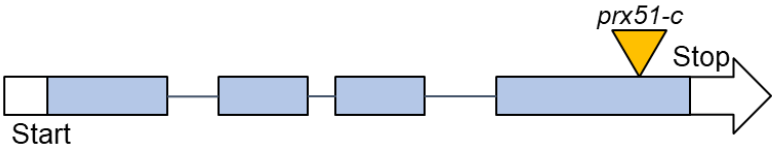	Francoz 2015
prx56	Col-0	SALK_010145	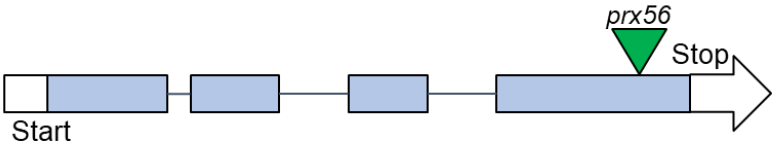	Francoz 2015

6.1.1.2. *Arabidopsis thaliana in vitro* culture

Culture medium was made of 4.4 $g.L^{-1}$ Murashige and Skoog (MS) basal medium powder (SIGMA M5519), 20 $g.L^{-1}$ saccharose and 10 $g.L^{-1}$ agar. The pH was then adjusted to 5.7 with KOH before sterilization. The appropriate antibiotic (**Table 6.2**) was added to the lukewarm liquid media before spreading in Petri dishes under a laminar flow hood.

Table 6.2: Antibiotics

Identifier	Final concentration	Use
Kanamycin	50 $\mu g.mL^{-1}$	Bacterial / Plant screening
Ampicillin	50 $\mu g.mL^{-1}$	Bacterial screening
Rifampicin	50 $\mu g.mL^{-1}$	Bacterial strain conservation
Gentamicin	15 $\mu g.mL^{-1}$	Bacterial screening
Spectinomycin	100 $\mu g.mL^{-1}$	Bacterial screening
Hygromycin	25 $\mu g.mL^{-1}$	Plant screening

All seeds were first sterilized for 10 min in a final concentration of 3.2 % bleach, diluted three times from the original 9.6 % solution (Orapi 2069433). Seeds were successively centrifugated 30 s at 4000 rpm, rinsed in sterile water three times and spread on agar plates containing 40 mL of culture medium. Seeds were synchronized by placing the plates at 4°C for 48 h before cultivation in a growth chamber under a 16 h day / 8 h night cycle at 22°C / 20°C.

6.1.1.3. *Arabidopsis thaliana* pot culture

For optimal seed production, plants were cultivated on soil under a 8 h day (sodium light (340.99 µmol/m/s-1)/ 16 h night cycle at 21°C / 20°C 70 % relative humidity during their vegetative stage for 4 weeks at https://www.fraib.fr/L-offre-technologique/Culture-des-vegetaux. They were then transferred in a S2 greenhouse (https://www.fraib.fr/L-offre-technologique/Culture-des-vegetaux) under a 14 h day / 10 h night cycle at a mean temperature of 25.8°C and mean hygrometry of 53.0 % H_2O over a one-year period based upon hourly monitoring. However, monitoring of climatic conditions allowed identifying peaks of abnormal conditions during experiments.

For regular assays, plants were cultivated on soil under a 16 h day (LED (86.02 µmol/m/s-1) / 8 h night cycle at 20°C 70 % relative humidity in a S2 culture room at

https://www.lipme.fr/tpmp. The first primary floral stem was cut off and then plants were kept in similar conditions until harvesting.

6.1.1.4. *Nicotiana benthamiana*

Seeds were cultivated on a 16 h day / 8 h night cycle at 23°C (Neon (86.90µmol/m/s-1) / 22°C in a 70 % humidity growth chamber at https://www.fraib.fr/L-offre-technologique/Culture-des-vegetaux. They were transplanted after 14 days and fertilized each week.

6.1.2. Bacterial growth conditions

6.1.2.1. *Escherichia coli*

Competent *E. coli* One Shot^{tm} TOP10 bacteria (Invitrogen C404010) of genotype F^- mcrA Δ(mrr-hsdRLS-mcrBC) φ80lacZΔM15 ΔlacX74 recA1 araD139 Δ(ara-leu) 7697 galU galK rpsL (Str^R) endA1 nupG λ- were used to clone and amplify each plasmid and vectors. They were grown for 17 h in the Luria Broth (LB, 10 $g.L^{-1}$ tryptone, 5 $g.L^{-1}$ yeast extract and 10 $g.L^{-1}$ NaCl) liquid medium at 37°C under a 250 rpm shaking. Solid medium additionally contained 1.5 % (m/v) agar.

6.1.2.2. *Agrobacterium tumefaciens*

The A. *tumefaciens* C58/GV3101 pMP90 strain (Hellens et al., 2000) was used for integrating the GoldenGate-created-plasmids and transforming for both transitory expression in *N. benthamiana* or stable expression in *A. thaliana*. It was cultivated with either liquid LB medium at 28°C under 250 rpm shaking or solid medium with added 1.5 % (w/v) agar.

6.1.3. Plasmid and vector

6.1.3.1. Template DNA

The original templates used for cloning originated from various sources and were harbored in various plasmids described in **Table 6.3**.

Table 6.3: cDNA and custom-ordered DNA plasmids used as template DNA for further cloning

Sequence identifier	Sequence type	Source	Supplier
PRX36 ORF	ORF of AT3G50990	RAFL22-03-B11 (pda20378)	RIKEN
PMEI6 ORF	ORF of AT2G47670	PGEM-T easy internal cloning (827bp)	P. Ranocha (LRSV)
PME16 ORF	ORF of AT2G43050	RAFL24-15-G11 (pdz69310)	RIKEN
PME6 ORF	ORF of AT1G23200	RAFL09-37-A17 (pda06147)	RIKEN

TBL38 ORF	ORF of A1T29050	RAFL09-90-M11 (pda09004)	RIKEN
TBL27 ORF	ORF of AT1G70230	RAFL06-86-I18 (pda07742)	RIKEN
DUF1191 ORF	ORF of AT4G01140	RAFL15-33-P07 (pda13020)	RIKEN
CASPL2A1 ORF	ORF of AT1G17200	RAFL15-42-M14 (pdx59702)	RIKEN
PRX03 ORF	ORF of AT1G05260	RAFL14-42-O04 (pda18567)	RIKEN
PRX17 ORF	ORF of AT2G42420	RAFL15-19-M20 (pda12861)	RIKEN
PRX50 ORF	ORF of AT4G37520	RAFL06-08-C18 (pda06253)	RIKEN
PRX51 ORF	ORF of AT4G37530	RAFL09-41-F02 (pda06253)	RIKEN
PRX56 ORF	ORF of AT5G15180	RAFL09-25-M23 (pda05794)	RIKEN
TagRFP	ORF of TagRFP (codon use optimized for Arabidopsis and Saccharomyces)	Gateway TagRFP-AS-N entry clone (FP149)	Evrogen
Gamillus	ORF of Gamillus	Gamillus / pcDNA3 (DDBJ ID : LC309249)	(Shinoda et al., 2018)
pPRX36	Promoter of AT3G50990	Sequence synthesis	GenScript
p35S_short	Promoter of CaMV and 5'UTR of CPMV	pEAQ-HT-DEST1 GQ497235 (5906-6769)	(Sainsbury et al., 2009)

6.1.3.2. Cloning vectors

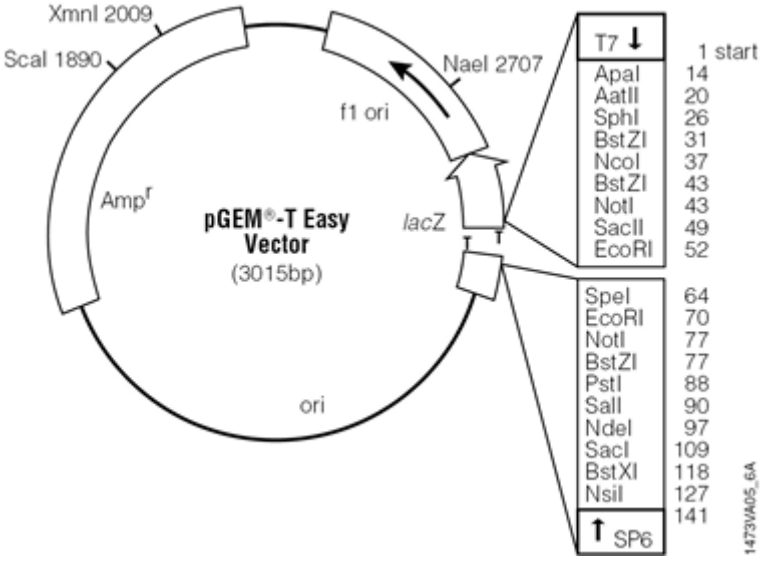

Figure 6.1 : pGEM-T easy (Level 0 GoldenGate TA cloning vector)

The pGEM-T easy (Promega A1360; **Figure 6.1**) is a pre-linearized vector with 3'-T overhangs at the insertion site allowing TA cloning of PCR products produced with the GoTaq polymerases, that contain single 3'-adenine overhangs to each end. Proper insertion was checked by PCR with T7/SP6 primers, M13 (not shown) duo or via digestion with EcoRI whose recognition sites flanked the insertion site. Although transformed *E. coli* could be selected with

its Ampicillin resistance gene, it provided similar resistance to the GoldenGate level 1 vector and thus this scenario was not preferentially used.

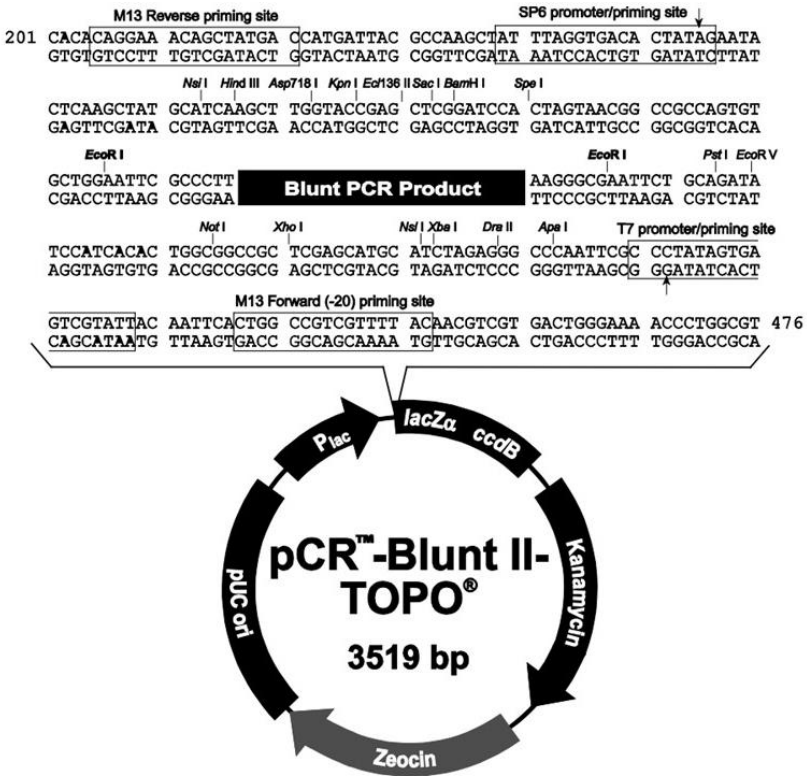

Figure 6.2 : pCR Blunt II-TOPO (Level 0 GoldenGate blunt cloning vector)

The pCR Blunt II-TOPO (ThermoFisher Scientific 450245;
Figure 6.2) was routinely used for most GoldenGate level 0 product. Its blunt edge made it compatible with the Phusion (ThermoScientific F553L) proof-reading polymerases producing blunt end products. Insertion was checked by PCR using M13 primers and through digestion with EcoRI. This is an extremely efficient cloning vector providing a Kanamycin resistance gene different from the Ampicillin resistance of Level 1 vector and thus was used in most instances of the GoldenGate assembly.

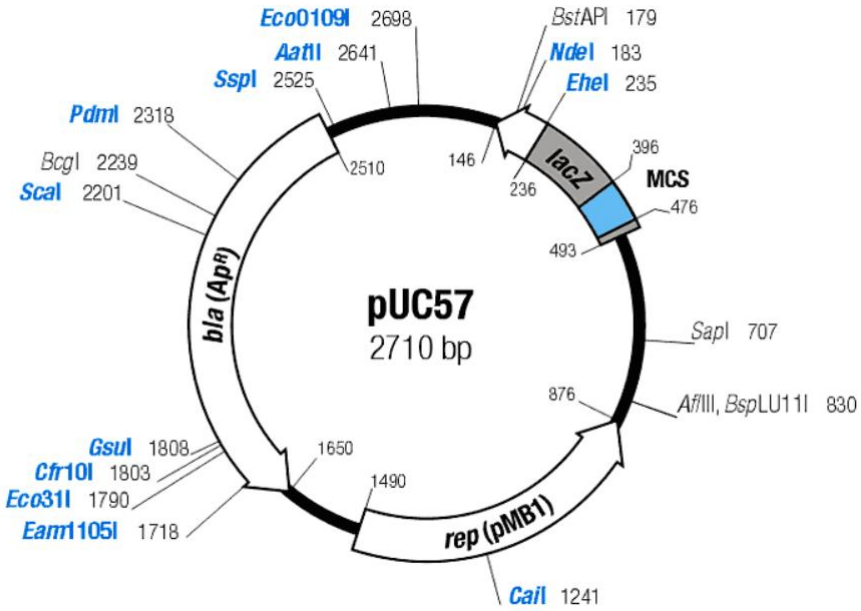

Figure 6.3: pUC57 (Level 0 cloning vector) supplied in Genscript orders.

The pUC57 cloning vector (**Figure 6.3**) was not used to manually clone DNA fragments directly but corresponded to the vector hosting the ordered Genscript sequences (**Table 6.2**). Similar enzymes or primers were used to assess proper size and sequence of the insert. Once transformed in *E. coli*, level 0 blocks cloned in this vector were screened with ampicillin.

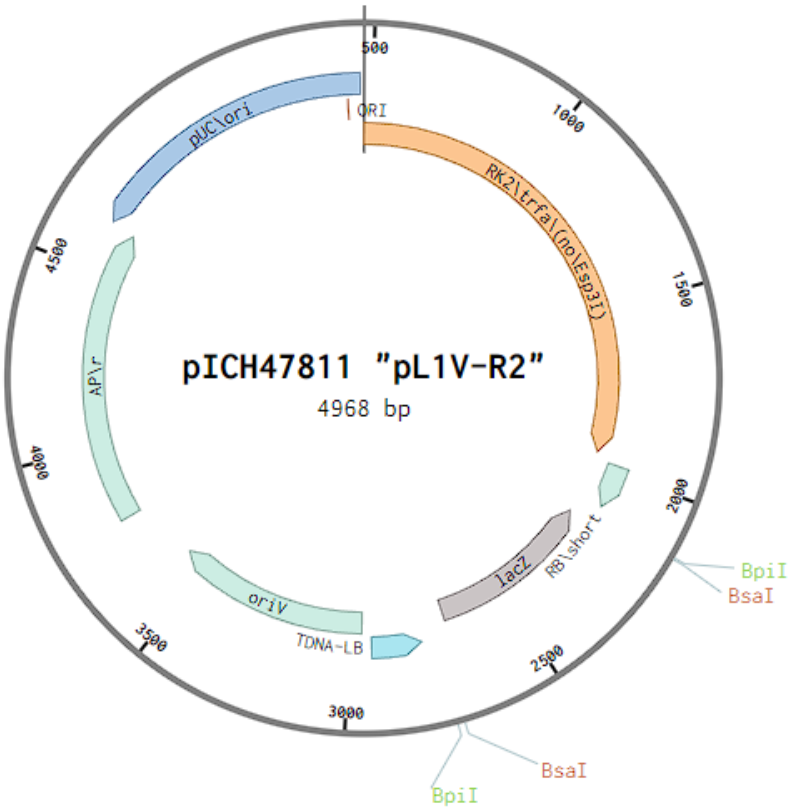

Figure 6.4 : pICH47811 "pL1V-R2" (GoldenGate Level 1 cloning vector)

The commonly named pL1V-R2 vector (Weber et al., 2011); **Figure 6.4**) was used for all level 1 GoldenGate assembly. For insertion, the vector was linearized by two BsaI cutting sites generating the corresponding extremities for linkage with the external level 0 blocks (promoter and terminator). For screening, it provided an Ampicillin resistance gene and the blue/white colony selection through the replacement of LacZ ORF by the inserts in recombinant vectors. Additionally, successfully inserted DNA fragments can be later linearized in the level 2 GoldenGate protocol thanks to two BpiI cutting sites external to the BsaI sites.

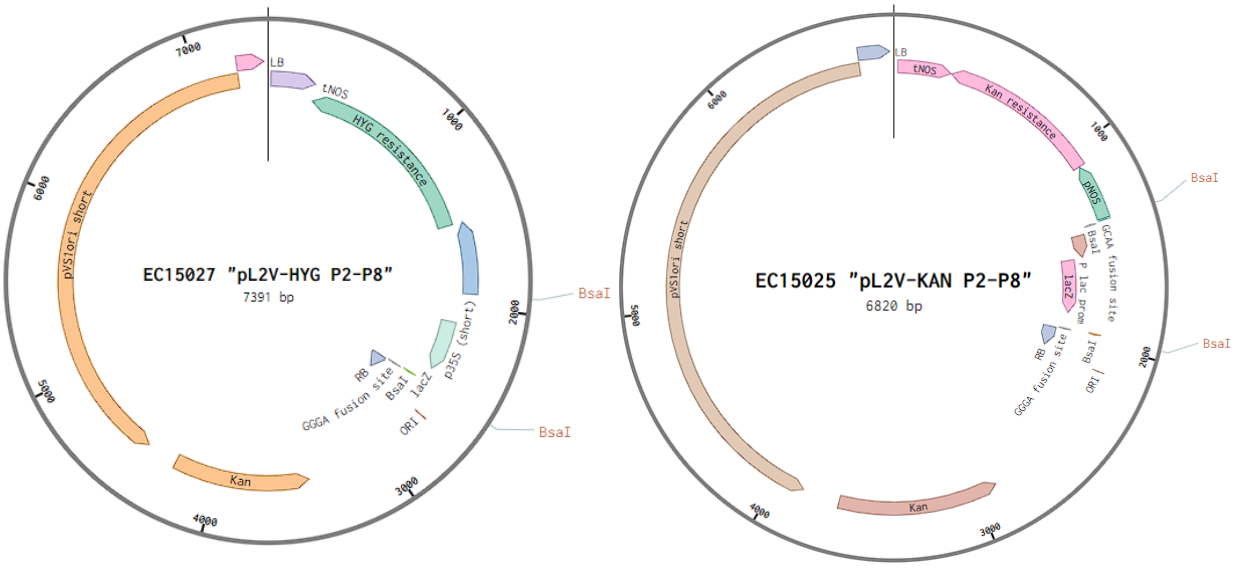

Figure 6.5 : EC15027 "pL2V-HYG P2-P8" and EC15025 "pL2V-KAN P2-P8" (GoldenGate Level 2 cloning vectors)

Both commonly named pL2V-HYG and pL2V-KAN vectors (Gift from PM Delaux; **Figure 6.5**) were used for level 2 GoldenGate assemblies. They were linearized thanks to two BsaI cutting sites generating corresponding extremities that could be linked to the ELE-linker undermentioned and the assembled Level 1 DNA construct. Both vectors provided a Kanamycin resistance and LacZ-mediated blue/white colony selection. Left and right border allowed for transfer of the full DNA construct and a plant resistance gene which is either the Hygromycin or the Kanamycin. Either level 2 vectors were used depending on already present resistance in *A. thaliana* mutated backgrounds.

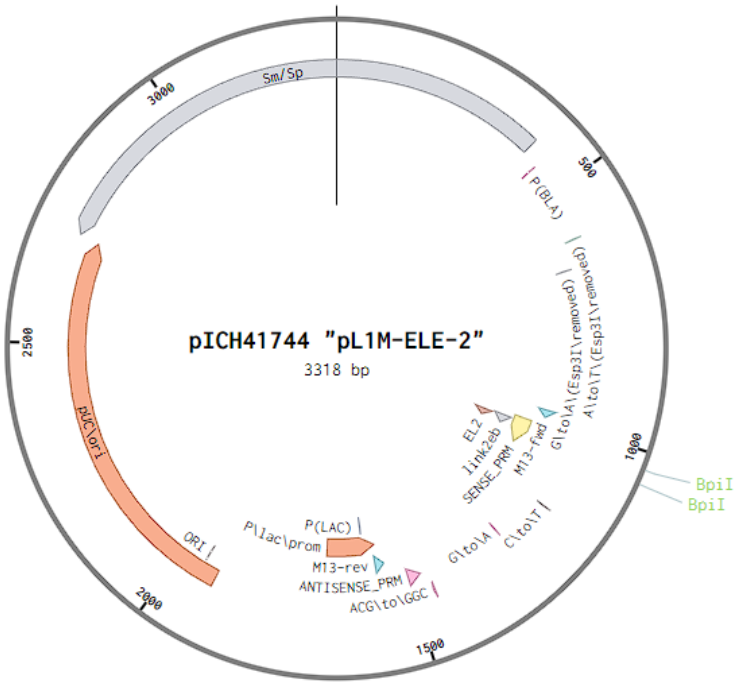

Figure 6.6 : pICH41744 "pL1M-ELE-2" (Linker-containing vector for Level 2 GoldenGate cloning)

Final assembly of level 2 GoldenGate required an additional linker that is extracted from the pL1M-ELE-2 vector through two BpiI cutting sites (**Figure 6.6**). The small linearized fragments allowed to link either used level 2 vectors with the assembled DNA construct linearized from the final level 1 plasmid. Particular care was used when designing the DNA construct linkers to avoid any mismatch.

6.1.3.3. Subcellular marker and fluorochrome properties

The subcellular marker constructs (**Table 6.4**) were ordered from the Nottingham Arabidopsis Stock Centre (https://www.arabidopsis.org/) and transferred in *A. tumefasciens*.

Table 6.4: Subcellular markers used for transient transformation

Identifier	Construct	Localisation	Bacterial resistance	Source
G-yb CD3-966	Sialyltransferase-YFP	Golgi	Kanamycin	(Nelson et al., 2007)/ NASC
pm-yb CD3-1006	Aquaporin-YFP	Plasma membrane		

The fluorescent proteins used for the markers and to localize the protein of interest had the following attributes (**Table 6.5**).

Table 6.5: Spectral and biochemical properties of YFP, TagRFP and Gamillus. Note that the low pKa of TagRFP and Gamillus allows their use in the acidic cell wall compartment. From https://www.fpbase.org/

	Excitation λ	Emission λ	pKa
YFP	513	527	6.9
TagRFP	555	584	3.8
Gamillus	504	519	3.4

6.1.4. Primers

Primers (**Table 6.6**) were designed and checked using SerialCloner2.6 or Benchling (https://www.benchling.com/) and their TM was estimated using two sources: the DSI_OligoTM from the University of Paris5 (http://www.dsi.univ-paris5.fr/bio2/OligoTM.html) and the Multiple Primer Analyzer available online (https://www.thermofisher.com/fr/fr/home/brands/thermo-scientific/molecular-biology/molecular-biology-learning-center/molecular-biology-resource-library/thermo-scientific-web-tools/multiple-primer-analyzer.html).

Table 6.6: PCR primers. For the Level 0 cloning, the extremities that were added were on the 5' end of the primer sequence. The light blue bases are identical to the template DNA, the purple bases were added either to separate ORF from the FP or preventing an early STOP codon, the red bases are the linkers connecting the level 0 blocks (displayed with various specific colors in **Figure 6.7**, and **Table 6.6**), one black base was added as to match the pattern of the BsaI cutting site which are the bold black bases.

Primer code	Primer name	Primer sequence (5'-3')	Usage/Utility	Target template	Tm
AF1	AT4G01140_For1	TCGTCTTCTGCATCATCTCTAATCTACAAACG	Genotyping	*caspl2a1* mutant	63,8
AR1	AT4G01140_Rev1	CTCATCGCGTAAGATAAACGTGAAGAAGTTC	Genotyping	*caspl2a1* mutant	67,8
BF1	AT1G29050_For1	GTGCATATACATACACAAATGAGTGTATAAAAG C	Genotyping	*tbl38_A* mutant	63,7
BR1	AT1G29050_Rev1	GTGCAAGATTCAGGTTGCCAAG	Genotyping	*tbl38_A* mutant	64,1
BF2	AT1G29050_For2	CTTGGCATTGGTGGACTCACAAAG	Genotyping	*tbl38_B* mutant	67
BR2	AT1G29050_Rev2	CATCGAACTCAACACTTTCGACACTACTCC	Genotyping	*tbl38_B* mutant	68,6
CF1	AT2G43050_For	GTGCATCGATGCTCAGTGGAAGGATAC	Genotyping	*pme16_A* mutant	69,7
CR1	AT2G43050_Rev	CAACAAATTCAGATTTTATTCGAGGACTTACTG	Genotyping	*pme16_A* mutant	66,3
CF2	AT2G43050_For2	ATGGCTTCATCATCATCAATATCAAA	Genotyping	*pme16_JIC* mutant	66,1
CR2	AT2G43050_Rev2	TCAATTCACAAGTCCTGGGTCGA	Genotyping	*pmei16_JIC* mutant	66,3
DF1	AT1G23200_For	GGCTCTCCGATCAAGTTCAG	Genotyping	*hms/pme6* mutant	74,4
DR1	AT1G23200_Rev	TCTCCACCGTGAATTTTTCC	Genotyping	*hms/pme6* mutant	70,3
EF1	AT1G17200_Forward	CCAGTTTCTAATTTGTTATTTGGTTTACCAG	Genotyping	*duf1191_A* mutant	63,8
ER1	AT1G17200_Reverse	GCAAACACATAAGCATTCTTTCTCTTGACC	Genotyping	*duf1191_A* mutant	67,6
T1	GK o8474	ATAATAACGCTGCGGACATCTACATTTT	Genotyping	GK mutants	64,7
T2	LB1 (SAIL T-DNA)	GCCTTTTCAGAAATGGATAAATAGCCTTGCTTCC	Genotyping	SAIL mutants	72,2
T3	Lba1 (SALK)	TGGTTCACGTAGTGGGCCATCG	Genotyping	SALK mutants	69,4
T3bis	LBb1.3 (SALK)	ATTTTGCCGATTTCGGAAC	Genotyping	SALK mutants	63,6
T4	Spm32	TACGAATAAGAGCGTCCATTTTAGAGTGA	Genotyping	JIC mutants (SM lines Transposon)	65,1
T5	3-1a (RIKEN DS transposon)	GGTTCCCGTCCGATTTCGACT	Genotyping	RIKEN mutants	61
T6	5-1a (RIKEN DS transposon)	ACGGGATCCCGGTGAAACGGT	Genotyping	RIKEN mutants	70,8
T7	Ds5'-1a	ACGGTCGGGAAACTAGCTCTAC	Genotyping	SGT mutants	61
F10	pPRX36_GGAG_F	**GGTCTC**CGGAGGGCCCATATAAGTT	GoldenGate lvl0	Primers not used : Genscript synthesis pUC57-*pPRX36* (Genscript)	68,8
R10	pPRX36_CATT_R	**GGTCTC**GCATTTTGGACTCTCAGC	GoldenGate lvl0		67,5

F11	PRX36CDS_AATG_F	**GGTCTC**CAATGAATACAAAAACGGT	GoldenGate lvl0	*PRX36* cDNA (RIKEN pda20378)	63,4
R11	PRX36CDS_TAGC_R	**GGTCTC**GTAGCAACATCATGGTTAA	GoldenGate lvl0		63,4
F12	TagRFP_GCTA_F	**GGTCTC**CGCTACCGGTATGGTGAG	GoldenGate lvl0	TagRFP-AS-N entry clone (Evrogen FP149)	68,8
R12	TagRFP_AAGC_R	**GGTCTC**GAAGCAAGAAAGCTGGGT	GoldenGate lvl0		68
F13	Gamillus_GCTA_F	**GGTCTC**CGCTAAAATGGTGAGC	GoldenGate lvl0	pcDNA3-Gamillus_DDBJID_LC309249	64,3
R13	Gamillus_AAGC_R	**GGTCTC**GAAGCTTATTACTTGTACAGC	GoldenGate lvl0		62
F15	TBL38CDS_AATG_F	**GGTCTC**CAATGATGGGTTTCAAACT	GoldenGate lvl0	*TBL38*cDNA (RIKEN pda09004)	66,3
R15	TBL38CDS_TAGC_R	**GGTCTC**CTAGCCATCGTAAGAGCTG	GoldenGate lvl0		65,6
F16	NTBL38CDS_AATG_F	**GGTCTC**CAATGATGGGTTTCAAACTC	GoldenGate lvl0	*TBL38*cDNA (RIKEN pda09004)	66,8
R16	NTBL38CDS_GGCT_R	**GGTCTC**CGGCTGAAGCAAAGG	GoldenGate lvl0		67,5
F17_B	CTBL38CDS-AGCC_FB	**GGTCTC**CAGCCATAGACAAG	GoldenGate lvl0	TBL38cDNA (RIKEN pda09004)	61,3
R17	CTBL38CDS-TAGC_R	**GGTCTC**CTAGCCATCGTAAGAGCTG	GoldenGate lvl0		65,6
F18	NTBL27CDS-AATG_F	**GGTCTC**CAATGCATGGGATTAAACGA	GoldenGate lvl0	*TBL27*cDNA (RIKEN pda07742)	68,2
R18	NTBL27CDS-GGCT_R	**GGTCTC**CGGCTGTCGAAACAGAG	GoldenGate lvl0		68,6
F20	PMEI6_CDS_AATG_F	**GGTCTC**CAATGACTTCGTCTTCTTC	GoldenGate lvl0	*PMEI6* cDNA (pGEMTeasy)	67,1
R20	PMEI6_CDS_TAGC_R	**GGTCTC**GTAGCCAAGCCATCAA	GoldenGate lvl0		69,3
F21	PME16_CDS_AATG_F	**GGTCTC**CAATGGCTTCATCATCAT	GoldenGate lvl0	*PME16* cDNA (RIKEN pdz69310)	69
R21	PME16_CDS_TAGC_R	**GGTCTC**GTAGCATTCACAAGTCCTG	GoldenGate lvl0		68,8
F22	HMS_CDS_AATG_F	**GGTCTC**CAATGGATCACAAAATCCTAC	GoldenGate lvl0	*HMS/PME6* cDNA (RIKEN pda06147)	68,9
R22	HMS_CDS_TAGC_R	**GGTCTC**GTAGCAAGTCCATCGTTG	GoldenGate lvl0		69,7
F25	M13_FOR	GTAAAACGACGGCCAGT	Lv0 sequencing	pGEM-T easy / pCR ZeroBlunt vectors	58,8

R25	M13_REV	CAGGAAACAGCTATGACCA	Lv0 sequencing		58,7
F26	PRX03_CDS_AATG_F	**GGTCTC**CAATGAATTGCTTGATAG	GoldenGate lvl0 / Genotyping	*PRX03* cDNA (RIKEN pda18567)	64,5
R26	PRX03_CDS_TAGC_R	**GGTCTC**CGGCTACTATTTGCAAC	GoldenGate lvl0 / Genotyping		66,6
F27	PRX17_CDS_AATG_F	**GGTCTC**CAATGTCTCTTCTTCC	GoldenGate lvl0 / Genotyping	*PRX17* cDNA (RIKEN pda12861)	62,9
R27	PRX17_CDS_TAGC_R	**GGTCTC**CGGCTAGATACAAGC	GoldenGate lvl0 / Genotyping		63,9
F28	PRX50_CDS_AATG_F	**GGTCTC**CAATGGTTGTGGTGA	GoldenGate lvl0 / Genotyping	*PRX50* cDNA (RIKEN pda02873)	67,1
R28	PRX50_CDS_TAGC_R	**GGTCTC**CGGCTATTAAAAGCTCCA	GoldenGate lvl0 / Genotyping		68,8
F29	PRX51_CDS_AATG_F	**GGTCTC**CAATGGTTGTGATGAACA	GoldenGate lvl0 / Genotyping	*PRX51* cDNA (RIKEN pda06253)	68,9
R29	PRX51_CDS_TAGC_R	**GGTCTC**CGGCTATTGAAAGCTCC	GoldenGate lvl0 / Genotyping		69,7
F30	PRX56_CDS_AATG_F	**GGTCTC**CAATGGCTGCTTTGAA	GoldenGate lvl0 / Genotyping	*PRX56* cDNA (RIKEN pda05794)	69,3
R30	PRX56_CDS_TAGC_R	**GGTCTC**CGGCTATTAACCATTCTG	GoldenGate lvl0 / Genotyping		67,3
F31	p35S CaMV_GGAG_F	**GGTCTC**CGGAGCCAGTGAATTGT	GoldenGate lvl0 / Genotyping	pEAQ-HT-DEST1	71,3
R31	5'UTR CPMV_CATT_R	**GGTCTC**GCATTATCGAATTTGGG	GoldenGate lvl0 / Genotyping		69
F32*	PRX03_F	CTTCCAAATTGCCTCATTGAAGTGTAAC	Genotyping	*PRX03 cDNA (RIKEN pda18567)*	68,7
F33*	pPRX36_3'_F	CATCCAACAAATTAAAAGCC	Lv1 sequencing	pL1V-R2 recombinant vector	58,6
F34*	pTBL38_3'_F	TTAATTTATGTGTGTGTGTCAG	Lv1 sequencing	pL1V-R2 recombinant vector	59
F35*	5'UTR CPMV_3'_F	TACTTCTGCTTGACGAGGTATTGTT	Lv1 sequencing	pL1V-R2 recombinant vector	63,8
R36*	TagRFP_N_R	GTACACTTAAAGTGGTGATTATTGACAG	Lv1 sequencing	pL1V-R2 recombinant vector	61,7
F37*	TagRFP_C_F	AAGCAGACAAAGAAACTTACGTGGA	Lv1 sequencing	pL1V-R2 recombinant vector	65,8
R38*	Gamillus_N_R	ATCTCGCCGTTCAGCTCG	Lv1 sequencing	pL1V-R2 recombinant vector	66,8
F39*	Gamillus_C_F	CACATCGTGCAGACAGAAC	Lv1 sequencing	pL1V-R2 recombinant vector	60,6
R40*	T-Nos_5'_R	ATTATATGATAATCATCGCAAGAC	Lv1 sequencing	pL1V-R2 recombinant vector	57,7
F41	P3a S	TCGCTACGTGTTTTAGAACATAC	Genotyping	*P3a.1 (SAIL_423_E01)*	59,8
R41	P3a AS/G	CCGTTAGGTTAGGAGTCGCG	Genotyping		65,7
F42	P3 ATG S	ATGAATTGCTTGATAGCTATAGCTCTT	Genotyping	*P3b.1 (SALK_140204)*	62,4

R42	3’P3	AATCCATACACACAAATCCC	Genotyping		58,6
F43	P17bS	GCTACTGTTTCTTGTGCCGA	Genotyping	*P17b.1 (SALK_034684)*	63
R43	P17b AS/G	CCAGGTCTCCCAGATTGCAA	Genotyping		67,4
F44	P17c S/G	GCTTCCGTCATGCGTTTCCA	Genotyping	*P17c.1 (SALK_003180)*	70,5
R44	3’ P17	TCACTAGATTCGTGTACAAAG	Genotyping		54,5
F45	P50b S	GCTATGTGATTTAATATTCCGGTT	Genotyping	*P50b.3 (SALK_063662)*	60,8
R45	3’P50	GAAACCCAAGACAGAGATTTATTAC	Genotyping		59,9
F46	P51b S/G	TAGCTGTATGCCATGTTGTTAGC	Genotyping	*P51c.3 (GABI_888H4)*	62,8
R46	P51b AS	ACTCATGATCCAACTTACTATACAAAGTAT	Genotyping		60,4
F47	P56a S	AGACCTCGTTGTGCTTTCAG	Genotyping	*P56a.2 (SALK_010145)*	62,1
R47	P56a AS/G	TCATAAAACAATCTCACAGACATA	Genotyping		57,8
F48	CTBL27CDS-AGCC_F	**GGTCTC**CAGCCATCTGTTTTAATA	GoldenGate lvl0	TBL27_324_At1g70230_pda07742	64,3
F49	TBL27CDS-AATG_F	**GGTCTC**CAATGTGGGATTAAACGA	GoldenGate lvl0	TBL27_324_At1g70230_pda07742	68,8
R49	TBL27CDS-TAGC_R	**GGTCTC**CTAGCTTTAAACCTTCCA	GoldenGate lvl0		64,7
F50	pL1V-R2_RBshort_F	GCCAATATATCCTGTCAAACACTG	Genotyping / Sequencing	pL1V-R2 / pL2V-HYG/KAN recombinant vectors	63,2
R51	pL1V-R2_LB_R	TAGACAACTTAATAACACATTGCGGAC	GoldenGate lvl1	pL1V-R2 recombinant vector	64,7
F52	pL2V-3'p35S_F	TTGGAGTAGACCAGAGTGTCGTG	GoldenGate lvl2	pL2V-HYG/KAN recombinant vector	65,4
R54	Prx03_R	TTAACTATTTGCAACGGAACATTGCCTCCTAAC	Genotyping	*prx03* mutant	73
F55	Prx03_F_START	ATGAATTGCTTGATAGCTATAGCTCTT	RT-PCR	*PRX03 cDNA*	62,4
R55	Prx03_R_STOP	TTAACTATTTGCAACGGAACATT			61,1
F56	Prx17_F_START	ATGTCTCTTCTTCCCCATCTCATCCT	RT-PCR / genotyping	*PRX17 cDNA*	68,8
R56	Prx17_R_STOP	TCAAGATACAAGCAATACATCAATAGGCCT			68,4
F57	Prx50_F_START	ATGGTTGTGGTGAACAAAACGAATCTCTTATTG	RT-PCR / genotyping	*PRX50* cDNA	72,8
R57	Prx50_R_STOP	TCAATTAAAAGCTCCACAATCACGACG			70,9
F58	Prx51_F_START	ATGGTTGTGATGAACAAAACGAAT	RT-PCR / genotyping	*PRX51* cDNA	65,1
R58	Prx51_R_STOP	ATACAAATGAGTGCAAATAAACAATATCT			61,7
F59	Prx56_F_START	ATGGCTGCTTTGAAGATGACTATCTCTTGTTTCT	RT-PCR / genotyping	*PRX56* cDNA	72,3
R59	Prx56_R_STOP	TTAATTAACCATTCTGCACTTCTTGCGAACTTC			72,1
F60	PRX36_RT_OUT_F	ATGGCGGGCATTGTTCTCTC	RT-PCR	*PRX36* cDNA	64,6
R60	PRX36_RT_OUT_R	CTATCCAATAATGGAAACTCTCTCAAACAT			63
F61	TBL38_RT_OUT_F	AAAACCCAAAACCTTTGATATTTGTCTAA	RT-PCR	*TBL38* CDNA	66
R61	TBL38_RT_OUT_R	CACTAGAAGATTTACGAATGTCATTTACAGA	RT-PCR		65,2
F61	DUF1191_RT_OUT_F	AAACTAAAGAAGCTAGAAGATGGAGAAAAGT	RT-PCR	*DUF1191* CDNA	64,8

R61	DUF1191_RT_OUT_R	GTACTTGAAGAGCAAATGGAGGATCTA	RT-PCR		65,6
F62	PME16_RT_OUT_F	ATGGCTTCATCATCATCAATATCAAA	RT-PCR	*PME16* cDNA	66,2
R62	PME16_RT_OUT_R	TCAATTCACAAGTCCTGGGTCGA	RT-PCR		70
F62	PME6_RT_OUT_F	AATATCCCACATCTCTACTCATCCACATTA	RT-PCR	*PME6* cDNA	67,1
R62	PME6_RT_OUT_R	AAAATCAACAAAGACCACACTAACAAAA	RT-PCR		65,4
F63	CASPL2A1_RT_OUT_F	ATGGGATCTACAAAGCTTGGTCTCA	RT-PCR	*CASPL2A1* cDNA	67,9
R63	CASPL2A1_RT_OUT_R	TCATGGTATATTCGAAGATGAAGGAAGA	RT-PCR		67,3
F64	PMEI6_RT_OUT_F	CCTCCAATAAAGAACATGACTTCGTCTT	RT-PCR	*PMEI6* cDNA	64,8
R64	PMEI6_RT_OUT_R	TATCATAGCGTAGATTACAAGCCATCAA	RT-PCR		63,1
F65	ACT-2_RT_OUT_F	GGTAACATTGTGCTCAGTGGTGG	RT-PCR	*ACT2* CDNA	67,8
R65	ACT-2_RT_OUT_R	CTCGGCCTTGGAGATCCAC	RT-PCR		67,5
F66	PRX36_RT_IN_F	CGTCGCCAATGCATACTTCA	RT-PCR	*PRX36* cDNA	63,1
R66	PRX36_RT_IN_R	GAAATCGGACATCCCTGCTG	RT-PCR		62,9
F67	TBL38_RT_IN_F	GAGTCGAGCAGGCCTTTGC	RT-PCR	*TBL38* CDNA	63,5
R67	TBL38_RT_IN_R	AGCACACGCCCAACTCTCTCT	RT-PCR		63,7
F68	DUF1191_RT_IN_F	AAACGTCGCCGTACGCTAAA	RT-PCR	*DUF1191* CDNA	62,8
R68	DUF1191_RT_IN_R	CGAGAAGCGTGAGGATCGAA	RT-PCR		63,8
F69	PME16_RT_IN_F	CTTCGTCGGAGCAACGGAG	RT-PCR	*PME16* cDNA	64,3
R69	PME16_RT_IN_R	CGACGGTGCCGGTGATATCC	RT-PCR		64,7
F70	PME6_RT_IN_F	AAGGCTGCTGCTGAGGCTG	RT-PCR	*PME6* cDNA	64,3
R70	PME6_RT_IN_R	GAGAGCCACCGCCTGATGT	RT-PCR		63,8
F71	CASPL2A1_RT_IN_F	AATCCGAACTGCCGAGACAA	RT-PCR	*CASPL2A1* cDNA	63
R71	CASPL2A1_RT_IN_R	GGCGGAGTCAACAATGGAAG	RT-PCR		62,9
F72	PMEI6_RT_IN_F	TTAGCCTCCACCGGTAGCAA	RT-PCR	*PMEI6* cDNA	62,9
R72	PMEI6_RT_IN_R	CGGCGAGCGACTTGTATAGG	RT-PCR		63
F73	ACT2_RT_IN_F	GGTAACATTGTGCTCAGTGGTGG	RT-PCR	*ACT2* CDNA	63,8
R73	ACT2_RT_IN_R	CTCGGCCTTGGAGATCCAC	RT-PCR		63,1
R75	TBL38STOP-AACG-R	**GGTCTCC**AAGCTCACATCGTAAGAGCTG	GoldenGate lvl0	*TBL38* cDNA (RIKEN pda09004)	70

6.1.5. Silique sampling and dry seed storage

Seeds are the main material used in this work. They have been analyzed both during their development or after desiccation.

6.1.5.1. Developing seed sampling

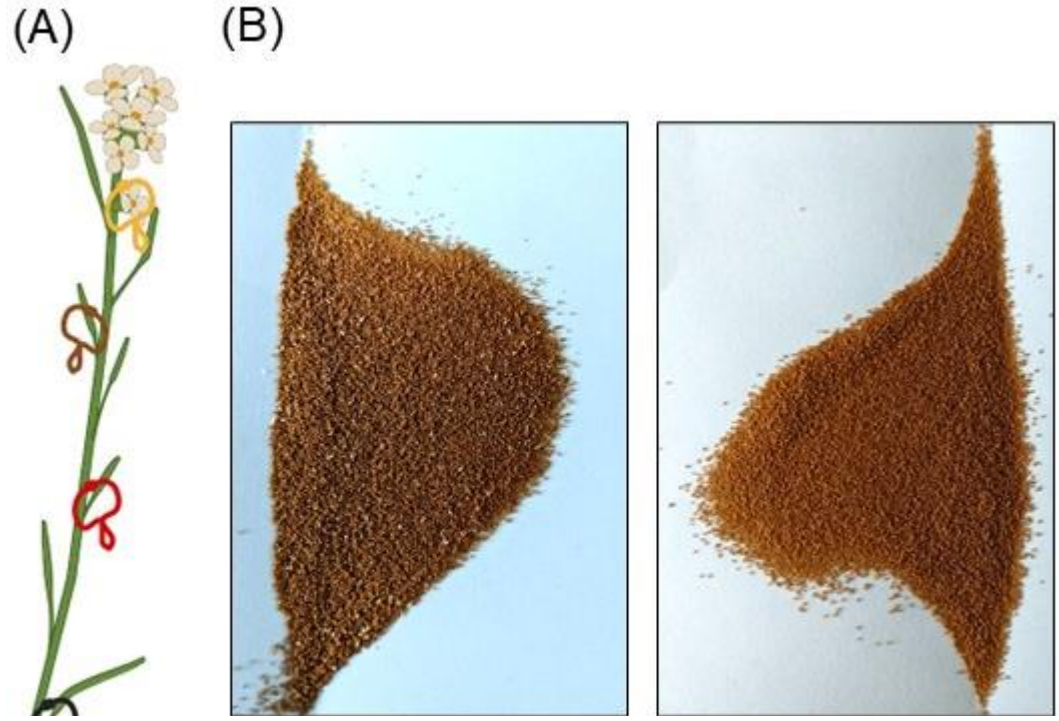

Figure 6.7: Developing seed staging and dry seed cleaning. (A) Different colored strands were deposited on flowers with open petals corresponding to the day of pollination. Siliques then grew across them and were harvested to match specific sequential day after pollination (DAP) stages. The whole ordered-siliques contained on floral stem could also have been harvested to either build paraffin tissue arrays covering the whole kinetics or to systematic confocal spinning disk microscopy. **(B)** Photographs of dry seeds before (left) and after (right) the extensive cleaning step required for biochemical analyses. Remaining silique valve fragments are manually removed until batch is pure.

Developing seeds were used for RNA extraction, Western-blot analyses, *in situ* RNA hybridization, immunolabeling on paraffin/resin sections and confocal microscopy. Developmental stages were assigned to sets of Days after pollination (DAP). Pollination event was assigned to the first moment where the flower's petals are open (**Figure 6.7.A**). Then, this flower was labeled with a small strand with a pre-determined color. This was sequentially repeated on multiple days. For most experiment, siliques were labeled with 6-8-10-12-14 DAP (**Figure 6.7.A**) such as corresponding siliques were simultaneously harvested 14 days after first labeling. They were then handled according to the future experiment to be performed.

6.1.5.2. Dry seed storage

Dry seeds were used for mucilage release assay, resin embedding and Immunofluorescence , MSC surface wall abrasive enrichment followed by Western-blot, ImmunoDotblot, enzymatic assay and Mass Spectrometry analyses. Seeds were harvested and filtered through a 425 µm mesh (RETSCH Z632422) to remove contaminant (aborted seed, parts of siliques or plant). Then, they were further cleaned with pliers until no contaminant could be found (**Figure 6.7.B**). Dry seeds were stored at room temperature with a recorded date of harvesting, as analyses on seeds stored for over 2 months or in conditions such as in a refrigerator showed alteration in some phenotypes as compared to freshly harvested seeds, particularly in mucilage release assay. Biochemical analyses showed stable phenotypes even after 1-2 years of seed storage.

6.1.6. Antibodies and histochemical dye

The concentration at which each markers or dyes (**Table 6.7**) were used varies for each experiment and can be found in their own sections.

Table 6.7: Histochemical dyes, primary and secondary antibodies. Note that the Alexa 488 and 555 conjugated secondary antibodies were highly cross-adsorbed allowing the used for double labeling with primary antibodies from different species. A488, Alexa fluor 488; A555, Alexa fluor 555; AP, alkaline phosphatase; IF, Immunofluorescence;

Identifier	Type	Target/epitope	Use	Source
Ruthenium Red	Dye	Negatively charged polysacharides	Mucilage release assays	Schuchardt Müchen
Calcofluor White M2R	Dye	Cellulose	Transient expression in *N. benthamiana*	Sigma-Aldrich F3543
JIM5	Rat IgG primary antibody	Partially ME HG	ImmunoDotblot	PlantProbes
JIM7	Rat IgA primary antibody	Highly ME HG	IF / ImmunoDotblot	Kerafast ELD005
JIM12	Rat Ig primary antibody	Extensin / Arabinan	IF / Western-blot / ImmunoDotblot	Kerafast ELD031
LM1	Rat Ig primary antibody	Extensin / Arabinan	IF / Western-blot / ImmunoDotblot	Kerafast ELD020
LM7	Rat IgM primary antibody	Partially ME HG	ImmunoDotblot	PlantProbes - discontinued

LM18	Rat IgG2c primary antibody	Partially / Un-ME HG	ImmunoDotblot	PlantProbes - discontinued
LM19	Rat IgM primary antibody	Partially ME HG	ImmunoDotblot	PlantProbes - discontinued
LM20	Rat IgM primary antibody	Highly ME HG	IF / ImmunoDotblot	Kerafast ELD003
LM25	Rat IgM primary antibody	Xyloglucans	IF / ImmunoDotblot	Kerafast ELD015
RU2	Mouse Ig primary antibody	RG-I	IF / ImmunoDotblot	Gift from M.C. Ralet (Nantes)
2F4	Mouse IgG1 primary antibody	Calcium bridged Un-ME HG	ImmunoDotblot	PlantProbes - discontinued
αPRX36	Rabbit polyclonal primary antibody	CSLIGSMENIPSPES PRX36 peptide-KLH conjugate	IF / ImmunoDotblot	Genscript private order
αPRX03	Rabbit polyclonal primary antibody	CFTGRGGQDPALDSE PRX03 peptide-KLH conjugate	IF	Genscript private order
αPRX17	Rabbit polyclonal primary antibody	CMFSEDQDEFFRAFA PRX17 peptide-KLH conjugate	IF	Genscript private order
αPRX50	Rabbit polyclonal primary antibody	CVGGKLPHPTDDVNK PRX50 peptide-KLH conjugate	IF	Genscript private order
αPRX51	Rabbit polyclonal primary antibody	CGKLPKPTFDLNQLN PRX51 peptide-KLH conjugate	IF	Genscript private order
αPRX56	Rabbit polyclonal primary antibody	CLITQFQSKGLDKKD PRX56 peptide-KLH conjugate	IF	Genscript private order
αPME	Rabbit polyclonal primary antibody	KTYLGRPWKEYSRTV consensus PME peptide conjugate	ICC	Courtesy of J Pelloux

αTagRFP	Polyclonal primary antibody	TagRFP	IF / Western-blot	Invitrogen R10367
Goat αRat IgG-A488	secondary antibody	Rat primary antibody	IF	Invitrogen A-11006
Goat αRat IgG-A555	secondary antibody	Rat primary antibody	IF	Invitrogen A-21434
Goat αRat IgG-AP	secondary antibody	Rat primary antibody	Western-blot / ImmunoDotblot	SIGMA A8438
Goat αRabbit IgG-A488	secondary antibody	Rabbit primary antibody	IF	Invitrogen A11034
Goat αRabbit IgG-AP	secondary antibody	Rabbit primary antibody	Western-blot / ImmunoDotblot	SIGMA A3687
Goat αMouse IgG-A488	secondary antibody	Mouse primary antibody	IF	Invitrogen A-11029
Goat αMouse IgG-A555	secondary antibody	Mouse primary antibody	IF	Invitrogen A-21424
Goat αMouse IgG-AP	secondary antibody	Mouse primary antibody	ImmunoDotblot	SIGMA A5153
αDig Fab-AP	Anti-Digoxigenin secondary antibody	Dig labeled riboprobes	*In situ* Hybridization	Roche 11 093 274 90

6.2. Methods

In this section, the final standard procedures that diverge from published protocols or commercial kits are described as extensively as possible to ensure both understanding and reproducibility.

6.2.1. DNA extraction

DNA extractions were conducted on mature leaves sample and used for genotyping and sequencing and were done using the Wizard® Genomic DNA Purification Kit (Promega A1120). Samples were resuspended in 50 µL of Milli-Q water and 1 µL was used to assess the purity and to quantify sample concentration with the Denovix® Ds-11 microspectrophotometer. Although the extracted DNA can be used immediately, better results were obtained after overnight storage at -20°C of resuspended DNA.

6.2.2. RNA extraction and reverse transcription

RNA extraction assays were conducted on a minimum of 25 mg of developing siliques (about 5-6 siliques) containing developing seeds at various stages. Samples were frozen in liquid nitrogen in a 2 mL tube and grinded with a metallic grindball for 2 x 45 s at 30 Hz (Mixer Mill MM 400, RETSCH®). RNA purification was then done according to the Promega SV Total RNA Isolation System protocol including DNase treatment. Residual DNA was further removed using the Ambion® TURBO DNA-free™ kit as instructed by the manufacturer. RNA was additionally precipitated overnight at -80°C in 1:10 volume of 3 M sodium acetate pH 5.2 and 2.5 volume of 100 % ethanol. Samples were centrifuged for 15 min; the RNA pellet was washed in 70 % ethanol and centrifuged for 15 min. Final samples were resuspended in 8 µL of RNase free water and 1 µL was used to evaluate sample concentration (300-1800 $ng.\mu L^{-1}$) and purity with the Denovix® Ds-11 microspectrophotometer. cDNAs were retrotranscribed directly on 7 µL of the concentrated RNA using the standard protocol of the ProtoScript® II First Strand cDNA Synthesis Kit. cDNA solution was diluted 25 times with RNase free Milli-Q water and stored at -20°C.

6.2.3. PCR genotyping and DNA amplification

Plant genotyping through Polymerase Chain Reaction (PCR) was performed either with the GoTaq DNA Polymerase (Promega M300) on DNA extracted from leaves or directly on small pieces of cotyledon with the KAPA3G Plant PCR Kit (®KAPA BIOSYSTEM). Either way, the corresponding protocols for both polymerases were strictly followed. The hybridization temperature was adjusted according to the mix of primers.

6.2.4. Agarose gel electrophoresis

DNA fragments were separated on a 1 % or 2 % (w/v) agarose gel electrophoresis. For KAPA3G PCR, 5 µL are mixed with 1 µL of 6 X loading dye (Promega G1881) whereas for GoTaq PCR, 6 µL of PCR product are directly deposited. DNA size was determined using 5 µL of either the 1 kb DNA Ladder (Promega G5711) for 1 % agarose gel or 100 bp DNA Ladder (Promega G2101) for 2 % agarose gel. Electrophoresis was done on a 0.5 X TAE buffer (40mM Tris-acetate, 1 mM EDTA pH 8) at 135 V for 30 min in the Mupid™-One (ADVANCE MU2) system. Then, bands were observed under UV light with the Gel Doc XR+ (Biorad 1708195) system after a 15 min incubation in 0.8 $\mu g.mL^{-1}$ Ethidium bromide.

6.2.5. Bacterial plasmid extraction

Plasmid extraction was done using the GeneJET Plasmid Miniprep Kit (Thermo Scientific K0502) and following the standard protocol. For the final step, plasmids were eluted with Milli-Q water instead of the supplied buffer.

6.2.6. Sequencing

About 250 ng of DNA was mixed with 2.5 µL of 10 µM primer **(Table 6.6**) and the total volume was adjusted to 10 µL with Milli-Q water. The mix was sequenced by Eurofins Genomics (https://eurofinsgenomics.eu/). Result sequence was read with SerialCloner 2.6 and sequencing quality was checked with BioEdit 7.0.

6.2.7. GoldenGate cloning

GoldenGate cloning technology is based on type II restriction enzymes cutting outside of their recognition sequence (Engler et al., 2008). The general philosophy is to add floating extremities containing enzyme recognition site followed by a specific linker of 4 bp to a DNA sequence of interested by PCR amplification. DNA sequences can be categorized in sets of "level 0 blocks" here consisting of "promoters", "coding sequences", "fluorescent Tags", "terminator", such as the linkers connecting two blocks are the same for each sequence of this block. To facilitate transfer of blocks between research teams, examples of block names and their corresponding linkers can be found in the literature (Patron et al., 2015). These examples were taken as such or slightly adapted to our preference (**Figure 6.8; Table 6.8**). Then, blocks are cloned together in a single plasmid and automatically assumed the right order in what will be a "level 1 plasmid" (**Figure 6.8**). Finally, the vector is transferred to the "level 2 plasmid" of choice that is better suited for plant transformation.

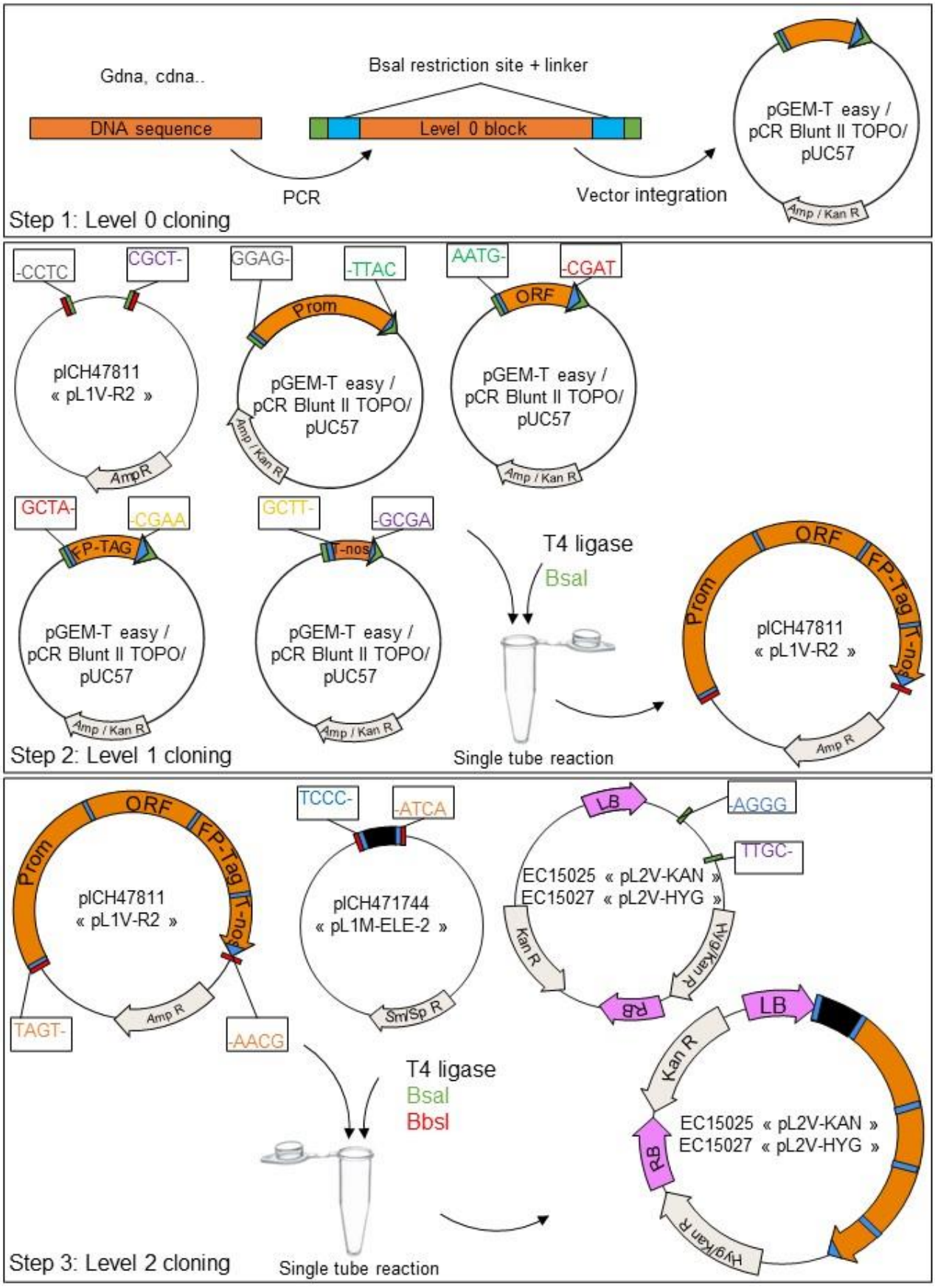
Gdna, cdna..
DNA sequence
PCR
BsaI restriction site + linker
Level 0 block
Vector integration
pGEM-T easy / pCR Blunt II TOPO/ pUC57
Amp / Kan R
Step 1: Level 0 cloning
-CCTC
CGCT-
pICH47811 « pL1V-R2 »
AmpR
GGAG-
-TTAC
Prom
pGEM-T easy / pCR Blunt II TOPO/ pUC57
AATG-
-CGAT
ORF
GCTA-
-CGAA
FP-TAG
GCTT-
-GCGA
T-nos
T4 ligase
BsaI
Single tube reaction
FP-Tag
Step 2: Level 1 cloning
TCCC-
-ATCA
pICH471744 « pL1M-ELE-2 »
Sm/Sp R
LB
-AGGG
TTGC-
EC15025 « pL2V-KAN »
EC15027 « pL2V-HYG »
Kan R
Hyg/Kan R
RB
TAGT-
-AACG
T4 ligase
BsaI
BbsI
Step 3: Level 2 cloning
Single tube reaction

Figure 6.8: Step by step GoldenGate cloning. (Step 1) Incorporation of extremities containing BsaI recognition site (green rectangles) and corresponding 4 bp linkers that will be cut by BsaI (blue rectangles) to the DNA sequence of interest by PCR or gene synthesis. Each sequence is then ligated in the vector of choice which forms the « level 0 ». **(Step 2)** GoldenGate assembly of DNA fragments generated in step 1. Each sequence are simultaneously excised from the corresponding level 0 vector by BsaI-mediated enzymatic cleavage. The acceptor vector is simultaneously opened by the same process and each sequence assembles itself in the level 1 vector thanks to linkers compatibility and the T4 ligase activity. **(Step 3)** Final assembly in the level 2 vector suited for *A. tumefaciens* transformation. The vector is chosen according to the desired plant-resistance (Kanamycin or Hygromycin). The assembled DNA sequence of interest is released from the level 1 vector through BbsI restriction site recognition on the vector. A small portion of the ELE vector is similarly and simultaneously released and acts as a linker. The level 2 vector is simultaneously opened by BsaI enzymatic cleavage and integration of DNA sequence is done through T4 ligase activity.

Table 6.8.: Multiple GoldenGate assembly strategy: Sequence assembly was done using a variable number of level 0 blocks, inferring that overhang linker must be adapted to fit the design. Linkers are named after Patron et al (2015) with the exception of B5bis that is used in this study. **(A)** The first commonly formed construct is the promoter, full lengh ORF followed by the fluorescent protein (FP) of choice (TagRFP or Gamillus) and terminator which was done for most of this work. **(B)** The secondary construct type includes a separation of the ORF in two N-ter and C-ter sections before FP which was done for TBL38/TBL27 related construct. **(C)** The third type includes a direct link between the ORF and the terminator with no added FP which was done to match endogenously produced proteins in one complementation assay.

Parts	Level 1 vector	Promotor		ORF		FP-Tag		Terminator		Level 1 vector
Orientation	3'	5'	3'	5'	3'	5'	3'	5'	3'	5'
5'-3' overhang Linker	CCTC	GGAG	TTAC	AATG	CGAT	GCTA	CGAA	GCTT	GCGA	CGCT
Identifier Patron et al (2015)		**A1~ B2**		**B3+B4**		**B5bis**		**B6**		

Parts	Level 1 vector	Promotor		N-ter ORF		C-ter ORF		FP-Tag		Terminator		Level 1 vector
Orientation	3'	5'	3'	5'	3'	5'	3'	5'	3'	5'	3'	5'
5'-3' overhang Linker	CCTC	GGAG	TTAC	AATG	TCGG	AGCC	CGAT	GCTA	CGAA	GCTT	GCGA	CGCT
Identifier Patron et al (2015)		**A1~ B2**		**B3**		**B4**		**B5bis**		**B6**		

Parts	Level 1 vector	Promotor		ORF		Terminator		Level 1 vector
Orientation	3'	5'	3'	5'	3'	5'	3'	5'
5'-3' overhang Linker	CCTC	GGAG	TTAC	AATG	CGAA	GCTT	GCGA	CGCT
Identifier Patron et al (2015)		**A1~ B2**		**B3+B4**		**B5bis + B6**		

6.2.7.1. In silico assembly

Following the standard protocol, GoldenGate assemblies were theorized with BsaI and BbsI restriction enzymes. In some cases, presence of endogenous sites in the sequences to be cloned was identified with some possible impairment on the yield and/or the feasibility of the future assembly. As such, silent mutation on these recognition sites were created during gene synthesis at GenScript for these sequences to ensure proper ligation steps (**Table 6.9**). If mutagenesis was not done, a maximum of 2 cutting sites in the whole construction was tolerated. Concerning CaMV 35 S promotor and 5'UTR of CPMV, a security margin was set on both sides of the sequence (**Table 6.9**). Otherwise, the original sequence was amplified.

In silico PCR amplification and generation of vectors was done using Benchling (https://www.benchling.com/) it provides a free and accessible platform to organize and generate GoldenGate mediated constructs with the "GoldenGate assembly" function for level 1 generation and the "Digest and Ligate" function for level 2. Theoretical translation was checked using both SerialCloner 2.6 and the ExPASy webtool (https://web.expasy.org/translate/).

6.2.7.2. PCR reactions

Floating extremities were added through PCR amplification using two different high-fidelity Polymerases: AccuPrime Taq DNA (Invitrogen 12346-086) or Phusion (ThermoScientific F553L). The former generates a non-templated A-tail ending the sequence suitable for TA cloning in pGEM-T easy (**Figure 6.1**) while the latter produces blunt ends suitable for cloning in pCR Blunt II-TOPO (**Figure 6.2**). Amplification was done using the corresponding plasmid template (Table 6.3) and their primers (**Table 6.6**) except for ordered synthetized DNA sequence as floating border were already part of the sequence (**Table 6.3**). PCR was performed using 50 to 75 µL final volume to guaranty having adequate DNA purity and at least 80 $ng.\mu L^{-1}$ after purification. PCR products were purified using Genejet PCR purification kit (K0702) and DNA purity and concentration were determined using the DeNovic DS-11 spectrophotomete.

6.2.7.3. Initial Level 0 blocs generation

Table 6.9: Domestication of some Level 0 sequences

Sequence name	Sequence type	Modification	Purpose
PME16 ORF	ORF of AT2G43050	1352: T to A 1373: T to A	BsaI site removal BsaI site removal
PME6 ORF	ORF of AT1G23200	1117: C to T	BbsI site removal
p35S_short	Promoter of CaMV 35S and 5'UTR of CPMV	Inclusion of GGTCTCCGGAG upstream of prom and AATGCGAGACC downstream of 5'UTR 6530: A to C 6549: T to C	5' and 3' security margin BbsI site removal BbsI site removal
TBL27 ORF	ORF of AT1G70230 (*TBL27*)	1103: A to G 551: A to G	BbsI site removal BsaI site removal
pTBL38	Promoter of At1g29050 (*TBL38*)	677: G to A 1284: A to G 1465: T to A	BbsI site removal BsaI site removal
pPMEI6	Promoter of At2g47670 (*PMEI6*)	772: T to A 827: G to T	BbsI site removal BsaI site removal
pPRX56	Promoter of At5g15175 (*PRX56*)	679: T to A 910: A to T 1162: T to A 1306: G to T	BbsI site removal

6.2.7.4. Ligation in level 0 plasmid and transformation

PCR products were cloned either in the pGEM®-T Easy (Promega A1360; **Figure 6.1**) or the pCR Blunt II-TOPO (ThermoFisher Scientific 450245; **Figure 6.2**) based on their complementarity (or lack thereof) with A-tailling DNA sequences. Ligation was done overnight at 4°C in 10 µL volumes containing:

-1 µL of cloning vector

-2 µL of T4 ligase buffer (NEB B0202)

-1 µL of ligase enzyme (NEB M0202)

-2-4 µL of purified PCR product (at least 80 ng.µL^{-1})

-Water (adjust to 15 µL).

The level 0 blocks were sequenced using the M13 primers duo then transformed in *E. coli* for amplification and constitution of glycerol stock for -80°C storage. *E. coli* transformation was done following the standard heat-shock protocol. Briefly, 16 µL of competent cells were

incubated with 4 µL of ligated vectors for 30 min at 4 °C. Then, vectors were integrated through a 45 s heat-shock step at 42 °C and 250 µL of LB media was added. Bacterias were grown for 1 h at 37 °C and 250 rpm and 130 µL was spread of solid LB media agar plate with the corresponding antibody. The final DNA concentration was adjusted to 100 ng.µL^{-1} before proceeding to level 1 cloning. The complete list of Level 0 constructs including the template and primers is presented **Table 6.10**.

6.2.7.5. Golden gate assembly of Level 1 vectors and *E. coli* transformation

The GoldenGate level 1 reaction was done in a microtube containing:

-1 µL of each desired level 0 blocks concentrated at 100 ng.µL^{-1}

-1 µL of Level 1 plasmid backbone (here, we selected the pICH47811 "pL1V-R2", **Figure 6.4)**

-1.5 µL BSA (NEB B9000)

-1.5 µL T4 DNA ligase buffer (NEB B0202)

-1 µL BsaI cutting enzyme (NEB R3733)

-1 µL T4 DNA ligase enzyme (NEB M0202)

-Milli-Q water (adjust to 15 µL).

The one-pot digestion and ligation assembly was then done according to the following PCR protocol:

$$40 \text{ x } \begin{cases} 2 \text{ min } 30 \text{ at } 37°C \text{ for digestion} \\ 2 \text{ min } 30 \text{ at } 16°C \text{ for ligation} \end{cases}$$

1 x 5 min at 50°C (or 16°C if some level 0 blocks contain either remaining non-domesticated BsaI or BpiI cutting sites)

1 x 5 min at 80°C for final denaturation

About 4 µL of reaction volume was used for *E. coli* transformation. Positive colonies were screened using the white/blue screening assay, Ampicillin resistance and PCR with lvl 1 sequencing primers (Table 6.6). Plasmids of selected positive colonies were purified and correct integration of insert was checked using PCR, enzymatic cleavage profiling and sequencing using multiple sets of construct-specific primers (**Table 6.4**). Then, plasmids concentration was adjusted to 100 ng.µL^{-1} for level 2 assembly. The complete list of Level 1 constructs including the is presented **Table 6.11**.

6.2.7.6. Golden gate assembly of Level 2 vectors and *E. coli* transformation

The GoldenGate level 2 reaction was done in a single microtube containing:

-1 µL of level 1 vector concentrated at 100 ng.µL^{-1}

-1 µL of Level 2 plasmid backbone (we selected the EC15027 "pL2V-HYG" or EC15025 "pL2V-KAN, **Figure 6.5**)

-1 µL of plasmid containing linker (we selected the pICH471744 "pL1M-ELE-2", **Figure 6.6**)

-1.5 µL BSA (NEB B9000)

-1.5 µL T4 DNA ligase buffer (NEB B0202)

-1 µL BsaI cutting enzyme (NEB R3733)

-1 µL BbsI cutting enzyme (NEB R0539)

-1 µL T4 DNA ligase enzyme (NEB M0202)

-Milli-Q water (adjust to 15 µL).

Each following steps were done in a similar fashion to level 1 assembly until purified level 2 plasmids were obtained (**Table 6.10**). Concentration was not diluted for *A. tumefaciens* transformation. The complete list of Level 2 constructs including the is presented **Table 6.11**.

Table 6.10: Level 0 Goldengate generated constructs: each block was individually made or ordered and further used to build the Level 1 block assembly (**Table 6.11**). The template used are detailed in **Table 6.3**.

Lvl 0 blocks	Identifiers	Forward primer (**Table 6.6**)	Reverse primer (**Table 6.6**)
pPRX36	1	**F10 (primer not used, genescript synthesis)**	**R10 (primer not used, genescript synthesis)**
p35S	3	**F31 (primer not used, genescript synthesis)**	**R31 (primer not used, genescript synthesis)**
PRX36 CDS	4	**F11**	**R11**
TBL38 CDS	5	**F15**	**R15**
TBL27 CDS	6	**F49**	**R49**
Nter-TBL38 CDS	7	**F16**	**R16**
Cter-TBL38 CDS	8	**F17_B**	**R17**
Nter-TBL27 CDS	9	**F18**	**R18**
Cter-TBL27 CDS	10	**F48**	**R49**
PMEI6 CDS	11	**F20**	**R20**
PME16 CDS	12	**F21**	**R21**
HMS/PME6 CDS	13	**F22**	**R22**
PRX03 CDS	14	**F26**	**R26**
PRX17 CDS	15	**F27**	**R27**
PRX50 CDS	16	**F28**	**R28**
PRX51 CDS	17	**F29**	**R29**
PRX56 CDS	18	**F30**	**R30**
Gamillus	19	**F13**	**R13**
Tag-RFP	20	**F12**	**R12**
T-Nos	21	Gift from P.Ranocha (LRSV)	
TBL38 CDS stop	27	**F15**	**R75**

Table 6.11: Level 1 and finalized Level 2 Goldengate generated constructs: Selected level 0 blocks (**Table 6.10**) were mixed together to produce different constructs used in stable or transient transformations.

Finalized constructs	Lvl 0 combination	Lvl 1& 2 Identifiers	Lvl 2 Resistance
p35S TBL38 Tag-RFP T-Nos	3-5-20-21	100	Hygromycin
p35S TBL27 Tag-RFP T-Nos	3-6-20-21	101	Hygromycin
p35S Nter-TBL27 Cter-TBL38 Tag-RFP T-Nos	3-9-8-20-21	102	Hygromycin
p35S Nter-TBL38 Cter-TBL27 Tag-RFP T-Nos	3-7-10-20-21	103	Hygromycin
p35S PME16 Tag-RFP T-Nos	3-12-20-21	104	Hygromycin
p35S PMEI6 Gamillus T-Nos	3-11-19-21	105	Hygromycin
p35S PRX36 Tag-RFP T-Nos	3-4-20-21	106	Hygromycin
pPRX36 TBL38 Tag-RFP T-Nos	1-5-20-21	107	Hygromycin
pPRX36 PRX36 Tag-RFP T-Nos	1-4-20-21	108	Hygromycin
pPRX36 PME16 Tag-RFP T-Nos	1-12-20-21	109	Hygromycin
pPRX36 PMEI6 Tag-RFP T-Nos	1-11-20-21	110	Hygromycin
pPRX36 PME6 Tag-RFP T-Nos	1-13-20-21	111	Hygromycin
pPRX36 PME6 Tag-RFP T-Nos	1-13-20-21	112	Kanamycine
pPRX36 PRX03 Tag-RFP T-Nos	1-22-20-21	113	Kanamycine
pPRX36 PRX17 Tag-RFP T-Nos	1-23-20-21	114	Hygromycin
pPRX36 PRX50 Tag-RFP T-Nos	1-24-20-21	115	Hygromycin
pPRX36 PRX51 Tag-RFP T-Nos	1-25-20-21	116	Kanamycine
pPRX36 PRX56 Tag-RFP TNos	1-26-20-21	117	Hygromycin
pPRX36 TBL38 TNos	1-27 -21	118	Hygromycin

6.2.7.7. Plasmid integration in *Agrobacterium tumefaciens*

Few colonies of the C58 pMP90 Gv3101 strain were inoculated in 3 mL LB media with gentamycin antibiotic and grown overnight. Once a OD_{600nm} between 0.5-1 was achieved, tubes were centrifuged for 6 min at 3000 rpm at 4°C. Pelleted bacteria were carefully resuspended in 300 µL 20 mM $CaCl_2$ cold solution. Around 150 µL of competent cells were mixed with 1 µg of plasmid DNA, frozen in liquid nitrogen for 1 min and placed at 37°C for 4 mins. One mL of LB media was added and transformed cells were incubated for 4 h at 28°C under agitation at 250 rpm. Bacteria were pelleted with a quick 30 s centrifugation at 3000 rpm and resuspended in 250 µL of liquid LB media. About 120 µL was spread on solid LB media containing Gentamycin, Rifampicin and Hygromycin.

6.2.8. Glycerol stock generation

For sustainable conservation of bacteria-integrated vectors, 500 µL of liquid culture of transformed *E. coli* or *A. tumefaciens* was gently mixed with 500 µL of Glycerol (Euromedex EU3550) and stocked at -80 °C.

6.2.9. *Agrobacterium tumefaciens*-mediated plant transformation

6.2.9.1. Arabidopsis thaliana

A. thaliana stable transformation was preferentially done on plants with manually removed as much as possible already formed siliques to minimize the amount of untransformed seed.
The adequate transformed *A. tumefaciens* strain was spread from glycerol stock on solid media such as to obtain complete coverage of the petri dish after 2-3 day growth at 28°C. Then, bacteria were recovered with a glass rake and resuspended in 1 mL of 5 % (w/v) saccharose. OD_{600nm} was determined from a 10-fold dilution and the cell suspension was diluted in 5 % (w/v) saccharose until an OD_{600nm} of 0.8 was obtained. Finally, 0.05 % (v/v) Silwet L-77 (Desangosse 2000235) was added and the final solution was transferred in spray bottles.
About 4 plants per construct were placed together put in a small culture chamber and the inoculum was spread directly on flowers. Then, plants were covered by a black plastic bag to block incoming light for 24-30 h before transfer in the greenhouse.

6.2.9.2. Nicotiana benthamiana

N. benthamiana transient expression experiments were done on multiples 5-week-old leaves.
Fresh *A. tumefaciens* colonies were inoculated in 2 mL of liquid LB media with corresponding antibiotic and grown overnight. Cultures were then transferred in 50 mL Falcon tubes containing 18 mL of liquid LB media and grown for 16-24 h at 28°C. The tubes were centrifuged at 4400 rpm for 10 min at 4°C, resuspended in 2 mL Agromix (1 % $MgCl_2$, 1 M MES pH 5.6, 0.3 % Acetosyringone, Milli-Q water) and centrifuged again at 4000 rpm for 15 min at 4°C. The pellet was resuspended in 5 mL Agromix and the OD_{600nm} was determined from a 10-fold dilution. The final volume was adjusted with Agromix until an OD_{600nm} of 0.5 was obtained, after which the tubes were placed at RT for 4 h.
The final inoculum consisted in a mix of various *A. tumefaciens* lines: 10 % (v/v) subcellular YFP-marker line (**Table 6.5**), 80% (v/v) RFP-tagged protein of interest line and 10 % (v/v) P19 silencing inhibitor-containing vector line. Leaves infiltration was done on the abaxial face through the stomata with a 1 mL syringe and pieces of leaves were mounted and analyzed under confocal microscopy 48 h-post Agro-infiltration.

(A)

T0 Screening	Transformed plants	Untransformed plants
Primary root	Long (3-7cm)	Short (1cm)
2nd Root	Yes	No
Hypocotyl	Long	Short
Leaves	Normal development	Absent



(B)

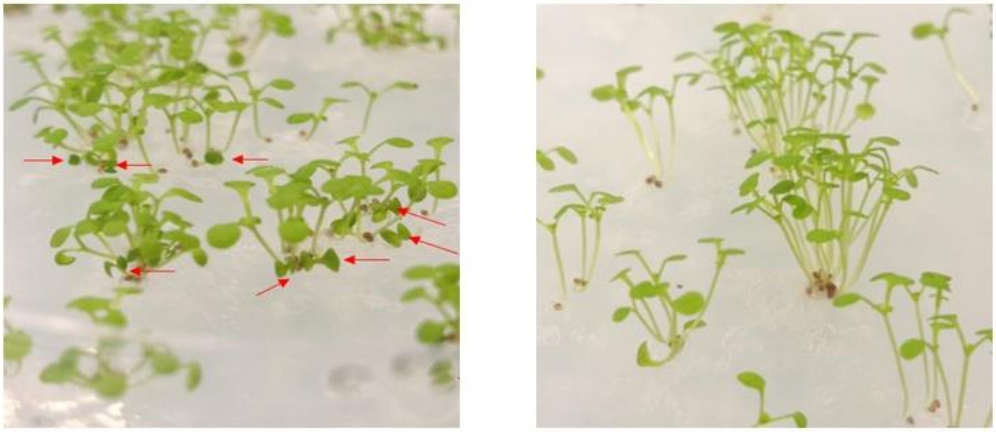

Ht offspring H0 offspring

Figure 6.9: Transformed plant screened on selective media have distinct features. **(A)** T0 Resistant plants display overall enhanced development (red circle) compared to sensible ones in a matter of two weeks growing on Hygromycin-containing media. Further growth would lead to death of sensible plants. **(B)** Left image shows that T2 screening plates could show about 75 % resistant (Heterozygous and Homozygous), and about 25 % non resistant plants (WT, red arrows).Right image shows 100 % resistant plants (Homozygous) Either way, resistant plants displayed similar features described in **(A)**.

6.2.10. Stable *A. thaliana* transformation screening

Dry seeds of transformed plants were harvested, sterilized and spread on MS plates (about 0.1 mL of seeds per plate) containing the adapted antibiotic. Residual water was air-dried for 30 min and plates were placed at 4°C for 48 h before being placed in growth chamber. After two weeks, sensible plants could be recognized from resistant plants (**Figure 6.9**). The latter were transplanted in soil in small greenhouses to maintain a high humidity for at least 2 days. These plants were named "T0" with each line being associated to a number such as "1, 2, 3…". Their seeds were harvested and around 10 plants per T0-plants were sowed on selective media and then on soil as "T1 plants" individually identified with an additional number (e.g. "1.1, 1.2, 1.3 …"). T1 seeds were then grown *in vitro* on selective media and named "T2". T2 lines that show no sensible plants were categorized as transformed homozygous lines whereas plates with some

or only sensible plants were categorized as heterozygous or WT lines, respectively. Resistant and sensible plants were counted to better evaluate the Mendelian proportions.

6.2.11. Adherent mucilage release assays and semi-quantitative analysis

About 150 dry seeds from all available lines were disposed in 2 mL tubes with 1.8 mL of 0.01 M Tris-HCl pH 7.5 and vigorously shaken in horizontal position at 250 rpm using a rotary agitator for 1 h at RT (Francoz et al., 2019). The supernatant containing the non-adherent mucilage was removed and replaced with 1.6 mL of a 0.02 % (w/v) ruthenium red solution in 0.01 M Tris-HCl pH 7.5 allowing to stain the pectinaceous adherent mucilage for 1 h at 250 rpm. Excess ruthenium red was drained and seeds were rinsed twice with 1.6 mL Tris-HCl. Seeds were transferred in 24 well microplates and scanned at 6400 dpi with an Epson Perfection V700 photo scanner. For subtle mucilage release phenotypes, the same protocol was used including Ethanol or $CaCl_2$ (various concentrations were tested) both in Tris-HCl and ruthenium red solutions.

Images were analyzed using ImageJ 1.8 (https://imagej.nih.gov/ij/) without edition of native images. Successive image analysis procedure developed by Aurélie Le Ru (FRAIB) allowed to measure the area, circularity and roundness of seed mucilage (**Figure 6.10**). Briefly, seed area (without mucilage) and whole seed area (seed + mucilage) were manually edged in a semi-automatic fashion Non-individualized seeds were automatically removed from the analysis and selected parameters were measured. A manual examination allowed to double check the absence of artifactual data. The cleaned data was extracted and pulled to a Microsoft Excel sheet for further analyses. Corresponding Wild-type values were assigned as “100 % of signal” and percentage of mutant signal values were calculated accordingly ± standard error of the mean (SEM). Statistical data was obtained using Kruskal-Wallis tests with $n \geq 3$.

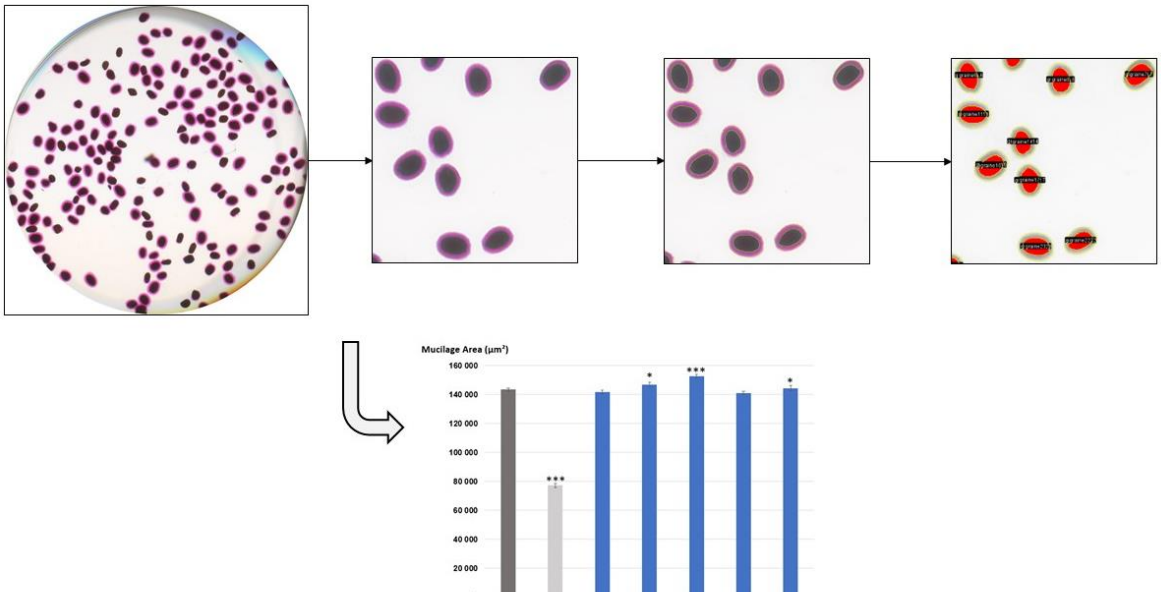

Figure 6.10: Ruthenium red data analysis. High resolution scans of ruthenium red stained seeds were taken for hundreds of seeds and analyzed using successive steps in ImageJ. The semi-automatic procedure allowed to separate seeds from whole seeds (seed+mucilage) and thus quantify a number of parameters of the mucilage. The data was extracted and analyzed through statistical tests.

6.2.12. Dry seed MSC surface wall abrasive fraction

A home-made method was set up in the Lab during a M2 internship (Trezel, 2018). Abrasion columns were a home-made design allowing for homogenous dry seed MSC surface wall abrasive enrichment using plastic column and collector tube similar to the ones found in the GeneJET Plasmid Miniprep Kit (Thermo Scientific K0502). The bottom of the column was cut with a razor blade, the silica layer of the column was removed and replaced with a 50 µm Seffar Nylon mesh (Dutscher 074010) thermos-sealed on or wrapped around the bottom of the open column. Then, a 2.1 x 1.6 cm piece of P500 sand-paper (Dexter, Castorama) was gently rolled in the column and placed with the abrasive side inward. The P500 sand paper theoretically corresponded to 30.2 µm average abrasive particle size (https://www.fine-tools.com/G10019.html), i.e. about 1:10 of *A. thaliana* seed length) Finally, the so-called abrasive column was put back in the collector tube (**Figure 6.11**). The collector tube was weighted at the time of use and about 50 mg of dry seeds were deposited inside the paper sand roll before locking the cap. Abrasion was done with a FastPrep (MP Biomedicals™ 116004500) for 5 to 6 cycles of 1 min at 6.5 $m.s^{-1}$. The abrasion was not linear and powder usually appeared after the 4th or 5th cycle probably corresponding to a breaking limit. While most of the extracted surface wall powder pass through the nylon mesh during the last cycles of abrasion, a final centrifugation step for 5 min at 14000 rpm allowed total recovery of the powder. The powder

was weighted and additionally grinded with a metallic grindball for 3 min 30 s at 30 hertz (Mixer Mill MM 400, RETSCH). The efficiency of the abrasion was evaluated by various methods (autofluorescence, SEM, immunofluorescence and ruthenium red assay of Col-0 seeds before and after abrasion). The powder of Col-0 was additionally visualized under SEM. All these controls reinforced the results during analysis of powder from various genotypes by immune dotblots, enzymatic assays and Mass spectrometry.

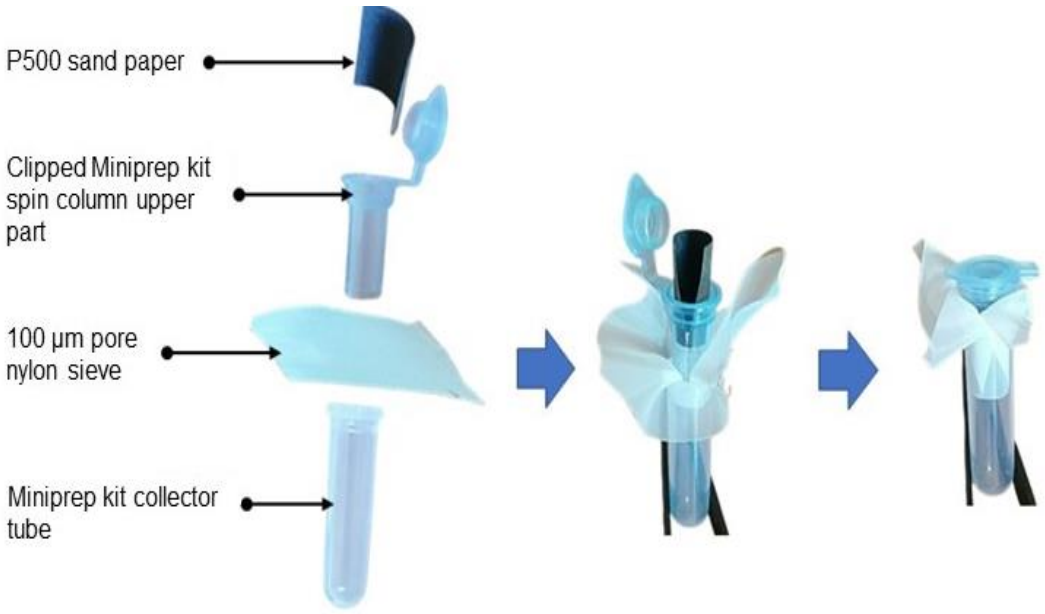

Figure 6.11: One time use home-made abrasion system. Seeds are abraded on the sand-paper rolled around the column. The thermos sealed or wrapped Nylon sieve filters the seeds from the MSCs enriched abraded powder fraction.

6.2.13. Immuno dotblot and semi-quantitative analysis from dry seed MSC abrasive fractions

Powder of MSC surface CW was chemically extracted with 80 µL of extraction buffer [80 µL of 5 mM sodium acetate pH 4.6 containing 1 $\mu L.mL^{-1}$ of plant protease inhibitor cocktail (Sigma P9599)] per mg of powder. The collector tube with cap was shaken at 250 rpm during 1 h at 4°C to ensure proper extraction. A nitrocellulose membrane was cut to fit inside the 96-well Bio-Dot microfiltration apparatus (BioRad) and soaked in TBS (0.02 M Tris-HCl pH 7.5, 0.15 M NaCl for 10 min. After a 5 min centrifugation at 14400 rpm, supernatant was recovered, diluted (1 µL in 50 µL milliQ-H_2O) and deposited into sample wells onto nitrocellulose membrane disposed into a 96-well Bio-Dot microfiltration apparatus (BioRad). A 1 min 30 s of vacuum insured homogeneous transfer among the wells. The membrane was briefly air-dried

to ensure proper adsorption and blocked in 5 % Milk (Regilait® non fat dry milk) in TTBS (0.05 % Tween 20, 0.02 M Tris-HCl pH 7.5, 0.5 M NaCl) overnight at 4°C, under a 50 rpm gentle shaking. The membranes were rolled in a hemolysis tube containing 5 mL of cell wall epitope-specific primary antibodies (**Table 6.7**) diluted 1:100 in TTBS-milk for 3-4 hours at RT. Membranes were washed 6 x 5 min each in about 50 mL TTBS before incubation for 1 h in a hemolysis tube filled with 5 mL of 1:5000 Alkaline phosphatase (AP) conjugated secondary antibody adapted to the species used to raise the primary antibody (**Table 6.7**). After 3 x 5 min wash in about 50 mL TTBS and 3 x 1 min in deionized water, membranes were immersed in the Alkaline phosphatase (AP) chromogenic substrate 0.3 $mg.mL^{-1}$ NBT 0.15 $mg.mL^{-1}$ BCIP in 100 mM Tris-HCl pH 9.5, 100 mM NaCl, 10 mM $MgCl_2$ for 5 to 15 min. The membranes were air dried and scanned with the Epson Perfection V700 photo or imaged with a Canon EOS 550D digital camera (**Figure 6.12.A**).

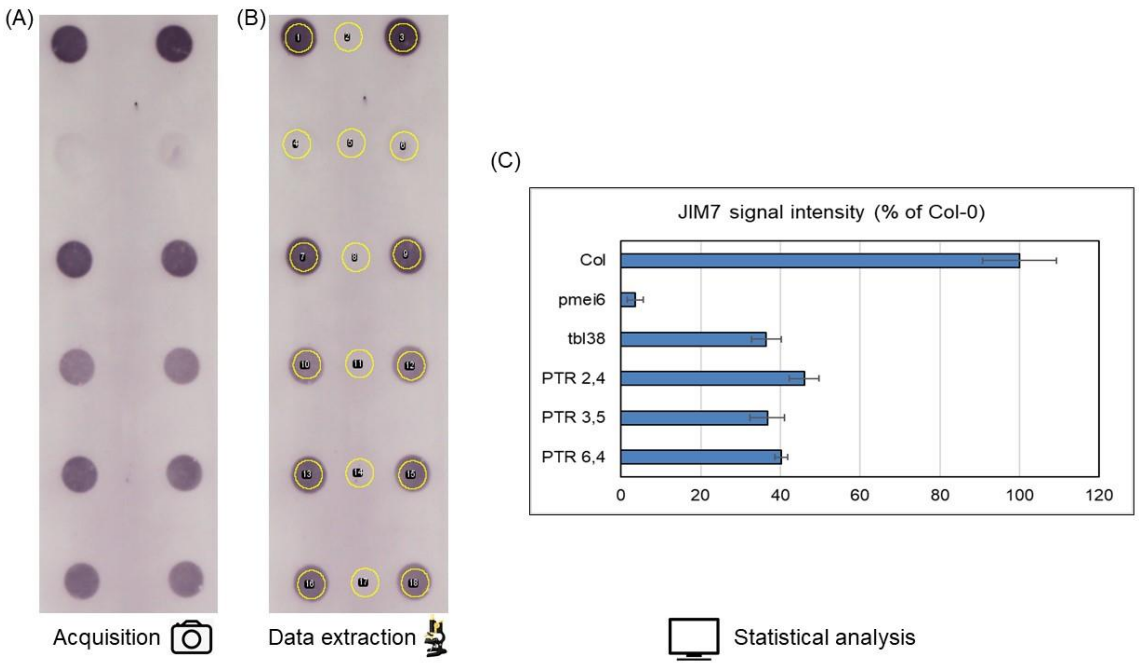

Figure 6.12 : DotBlot semi-quantitative data analysis. **(A)** and **(B)** High resolution images of blotted membranes were taken and analyzed using ImageJ. **(C)** Pixel intensity from each dot and corresponding background noise was extracted and statistically compared.

DotBlots were analyzed using ImageJ 1.8 (https://imagej.nih.gov/ij/) without edition of native images. Multiple regions of interest (ROI) of a similar selected size were used to measure mean intensity of the signal (**Figure 6.12.B**). Two negative controls were used (i) the extraction buffer that was blotted on the membrane and (ii) for each lane, another ROI placed outside of the dots to account for possible vertically different background noises. Measurements were extracted on

an Excel file for analyses. Corresponding Wild-type values were assigned as “100 % of signal” and percentage of mutant signal values were calculated accordingly ± standard error of the mean (SEM) Statistical data was obtained using Anova / Tukey tests. with n ≥ 3 (**Figure 6.11.C**).

6.2.14. SDS-PAGE and Western-blots from dry seed MSC abrasive fractions

For SDS-PAGE analysis, MSC-enriched powder samples were extracted under 5 conditions for comparison. **(1)** 80 µL of 5 mM sodium acetate pH 4.6, 0.2 M $CaCl_2$ containing 1 $\mu L.mL^{-1}$ of plant protease inhibitor cocktail (Sigma P9599)] were added per mg of powder. Samples were grinded with a metallic grindball until the pellet was completely resuspended. Then, they were horizontally extracted at 250 rpm on an orbital shaker at 4°C for 1 h. After 10 min of centrifugation at 14000 rpm, the supernatant was carefully transferred in a clean 1.5 mL tube containing 4 µL of Laemmli 4X (Bio-Rad Laboratories) per 40 µl of supernatant. The mix was heated to 100°C for 10 min prior to loading. **(2 and 3)** The remaining pellet of MSC CW fraction was mixed with 80 µl of denaturation solution containing 10 % (v/v) β-mercaptoethanol, 6 M urea, 10 % (v/v) glycerol, 5 % (v/v) sodium dodecyl sulfate (Kato et al., 2002), 0.01 % Bromophenol blue and with **(2)** or without **(3)** additional 0.2 M calcium chloride per mg of initial powder. Samples were run for a second horizontal extraction again at 250 rpm on an orbital shaker at 4°C for 1 hour. After 10 min of centrifugation at 14000 rpm, the supernatant was carefully transferred in a clean 1.5 ml tube. **(4 and 5)** MSC-enriched powder samples were also directly extracted in the same denaturation solutions with **(4)** or without **(5)** 0.2 M calcium chloride. Twenty-five µl of each sample were analysed by SDS-PAGE on a 11 % or 6 % Acrylamide resolving SDS-PAGE gel equipped with a 4 % Acrylamide stacking gel under electric current set at 120 mA and 500 V. After inititial comparison protocols **(1)** and **(2)** were selected for further analysis.

After migration, gels were either incubated overnight in PageBlue Protein staining solution (Thermo Scientific) with constant agitation or transferred onto nitrocellulose membrane for 45 min to 1 h under electric current set at 20 V and 800 mA. Stained gels were washed in clean deionized water changed twice a day for 6 days then scanned at 600 dpi with Epson Perfection V700 photo scanner. Membranes were transiently stained in Ponceau Red solution and imaged. Nitrocellulose membranes were blocked overnight in 0.02 M Tris-HCl pH 7.5, 0.5 M NaCl, 0.5 $g.L^{-1}$ Tween 20 and 5 % Régilait non-fat milk (TTBS-milk) under constant agitation at 4°C and 60 rpm on an orbital shaker. Membranes were incubated for 4 h in 10 ml of JIM12 or LM1 primary antibody diluted 1:100 in TTBS-milk at room temperature, then rinsed 6 x 5 min with

TTBS. Secondary antibody incubation was performed for 2 h in 10 ml of secondary antibody coupled with alkaline phosphatase (anti-rat IgG-AP, Sigma A8438) diluted 1:5000 in TTBS-milk at room temperature. Membranes were rinsed 3 x 5 min with TTBS and once with deionized water before revelation in 50 ml of alkaline phosphatase BCIP/NBT chromogenic substrate (see section 6.2.13) for 10 to 15 min. Once dried at 37°C on Slide Warmer overnight, membranes were scanned at 600 dpi with Epson Perfection V700 photo scanner or imaged with a Canon EOS 550D digital camera.

6.2.15. Acetyl group deesterification and acetic acid semi-quantitative analysis from dry seed MSC abrasive fractions

The acetylation of cell wall polymer in MSC surface wall abrasive samples was analyzed following adaptation of previously described method (Stranne et al., 2018)Acetyl groups were released by ester alkaline hydrolysis with 1 M NaOH (80 µL of NaOH per mg powder). The samples were vigorously shaken horizontally for 1 h at 250 rpm at 4°C. The reaction was stopped with an equal volume of 1 M HCl which stabilizes pH at a neutral value. Acetic acid content was then determined using an enzymatic Acetic Acid Assay Kit (Megazyme, K-ACET) by measuring the stoichiometric conversion of acetic acid to NADH following three enzymatic reactions. The same volume of samples (100 µL) was used following the suggested protocol with the following adaptation (1.5 mL of final reaction volume was used instead of 2.84 mL). NADH was measured at 340 nm with a ©Agilent Cary 60 UV-Vis spectrophotometer using the Eppendorf Uvette (Dutscher 033189). The linearity of the assay was checked with acetic acid standard provided with the kit and with an acetic acid standard curve (0-5µg). The final results were expressed as µg of acetic acid released per mg of original powder ± standard error of the mean (SEM) Statistical data was obtained using Anova / Tukey tests. with $n \geq 3$.

6.2.16. Mass spectrometry analyses from dry seed MSC abrasive fractions

MSC surface wall powders were sent to MicroWall ANR project partner Marie-Christine RALET-RENARD and team (BIA, INRAe-Nantes) for mass spectrometry analyses. Briefly, samples were resuspended in 1 mL distilled water for 1 h. An aliquot (450 µL) was mixed with 50 µL of 500 mM sodium acetate buffer pH 5.0 and polysaccharides were either hydrolysed for 24 h at 40°C under 500 rpm shaking with a polygalacturonase (produced by Jérôme Pelloux team, BIOPI, Amiens) with higher affinity for HG with a higher degree of methylesterification or a pectin lyase that preferentially digest HG with a lower degree of methylesterification. Resulting oligogalacturonan fragments were filtered on 0.45 µm and analyzed in LC-MS and

correlated with a prediction database (MZ Mine) allowing identifying their degree of polymerization (DP), degree or methylation (DM) and degree of acetylation (DA). Only molecular species present in at least 4 / 5 runs were kept for analysis.

6.2.17. Arabidopsis silique fixation, paraffin tissue array embedding and microtomy

Sequential kinetics of developing siliques of each genotype were harvested, placed in order (pedicel on top) and sandwiched in Deltalab histoset 2 embedding cassettes (Dutscher 039751) between two 30,2 × 25,4 × 2 mm SimPort^{TM} biopsy foam (Dutscher 040666). Selected siliques that were initially labeled to account for a corresponding DAP were placed with pedicels facing down for better identification. Shortly after, cassettes were submerged in FAA fixative (3.7 % (v/v) formaldehyde from 37 % formaldehyde solution (Sigma 1.04002); 5 % (v/v) acetic acid; 50 % (v/v) ethanol; 35 % (v/v) Milli-Q water or RNase-free DEPC-treated water, depending on the necessity), vacuum infiltrated for 8 x 1 min and fixed at 4°C for 6-8 h. Cassettes were then washed 4 times in 50 % ethanol and placed at 4°C for 72-84 h. Samples dehydration and paraffin embedding was done according to Francoz et al 2016. The ordered siliques containing seed development kinetics were used to assemble organized tissue arrays each encompassing up to 1000 seeds (Francoz et al., 2019b, 2019a) To assemble paraffin blocs, cassettes were delicately opened on a slide warmer set to 60°C (LabScientific XH-2001) and siliques were deposited on metallic mold with respect to the initial order. The molds were covered with a fitting plastic ring (Simport M460), the paraffin tissue-array blocks were allowed to solidify at least O/N at 4°C and could be stored for months/years. Ten-to twelve µm-thick serial sections were made with a rotary microtome and spread on silane coated slides (**Figure 6.13**)

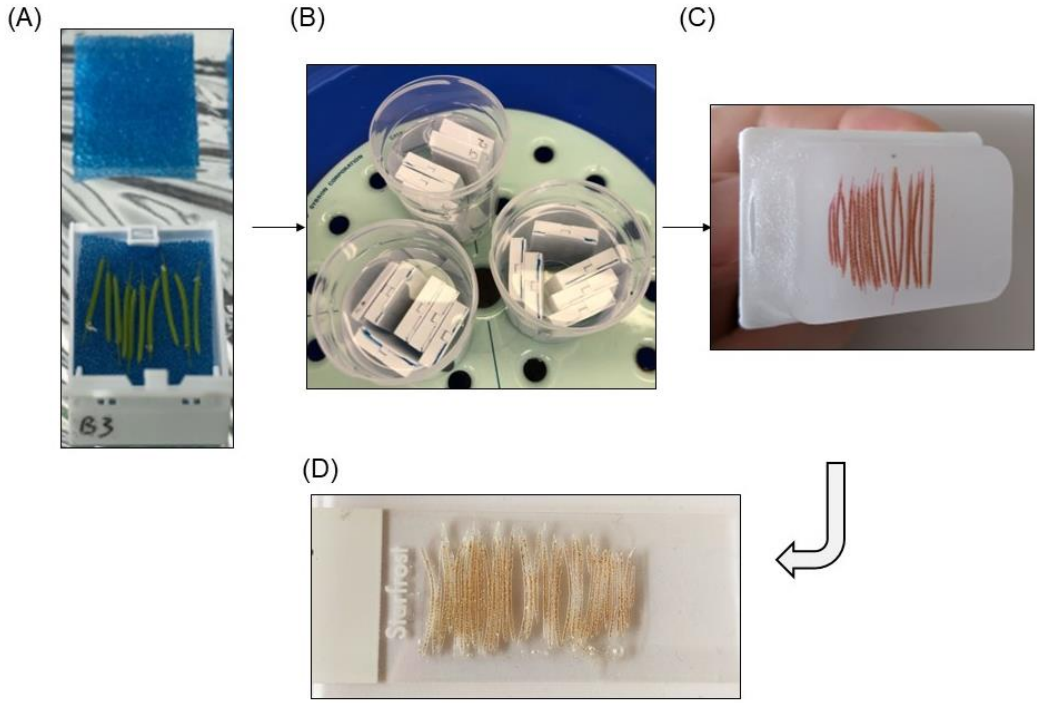

Figure 6.13 Developing siliques harvesting, fixation and microtomy. **(A)** and **(B)** developing siliques were harvested and sandwiched between two biopsy foam in biopsy cassettes. Multiple cassettes could be fit in plastic pot for fixation and paraffin embedding steps. **(C)** and **(D)** Keeping similar organization, siliques were gathered in paraffin blocks to generate 40 10 µm serial-sections (1 serial section per slide; only one slide is shown here).

6.2.18. Developing seed and dry seed resin embedding, and (ultra)microtomy

6.2.18.1. *In situ* RNA hybridization on serial section of paraffin –embedded tissue arrays

In situ RNA Hybridization experiments were performed as described in details in Francoz et al., (2016) and Francoz et al., (2019a). In short, fill length cDNA including 5'-UTR and 3'-UTR were used as template for riboprobe synthesis (**Table 6.11**). The plasmids were first linearized at 5' end and 3' end to further generate anti-sense and sense probes, respectively **(Table 6.11**). Synthesis of digoxygenin-labeled riboprobes was performed by *in vitro* transcription using DigRNA labeling mix (Roche11277073910) and T3 (Promega P2083) or T7 RNA polymerase (Promega P2075) depending on the initial orientation of the cDNA in the vector (**Table 6.9**). Sense riboprobes were used as a negative control and the antisense *PRX36* riboprobe (Francoz et al., 2016) as a positive control. Serial sections of paraffin-embedded wild-type seed development kinetics were first deparaffinized with xylene and rehydrated with an inverted ethanol series up to water (Francoz et al., 2016). Each probe was hybridized overnight on paraffin wild-type serial sections of seeds encompassing all developmental stages. Following stringent washing steps, detection of hybridized riboprobes was performed with the

anti-digoxigenin antibody coupled with alkaline phosphatase and the revelation with its chromogenic substrate (BCIP/NBT) overnight. Finally, slides were mounted in EUKITT® (Dutscher 045799) and scanned with the nanozoomer HT (Hamamatsu, https://www.hamamatsu.com/). Image analysis was performed using NDPview (Hamamatsu, https://www.hamamatsu.com/) and Figures were assembled using Corel Photopaint.

Table 6.11: Digoxigenin-labeled riboprobe synthesis parameters

Accession	Annotation	cDNA size	Linearizing enzyme	RNA Polymerase	antisense (AS) or sense (S) Riboprobe	rIboprobe length (b)	hydrolysis time (min) to chopp off down to 400b
AT4G01140	*DUF1191*	1474bp	NotI	T3	AS	1639	17.18
			BamHI	T7	S	1611	17.08
AT1G29050	*TBL38 (DUF231)*	1304bp	EcoRI	T3	AS	1415	16.30
			BamHI	T7	S	1455	16.48
AT2G43050	*PMEPCRD / PME16*	1734bp	NotI	T3	AS	1899	17.94
			BamHI	T7	S	1871	17.87
AT1G23200	*HMS / PME6*	1839bp	EcoRI	T3	AS	1950	18.07
			BamHI	T7	S	1990	18.16
AT1G17200	*CASPL2A1*	777bp	EcoRI	T3	AS	876	12.35
			BamHI	T7	S	914	12.78

6.2.19. Immunofluorescence on tissue-array sections

The protocol described in Francoz et al., (2019b) was used. Serial sections of paraffin-embedded wild-type or mutant seed development kinetics were first deparaffinized with xylene and rehydrated with an inverted ethanol series up to water. The slides were placed in 20-slide plastic rack and collectively blocked in 200 mL 5 % TTBS-Milk (5 % non fat dry milk (Regilait), 0.3 % Tween 20, 0.01 M Tris-HCl pH 7.5, 0.5 M NaCl) for 30 min at RT. The slides were individually incubated in 150 µL of a 1:10 dilution of primary antibodies (**Table 6.7**) deposited for a 3-to-4 h incubation under a coverslip in a home-made humid chamber. For double immunolabeling, two antibodies from different species were mixed together at this step. The coverslip was carefully removed by dipping the slide in TTBS-milk and the slides were collectively washed 6 x 5 min in 200 mL TTBS. The adapted secondary antibody (**Table 6.7**)

(150 µL 1:100 dilution in TTBS-milk) was hybridized for 1-2 h at RT under a coverslip in a home-made humid chamber. In case of double immunofluorescence, one seondary antibody was labeled with Alexa fluor 488 while the other was labeled with Alexa fluor 555 (**Table 6.7**). The coverslips were carefully removed and the slides were collectively washed 3 x 5 min in 200 mL TTBS and 3 x 1 min in Milli-Q water. Slides were mounted in Prolong Gold antifade (Molecular probes P36934) or Fluoromount-G™ (Invitrogen 15586276). Slides were scanned using a Nanozoomer 2.0RS scanner (Hamamatsu, Hamamatsu City, Japan) at 20 × or 40 ×. The FITC (excitation: 482/18 nm; dichroic mirror 488 nm; emission: 525/30 nm) and TRITC (excitation: 563/9 nm; dichroic mirror 561 nm; emission: 607/36 nm) filter sets were used sequentially to visualize Alexa488 and Alexa555 fluorescence, respectively. The bright field (BF) mode was also sequentially used to visualize the morphology. Scans were analyzed using NDP view (Hamamatsu, Hamamatsu City, Japan).

6.2.20. Confocal spinning disk microscopy of seed development kinetics of *A. thaliana* stable transformants (High throughput strategy)

Developing siliques taken from plants expressing the different TagRFP constructs in various genetic backgrounds were dissected and the replums containing the seeds were mounted under a coverslip in distilled water. Image were taken with a PLAN APO 20x/0.75 dry objective using the confocal spinning disk microscope from Perkin Elmer driven by the Volocity 6.3.0 software and equipped with a YokogamaCSU-X1 scan head, two EmCCD Hamamatsu C9100-13 cameras (Hamamatsu, Hamamatsu City, Japan) and a 580 nm beam splitter to separate dual staining on the 2 cameras. Images were sequentially acquired for TagRFP fluorescence then chloroplast autofluorescence used as control. TagRFP was excited with a 561 nm laser (Laser power intensity: 7% or 15%, exposure time: 200 msec, gain: 5, sensitivity: 148) and the fluorescence was selected between 580 and 612 nm. Chloroplast autofluorescence was excited with a 561 nm laser and the fluorescence was detected with a 656 long-pass filter. Image J was used to analyze the Z distribution of the fluorescence intensity profile along regions of interest (ROIs). The set display range was set to 16-bit (0-65635) for the 16-bit spinning disk images that were further calibrated using the set scale option (1 pixel = 0.66 µm). Four modes were used: (i) The maximum intensity Z projection mode was used to build a stack image of a given number of 1 µm-slices taking the maximum fluorescence value among the slices for each pixel. (ii) The sum intensity Z projection mode was used for quantification analysis since all the intensity values from all selected slices were summed for each pixel. (iii) The orthogonal view

along an axis positioned in the XY plan was used to better visualize the Z distribution of the fluorescence along the chosen XY axis. (iv) Image J was also used to analyze the fluorescence intensity profile along regions of interests (ROIs) along the cell wall between two intercellular junctions. A sum slice Z projection was first made using 30 slices from the confocal pile. The resulting image was calibrated (1 pixel = 0.66 µm) and the segmented line tool (width 5) was used to define the ROIs between two successive tricellular junctions from the mucilage secretory cell. The data was processed using Microsoft Excel and the fluorescence intensities were expressed as relative expression values (% of the maximum value for each individual ROI).

6.2.21. Multiphoton confocal microscopy of leaves from *N. benthamiana* transient transformants (High resolution strategy)

Transiently transformed *N. benthamiana* leaves were observed 48 h post agroinfiltration using an upright confocal laser scanning microscope (LEICA SP8) with a 40 x apochromatic water immersion lens. TagRFP and YFP protein fluorescence were imaged with the following settings (excitation: 561 nm; emission: 582–622 nm; excitation 513nm, emission: 527-530nm), respectively. Z stacks (maximum intensity) were performed using ImageJ.

6.2.22. Scanning electron microscopy

Wild type dry and abraded dry seeds, 100 µm nylon mesh and abrasion powder were used for scanning electron microscopy assays. Samples were metallized using a **MED 020** modular high vacuum coating and directly observed with no further treatment using a Quanta 250 FEG FEI electron microscopy. Images were taken with the following settings (spot size: 2.0, acceleration: 10.00 kV).

6.2.23. *In silico* model and docking simulations

Homology model for PRX36, TBL38 and PRX56 (UniProt accession number Q9SD46, Q8VY22 and Q9LXG3, respectively) was built with the Phyre2 server (Alberts et al., 2002). For PRX36 and PRX56, the template was the crystallographic structure (X-Ray diffraction, 1.45 A˚) of *A. thaliana* PRX53 (At5g06720; Protein Data Bank no.1PA2) (Østergaard et al., 2000). For TBL38, the template was the crystallographic structure (X-Ray diffraction, 1.85 Å) of *A. thaliana* TBL29/ESK1/XOAT1 (Lunin et al., 2020).

For docking experiments, α-D-(1-4) polygalacturonic acid structural model (Braccini et al., 1999) was retrieved from the Glyco3D portal (Pérez et al., 2015)

http://glyco3d.cermav.cnrs.fr/mol.php?type=polysaccharide&molecule=2504) and was modified to initially build the five hexagalacturonates models used to establish JIM7 specificity (Clausen et al., 2003). This selection was extended to the 124 oligogalacturonates (OGAs) from DP2 to DP6 covering all the theoretical combination of methylation (64 OGAs of DP6 + 32 OGAs of DP5 + 16 OGAs of DP4 + 8 OGAs of DP3 +4 OGAs of DP2). AutoDock Tools (Morris et al., 2009) and AutoDock Vina (Trott and Olson, 2010) were used for simulating the binding of the 124 OGAs to PRX36 within a search box encompassing the whole target protein enabling to recover the 9 best poses for each OGA. Energy level and Root-mean-square deviation (RMSD) upper bound values were obtained with AutoDock tools, representing the affinity of each pose and distances from pose 1 for a given OGA, respectively. RMSD upper bound matches each atom of a given OGA in each conformations (poses) with itself in the conformation of reference (pose 1). As an imperfect mean to sort and rank the 124 OGAs, we used the following proxy: We summed the energy levels (negative values) of the 9 poses (the lower, the higher affinity) and summed the 9 RMSD for each OGA (the lower, the less dispersed). The ratio of both was used as a proxy integrating both parameters (the lower ratio, the higher affinity and higher gathering of the poses on the protein). Structural models were visualized and analyzed with Swiss-PdbViewer (Guex and Peitsch, 1997). The visualization of the models, color edition and identification of the amino acids distant of less than 5 Å from the best hexagalacturonate docking models were performed using Swiss-PdbViewer (Guex and Peitsch, 1997) (http://www.expasy.org/spdbv/). Similar analysis was performed with PRX56 against the 64 OGAs of DP6. Finally, concerning PRX36 an aditional docking simulation was made with the two best hits (OGAof DP 6 so-called Clausen 4 and Clausen 3) that

General bibliography

Akoh, C.C., Lee, G.C., Liaw, Y.C., Huang, T.H., and Shaw, J.F. (2004). GDSL family of serine esterases/lipases. Prog. Lipid Res. **43**: 534–552.

Albenne, C., Canut, H., and Jamet, E. (2013). Plant cell wall proteomics: the leadership of *Arabidopsis thaliana*. Front. Plant Sci. **4**: 111.

Alberts B, Johnson A, Lewis J, et al. (2002). The Phyre2 web portal for protein modeling, prediction and analysis. In Molecular Biology of the Cell. 4th edition. (Nat Protoc), pp. 845–858.

Amsbury, S., Hunt, L., Elhaddad, N., Baillie, A., Lundgren, M., Verhertbruggen, Y., Scheller, H. V., Knox, J.P., Fleming, A.J., and Gray, J.E. (2016). Stomatal function requires pectin de-methyl-esterification of the guard cell wall. Curr. Biol. **26**: 2899–2906.

Anderson, C.T. and Kieber, J.J. (2020). Dynamic construction, perception, and remodeling of plant cell walls. Annu. Rev. Plant Biol. **71**: 39–69.

Anterola, A.M. and Lewis, N.G. (2002). Trends in lignin modification: a comprehensive analysis of the effects of genetic manipulations/mutations on lignification and vascular integrity. Phytochemistry **61**: 221–294.

Arsovski, A.A., Haughn, G.W., and Western, T.L. (2010). Seed coat mucilage cells of *Arabidopsis thaliana* as a model for plant cell wall research. Plant Signal. Behav. **5**: 796–801.

Arsovski, A.A., Popma, T.M., Haughn, G.W., Carpita, N.C., McCann, M.C., and Western, T.L. (2009). AtBXL1 encodes a bifunctional β-d-xylosidase/α-l-arabinofuranosidase required for pectic arabinan modification in Arabidopsis mucilage secretory cells. Plant Physiol. **150**: 1219.

Bacete, L. and Hamann, T. (2020). The role of mechanoperception in plant cell wall integrity maintenance. Plants **9**: 574.

Bar-Peled, M., Urbanowicz, B.R., and O'Neill, M.A. (2012). The synthesis and origin of the pectic polysaccharide rhamnogalacturonan II - Insights from nucleotide sugar formation and diversity. Front. Plant Sci. **3**.

Barbosa, I., Bellis, D. De, Flückiger, I., Bellani, E., Grangé-Guerment, M., Hématy, K., and Geldner, N. (2022). Directed growth and fusion of membrane-wall microdomains requires CASP-mediated inhibition and displacement of secretory foci. Unpublished: 2022.07.03.498613.

Barbosa, I.C.R., Rojas-Murcia, N., and Geldner, N. (2019). The Casparian strip—one ring to bring cell biology to lignification? Curr. Opin. Biotechnol. **56**: 121–129.

Barnes, W.J., Zelinsky, E., and Anderson, C.T. (2022). Polygalacturonase activity promotes aberrant cell separation in the *quasimodo2* mutant of *Arabidopsis thaliana*. Cell Surf. **8**.

Barros, J., Serk, H., Granlund, I., and Pesquet, E. (2015). The cell biology of lignification in higher plants. Ann. Bot. **115**: 1053–1074.

Belmonte, M.F. et al. (2013). Comprehensive developmental profiles of gene activity in regions and subregions of the Arabidopsis seed. Proc. Natl. Acad. Sci. **110**: E435–E444.

Bernards, M.A., Summerhurst, D.K., and Razem, F.A. (2004). Oxidases, peroxidases and hydrogen peroxide: The suberin connection. Phytochem. Rev. **3**: 113–126.

Berthet, S., Demont-Caulet, N., Pollet, B., Bidzinski, P., Cézard, L., le Bris, P., Herve, J., Blondet, E., Balzergue, S., Lapierre, C., and Jouanin, L. (2011). Disruption of LACCASE4 and 17 results in tissue-specific alterations to lignification of *Arabidopsis thaliana* stems. Plant Cell **23**: 1124–1137.

Berthet, S., Thevenin, J., Baratiny, D., Demont-Caulet, N., Debeaujon, I., Bidzinski, P., Leple, J.C., Huis, R., Hawkins, S., Gomez, L.D., Lapierre, C., and Jouanin, L. (2012). Role of plant laccases in lignin polymerization. In Advances in Botanical Research (Elsevier), pp. 145–172.

Bischoff, V., Nita, S., Neumetzler, L., Schindelasch, D., Urbain, A., Eshed, R., Persson, S., Delmer, D., and Scheible, W.R. (2010). TRICHOME BIREFRINGENCE and its homolog AT5G01360 encode plant-specific DUF231 proteins required for cellulose biosynthesis in Arabidopsis. Plant Physiol. **153**: 590.

Bonavita, A., Carratore, V., Ciardiello, M.A., Giovane, A., Servillo, L., and D'Avino, R. (2016). Influence of pH on the structure and function of kiwi pectin methylesterase inhibitor. J. Agric. Food Chem. **64**: 5866–5876.

Bonnett, H.T. (1968). The root endodermis: fine structure and function. J. Cell Biol. **37**: 199–205.

Bonnin, E., Dolo, E., Le Goff, A., and Thibault, J.F. (2002). Characterisation of pectin subunits released by an optimised combination of enzymes. Carbohydr. Res. **337**: 1687–1696.

Borassi, C., Sede, A.R., Mecchia, M.A., Salgado Salter, J.D., Marzol, E., Muschietti, J.P., and Estevez, J.M. (2016). An update on cell surface proteins containing extensin-motifs. J. Exp. Bot. **67**: 477–487.

Bosch, M., Cheung, A.Y., and Hepler, P.K. (2005). Pectin methylesterase, a regulator of pollen tube growth. Plant Physiol. **138**: 1334–1346.

Braccini, I., Grasso, R.P., and Pérez, S. (1999). Conformational and configurational features of acidic polysaccharides and their interactions with calcium ions: a molecular modeling investigation. Carbohydr. Res. **317**: 119–130.

Brett, C. and Waldron, K. (1990). Physiology and biochemistry of plant cell walls (Springer Netherlands).

Breygina, M., Klimenko, E., and Schekaleva, O. (2021). Pollen germination and pollen tube growth in gymnosperms. Plants **10**: 1301.

Busse-Wicher, M., Gomes, T.C.F., Tryfona, T., Nikolovski, N., Stott, K., Grantham, N.J., Bolam, D.N., Skaf, M.S., and Dupree, P. (2014). The pattern of xylan acetylation suggests xylan may interact with cellulose microfibrils as a twofold helical screw in the secondary plant cell wall of *Arabidopsis thaliana*. Plant J. **79**: 492–506.

Cannon, M.C., Terneus, K., Hall, Q., Tan, L., Wang, Y., Wegenhart, B.L., Chen, L., Lamport, D.T.A., Chen, Y., and Kieliszewski, M.J. (2008). Self-assembly of the plant cell wall requires an extensin scaffold. Proc. Natl. Acad. Sci. U. S. A. **105**: 2226–2231.

Carpin, S., Crèvecoeur, M., de Meyer, M., Simon, P., Greppin, H., and Penel, C. (2001). Identification of a Ca_{2+} -pectate binding site on an apoplastic peroxidase. Plant Cell **13**: 511–520.

Carter, R., Woolfenden, H., Baillie, A., Amsbury, S., Carroll, S., Healicon, E., Sovatzoglou, S., Braybrook, S., Gray, J.E., Hobbs, J., Morris, R.J., and Fleming, A.J. (2017). Stomatal opening involves polar, not radial, stiffening of guard cells. Curr. Biol. **27**: 2974-2983.

Cascallares, M., Setzes, N., Marchetti, F., López, G.A., Distéfano, A.M., Cainzos, M., Zabaleta, E., and Pagnussat, G.C. (2020). A complex journey: cell wall remodeling, interactions, and integrity during pollen tube growth. Front. Plant Sci. **11**: 599247.

Celus, M., Kyomugasho, C., Van Loey, A.M., Grauwet, T., and Hendrickx, M.E. (2018). Influence of pectin structural properties on interactions with divalent cations and its associated functionalities. Compr. Rev. Food Sci. Food Saf. **17**: 1576–1594.

Chan, J. and Coen, E. (2020). Interaction between autonomous and microtubule guidance systems controls cellulose synthase trajectories. Curr. Biol. **30**: 941-947.e2.

Chebli, Y. and Geitmann, A. (2017). Cellular growth in plants requires regulation of cell wall biochemistry. Curr. Opin. Cell Biol. **44**: 28–35.

Chiniquy, D., Underwood, W., Corwin, J., Ryan, A., Szemenyei, H., Lim, C.C., Stonebloom, S.H., Birdseye, D.S., Vogel, J., Kliebenstein, D., Scheller, H. V., and Somerville, S. (2019). PMR5, an acetylation protein at the intersection of pectin biosynthesis and defense against fungal pathogens. Plant J. **100**: 1022–1035.

Clausen, M.H., Willats, W.G.T., and Knox, J.P. (2003). Synthetic methyl hexagalacturonate hapten inhibitors of anti-homogalacturonan monoclonal antibodies LM7, JIM5 and JIM7. Carbohydr. Res. **338**: 1797–1800.

Clemente, H.S., Kolkas, H., Canut, H., and Jamet, E. (2022). Plant cell wall proteomes: the core of conserved protein families and the case of non-canonical proteins. Int. J. Mol. Sci. **23**: 4273.

Cocking, E.C. (1972). Plant cell protoplasts-isolation and development. Annu. Rev. Plant Physiol. **23**: 29–50.

Coculo, D. and Lionetti, V. (2022). The plant invertase/pectin methylesterase inhibitor superfamily. Front. Plant Sci. **13**: 780.

Cosgrove, D.J. and Jarvis, M.C. (2012). Comparative structure and biomechanics of plant primary and secondary cell walls. Front. Plant Sci. **3**: 204.

Cosio, C., Ranocha, P., Francoz, E., Burlat, V., Zheng, Y., Perry, S.E., Ripoll, J.J., Yanofsky, M., and Dunand, C. (2017). The class III peroxidase PRX17 is a direct target of the MADS-box transcription factor AGAMOUS-LIKE15 (AGL15) and participates in lignified tissue formation. New Phytol. **213**: 250–263.

Dardelle, F., Lehner, A., Ramdani, Y., Bardor, M., Lerouge, P., Driouich, A., and Mollet, J.C. (2010). Biochemical and immunocytological characterizations of *Arabidopsis* pollen tube cell wall. Plant Physiol. **153**: 1563–1576.

Dauphin, B.G., Ranocha, P., Dunand, C., and Burlat, V. (2022). Cell-wall microdomain remodeling controls crucial developmental processes. Trends Plant Sci. **27**: 1033-1048

Dea, I.C.M. and Madden, J.K. (1986). Acetylated pectic polysaccharides of sugar beet. Food Hydrocoll. **1**: 71–88.

Dean, G.H., Pang, F., Haughn, G.W., and Kunst, L. (2020). A simple, non-toxic method for separating seeds based on density, and its application in isolating *Arabidopsis thaliana* seed oil mutants. Appl. Plant Sci. **8**.

Debeaujon, I., Nesi, N., Perez, P., Devic, M., Grandjean, O., Caboche, M., and Lepiniec, L. (2003). Proanthocyanidin-accumulating cells in Arabidopsis testa: regulation of differentiation and role in seed development. Plant Cell **15**: 2514–2531.

Dehors, J., Mareck, A., Kiefer-Meyer, M.C., Menu-Bouaouiche, L., Lehner, A., and Mollet, J.C. (2019). Evolution of cell wall polymers in tip-growing land plant gametophytes: composition, distribution, functional aspects and their remodeling. Front. Plant Sci. **10**: 441.

Doll, N.M., Berenguer, E., Truskina, J., and Ingram, G. (2022). AtEXT3 is not essential for early embryogenesis or plant viability in Arabidopsis. New Phytol.: doi:10.1111/nph.18452.

Driouich, A., Durand, C., and Vicré-Gibouin, M. (2007). Formation and separation of root border cells. Trends Plant Sci. **12**: 14–19.

Driouich, A., Follet-Gueye, M.L., Bernard, S., Kousar, S., Chevalier, L., Vicré-Gibouin, M., and Lerouxel, O. (2012). Golgi-mediated synthesis and secretion of matrix polysaccharides of the primary cell wall of higher plants. Front. Plant Sci. **3**.

Dronnet, V.M., Renard, C.M.G.C., Axelos, M.A.V., and Thibault, J.F. (1996). Characterisation and selectivity of divalent metal ions binding by citrus and sugar-beet pectins. Carbohydr. Polym. **30**: 253–263.

Du, J. et al. (2020). Mutations in the pectin methyltransferase QUASIMODO2 influence cellulose biosynthesis and wall integrity in Arabidopsis. Plant Cell **32**: 3576–3597.

Du, J., Anderson, C.T., and Xiao, C. (2022a). Dynamics of pectic homogalacturonan in cellular morphogenesis and adhesion, wall integrity sensing and plant development. Nat. Plants **8**: 332–340.

Du, J., Ruan, M., Li, X., Lan, Q., Zhang, Q., Hao, S., Gou, X., Anderson, C.T., and Xiao, C. (2022b). Pectin methyltransferase QUASIMODO2 functions in the formation of seed coat mucilage in Arabidopsis. J. Plant Physiol. **274**: 153709.

Duruflé, H., Clemente, H.S., Balliau, T., Zivy, M., Dunand, C., and Jamet, E. (2017). Cell wall proteome analysis of *Arabidopsis thaliana* mature stems. Proteomics **17**: 1600449.

Engler, C., Kandzia, R., and Marillonnet, S. (2008). A one pot, one step, precision cloning method with high throughput capability. PLoS One **3**: e3647.

Escamez, S. and Tuominen, H. (2014). Programmes of cell death and autolysis in tracheary elements: when a suicidal cell arranges its own corpse removal. J. Exp. Bot. **65**: 1313–1321.

Ezquer, I., Mizzotti, C., Nguema-Ona, E., Gotté, M., Beauzamy, L., Ebeling, V.V., Dubrulle, N., Costa de Oliveira, A., Caporali, E., Koroney, A.S., Boudaoud, A., Driouich, A., Colombo. (2016). The

developmental regulator SEEDSTICK controls structural and mechanical properties of the Arabidopsis seed coat. Plant Cell **28**: 2478–2492.

Fangel, J.U., Ulvskov, P., Knox, J.P., Mikkelsen, M.D., Harholt, J., Popper, Z.A., and Willats, W.G.T. (2012). Cell wall evolution and diversity. Front. Plant Sci. **3**.

Fawal, N., Li, Q., Savelli, B., Brette, M., Passaia, G., Fabre, M., Mathé, C., and Dunand, C. (2013). PeroxiBase: a database for large-scale evolutionary analysis of peroxidases. Nucleic Acids Res. **41**: D441–D444.

Ferrari, S., Savatin, D. V., Sicilia, F., Gramegna, G., Cervone, F., and De Lorenzo, G. (2013). Oligogalacturonides: plant damage-associated molecular patterns and regulators of growth and development. Front. Plant Sci. **4**.

Francoz, E. (2015). Hybridation d'ARN in situ systématique de la famille multigénique des peroxydases de classe III durant le développement des graines d'Arabidopsis thaliana et étude fonctionnelle de AtPrx36 dans le dynamisme pariétale des cellules sécrétrices. http://www.theses.fr.

Francoz, E., Ranocha, P., Burlat, V., and Dunand, C. (2015a). *Arabidopsis* seed mucilage secretory cells: regulation and dynamics. Trends Plant Sci. **20**: 515–524.

Francoz, E., Ranocha, P., Dunand, C., and Burlat, V. (2019a). Medium-throughput RNA in situ hybridization of serial sections from paraffin-embedded tissue microarrays. In Methods in Molecular Biology (Humana Press Inc.), pp. 99–130.

Francoz, E., Ranocha, P., Nguyen-Kim, H., Jamet, E., Burlat, V., and Dunand, C. (2015b). Roles of cell wall peroxidases in plant development. Phytochemistry **112**: 15–21.

Francoz, E., Ranocha, P., Pernot, C., Ru, A. Le, Pacquit, V., Dunand, C., and Burlat, V. (2016). Complementarity of medium-throughput in situ RNA hybridization and tissue-specific transcriptomics: Case study of Arabidopsis seed development kinetics. Sci. Rep. **6**.

Francoz, E., Ranocha, P., Le Ru, A., Martinez, Y., Fourquaux, I., Jauneau, A., Dunand, C., and Burlat, V. (2019b). Pectin demethylesterification generates platforms that anchor peroxidases to remodel plant cell wall domains. Dev. Cell **48**: 261-276.

Freshour, G., Clay, R.P., Fuller, M.S., Albersheim, P., Darvill, A.G., and Hahn, M.G. (1996). Developmental and tissue-specific structural alterations of the cell-wall polysaccharides of *Arabidopsis thaliana roots*. Plant Physiol. **110**: 1413–1429.

Le Gall, H., Philippe, F., Domon, J.M., Gillet, F., Pelloux, J., and Rayon, C. (2015). Cell wall metabolism in response to abiotic stress. Plants **4**: 112–166.

Gao, Y., He, C., Zhang, D., Liu, X., Xu, Z., Tian, Y., Liu, X.H., Zang, S., Pauly, M., Zhou, Y., and Zhang, B. (2017). Two trichome birefringence-like proteins mediate xylan acetylation, which is essential for leaf blight resistance in rice. Plant Physiol. **173**: 470–481.

Gardiner, J.C., Taylor, N.G., and Turner, S.R. (2003). Control of cellulose synthase complex localization in developing xylem. Plant Cell **15**: 1740–1748.

Geldner, N. (2013). The endodermis. Annu. Rev. Plant Biol. **64**: 531–558.

Giannoutsou, E., Apostolakos, P., and Galatis, B. (2016). Spatio-temporal diversification of the cell wall matrix materials in the developing stomatal complexes of *Zea mays*. Planta **244**: 1125–1143.

Gille, S. and Pauly, M. (2012). *O*-Acetylation of plant cell wall polysaccharides. Front. Plant Sci. **3**: 12.

Gonneau, M., Höfte, H., and Vernhettes, S. (2012). Fluorescent tags to explore cell wall structure and dynamics. Front. Plant Sci. **3**: 145.

Gou, J.Y., Miller, L.M., Hou, G., Yu, X.H., Chen, X.Y., and Liu, C.J. (2012). Acetylesterase-mediated deacetylation of pectin impairs cell elongation, pollen germination, and plant reproduction. Plant Cell **24**: 50–65.

Goujon T, Ferret, V., Mila, I., Pollet, B., Ruel, K., Burlat, V., Joseleau, J.-P., Barrière, Y., Lapierre, C., and Jouanin, L. (2003). Down-regulation of the AtCCR1 gene in *Arabidopsis thaliana*: effects on

phenotype, lignins and cell wall degradability. Planta 2003 2172 **217**: 218–228.

Grantham, N.J., Wurman-Rodrich, J., Terrett, O.M., Lyczakowski, J.J., Stott, K., Iuga, D., Simmons, T.J., Durand-Tardif, M., Brown, S.P., Dupree, R., Busse-Wicher, M., and Dupree, P. (2017). An even pattern of xylan substitution is critical for interaction with cellulose in plant cell walls. Nat. Plants **3**: 859–865.

Griffiths, J.S., Crepeau, M.J., Ralet, M.C., Seifert, G.J., and North, H.M. (2016). Dissecting seed mucilage adherence mediated by FEI2 and SOS5. Front. Plant Sci. **7**: 1073.

Griffiths, J.S. and North, H.M. (2017). Sticking to cellulose: exploiting Arabidopsis seed coat mucilage to understand cellulose biosynthesis and cell wall polysaccharide interactions. New Phytol. **214**: 959–966.

Gu, Y. and Rasmussen, C.G. (2022). Cell biology of primary cell wall synthesis in plants. Plant Cell **34**: 103–128.

Guex, N. and Peitsch, M.C. (1997). SWISS-MODEL and the Swiss-PdbViewer: an environment for comparative protein modeling. Electrophoresis **18**: 2714–2723.

Guo, J. and Yang, Z. (2020). Exocytosis and endocytosis: coordinating and fine-tuning the polar tip growth domain in pollen tubes. J. Exp. Bot. **71**: 2428–2438.

Guo, S., Wang, M., Song, X., Zhou, G., and Kong, Y. (2022). The evolving views of the simplest pectic polysaccharides: homogalacturonan. Plant Cell Rep. **1**: 211-223.

Haas, K.T., Wightman, R., Meyerowitz, E.M., and Peaucelle, A. (2020). Pectin homogalacturonan nanofilament expansion drives morphogenesis in plant epidermal cells. Science (80-.). **367**: 1003–1007.

Hall, Q. and Cannon, M.C. (2002). The cell wall hydroxyproline-rich glycoprotein RSH is essential for normal embryo development in Arabidopsis. Plant Cell **14**: 1161–1172.

Hellens, R., Mullineaux, P., and Klee, H. (2000). Technical focus: a guide to Agrobacterium binary Ti vectors. Trends Plant Sci. **5**: 446–451.

Herrero, J., Fernández-Pérez, F., Yebra, T., Novo-Uzal, E., Pomar, F., Pedreño, M.Á., Cuello, J., Guéra, A., Esteban-Carrasco, A., and Zapata, J.M. (2013). Bioinformatic and functional characterization of the basic peroxidase 72 from *Arabidopsis thaliana* involved in lignin biosynthesis. Planta **237**: 1599–1612.

Higaki, T., Takigawa-Imamura, H., Akita, K., Kutsuna, N., Kobayashi, R., Hasezawa, S., and Miura, T. (2017). Exogenous cellulase switches cell interdigitation to cell elongation in an RIC1-dependent manner in *Arabidopsis thaliana* cotyledon pavement cells. Plant Cell Physiol. **58**: 106–119.

Hocq, L. et al. (2017a). Combined experimental and computational approaches reveal distinct pH dependence of pectin methylesterase inhibitors. Plant Physiol. **173**: 1075–1093.

Hocq, L., Pelloux, J., and Lefebvre, V. (2017b). Connecting homogalacturonan-type pectin remodeling to acid growth. Trends Plant Sci. **22**: 20–29.

Hoffmann, N., Benske, A., Betz, H., Schuetz, M., and Lacey Samuels, A. (2020). Laccases and peroxidases co-localize in lignified secondary cell walls throughout stem development. Plant Physiol. **184**: 806–822.

Hofhuis, H. et al. (2016). Morphomechanical innovation drives explosive seed dispersal. Cell **166**: 222–233.

Höfte, H. and Voxeur, A. (2017). Plant cell walls. Curr. Biol. **27**: R865–R870.

Hothorn, M., Wolf, S., Aloy, P., Greiner, S., and Scheffzek, K. (2004). Structural insights into the target specificity of plant invertase and pectin methylesterase inhibitory proteins. Plant Cell **16**: 3437–3447.

Jacobowitz, J.R., Doyle, W.C., and Weng, J.K. (2019). PRX9 and PRX40 are extensin peroxidases essential for maintaining tapetum and microspore cell wall integrity during arabidopsis anther development. Plant Cell **31**: 848–861.

Javelle, M., Vernoud, V., Rogowsky, P.M., and Ingram, G.C. (2011). Epidermis: the formation and functions of a fundamental plant tissue. New Phytol. **189**: 17–39.

Jemmat, A.M., Ranocha, P., Le Ru, A., Neel, M., Jauneau, A., Raggi, S., Ferrari, S., Burlat, V., and Dunand, C. (2020). Coordination of five class III peroxidase-encoding genes for early germination events

of *Arabidopsis thaliana*. Plant Sci. **298**: 110565.

Jiang, L., Yang, S.L., Xie, L.F., Puah, C.S., Zhang, X.Q., Yang, W.C., Sundaresan, V., and Ye, D. (2005). VANGUARD1 encodes a pectin methylesterase that enhances pollen tube growth in the *Arabidopsis* style and transmitting tract. Plant Cell **17**: 584–596.

Jones, L., Milne, J.L., Ashford, D., McCann, M.C., and McQueen-Mason, S.J. (2005). A conserved functional role of pectic polymers in stomatal guard cells from a range of plant species. Planta **221**: 255–264.

Joseleau, J.P. and Ruel, K. (1997). Study of lignification by noninvasive techniques in growing maize internodes (an investigation by fourier transform infrared cross-polarization-magic angle spinning ^{13}C-nuclear magnetic resonance spectroscopy and immunocytochemical transmission electron microscopy). Plant Physiol. **114**: 1123–1133.

Kalmbach, L., Hématy, K., De Bellis, D., Barberon, M., Fujita, S., Ursache, R., Daraspe, J., and Geldner, N. (2017). Transient cell-specific EXO70A1 activity in the CASP domain and Casparian strip localization. Nat. Plants **3**: 17058.

Kato, N., Pontier, D., and Lam, E. (2002). Spectral profiling for the simultaneous observation of four distinct fluorescent proteins and detection of protein-protein interaction via fluorescence resonance energy transfer in tobacco leaf nuclei. Plant Physiol. **129**: 931–942.

Kim, M.J., Ciani, S., and Schachtman, D.P. (2010). A peroxidase contributes to ros production during Arabidopsis root response to potassium deficiency. Mol. Plant **3**: 420–427.

Kiyoto, S., Yoshinaga, A., and Takabe, K. (2014). Relative deposition of xylan and 8-5′-linked lignin structure in *Chamaecyparis obtusa*, as revealed by double immunolabeling by using monoclonal antibodies. Planta **241**: 243–256.

Kohn, R. and Furda, I. (1968). Binding of calcium ions to acetyl derivatives of pectin. Collect. Czechoslov. Chem. Commun. **33**: 2217–2225.

Kunieda, T., Shimada, T., Kondo, M., Nishimura, M., Nishitani, K., and Hara-Nishimura, I. (2013). Spatiotemporal secretion of PEROXIDASE36 is required for seed coat mucilage extrusion in *Arabidopsis*. Plant Cell **25**: 1355–1367.

Lai, C.P., Huang, L.M., Chen, L.F.O., Chan, M.T., and Shaw, J.F. (2017). Genome-wide analysis of GDSL-type esterases/lipases in Arabidopsis. Plant Mol. Biol. **95**: 181–197.

Laloi, C., Apel, K., and Danon, A. (2004). Reactive oxygen signalling: The latest news. Curr. Opin. Plant Biol. **7**: 323–328.

Lee, C., Teng, Q., Zhong, R., Yuan, Y., Haghighat, M., and Ye, Z.H. (2012). Three arabidopsis DUF579 domain-containing GXM proteins are methyltransferases catalyzing 4-o-methylation of glucuronic acid on xylan. Plant Cell Physiol. **53**: 1934–1949.

Lee, K.J.D., Marcus, S.E., and Knox, J.P. (2011). Cell wall biology: perspectives from cell wall imaging. Mol. Plant **4**: 212–219.

Lee, Y. et al. (2018). A lignin molecular brace controls precision processing of cell walls critical for surface integrity in Arabidopsis. Cell **173**: 1468-1480.e9.

Lee, Y., Rubio, M.C., Alassimone, J., and Geldner, N. (2013). A mechanism for localized lignin deposition in the endodermis. Cell **153**: 402–412.

Lefebvre, V., Fortabat, M.N., Ducamp, A., North, H.M., Maia-Grondard, A., Trouverie, J., Boursiac, Y., Mouille, G., and Durand-Tardif, M. (2011). ESKIMO1 disruption in Arabidopsis alters vascular tissue and impairs water transport. PLoS One **6**: e16645.

Levesque-Tremblay, G., Müller, K., Mansfield, S.D., and Haughn, G.W. (2015). HIGHLY METHYL ESTERIFIED SEEDS is a pectin methyl esterase involved in embryo development. Plant Physiol. **167**: 725–737.

Li, B., Kamiya, T., Kalmbach, L., Yamagami, M., Yamaguchi, K., Shigenobu, S., Sawa, S., Danku, J.M.C., Salt, D.E., Geldner, N., and Fujiwara, T. (2017). Role of LOTR1 in nutrient transport through

organization of spatial distribution of root endodermal barriers. Curr. Biol. **27**: 758–765.

Li, G., Yang, X., Zhang, X., Song, Y., Liang, W., and Zhang, D. (2018a). Rice morphology determinant-mediated actin filament organization contributes to pollen tube growth. Plant Physiol. **177**: 255–270.

Li, P., Yang, M., Chang, J., Wu, J., Zhong, F., Rahman, A., Qin, H., and Wu, S. (2018b). Spatial expression and functional analysis of casparian strip regulatory genes in endodermis reveals the conserved mechanism in tomato. Front. Plant Sci. **9**: 832.

Lin, D., Lopez-Sanchez, P., and Gidley, M.J. (2016). Interactions of pectins with cellulose during its synthesis in the absence of calcium. Food Hydrocoll. **52**: 57–68.

Liners, F., Letesson, J.J., Didembourg, C., and Van Cutsem, P. (1989). Monoclonal aantibodies against pectin: recognition of a conformation induced by calcium. Plant Physiol. **91**: 1419–24.

Lion, C., Simon, C., Huss, B., Blervacq, A.S., Tirot, L., Toybou, D., Spriet, C., Slomianny, C., Guerardel, Y., Hawkins, S., and Biot, C. (2017). BLISS: a bioorthogonal dual-labeling strategy to unravel lignification dynamics in plants. Cell Chem. Biol. **24**: 326–338.

Lopez-Sanchez, P., Martinez-Sanz, M., Bonilla, M.R., Wang, D., Walsh, C.T., Gilbert, E.P., Stokes, J.R., and Gidley, M.J. (2016). Pectin impacts cellulose fibre architecture and hydrogel mechanics in the absence of calcium. Carbohydr. Polym. **153**: 236–245.

Lunin, V. V. et al. (2020). Molecular mechanism of polysaccharide acetylation by the arabidopsis xylan *O*-acetyltransferase XOAT1. Plant Cell **32**: 2367–2382.

Luo, N., Yan, A., Liu, G., Guo, J., Rong, D., Kanaoka, M.M., Xiao, Z., Xu, G., Higashiyama, T., Cui, X., and Yang, Z. (2017). Exocytosis-coordinated mechanisms for tip growth underlie pollen tube growth guidance. Nat. Commun. **8**: 1–10.

Lv, M. et al. (2019). Molecular characterization and function analysis of the rice OsDUF1191 family. Biotechnol. Biotechnol. Equip. **33**: 1608–1615.

Lynch, M.A. and Staehelin, L.A. (1992). Domain-specific and cell type-specific localization of two types of cell wall matrix polysaccharides in the clover root tip. J. Cell Biol. **118**: 467–479.

Macquet, A., Ralet, M.C., Kronenberger, J., Marion-Poll, A., and North, H.M. (2007). *In situ*, chemical and macromolecular study of the composition of *Arabidopsis thaliana* seed coat mucilage. Plant Cell Physiol. **48**: 984–999.

Majda M, Grones P, Ida Maria S, Thomas V, Pascale M, Pawel K, Beata Z.M, Corrado V, Henrik J, Ewa J. M, Olivier H, and Stéphanie R (2017). Mechanochemical polarization of contiguous cell walls shapes plant pavement cells. Dev. Cell **43**: 290–304.

Malinovsky, F.G., Fangel, J.U., and Willats, W.G.T. (2014). The role of the cell wall in plant immunity. Front. Plant Sci. **5**: 178.

Manabe, Y. et al. (2011). Loss-of-function mutation of REDUCED WALL ACETYLATION2 in Arabidopsis leads to reduced cell wall acetylation and increased resistance to Botrytis cinerea. PLANT Physiol. **155**: 1068–1078.

Manabe, Y., Verhertbruggen, Y., Gille, S., Harholt, J., Chong, S.L., Pawar, P.M.A., Mellerowicz, E.J., Tenkanen, M., Cheng, K., Pauly, M., and Scheller, H.V. (2013). Reduced wall acetylation proteins play vital and distinct roles in cell wall *O*-acetylation in Arabidopsis. Plant Physiol. **163**: 1107–1117.

Marty, P., Goldberg, R., Liberman, M., Vian, B., Bertheau, Y., and Jouan, B. (1995). Composition and localization of pectic polymers in the stems of two *Solanum tuberosum genotypes*. Plant Physiol. Biochem. **33**: 409–417.

Mase, K. and Tsukagoshi, H. (2021). Reactive oxygen species link gene regulatory networks during Arabidopsis root development. Front. Plant Sci. **12**.

McCann, M.C., Wells, B., and Roberts, K. (1992). Complexity in the spatial localization and length distribution of plant cell-wall matrix polysaccharides. J. Microsc. **166**: 123–136.

McFarlane, H.E., Döring, A., and Persson, S. (2014). The cell biology of cellulose synthesis. Annu. Rev. Plant

Biol. **65**: 69–94.

McGee, R., Dean, G.H., Mansfield, S.D., and Haughn, G.W. (2019). Assessing the utility of seed coat-specific promoters to engineer cell wall polysaccharide composition of mucilage. Plant Mol. Biol. **101**: 373–387.

McNamara, J.T., Morgan, J.L.W., and Zimmer, J. (2015). A molecular description of cellulose biosynthesis. Annu. Rev. Biochem. **84**: 895–921.

McNeil, M., Darvill, A.G., Fry, S.C., and Albersheim, P. (1984). Structure and function of the primary cell walls of plants. Annu. Rev. Biochem. **53**: 625–663.

Mendrinna, A. and Persson, S. (2015). Root hair growth: it's a one way street. F1000Prime Rep. **7**: 23.

Miao, Y., Li, H.Y., Shen, J., Wang, J., and Jiang, L. (2011). QUASIMODO 3 (QUA3) is a putative homogalacturonan methyltransferase regulating cell wall biosynthesis in Arabidopsis suspension-cultured cells. J. Exp. Bot. **62**: 5063–5078.

Micheli, F. (2001). Pectin methylesterases: cell wall enzymes with important roles in plant physiology. Trends Plant Sci. **6**: 414–419.

Mishler-Elmore, J.W., Zhou, Y., Sukul, A., Oblak, M., Tan, L., Faik, A., and Held, M.A. (2021). Extensins: self-assembly, crosslinking, and the role of peroxidases. Front. Plant Sci. **12**: 872.

Mizukami, A.G. et al. (2016). The AMOR arabinogalactan sugar chain induces pollen-tube competency to respond to ovular guidance. Curr. Biol. **26**: 1091–1097.

Mnich, E. et al. (2020). Phenolic cross-links: building and de-constructing the plant cell wall. Nat. Prod. Rep. **37**: 919–961.

Mohnen, D. (2008). Pectin structure and biosynthesis. Curr. Opin. Plant Biol. **11**: 266–277.

Mølgaard, A. and Larsen, S. (2004). Crystal packing in two pH-dependent crystal forms of rhamnogalacturonan acetylesterase. Acta Crystallogr. Sect. D Biol. Crystallogr. **60**: 472–478.

Mollet, J.C., Leroux, C., Dardelle, F., and Lehner, A. (2013). Cell wall composition, biosynthesis and remodeling during pollen tube growth. Plants **2**: 107–147.

Morel, O., Lion, C., Neutelings, G., Stefanov, J., Baldacci-Cresp, F., Simon, C., Biot, C., Hawkins, S., and Spriet, C. (2021). REPRISAL: mapping lignification dynamics using chemistry, data segmentation, and ratiometric analysis. Plant Physiol.: DOI: 10.1093/PLPHYS/KIAB490.

Morris, G.M., Ruth, H., Lindstrom, W., Sanner, M.F., Belew, R.K., Goodsell, D.S., and Olson, A.J. (2009). AutoDock4 and AutoDockTools4: automated docking with selective receptor flexibility. J. Comput. Chem. **30**: 2785–2791.

Morvan, O., Quentin, M., Jauneau, A., Mareck, A., and Morvan, C. (1998). Immunogold localization of pectin methylesterases in the cortical tissues of flax hypocotyl. Protoplasma **202**: 175–184.

Mouille, G., Ralet, M.C., Cavelier, C., Eland, C., Effroy, D., Hématy, K., McCartney, L., Truong, H.N., Gaudon, V., Thibault, J.F., Marchant, A., and Höfte, H. (2007). Homogalacturonan synthesis in *Arabidopsis thaliana* requires a golgi-localized protein with a putative methyltransferase domain. Plant J. **50**: 605–614.

Mravec, J. et al. (2014). Tracking developmentally regulated post-synthetic processing of homogalacturonan and chitin using reciprocal oligosaccharide probes. Dev. **141**: 4841–4850.

Mravec, J., Kračun, S.K., Rydahl, M.G., Westereng, B., Pontiggia, D., De Lorenzo, G., Domozych, D.S., and Willats, W.G.T. (2017). An oligogalacturonide-derived molecular probe demonstrates the dynamics of calcium-mediated pectin complexation in cell walls of tip-growing structures. Plant J. **91**: 534–546.

Muller, K., Linkies, A., Vreeburg, R.A.M., Fry, S.C., Krieger-Liszkay, A., and Leubner-Metzger, G. (2009). *In vivo* cell wall loosening by hydroxyl radicals during cress seed germination and elongation growth. Plant Physiol. **150**: 1855–1865.

Nakamura, M. and Grebe, M. (2018). Outer, inner and planar polarity in the Arabidopsis root. Curr. Opin.

Plant Biol. **41**: 46–53.

Nakayama, T., Shinohara, H., Tanaka, M., Baba, K., Ogawa-Ohnishi, M., and Matsubayashi, Y. (2017). A peptide hormone required for Casparian strip diffusion barrier formation in Arabidopsis roots. Science (80-.). **355**: 284–286.

Nassar, A., Darrasse, A., Lemattre, M., Kotoujansky, A., Dervin, C., Vedel, R., and Bertheau, Y. (1996). Characterization of *Erwinia chrysanthemi* by pectinolytic isozyme polymorphism and restriction fragment length polymorphism analysis of PCR- amplified fragments of pel genes. Appl. Environ. Microbiol. **62**: 2228–2235.

Nelson, B.K., Cai, X., and Nebenführ, A. (2007). A multicolored set of in vivo organelle markers for co-localization studies in Arabidopsis and other plants. Plant J. **51**: 1126–1136.

Ogawa, M., Kay, P., Wilson, S., and Swain, S.M. (2009). *Arabidopsis* dehiscence zone polygalacturonase1 (ADPG1), ADPG2, and QUARTET2 are polygalacturonases required for cell separation during reproductive development in *Arabidopsis*. Plant Cell **21**: 216–233.

Oliver, D.J., Nikolau, B.J., and Wurtele, E.S. (2009). Acetyl-CoA-Life at the metabolic nexus. Plant Sci. **176**: 597–601.

Oosterveld, A., Beldman, G., Searle-Van Leeuwen, M.J.F., and Voragen, A.G.J. (2000). Effect of enzymatic deacetylation on gelation of sugar beet pectin in the presence of calcium. Carbohydr. Polym. **43**: 249–256.

Østergaard, L., Teilum, K., Mirza, O., Mattsson, O., Petersen, M., Welinder, K.G., Mundy, J., Gajhede, M., and Henriksen, A. (2000). Arabidopsis ATP A2 peroxidase. Expression and high-resolution structure of a plant peroxidase with implications for lignification. Plant Mol. Biol. **44**: 231–243.

Pacheco, J.M. et al. (2022). Apoplastic class III peroxidases PRX62 and PRX69 promote Arabidopsis root hair growth at low temperature. Nat. Commun. **13**.

Park, S., Szumlanski, A.L., Gu, F., Guo, F., and Nielsen, E. (2011). A role for CSLD3 during cell-wall synthesis in apical plasma membranes of tip-growing root-hair cells. Nat. Cell Biol. **13**: 973–980.

Park, Y.B. and Cosgrove, D.J. (2015). Xyloglucan and its interactions with other components of the growing cell wall. Plant Cell Physiol. **56**: 180–194.

Passardi, F., Cosio, C., Penel, C., and Dunand, C. (2005). Peroxidases have more functions than a swiss army knife. Plant Cell Rep. **24**: 255–265.

Patron, N.J. et al. (2015). Standards for plant synthetic biology: A common syntax for exchange of DNA parts. New Phytol. **208**: 13–19.

Pauly, M. and Ramírez, V. (2018). New insights into wall polysaccharide o-acetylation. Front. Plant Sci. **9**: 1210

Penel, C. and Dunand, C. (2009). Signaling via plant peroxidases. In Signaling and Communication in Plants (Springer, Berlin, Heidelberg), pp. 155–171.

Pérez, S., Mazeau, K., and Hervé du Penhoat, C. (2000). The three-dimensional structures of the pectic polysaccharides. Plant Physiol. Biochem. **38**: 37–55.

Pérez, S., Sarkar, A., Rivet, A., Breton, C., and Imberty, A. (2015). Glyco3d: a portal for structural glycosciences. Methods Mol. Biol. **1273**: 241–258.

Pfister, A. et al. (2014). A receptor-like kinase mutant with absent endodermal diffusion barrier displays selective nutrient homeostasis defects. Elife **3**: e03115.

Phan, J.L. and Burton, R.A. (2018). New insights into the composition and structure of seed mucilage. Annu. Plant Rev. Online **1**: 63–104.

Philippe, F., Pelloux, J., and Rayon, C. (2017). Plant pectin acetylesterase structure and function: new insights from bioinformatic analysis. BMC Genomics **18**: 456.

Popper, Z.A., Michel, G., Hervé, C., Domozych, D.S., Willats, W.G.T., Tuohy, M.G., Kloareg, B., and Stengel, D.B. (2011). Evolution and diversity of plant cell walls: from algae to flowering plants. Annu.

Rev. Plant Biol. **62**: 567–590.

Potikha, T. and Delmer, D.P. (1995). A mutant of *Arabidopsis thaliana* displaying altered patterns of cellulose deposition. Plant J. **7**: 453–460.

Qin, P., Ting, D., Shieh, A., and McCormick, S. (2012). Callose plug deposition patterns vary in pollen tubes of *Arabidopsis thaliana* ecotypes and tomato species. BMC Plant Biol. **12**: 178.

Ralet, M.C., Crépeau, M.J., Buchholt, H.C., and Thibault, J.F. (2003). Polyelectrolyte behaviour and calcium binding properties of sugar beet pectins differing in their degrees of methylation and acetylation. Biochem. Eng. J. **16**: 191–201.

Ranocha, P., Ranocha, P., Francoz, E., Francoz, E., Burlat, V., Dunand, C., and Dunand, C. (2014). Expression of *PRX36 PMEI6* and *SBT1.7* is controlled by complex transcription factor regulatory networks for proper seed coat mucilage extrusion. Plant Signal. Behav. **9**: e977734.

Renard, C.M.G.C. and Jarvis, M.C. (1999). Acetylation and methylation of homogalacturonans 2: Effect on ion-binding properties and conformations. Carbohydr. Polym. **39**: 209–216.

Reyt, G., Chao, Z., Flis, P., Salas-González, I., Castrillo, G., Chao, D.Y., and Salt, D.E. (2020). Uclacyanin proteins are required for lignified nanodomain formation within Casparian strips. Curr. Biol. **30**: 4103–4111.

Ridley, B.L., O'Neill, M.A., and Mohnen, D. (2001). Pectins: structure, biosynthesis, and oligogalacturonide-related signaling. Phytochemistry **57**: 929–967.

Rihouey, C., Jauneau, A., Cabin-Flaman, A., Demarty, M., Lefebvre, F., and Morvan, C. (1995). Calcium and acidic pectin distribution in flax cell walls: evidence for different kinds of linkages in the cell junction and middle lamella of the cortical parenchyma of *flax hypocotyl*. Plant Physiol. Biochem. **33**: 497–508.

Roberts, K. (1990). Structures at the plant cell surface. Curr. Opin. Cell Biol. **2**: 920–928.

Roberts, K. (1994). The plant extracellular matrix: in a new expansive mood. Curr. Opin. Cell Biol. **6**: 688–694.

Röckel, N., Wolf, S., Kost, B., Rausch, T., and Greiner, S. (2008). Elaborate spatial patterning of cell-wall PME and PMEI at the pollen tube tip involves PMEI endocytosis, and reflects the distribution of esterified and de-esterified pectins. Plant J. **53**: 133–143.

Rojas-Murcia, N., Hématy, K., Lee, Y., Emonet, A., Ursache, R., Fujita, S., de Bellis, D., and Geldner, N. (2020). High-order mutants reveal an essential requirement for peroxidases but not laccases in Casparian strip lignification. Proc. Natl. Acad. Sci. U. S. A. **117**: 29166–29177.

Roppolo, D., Boeckmann, B., Pfister, A., Boutet, E., Rubio, M.C., Dénervaud-Tendon, V., Vermeer, J.E.M., Gheyselinck, J., Xenarios, I., and Geldner, N. (2014). Functional and evolutionary analysis of the CASPARIAN STRIP MEMBRANE DOMAIN PROTEIN family. Plant Physiol. **165**: 1709.

Roppolo, D., De Rybel, B., Tendon, V.D., Pfister, A., Alassimone, J., Vermeer, J.E.M., Yamazaki, M., Stierhof, Y.D., Beeckman, T., and Geldner, N. (2011). A novel protein family mediates Casparian strip formation in the endodermis. Nature **473**: 381–384.

Ros Barceló, A. (2005). Xylem parenchyma cells deliver the H_2O_2 necessary for lignification in differentiating xylem vessels. Planta **220**: 747–756.

Rounds, C.M., Lubeck, E., Hepler, P.K., and Winship, L.J. (2011). Propidium iodide competes with Ca^{2+} to label pectin in pollen tubes and *Arabidopsis* root hairs. Plant Physiol. **157**: 175–187.

Roy, S., Gillen, G., Conway, W.S., Watada, A.E., and Wergin, W.P. (2003). Endoxylanase expressed during papaya fruit ripening: purification, cloning and characterization. Funct. Plant Biol. **30**: 433–441.

Roy, S., Gillen, G., Conway, W.S., Watada, A.E., and Wergin, W.P. (1995). Use of secondary ion mass spectrometry to image ^{44}calcium uptake in the cell walls of apple fruit. Protoplasma **189**: 163–172.

Roy, S., Jauneau, A., and Vian, B. (1994). Analytical detection of calcium ions and immunocytochemical visualization of homogalacturonic sequences in the ripe cherry tomato. Plant Physiol. Biochem. **32**: 633–640.

Roy, S., Vian, B., and Roland, J.-C. (1992). Immunocytochemical study of the deesterification patterns during cell wall autolysis in the ripening of cherry tomato. Plant Physiol. Biochem. **30**: 139–146.

Roy, S., Watada, A.E., and Wergin, W.P. (1997). Characterization of the cell wall microdomain surrounding plasmodesmata in apple fruit. Plant Physiol. **114**: 539–547.

Rui, Y., Chen, Y., Yi, H., Purzycki, T., Puri, V.M., and Anderson, C.T. (2019). Synergistic pectin degradation and guard cell pressurization underlie stomatal pore formation. Plant Physiol. **180**: 66–77.

Rui, Y., Xiao, C., Yi, H., Kandemir, B., Wang, J.Z., Puri, V.M., and Anderson, C.T. (2017). POLYGALACTURONASE INVOLVED IN EXPANSION3 functions in seedling development, rosette growth, and stomatal dynamics in *Arabidopsis thaliana*. Plant Cell **29**: 2413–2432.

Saez-Aguayo, S., Ralet, M.-C., Berger, A., Botran, L., Ropartz, D., Marion-Poll, A., and North, H.M. (2013). Pectin methylesterase inhibitor6 promotes Arabidopsis mucilage release by limiting methylesterification of homogalacturonan in seed coat epidermal cells. Plant Cell **25**: 308–323.

Sainsbury, F., Thuenemann, E.C., and Lomonossoff, G.P. (2009). PEAQ: versatile expression vectors for easy and quick transient expression of heterologous proteins in plants. Plant Biotechnol. J. **7**: 682–693.

Sampathkumar, A., Krupinski, P., Wightman, R., Milani, P., Berquand, A., Boudaoud, A., Hamant, O., Jönsson, H., and Meyerowitz, E.M. (2014). Subcellular and supracellular mechanical stress prescribes cytoskeleton behavior in Arabidopsis cotyledon pavement cells. Elife **3**: e01967.

Scheler, C. et al. (2015). Promotion of testa rupture during garden cress germination involves seed compartment-specific expression and activity of pectin methylesterases. Plant Physiol. **167**: 200–215.

Scheller, H.V. and Ulvskov, P. (2010). Hemicelluloses. Annu. Rev. Plant Biol. **61**: 263–289.

Schindler, T.M. (1998). The new view of the primary cell wall. Zeitschrift für Pflanzenernährung und Bodenkd. **161**: 499–508.

Schoenaers, S., Balcerowicz, D., and Vissenberg, K. (2017). Molecular mechanisms regulating root hair tip growth: a comparison with pollen tubes. In Pollen Tip Growth (Springer International Publishing), pp. 167–243.

Schuetz, M., Benske, A., Smith, R.A., Watanabe, Y., Tobimatsu, Y., Ralph, J., Demura, T., Ellis, B., and Samuels, A.L. (2014). Laccases direct lignification in the discrete secondary cell wall domains of protoxylem. Plant Physiol. **166**: 798–807.

Schultink, A., Naylor, D., Dama, M., and Pauly, M. (2015). The role of the plant-specific ALTERED XYLOGLUCAN9 protein in Arabidopsis cell wall polysaccharide O-acetylation. Plant Physiol. **167**: 1271–1283.

Schweikert, C., Liszkay, A., and Schopfer, P. (2000). Scission of polysaccharides by peroxidase-generated hydroxyl radicals. Phytochemistry **53**: 565–570.

Seifert, G.J. and Blaukopf, C. (2010). Irritable walls: The plant extracellular matrix and signaling. Plant Physiol. **153**: 467–478.

Sénéchal, F., Habrylo, O., Hocq, L., Domon, J.M., Marcelo, P., Lefebvre, V., Pelloux, J., and Mercadante, D. (2017). Structural and dynamical characterization of the pH-dependence of the pectin methylesterase-pectin methylesterase inhibitor complex. J. Biol. Chem. **292**: 21538–21547.

Sénéchal, F., Wattier, C., Rustérucci, C., and Pelloux, J. (2014). Homogalacturonan-modifying enzymes: structure, expression, and roles in plants. J. Exp. Bot. **65**: 5125–5160.

Shi, C.L., Alling, R.M., Hammerstad, M., and Aalen, R.B. (2019). Control of organ abscission and other cell separation processes by evolutionary conserved peptide signaling. Plants **8**: 225.

Shin, Y., Chane, A., Jung, M., and Lee, Y. (2021). Recent advances in understanding the roles of pectin as an active participant in plant signaling networks. Plants **10**.

Shinoda, H., Ma, Y., Nakashima, R., Sakurai, K., Matsuda, T., and Nagai, T. (2018). Acid-tolerant monomeric GFP from *Olindias formosa*. Cell Chem. Biol. **25**: 330-338.e7.

Simon, C., Spriet, C., Hawkins, S., and Lion, C. (2018). Visualizing lignification dynamics in plants with click chemistry: dual labeling is BLISS! J. Vis. Exp. **2018**: e56947.

Sinclair, S.A., Larue, C., Bonk, L., Khan, A., Castillo-Michel, H., Stein, R.J., Grolimund, D., Begerow, D., Neumann, U., Haydon, M.J., and Krämer, U. (2017). Etiolated seedling development requires repression of photomorphogenesis by a small cell-wall-derived dark signal. Curr. Biol. **27**: 3403-3418.e7.

Smallwood, M., Martin, H., and Knox, J.P. (1995). An epitope of rice threonine- and hydroxyproline-rich glycoprotein is common to cell wall and hydrophobic plasma-membrane glycoproteins. Planta An Int. J. Plant Biol. **196**: 510–522.

Šola, K., Dean, G.H., and Haughn, G.W. (2019a). Arabidopsis seed mucilage: a specialised extracellular matrix that demonstrates the structure-function versatility of cell wall polysaccharides. Annu. Plant Rev. Online **2**: 1085–1115.

Šola, K., Gilchrist, E.J., Ropartz, D., Wang, L., Feussner, I., Mansfield, S.D., Ralet, M.C., and Haughn, G.W. (2019b). RUBY, a putative galactose oxidase, influences pectin properties and promotes cell-to-cell adhesion in the seed coat epidermis of Arabidopsis. Plant Cell **31**: 809–831.

Somerville, C., Bauer, S., Brininstool, G., Facette, M., Hamann, T., Milne, J., Osborne, E., Paredez, A., Persson, S., Raab, T., Vorwerk, S., and Youngs, H. (2004). Toward a systems approach to understanding plant cell walls. Science (80-.). **306**: 2206–2211.

Sotiriou, P., Giannoutsou, E., Panteris, E., Galatis, B., and Apostolakos, P. (2018). Local differentiation of cell wall matrix polysaccharides in sinuous pavement cells: its possible involvement in the flexibility of cell shape. Plant Biol. **20**: 223–237.

Stoddard, A. and Rolland, V. (2019). I see the light! fluorescent proteins suitable for cell wall/apoplast targeting in *Nicotiana benthamiana* leaves. Plant Direct **3**.

Stranne, M., Ren, Y., Fimognari, L., Birdseye, D., Yan, J., Bardor, M., Mollet, J.C., Komatsu, T., Kikuchi, J., Scheller, H. V, and Sakuragi, Y. (2018). TBL10 is required for O-acetylation of pectic rhamnogalacturonan-I in *Arabidopsis thaliana*. Plant J. **96**: 772–785.

Sun, A., Yu, B., Zhang, Q., Peng, Y., Yang, J., Sun, Y., Qin, P., Jia, T., Smeekens, S., and Teng, S. (2020). MYC2-activated TRICHOME BIREFRINGENCE-LIKE37 acetylates cell walls and enhances herbivore resistance. Plant Physiol. **184**: 1083–1096.

Swanson, S. and Gilroy, S. (2010). ROS in plant development. Physiol. Plant. **138**: 384–392.

Temple, H. et al. (2022). Golgi-localized putative S-adenosyl methionine transporters required for plant cell wall polysaccharide methylation. Nat. Plants **8**: 656–669.

Temple, H., Mortimer, J.C., Tryfona, T., Yu, X., Lopez-Hernandez, F., Sorieul, M., Anders, N., and Dupree, P. (2019). Two members of the DUF579 family are responsible for arabinogalactan methylation in Arabidopsis. Plant Direct **3**: e00117.

Tian, Y., Zhang, S., Liu, X., and Zhang, Z. (2021). Global investigation of TBL gene family in Rose (*Rosa chinensis*) unveils RcTBL16 is a susceptibility gene in gray mold resistance. Front. Plant Sci. **12**.

Tobimatsu, Y. and Schuetz, M. (2019). Lignin polymerization: how do plants manage the chemistry so well? Curr. Opin. Biotechnol. **56**: 75–81.

Trezel P (2018). Molecular interactions within cell-wall microdomains control Arabidopsis seed mucilage release.

Trinh, D.C., Alonso-Serra, J., Asaoka, M., Colin, L., Cortes, M., Malivert, A., Takatani, S., Zhao, F., Traas, J., Trehin, C., and Hamant, O. (2021). How mechanical forces shape plant organs. Curr. Biol. **31**: R143–R159.

Tsai, A.Y.L., Kunieda, T., Rogalski, J., Foster, L.J., Ellis, B.E., and Haughn, G.W. (2017). Identification and characterization of Arabidopsis seed coat mucilage proteins. Plant Physiol. **173**: 1059–1074.

Turbant, A., Fournet, F., Lequart, M., Zabijak, L., Pageau, K., Bouton, S., and Van Wuytswinkel, O. (2016). PME58 plays a role in pectin distribution during seed coat mucilage extrusion through homogalacturonan modification. J. Exp. Bot. **67**: 2177–2190.

Turner, S., Gallois, P., and Brown, D. (2007). Tracheary element differentiation. Annu. Rev. Plant Biol. **58**: 407–433.

Uluisik, S. and Seymour, G.B. (2020). Pectate lyases: their role in plants and importance in fruit ripening. Food Chem. **309**.

Ventimilla, D., Velázquez, K., Ruiz-Ruiz, S., Terol, J., Pérez-Amador, M.A., Vives, M.ª. C., Guerri, J., Talon, M., and Tadeo, F.R. (2021). IDA (INFLORESCENCE DEFICIENT IN ABSCISSION)-like peptides and HAE (HAESA)-like receptors regulate corolla abscission in *Nicotiana benthamiana* flowers. BMC Plant Biol. **21**: 226.

Verhertbruggen, Y., Marcus, S.E., Haeger, A., Ordaz-Ortiz, J.J., and Knox, J.P. (2009). An extended set of monoclonal antibodies to pectic homogalacturonan. Carbohydr. Res. **344**: 1858–1862.

Viudes, S., Burlat, V., and Dunand, C. (2020). Seed mucilage evolution: diverse molecular mechanisms generate versatile ecological functions for particular environments. In Plant Cell and Environment (John Wiley & Sons, Ltd), pp. 2857–2870.

Viudes, S., Dunand, C., and Burlat, V. (2021). Myxospermy evolution in brassicaceae: a highly complex and diverse trait with Arabidopsis as an uncommon model. Cells **10**.

Volokita, M., Rosilio-Brami, T., Rivkin, N., and Zik, M. (2011). Combining comparative sequence and genomic data to ascertain phylogenetic relationships and explore the evolution of the large gdSL-lipase family in land plants. Mol. Biol. Evol. **28**: 551–565.

Voxeur, A. et al. (2019). Oligogalacturonide production upon *Arabidopsis thaliana-Botrytis cinerea* interaction. Proc. Natl. Acad. Sci. U. S. A. **116**: 19743–19752.

Wang, L., Gao, Y., Wang, S., Zhang, Q., and Yang, S. (2021). Genome-wide identification of PME genes, evolution and expression analyses in soybean (*Glycine max L.*). BMC Plant Biol. **21**: 1–20.

von Wangenheim, D., Goh, T., Dietrich, D., and Bennett, M.J. (2017). Plant Biology: building barriers… in roots. Curr. Biol. **27**: R172–R174.

Weber, E., Engler, C., Gruetzner, R., Werner, S., and Marillonnet, S. (2011). A modular cloning system for standardized assembly of multigene constructs. PLoS One **6**: e16765.

Willats, W.G.T., McCartney, L., and Knox, J.P. (2001). *In-situ* analysis of pectic polysaccharides in seed mucilage and at the root surface of *Arabidopsis thaliana*. Planta **213**: 37–44.

Wolf, S., Mouille, G., and Pelloux, J. (2009). Homogalacturonan methyl-esterification and plant development. Mol. Plant **2**: 851–860.

Wormit, A. and Usadel, B. (2018). The multifaceted role of pectin methylesterase inhibitors (PMEIs). Int. J. Mol. Sci. **19**: 2878.

Wu, H.C., Huang, Y.C., Stracovsky, L., and Jinn, T.L. (2017). Pectin methylesterase is required for guard cell function in response to heat. Plant Signal. Behav. **12**: e1338227.

Wu, X.M., Yu, Y., Han, L.B., Li, C.L., Wang, H.Y., Zhong, N.Q., Yao, Y., and Xia, G.X. (2012). The tobacco BLADE-ON-PETIOLE2 gene mediates differentiation of the corolla abscission zone by controlling longitudinal cell expansion. Plant Physiol. **159**: 835–850.

Xu, F., Gonneau, M., Faucher, E., Habrylo, O., Lefebvre, V., Domon, J.-M., Martin, M., Sénéchal, F., Peaucelle, A., Pelloux, J., and Höfte, H. (2022). Biochemical characterization of pectin methylesterase inhibitor 3 from *Arabidopsis thaliana*. Cell Surf. **8**: 100080.

Yadav, S., Yadav, P.K., Yadav, D., and Yadav, K.D.S. (2009). Pectin lyase: a review. Process Biochem. **44**: 1–10.

Yang, J., Ding, C., Xu, B., Chen, C., Narsai, R., Whelan, J., Hu, Z., and Zhang, M. (2015). A Casparian strip domain-like gene, CASPL, negatively alters growth and cold tolerance. Sci. Rep. **5**.

Yang, Y., Yu, Y., Liang, Y., Anderson, C.T., and Cao, J. (2018). A profusion of molecular scissors for pectins: classification, expression, and functions of plant polygalacturonases. Front. Plant Sci. **9**: 1208.

Yi Chou, E., Schuetz, M., Hoffmann, N., Watanabe, Y., Sibout, R., and Samuels, A.L. (2018). Distribution, mobility, and anchoring of lignin-related oxidative enzymes in Arabidopsis secondary cell walls. J. Exp. Bot. **69**: 1849–1859.

Yi, H., Rui, Y., Kandemir, B., Wang, J.Z., Anderson, C.T., and Puri, V.M. (2018). Mechanical effects of cellulose, xyloglucan, and pectins on stomatal guard cells of *Arabidopsis thaliana*. Front. Plant Sci. **9**: 1566.

Yuan, Y., Teng, Q., Zhong, R., and Ye, Z.H. (2016). Roles of Arabidopsis TBL34 and TBL35 in xylan acetylation and plant growth. Plant Sci.

Zhang, B., Gao, Y., Zhang, L., and Zhou, Y. (2021). The plant cell wall: biosynthesis, construction, and functions. J. Integr. Plant Biol. **63**: 251–272.

Zhang, B., Zhang, L., Li, F., Zhang, D., Liu, X., Wang, H., Xu, Z., Chu, C., and Zhou, Y. (2017). Control of secondary cell wall patterning involves xylan deacetylation by a GDSL esterase. Nat. Plants **3**: 17017.

Zhang, P., Wang, H., Qin, X., Chen, K., Zhao, J., Zhao, Y., and Yue, B. (2019a). Genome-wide identification, phylogeny and expression analysis of the PME and PMEI gene families in maize. Sci. Rep. **9**: 1–12.

Zhang, T., Tang, H., Vavylonis, D., and Cosgrove, D.J. (2019b). Disentangling loosening from softening: insights into primary cell wall structure. Plant J. **100**: 1101–1117.

Zhao, Q., Nakashima, J., Chen, F., Yin, Y., Fu, C., Yun, J., Shao, H., Wang, X., Wang, Z.Y., and Dixon, R.A. (2013). LACCASE is necessary and nonredundant with PEROXIDASE for lignin polymerization during vascular development in Arabidopsis. Plant Cell **25**: 3976–3987.

Zheng, L., Xu, Y., Li, Q., and Zhu, B. (2021). Pectinolytic lyases: a comprehensive review of sources, category, property, structure, and catalytic mechanism of pectate lyases and pectin lyases. Bioresour. Bioprocess. **8**: 1–13.

Zhong, R., Cui, D., Phillips, D.R., Richardson, E.A., and Ye, Z.H. (2020). A group of *O*-acetyltransferases catalyze xyloglucan backbone acetylation and can alter xyloglucan xylosylation pattern and plant growth when expressed in Arabidopsis. Plant Cell Physiol. **61**: 1064.

Zhong, R., Cui, D., and Ye, Z.H. (2017). Regiospecific acetylation of xylan is mediated by a group of DUF231-containing *O*-acetyltransferases. Plant Cell Physiol. **58**: 2126–2138.

Zhong, R. and Ye, Z.H. (2007). Regulation of cell wall biosynthesis. Curr. Opin. Plant Biol. **10**: 564–572.

Zipor, G. and Oren-Shamir, M. (2013). Do vacuolar peroxidases act as plant caretakers? Plant Sci. **199**–**200**: 41–47.

Ziv, C., Zhao, Z., Gao, Y.G., and Xia, Y. (2018). Multifunctional roles of plant cuticle during plant-pathogen interactions. Front. Plant Sci. **9**: 1088.